UNIVERSIDAD DE CHILE
FACULTAD DE CIENCIAS FÍSICAS Y MATEMÁTICAS
DEPARTAMENTO DE ASTRONOMÍA

SEARCHING FOR DISTANT RR LYRAE IN THE GALACTIC HALO USING THE HIGH CADENCE TRANSIENT SURVEY

TESIS PARA OPTAR AL GRADO DE MAGISTER EN CIENCIAS, MENCION ASTRONOMÍA

GUSTAVO ENRIQUE MEDINA TOLEDO

PROFESOR GUÍA:
RICARDO MUÑOZ VIDAL

MIEMBROS DE LA COMISIÓN:
VALENTINO GONZÁLEZ CORVALÁN
KATHERINA VIVAS MALDONADO
FRANCISCO FÖRSTER BURÓN

Este trabajo ha sido parcialmente financiado por la Comisión Nacional de Investigación Científica y Tecnológica (CONICYT) y el Instituto Milenio de Astrofísica (MAS)

SANTIAGO DE CHILE
2017

RESUMEN DE LA MEMORIA PARA OPTAR
AL TÍTULO DE MAGISTER EN CIENCIAS, MENCION ASTRONOMÍA
POR: GUSTAVO ENRIQUE MEDINA TOLEDO
FECHA: 2017
PROF. GUÍA: SR. RICARDO MUÑOZ VIDAL

SEARCHING FOR DISTANT RR LYRAE IN THE GALACTIC HALO USING THE HIGH CADENCE TRANSIENT SURVEY

Búsqueda de estrellas RR Lyrae distantes en el halo Galáctico usando el High cadence Transient Survey

Utilizando datos del High cadence Transient Survey (HiTS), inspeccionamos el halo de la Vía Láctea en busca de estrellas variables RR Lyrae distantes ($\mathrm{d_H} > 100\,\mathrm{kpc}$). Los datos del proyecto HiTS, diseñado principalmente para encontrar explosiones de supernova en tiempo real, consisten en imágenes tomadas con la Dark Energy Camera que está montada en el telescopio Blanco (4 m) del Observatorio Inter-Americano de Cerro Tololo, en tres campañas distintas, y cubren con gran profundidad $\sim$ 200 grados cuadrados del Halo. Como resultado, identificamos un total de 332 RR Lyrae (173 en los datos tomados el año 2014 y 159 con datos del 2015), cubriendo un rango de distancias desde $\sim$ 9 hasta $\sim$ 260 kpc, aproximadamente. De acuerdo con nuestro estudio, dentro del grupo de RR Lyrae encontradas al menos 18 están a más de 90 kpc del Sol (16 más allá de 100 kpc).

El análisis del catálogo creado nos permitió estudiar la distribución espacial de RR Lyrae y relacionar tres sobredensidades con galaxias enanas esferoidales conocidas (Sextans, Leo IV y Leo V). Lo anterior se utilizó como validación de ideas asociadas al uso de RR Lyrae para el descubrimiento de galaxias de ultra-baja luminosidad difíciles de detectar con otros métodos. Usando la distribución espacial de las estrellas encontradas con HiTS 2014, construimos y analizamos perfiles de densidad de la Vía Láctea, de la forma $\rho(r) \sim r^{-n}$. Siguiendo una metodología de Monte Carlo vía cadenas de Markov, encontramos que el perfil que mejor ajusta a los datos es un perfil simple, con $n = -4{,}18^{+0{,}18}_{-0{,}19}$. Sin embargo, el ajuste de un perfil con quiebre es también válido, con el quiebre en $R_b = 19{,}34^{+10{,}66}_{-3{,}16}$ kpc, y pendientes interna y externa de $n_1 = -3{,}47^{+2{,}26}_{-1{,}32}$ y $n_2 = -4{,}23^{+0{,}33}_{-0{,}25}$, respectivamente.

Using data from the High cadence Transient Survey (HiTS), we inspected the halo of the Milky Way looking for distant RR Lyrae variable stars ($\mathrm{d}_H > 100\,\mathrm{kpc}$). The HiTS project, which was originally designed to find supernovae explosions in real time, consists of images taken with the Dark Energy Camera mounted at the Blanco telescope (4 m) at the Cerro Tololo Inter-American Observatory during three different campaigns, covering $\sim$ 200 sq. degrees of the Galactic halo. We identified a total of 332 RR Lyrae stars (173 with data from HiTS 2014, and 159 with HiTS 2015), covering a range in distance from $\sim$ 9 to $\sim$ 260 kpc. According to this study, within our sample of RR Lyrae stars at least 18 are beyond 90 kpc from the Sun (and 16 beyond 100 kpc).

The analysis of the catalog allowed us to study the spatial distribution of RR Lyrae stars and to associate three ovendensities with known dwarf spheroidal galaxies (Sextans, Leo IV y Leo V). We used this as a proof-of-concept for ideas about the role of RR Lyrae in the discovery of ultra-faint dwarf galaxies that might be difficult to find by other methods. Using the spatial distribution of RR Lyrae from HiTS 2014, we built and analyzed number density profiles of the Milky Way, of the form $\rho(r) \sim r^{-n}$. Following a Markov chain Monte Carlo methodology, we found that the best fit for the data is a simple power law with $n = -4{,}18^{+0{,}18}_{-0{,}19}$. However, fitting a broken profile is also valid, with a break at $R_b = 19{,}34^{+10{,}66}_{-3{,}16}$ kpc, and inner/outer slope of $n_1 = -3{,}47^{+2{,}26}_{-1{,}32}/n_2 = -4{,}23^{+0{,}33}_{-0{,}25}$.

Agradecimientos

Agradezco en primer lugar a mi familia por ser una continua fuente de motivación. En particular al Benja, al Seba y a mi mamá, la base de todo lo que soy y he podido hacer. Sin su ayuda nada de esto habría sido posible. Gracias!
A Nina, por ser una importante adición a mi vida, y por todo el cariño entregado :).
Quisiera agradacer a mis compañeros de Calán, Juanpi, Pepe, Seba Marino, Chelo, Grecco, Jorel, Juan, Mati, Seba, Nicolás, Julián, Ale, Amber, Blake, Valentin, Nathan, Ricardo, Sudeep, Coni, Suafle, Paula, José y Mari, por ser fuentes inagotables de entretención en momentos de distracción (y procrastinación), y por la ayuda prestada siempre que la necesité.
Mis agradecimientos a los miembros de la comisión, por ayudarme a mejorar la calidad de este trabajo. A Kathy por sus comentarios y por mantenerme continuamente motivado al permitirme trabajar con ella. Gracias por ser una tremenda influencia para mí. A Valentino González por su cuidadosa revisión de esta tesis. Al Pancho y a Ricardo por confiar en mí al permitirme trabajar en un proyecto sumamente interesante y con un tremendo potencial. Gracias por el apoyo entregado y su enorme comprensión en momentos difíciles. Quisiera también agradecer al Franco, Lander, Camilo y Pablo por los momentos de ocio compartidos en Final Destination, y a todos quienes semana a semana participaron de emocionantes encuentros futboleros. No puedo olvidar mencionar al cuerpo docente y a los funcionarios del departamento, cuya permanente buena onda ayudó a hacer más ameno el día a día en Calán.
Por último, agradezco el apoyo financiero otorgado por el MAS y a CONICYT a traves su Programa de Capital Humano Avanzado a través de las becas de Magíster Nacional, folio 22162353.

Contents

List of Tables

List of Figures

Chapter 1

Introduction

1.1. Galactic Background

In an expanding universe, the study of galaxies, how they form and evolve, is an essential field that help astronomers to explore the evolution of the universe as a whole. Topics like its radiation and particle content, the growth of cosmic structures, the processes regarding the gaseous and dark matter component of galaxies, and how they interact, are good examples of this. This universe, in which all hundreds of billions of galaxies recede from each other (and from us), has brought together astronomers, cosmologists, and physicists throughout decades to find models to link observations with a valid theoretical background that permit making predictions and exploring the initial conditions of its expansion. The currently accepted Lambda Cold Dark Matter models (ΛCDM), for instance, are simple models that provide explanations to observables (e.g., White & Frenk, 1991; Rong et al., 2017) like the structure of the cosmic microwave background, the large scale structure in the distribution of galaxies, the abundance of species like hydrogen and helium, and the acceleration in the expansion of the universe.

In that sense, the Milky Way (MW) is the best and closest cosmic laboratory for studying the physical processes that rule individual and close groups of galaxies in a universal context. Because of the position of the Earth (and the Sun) within the Galaxy, that allows the scientists to study its stellar and gas content in detail, it is probably the best known galaxy in the Universe. The MW is a barred spiral galaxy with a flat disk (of ~ 30 kiloparsecs) and a central bulge with gas and dust containing $\sim 10^{11}$ stars. The Galactic disk is surrounded by a dark matter dominated halo of old stars and globular clusters, and in which several large substructures are present (Ibata et al., 2001; Majewski et al., 2003; Duffau et al., 2006), including embedded satellite galaxies.

1.1.1. The Halo of the Milky Way

Although it is not possible to observe directly the strong dark matter content of the halo, its presence can be inferred from the outer rotation curve of the Galaxy, the rotation curve of old population II stars that inhabit it and the kinematics of globular clusters and dwarf galaxies. However, fully understanding some of its fundamental properties keeps being the focus of attention of astronomers to this day. For instance, the estimated mass of this dark matter is about 10^{12} solar masses (Boylan-Kolchin et al., 2013), but both this number and the total extension of the halo are still a matter of debate.

The dark matter halo is one of the most important regions of the Galaxy to be studied, as it contains probes of the recent assembly history of the MW. Regarding galaxy formation models, clumped stellar distributions in the phase-space of the halo are generally interpreted as an outcome of the hierarchical structure formation of the Galaxy (Johnston et al., 2008). Thus, the presence of substructures in the surroundings of galaxies can be used to reconstruct their merger histories. In fact, models suggest that stars in the outer regions of the halo (beyond Galactocentric radii of $R_{\mathrm{GC}} \gtrsim 100$ kpc) likely originated in relatively recently-accreted satellite galaxies (e.g., Bullock & Johnston, 2005; Zolotov et al., 2009). Also, numerous works have studied how individual debris features around galaxies are related to the properties of the progenitor dwarfs (Law et al., 2005; Warnick et al., 2008).

The accreted dwarfs that are expected to have contributed their stellar components to the MW halo imprint evidence of the MW's accretion history in the radial stellar density profile (Bullock & Johnston, 2005). Studies of the halo density profile with various tracers have found widely varying stellar density slopes for power law models at large radii (Watkins et al., 2009; Deason et al., 2011; Sesar et al., 2011), making it difficult to place the MW in a broader context. The discrepancies may be due, in part, to the different lines of sight covered by these works, as well as to the small size of the samples at large distances from the Galactic center.

The most distant stars of the MW are vital tracers for the estimation of the total mass of the Galaxy, since mass modeling of the halo is most strongly constrained by tracers in the outermost regions. Detailed predictions (e.g., the number and luminosity function of satellites) for MW-like galaxies extracted from cosmological models for comparison with observations are highly sensitive to the total mass of the host halo (e.g., Geha et al., 2017); thus, determining a reliable total mass for the Galaxy becomes essential if one wishes to use it as a cosmological laboratory. Unfortunately, the total mass of the MW within 150 kpc is known only within a factor of two (e.g., Eadie & Harris, 2016; Ablimit & Zhao, 2017).

Regarding remote MW stars, only a small number has been detected at heliocentric distances ($\mathrm{d_H}$) larger than 100 kpc. In Bochanski et al. (2014) the authors reported the discovery of the two most distant MW stars known to date, with estimated distances larger than 200 kpc and classified as M giants. These stars are intrinsically bright which makes them good tracers of halo structure at large distances, but the distance estimations suffer from significant uncertainties. Other tracers, such as RR Lyrae stars, have been identified from a few parsecs to beyond 100 kpc (e.g., Watkins et al., 2009; Drake et al., 2013b; Sesar et al., 2017b, reaching $\mathrm{d}_H \sim 120$ kpc).

In the next subsection a description of different kinds of subhalos that are located within the halo is given.

1.1.2. The Galactic Neighborhood

The group of galaxies of which the MW is part is the denominated Local Group (LG). The LG contains more than 50 galaxies within about one megaparsec (McConnachie, 2012), and it has its center between the MW and the Andromeda galaxy (M31). The three most prominent members of this group are the MW, M31 and M33, being the three of them responsible for $\sim 90\,\%$ of the visible light of the group, and the MW the least luminous among the three. These galaxies are spiral galaxies and most of the remaining systems are classified as irregular galaxies, dwarf irregulars, dwarf ellipticals, and dwarf spheroidals. A considerable number of these smaller systems are bound to the MW or Andromeda.

The two most prominent companion galaxies of the MW are the Large and Small Magellanic Clouds (LMC and SMC). These two satellites are even visible to the naked eye in the southern sky. By contrast, the rest of the satellites (dwarf galaxies) are diffuse systems containing an old- and middle-aged stellar component with hardly any gaseous material to make stars from. The dwarf spheroidal galaxies (dSph), which are commonly named after the constellations in which they appear, are hundreds of times fainter than the Magellanic Clouds.

Over the last decade and a half, a large number of new MW satellites have been discovered (e.g., Willman et al., 2005; Belokurov et al., 2006a,b, 2008, 2010; Zucker et al., 2006a,b; Irwin et al., 2007; Bechtol et al., 2015; Koposov et al., 2015; Drlica-Wagner et al., 2015, 2016; Martin et al., 2015). These discoveries are of particular relevance since they allow astronomers to probe the faint end of the galaxy luminosity function and shed new light into known discrepancies between predictions from cosmological simulations and observations. Among these stands the well-known “missing satellites problem” present in the ΛCDM model (e.g., Kauffmann et al., 1993; Klypin et al., 1999; Moore et al., 1999; Simon & Geha, 2007) wherein hundreds to thousands of low mass subhalos should be orbiting around the MW but only a few dozen actual dwarf satellites are known. In this context, a reliable census of satellite galaxies, particularly at the faint end, is essential to make progress toward solving these inconsistencies. This has led to focused efforts to discover dwarf galaxies and extremely low luminosity sub-halos, and finding new ways to use the data available from wide and deep field surveys in an efficient way (e.g., Bechtol et al., 2015; Koposov et al., 2015; Baker & Willman, 2015).

In the next section, the main properties of variable stars are given, as well as an explanation of the role they play in understanding the MW in a Galactic context.

1.2. Variable Stars

This sections details, in a concise manner, basic information regarding variable sources in general. This includes a summary of the definitions of variable stars and how they are classified, among others. In Section 1.2.2 the approach that is usually followed to connect the previous information to the general understanding of the Milky Way is provided.

Roughly speaking, a variable star is defined, as the name suggests, as a star whose brightness fluctuates with time as seen from Earth. For this reason, in order to characterize the variations, it is usually required for the observations to be made with times known to high precision and with a good sampling of the light curves. A light curve is defined as a plot of the dependence of the apparent magnitude of a star with time, where the time variable is usually chosen to be expressed in Julian Dates. In order to visualize how a periodic variable star changes its brightness during a single cycle, phased light curves are commonly used . To obtain the phase of an observation in time series, the following equation is used:

$$\Phi = \frac{t - t_0}{P} - [\frac{t - t_0}{P}] \tag{1.1}$$

where Φ is the phase, t is the time of an individual observation, t_0 is an adopted reference time and P is the period of the variation. The brackets in Equation 1.1 represent the integer part of the expression inside. Therefore, only the numbers after the decimal point of the fraction are retained.

There are limits for the periods that can be found using an specific data set (Catelan & Smith, 2015). For example, generally the time interval spanned by the observations needs to be at least a couple of times longer than the longest period that wants to be determined. Also, the accuracy to which a period can be obtained reliably depends on the total number of data points (n) and the time separation between observations Δt, in the form $\Delta P = \frac{P^2}{n \ \Delta t}$.

A broad variety of techniques to determine periods of astronomical time series have been developed during the last decades (Lomb, 1976; Stellingwerf, 1978; Scargle, 1982; Graham et al., 2013). Examples of these techniques include the determination of the goodness of fit for the light curves under several trial periods, the minimization of the scatter of the binned observations based on the phases calculated with different periods, methods that work with the Fourier spectrum of a dataset looking for peaks, among others.

Since variable stars have many different characteristics which depende on a considerable number of factors (the driving mechanim of the variation, the periods and the amplitudes of the variations, spectral types, luminosity classes, and so on), several classes and distinctions have been defined to classify them. The General Catalogue of Variable Stars (GCVS; Kholopov et al., 1998), for example, lists definitions based on those factors for over 110 different classes and subclasses of variable stars.

One accepted manner of separating variables is to differenciate them according to the shape of their light curves. Based on this, three types are used to group them: regular, semiregular, and irregular variables. The first type applies to light curves that repeat with a

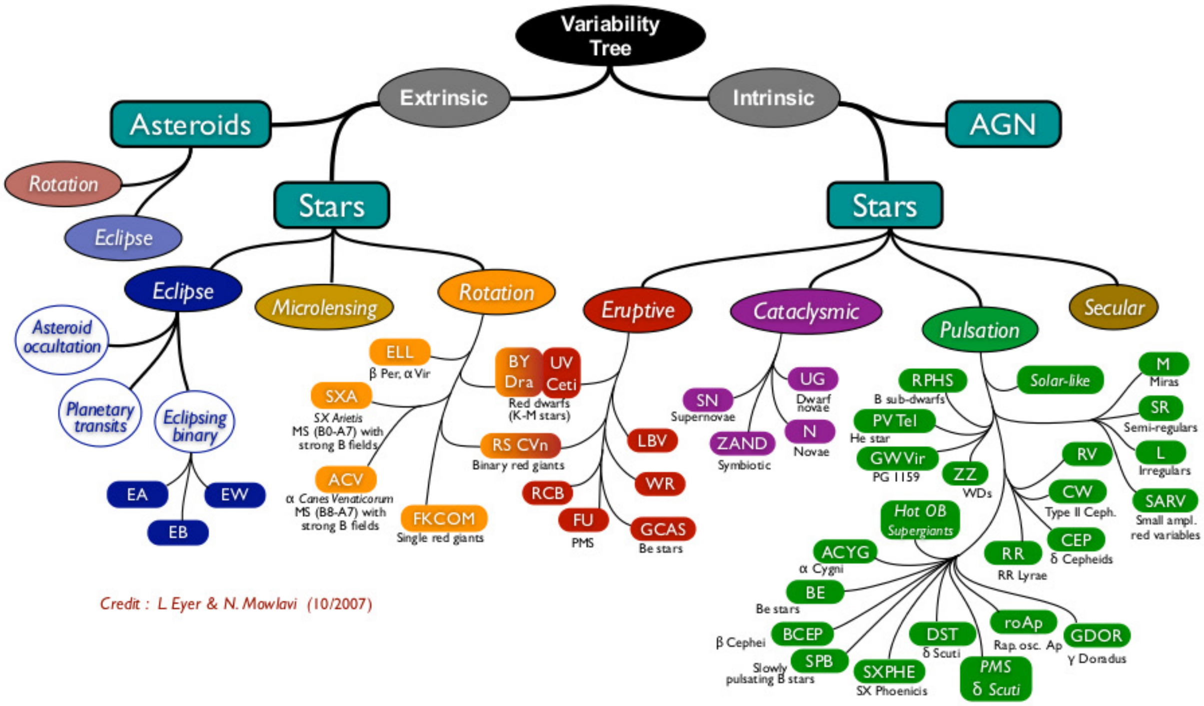

Credit : L Eyer & N. Mowlavi (10/2007)

Figure 1.1 Different types of stellar and non-stellar variable phenomena (in astronomy). Image taken from Eyer & Mowlavi (2008).

well-defined periodicity, while the semi-regular and irregular refers to when that periodicity is defined in a substantial degree and not at all, respectively.

On the other hand, variability classes have been made to label based on the physical reason why the changes in brightness occur, instead of the shape of the light curves. The main distinction in this sense is to determine if the variation is due to alterations in the physical processes inherent to the source, or if the reason is external to it. These classes are defined as *intrinsic* and *extrinsic* variables, respectively. Examples of the former are active galactic nuclei (AGN's), the rotational variables, cataclysmic variables (CV's), and pulsational variables (Catelan & Smith, 2015). Among the latter one can find eclipsing variables, asteroids, and microlensing phenomena.

Figure 1.1 shows the so called *variability tree*, which displays the many different variability phenomena that are found in astronomy separated according to their nature (Eyer & Mowlavi, 2008).

Stellar pulsations, responsible for triggering intrinsic stellar variations, are found throughout the Hertzprung-Russel diagram (H-R diagram). Therefore, it is expected for this class of variables to have numerous subclasses depending on different factors. For instance, stars can be divided into two categories: *radial* and *non-radial* pulsators, based on how the internal displacements are occuring. Among the former lie most of the "classical" pulsators, such as

Cepheids (classical and type II), Miras, and RR Lyrae stars. Variables like ZZ Ceti's are an example of non-radial classified stars, while δ Scuti stars are known for having both modes.

Pulsating variables can also be broadly classified as a function of their evolutionary status or their mass. Main-sequence variables, red evolved variables, blue evolved variables and compact pulsators are examples of the former. For the latter, their mass classifications are associated to specific stellar populations. Typical low-mass population II variables are RR Lyrae stars, type II Cepheids, and SX Phe stars. On the other hand, δ Scutis, classical Cepheids, and β Cepheids are examples of intermediate/high-mass pulsators, and are typically Population I objects (Catelan & Smith, 2015).

In this thesis the focus is made on pulsational variables, in particular RR Lyrae stars (see Section 1.2.1).

1.2.1. RR Lyrae stars

RR Lyrae stars (RRLs) are one of the most studied types of variable objects, due to their properties that make them useful to study old stellar populations. These kind of pulsating variables are low-mass horizontal branch (HB) stars that fall in the instability strip, and are widely known for their relatively short periods, from 4,8 to 24 hrs (0,2 d to 1,0 d), mean effective temperatures between $\sim$ 6000 and $\sim$ 7250 K, and absolute visual magnitudes of +0,6 (Catelan et al., 2004). Their masses usually ranges between $\sim$ 0,6 to $\sim$ 0,8 solar masses. The prototype of this kind of variable is the star RR Lyrae, a seventh-magnitude star with a 0,56 d period discovered by Williamina Fleming (Pickering, 1901) and that remains being the brightest of its class (to this day).

A study of the globular cluster ω Centauri made by Bailey (1902) allowed him to separate the RRLs within the cluster intro three subtypes: a, b and c (the Bailey types; hereafter RRa, RRb, RRc). The first type is characterized by their large amplitudes and the particular saw-tooth shape of their light curves (steep rises and gradual declinations). The stars from the second subclass were similar to the a types but with smaller amplitudes and longer periods. Finally, Bailey's RRc stars have more symmetric light curves (sinusoidal), with shorter periods and lower amplitudes. Based on their positions in the so called Bailey-diagram (period versus amplitude plot, Figure 1.2) and the pulsation mechanism of each type, Schwarzschild (1940) proposed the ab-type (RRab), since both a's and b's form a continuous sequence in the diagram and pulsate in the fundamental radial mode. RRc's are known to be first-overtone radial pulsators. A smaller number of RRLs have been found to be pulsating in both modes fundamental and first overtone modes. These double-mode RRLs are classified as d-type (RRd). The typical light curve shape of RRab's and RRc's are shown in Figure 1.3. It is worth noticing that the amplitude of the oscillations increases when going from the near-infrared to bluer filters. In fact, amplitudes of around 4 magnitudes are found at ultraviolet wavelenghts (Downes et al., 2004). In terms of their possitions within the instability strip, RRab's are found towards the cooler side of this region, while RRc's usually lie in the hotter side (bluer). RRd's are found in the intermediate region.

One of the main properties that make RRLs a useful kind of object to study is that they

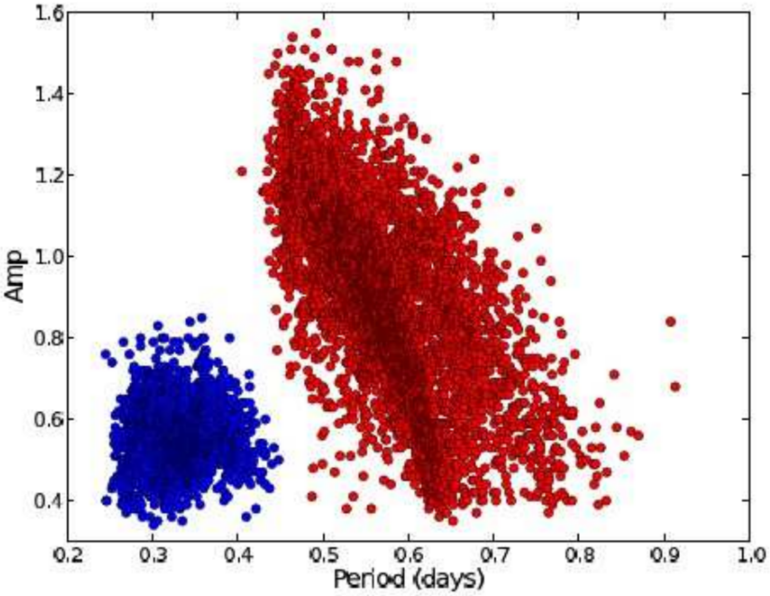

Figure 1.2 Bailey diagram of a sample of RRLs presented in Abbas et al. (2014). This plot shows the different location of RRab's (red points) and RRc's (blue points), as described in Section 1.2.1.

are standard candles. Since they are low-mass stars in the HB stage, they can be used to determine distances to systems with old stellar populations. As the HB is nearly horizontal in the V photometric filter close to the instability strip, all the RRLs stars within a given stellar population (for instance, in a globular cluster) have about the same visual apparent magnitude. Although, this behaviour is not the same when other bandpasses are considered. On the infrared, for instance, all these RRLs develope a well-defined period-luminosity (PL) relation (Catelan et al., 2004).

In order to use RRLs as distance indicators their observed magnitudes must be converted to absolute magnitude, before using the distance modulus expression:

$$\begin{gathered}\mu = m - M = 5\ log_{10}\ (\mathrm{d}) - 5 \\ \mathrm{d} = 10^{(m-M+5)/5}\end{gathered} \tag{1.2}$$

where m and M are the apparent and absolute magnitudes of the star, μ is the distance modulus, and d is the distance to the star from the sun (heliocentric distance; $\mathrm{d_H}$), in parsecs.

However, obtaining values for the absolute magnitude of RRLs in bandpasses other than V is not a simple task. For a long time it was assumed that all RRLs had the same absolute magnitude independently of their properties. In the literature, it is usual to find relationships of the type $< M >= a + b\ [Fe/H]$ (Catelan et al., 2004). Longmore et al. (1986) found a tight PL relation in the K (2.2 μm) filter for RRLs in globular clusters, roughly insensitive to interstellar exctinction and metallicity. More recent studies have investigated correlations for

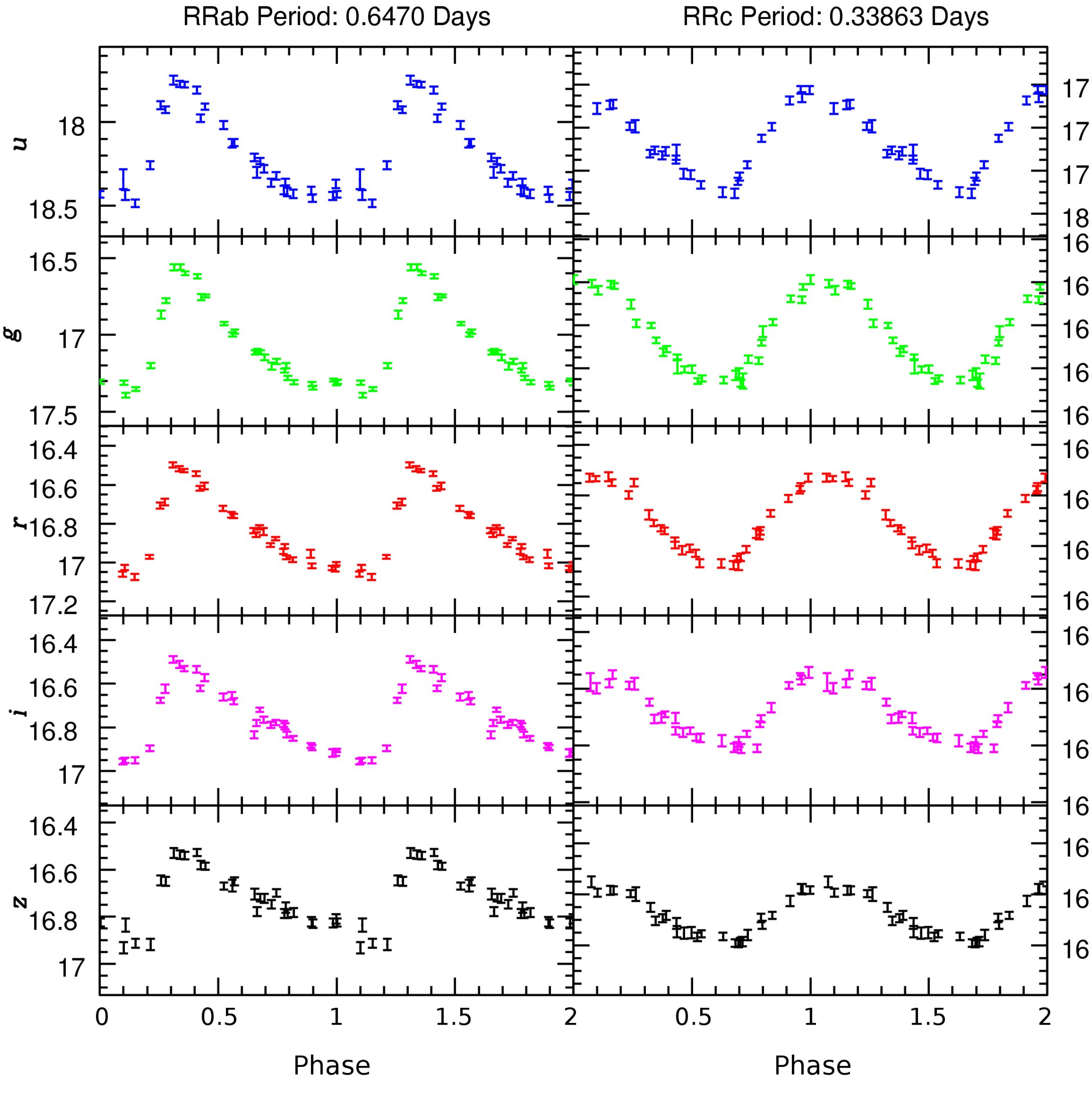

Figure 1.3 Typical light curves of RRab and RRc stars, in different filters (from SDSS). Image taken from De Lee (2008)

different photometric systems. Catelan et al. (2004), for example, searched for PL relations for the Jhonson-Cousins-Glass $IJHK$ and V bandpasses. The same kind of study was performed by Cortés & Catelan (2008) and Cáceres & Catelan (2008), for the Stromgren *uvby* and SDSS *ugriz*, respectively.

Getting independent measurements of the distances by using parallaxes is a good method to get calibrated expressions to determine absolute magnitudes, but even the closest RRL variables are too distant to measure precise parallaxes using ground-based facilities. Benedict et al. (2011) provide calibrations for the infrared K bandpass and V absolute magnitudes based on parallaxes of nearby RRLs measured with the Hubble Space Telescope (HST). A recent study (Sesar et al., 2017a) found calibrations for the period-luminosity-metallicity relation of RRLs based on parallax measurements from the HST for RRab's in the *grizy* bandpasses of the Pan-STARRS catalogs. These relations are used later on in this work.

Regarding the physics that causes the pulsation of RRLs, the κ and γ mechanisms are the main processes that drive the oscillations. When a stellar atmosphere becomes unstable, if a layer moves inward the material within becomes more dense and opaque, which restrain the flow of energy from the interior. As a consequence, the heat gets amplified causing an increase of the pressure, pushing that layer back out again. This processes becomes cyclic as the layer moves inward and outward repeatedly, causing the pulsation (Catelan & Smith, 2015). The zone in which this happens for RRLs is the zone in the star within where the helium is partly ionized.

It is interesting to note that the shape of the RRLs' light curves not always repeats over different cycles, and some RRLs have been found to show cycle-to-cycle variations. This modulation effect, the so called Blazhko effect, was noted for the first time in 1907 by Sergei Blazhko when analyzing changes in the time of maximum light of the RRLs RW Dra (Blazhko, 1907). The Blazhko effect is currently known to be present in nearly 50 % of the fundamental mode RRLs (Jurcsik et al., 2009). Another interesting fact about this effect is that its amplitude is not always constant over time. Some stars are known to be undergoing strong Blazhko modulations at some times, and negligible effects at other times. In spite of being discovered more than 100 years ago, there is still no consensus about the physics that drives this effect.

1.2.2. The Role of RR Lyrae Stars in Galactic Astronomy

RR Lyrae stars have played a major role in the context of studying crucial aspects of the different stellar populations within the Milky Way, its galactic neighbors and stellar clusters, its accretion history and interactions in general. This is mainly given that these stars have been found mostly in systems containing stellar components older than 10 Gigayears, in addition to their useful condition of being excelent distant indicators. In fact, distance estimations made with RRLs have typical uncertainties of $\sim 5\,\%$.

The detection of variable stars in globular clusters and satellite galaxies has been a key factor to permit the study of their properties and populations. In fact, more than a century ago over 500 variable stars were known as members of globular clusters, most of which are currently classified as RRLs. The latter gave them the name of "cluster variables" in the early literature. Also, historically the discovery of RRLs in dSph galaxies was the first confirmation that these systems contained old, population II stars (e.g., Baade & Hubble, 1939; Saha et al., 1986; Siegel, 2006). Additionally, this type of variable stars play an important role since they provide reliable distances to their host dwarf satellites. In this context, at least one RRL has been reported in every Milky Way's satellite classified as a dwarf galaxy that has been searched for them (Vivas et al., 2016), including systems with extremely low luminosity and surface brightness like Segue 1 (Simon et al., 2011) and Segue 2 (Boettcher et al., 2013). This fact has brought forth the idea that RRL can actually be used to discover new stellar systems in the outer halo (Sesar et al., 2014; Baker & Willman, 2015; Sanderson et al., 2016), as well as to study the properties of halo substructures (Vivas et al., 2001; Sesar et al., 2013; Drake et al., 2013b; Torrealba et al., 2015). Since distant RRLs are rare, these works suggest that they can trace the existence of faint stellar systems (as the light of the lighthouse). In particular, Baker & Willman (2015) suggested that groups of two or more RRLs at heliocentric distances $> 50\,\mathrm{kpc}$ could reveal stellar systems as faint as $M_V = -3{,}2$. This make RRLs potential tracers of faint satellite systems in the outer halo that would be significantly difficult to find by other methods.

An example of one of the common uses of RRLs in a Galactic context is the referred to the study of the Galactic halo itself. These stars have been used to explore the outermost regions of the halo, its structure, and the presence of past merger signatures within its limits. Because RRLs are precise standard candles and easily identified in time-series data, they have become an effective way of probing the distant halo at distances beyond d $\gtrsim$ 100 kpc. Sanderson et al. (2017) predicted that different accretion histories of 12 synthetic halos (from Bullock & Johnston, 2005) yield populations of $2,000-10,000$ RRLs between $100 <$ d < 300 kpc in the MW halo, with roughly half of these in intact dwarf galaxies, and half unbound from their parent satellite.

The discovery of groups of RRLs at medium to large distances has become particularly important for the physical description of substructures in the inner and outer halo. Some examples are the discovery and characterization of the Sagittarius stellar tidal stream (Vivas et al., 2001; Vivas & Zinn, 2006; Prior et al., 2009; Watkins et al., 2009; Sesar et al., 2010, 2017b; Drake et al., 2013a; Zinn et al., 2014), the Virgo stellar stream (Duffau et al., 2006; Vivas et al., 2016; Sesar et al., 2017b), the Pisces overdensity (Sesar et al., 2010), or the Gemini stream that extends beyond 100 kpc (Drake et al., 2013b), among others. However, the discovery of very distant, isolated stars in the halo brings out questions related to the understanding of their origin. Since they are not expected to have formed in the outskirts of the halo, the origin of distant stars is generally thought to be either the gravitational interaction between the Milky Way and its satellites or the ejection from the center (or disk) of the Galaxy (Bullock & Johnston, 2005; Brown et al., 2005; Zolotov et al., 2009). Simulations suggest that it is possible to reproduce important stellar halo properties (the break in the density profiles, for instance) taking only accretion events into consideration (Deason et al., 2013).

1.3. Previous Surveys

With the arrival of CCD cameras into the astronomical imaging surveys in the late 1970s, the number of cataloged RRLs rapidly increased as large scale surveys began to discover thousands of new variable stars.

To date, large RRLs catalogs have been constructed using data from different variability surveys that map different parts of the halo. Among them, the Quasar Equatorial Survey Team (QUEST) RRL catalog (Vivas et al., 2004) contains 457 objects with $V < 19{,}5$, and subsequently with La Silla QUEST Southern Hemisphere Variability Survey (LSQ) came the discovery of 1013 RRab and 359 RRc distributed across ~ 840 deg^2 of the sky in the range $150° < \mathrm{RA} < 210°$ and $-10° < \mathrm{Dec} < 10°$ (Zinn et al., 2014). The latter contains stars with $\mathrm{d_H}$ between 5 and 80 kpc. More recently, the Catalina Surveys identified $\sim 43,500$ RRLs over $\sim 30,000$ sq degrees of the sky up to heliocentric distances of $\sim 60 - 110$ kpc (Drake et al., 2017). Recently, Abbas et al. (2014) reported the detection of $\sim 2,021$ new RRL stars ($1,449$ RRc and ~ 572 RRab) with $\mathrm{d_H} < 28$ kpc, using combined data from the Sloan Digital Sky Survey (SDSS), the Panoramic Survey Telescope and Rapid Response System 1 (Pan-STARRS1) and the second photometric catalog from the Catalina Survey (CSDR2). The Pan-STARRS1 (PS1) 3π survey has proven to be also an excellent source for RRLs, despite its poor temporal sampling, by identifying a sample of $\sim 45,000$ RRLs up to ~ 130 kpc from the Sun with a 90 % purity (Sesar et al., 2017a). All these surveys have found several distant RRLs, but the surveys' low completenesses at faint magnitudes limit the depth of the findings.

1.4. This Work

While current models of galaxy formation generate specific predictions for the amount of stellar substructure in the outer halo, these have been hard to explore because of the lack of deep, large area surveys of tracers with reliable distance estimates. The work presented in this document is one of the first steps to meet these requirements, having in mind the advent of large wide field and deep sky projects like the Large Synoptic Survey Telescope (LSST; LSST Science Collaboration et al., 2009).

In this thesis, data from the High Cadence Transient Survey (HiTS; Förster et al., 2016) is used to search for distant RRL in the Galactic halo (beyond 100 kpc). HiTS is a survey designed for the detection of young supernovae events with a total sky coverage of ~ 350 square degrees and a limiting g magnitude that varies between 23 and 24.5 (Förster et al., 2016). Because of the photometric depth and wide field construction of the survey, in addition to its cadence and observing strategy (well matched for RRL detection), it should provide an ideal dataset to find distant RRL in the observed region, if present. Here the results from a search using $\sim 200\,\mathrm{deg}^2$ of HiTS surveyed data is presented, corresponding to the second and third campaigns held during semesters 2014A and 2015A.

The structure of this work is organized as follows: In Chapter 3 a complete analysis of

HiTS data from 2014 is provided. Chapter 4 gives a brief description of the preliminary results from using HiTS 2015's data. A conclusion and final words, summarizing the results and highlighting their scientific relevance are given in the last chapter.

Chapter 2

Dataset

2.1. Context & Observations

The data used for this project were taken from the High cadence Transient Survey (HiTS; Förster et al., 2016). HiTS is an optical campaign carried out during 2013, 2014 and 2015, making use of the Dark Energy Camera (DECam; Flaugher et al., 2015). The DECam is a 520 megapixels prime focus CCD imager that is mounted on the Blanco-4 m telescope at the Cerro Tololo Inter-American Observatory (CTIO). The camera contains 62 CCDs that, all together, generate three square degree images. The physical orientation of the CCDs is shown in Figure 2.1.

HiTS is a survey originally focused on the detection of young supernovae, with special emphasis on the early stages of the explosions so that empirical evidence of the so called "shock breakout" phenomenon could be found (Förster et al., 2016). The design of this survey was originally thought to optimize the number of events to be detected, with cadences of the order of the shock breakouts timescales ($\sim 1\,\mathrm{hr}$) and long enough so data can be processed in real-time.

However, the survey search strategy and depth reached by the observations made the survey well matched for purposes other than supernovae studies as well. Examples of works made with HiTS' data are the automated classification and characterization of light curves (Martínez et al., 2017), the discovery and study of thousands of asteroids in the solar system (Peña et al. 2017 in preparation), and this work.

The properties of the data taken by the survey (number of fields, galactic latitude/longitude, exposure times, filters) slightly varied through the years, altough the three years of campaing consisted in mostly blindly selected fields with long exposure times. An important requirement for the fields selection was that they had to remain visible for the entire night with overall low airmasses, and cluster/supercluster fields were observed only when they were adjacent to the blind fields.

The first year (2013A) was a pilot campaign with observations made in the *u* SDSS

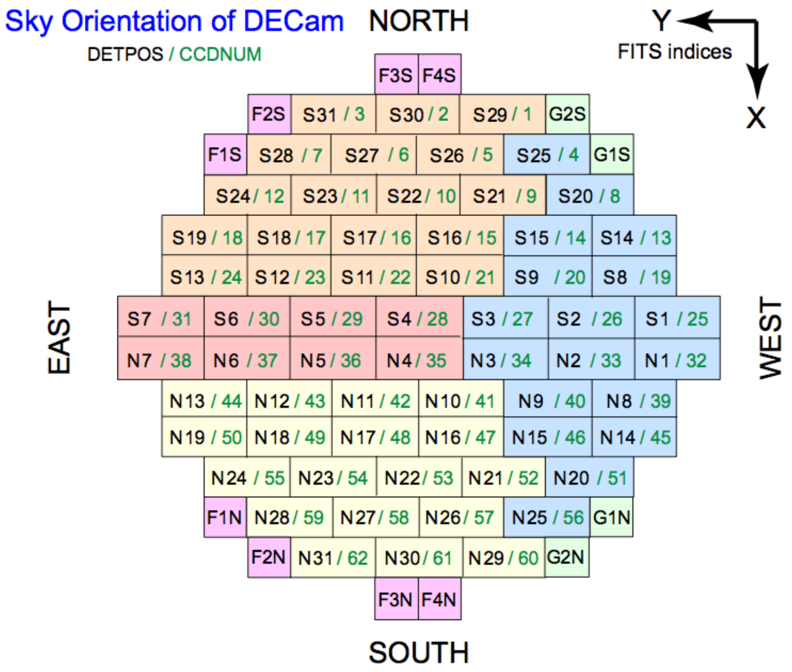

Figure 2.1 Orientation on the sky and spatial footprint of the Dark Energy Camera's focal plane array. The image shows the 62 individual CCD imagers of the camera. At the time of the observations, for all three campaigns of HiTS, CCDs S30 and N30 were not functional. Image taken from `http://www.ctio.noao.edu/noao/content/DECam-What`.

photometric filter ($\sim$ 3000 to 4000 angstroms), with 40 fields observed and 4 epochs per night per field, during 4 consecutive nights (Mar 12th - Mar 15th). In 2014A, the number of fields and cadence of the pilot campaign were maintained, but this time in the $g-$band($\sim$ 4000 to 5000 angstroms), during 5 consecutive nights (Mar 1st - Mar 5th) and with lower galactic latitude for the fields. This gives a total of 20 epochs per field for 2014A, with the exception of field 1 (located at 151,5° RA, $-2°$ DEC) which has 37. The exposure times varied as well, from 160 seconds (83 % of the observations) to 173 and 174 seconds (3 % and 14 %). The sky conditions were good overall, but not optimal, with a typical seeing of 1,5 arcseconds. In 2015A, the observed number of fields increased to 50 fields and 5 epochs per night. These fields include 14 already observed in 2014A. The fields were observed during 6 consecutive nights (Feb 17th - Feb 22nd), in addition to 3 non-consecutive half nights. The observations in this campaign consisted in $g-$band data, in addition to images taken in the $r-$band ($\sim$ 5500 to 7000 angstroms) in order to have a broader photometric dataset. The latter is particularly important for RRLs searches, for example. In this thesis, the work described is done regarding the search of RRLs with the data from 2014A and 2015A only.

The data obtained were stored and processed at the National Laboratory for High Performance Computing (NLHPC), located at the Center for Mathematical Modeling (CMM), Universidad de Chile. The basic image reduction steps (zero substraction and flatfielding) were performed using the Dark Energy Survey (DES) community pipeline (Valdes et al., 2014).

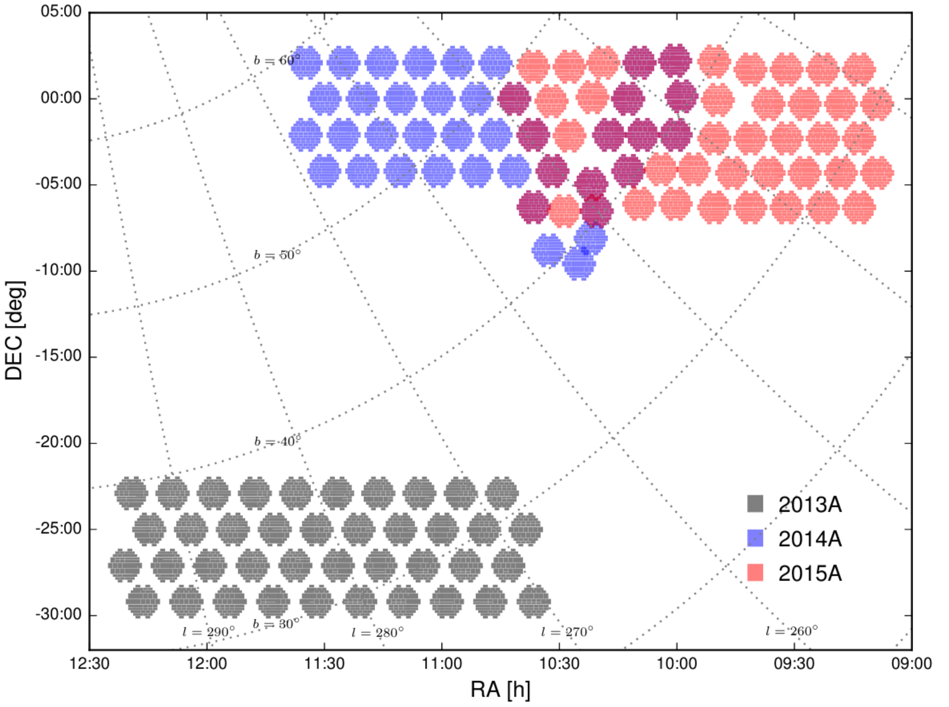

Figure 2.2 Spatial distribution of the fields observed by HiTS in 2013A, 2014A and 2015A, from Förster et al. (2016). The different campaigns are color coded. The plot shows the fields position both in equatorial (RA,DEC) and galactic (b,l) coordinates.

2.2. Data Analysis

The HiTS main pipeline flow outline is a high complexity process based on image substraction (Förster et al., 2016). The images taken with the telescope were analyzed in real-time with the purpose of finding early supernovae, and to perform follow-up observations of interesting candidates, if possible. In this sense, one of the most important technical goals the pipeline accomplishes is the capability of uploading every image to the CMM storage center and processing all 62 CCD data faster than one exposure time. This process includes readout time ($\sim 17\,\mathrm{sec}$), data transfer from CTIO to La Serena ($\sim 120\,\mathrm{sec}$) and from La Serena to Santiago through the REUNA digital network ($\sim 10\,\mathrm{sec}$), running the DECam community pipeline ($\sim 80\,\mathrm{sec}$), a CRBlaster filter ($\sim 20\,\mathrm{sec}$) and finally the image substraction pipeline ($\sim 60\,\mathrm{sec}$). The data analyzed for this project is the one stored at the CMM computer cluster *leftraru*, with no further image substraction processing. The data in *leftraru* were originally organized in folders, which made clear the CCD, field, and epoch each image corresponds to. The following steps are performed once cosmic rays are removed from the reduced images:

(i) From image to catalogs: For this work, the first step is to generate catalogs using the SExtractor photometry software, (Source Extractor; Bertin & Arnouts, 1996). This software is a reliable automated tool used to identify stars from fits formated images, and is well known for its speed and precision. Sextractor offers a large variety of input options, which have to be established through a parameters file. These parameters include details such as the number of pixels with flux values above certain threshold, the saturation level, masks, or special weights for the sources, among others. The output information can also be modified, in terms of format (ascii, FITS, VOTable), name of the output catalog and parameters of the extracted sources. The most important column selected as "useful" for this work are: the X and Y pixel-coordinates in the CCD and values of the flux for each star (FLUX_AUTO, FLUXERR_AUTO). The output from running Sextractor on a single field, CCD, and epoch is what is called, hereafter, a "catalog".

(ii) Catalog alignments: An important step for this procedure is to identify the sources from the Sextractor catalogs throughout the different epochs. This can be understood as setting a reference frame for which each star has a unique set of values (X_{i}, Y_{i}). These values (X_{i}, Y_{i}) should be the position on the CCD in which the star i fall on each CCD. By doing this, if a star does not appear in a given epoch in the position it is expected to be, that epoch is not be considered as part of the time series for that star.

In order to carry out the catalog alignment and pixel-to-sky coordinate conversion, transformation constants are found by the HiTS pipeline (Förster et al., 2016). The reference used for setting the common coordinates are the second and the third epoch (for 2014A and 2015A, respectively), for which the observing conditions were more photometric (overall) than for the rest. This frame will hereafter be called "reference frame", "reference image" or simply the "reference".

(iii) Building a master catalog: Once all the stars in the individual catalogs are transformed to the reference frame coordinate system (aligned), a master catalog is created for each field and CCD, in which all the epochs were stored. Each star in the reference catalogs is then searched for in all the epochs, allowing offsets of up to 3 pixels. Stars with less than 5 matches (less than 5 observations) are filtered out. The result of this crossmatch are time-series that include: the epoch, the number of the observation, the (X,Y) pixel values in the reference frame, the flux and its associated uncertainty. Since one of the goals of this work is to handle variable sources, objects with mean flux uncertainties larger than two times the flux standard deviation are filtered out.

(iv) Instrumental magnitudes: By this step, time-series with fluxes are available. Instrumental magnitudes, in g and r are obtained by:

$$g_{\mathrm{std}} = -2{,}5 \cdot log10(\frac{counts}{sec}) - a_g - k_g \cdot A - b_g \cdot ((g-r)_{\mathrm{std}} - 0{,}53)$$

$$r_{\mathrm{std}} = -2{,}5 \cdot log10(\frac{counts}{sec}) - a_r - k_r \cdot A - b_r \cdot ((g-r)_{\mathrm{std}} - 0{,}53)$$

where A is the airmass, a is the photometric zero-point in the respective band (one for each CCD), b is the instrumental color term coefficient (one for each CCD) and k is the first-order extinction in that band [1]. The value 0,53 is a fiducial reference color for stars in $g - r$, based on SDSS experience.

---

[1] `http://www.ctio.noao.edu/noao/content/Mean-Photometric-Standard-Star-Module-PSM\-Solutions-mean-zeropoints-color-terms-extinctions.`

Given that the data from 2014A do not have observations in the $r-$band, the color term of the instrumental g magnitude equation is neglected when computing the magnitudes for the data from that campaign. However, this should not introduce significant uncertainties since the $g - r$ color for RRL are restricted to a small range between $-0{,}15 - -0{,}40$ (Sesar et al., 2010), which would result in a magnitude difference of the order of 10^{-2}.

To take into account the effects of the atmospheric conditions over the epochs, a zero-point relative to the reference is calculated. This is performed with the idea of doing calibrations with the data in a common reference system comparing with other surveys later on (see Sections 2.6.1 and 2.6.2). Therefore, every field/CCD would have a zero point file to correct by. Each of these values is calculated by comparing the instrumental magnitudes given by the previous equations for all the matched stars from different epochs (see Figure 2.3). Since the scatter of the magnitude difference is large for faint sources due to photometric uncertainties, a sigma-clipping procedure is performed. After filtering in only the objects within 2σ, the median value of the difference of magnitudes was set as the zeropoint. For reliability of the estimation, the uncertainties of the value of the zeropoint are calculated using only the objects with a magnitude $< 20{,}5$. Therefore, by this time the time-series have magnitudes given by:

$$g_{ref} = g_{std} + \Delta g_{\rm rel}$$

$$r_{ref} = r_{std} + \Delta r_{\rm rel}$$

where $\Delta_{\rm rel}$ is the relative zero-point. Because of the way $\Delta_{\rm rel}$ is computed, its value is zero for the stars in the reference catalog.

2.3. Selection of RR Lyrae Star Candidates

As RRLs are objects that have been studied for many decades (as described in Chapter 1), several selection cuts can be made to reduce the number of possible RRL candidates to a reasonable sample (hundreds). In this section these selection cuts are described.

2.3.1. Period Determination

Since the period in RRLs is one of the main observable constraints, the large number of potential candidates (time-series) needed to pass through a period determination criteria.

For period determination, the Lomb-Scargle methodology is used (LS; Lomb, 1976; Scargle, 1982). The LS periodogram is a tool commonly used in time domain studies and frequency analysis of unequally spaced data. This method consists in generating a power spectrum from an unevenly-sampled dataset to detect a periodic component, equivalent to fitting sine waves of the form $y = a\ cos\ (wt) + b\ sin\ (wt)$. In the case of this work, the Standard version of the LS periodogram (Lomb, 1976; Scargle, 1982) was first used in the data, through the astroML python module (VanderPlas et al., 2012). Although the LS method in general works well and

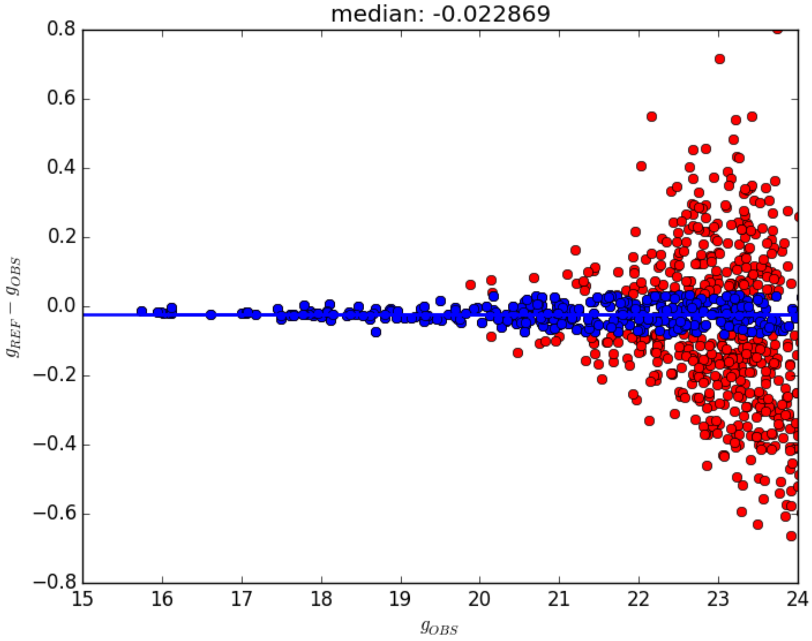

Figure 2.3 Instrumental magnitude difference for the stars in Field 33, N23. The stars compared in this plot correspond to the reference and the seventh epoch, for 2014A data. The red dots represent all the objects present in both epochs, while the blue dots show the sigma-clipped data. The median is shown as a blue line as a reference.

gives precise results, several problems were evident in the first results of the methodology, with most of them being related to aliasing. This phenomenon is related to the difficulty of distinguishing signals in the frequency space due to the way the data is sampled (in this case, the cadence and timescale of the observations). In Figure 2.4 the results of the use of the LS periodogram on a specific field and chip is shown. The peaks associated with the periods 0,33 and 0,50 days (sub-harmonics of the natural diurnal cycle) are clearly visible.

To address the aliasing issues, it was necessary to ran the generalized version of the periodogram (GLS; Zechmeister & Kürster, 2009), which adds a constant to the sinusoid fitting procedure ($y = a\ cos\ (wt) + b\ sin\ (wt) + c$). The use of the GLS is a convenient way to proceed since the results of running it are less susceptible to aliasing and provide more accurate frequencies. Although this measure reduced the aliasing near the sub-harmonics of a day, it does not solve the problem. The candidates with frequencies between 0,32 and 0,34 days, and within 0,49 and 0,51 are filtered out to diminish the number of spurious variables. Objects with periods larger than 21,6 hours (0,9 days) and less than 4,8 hours (0,2 days) are also filtered out.

The statistical significance of the period detection, provided by the GLS sofware, is used as a final period-related filter. Only objects with a statistical level detection $<$ 0,08 are selected as RRLs pre-candidates. In the case where more than one significant period met these requirements, the two most significant periods are selected as tentative. An example of sampled light curves as result of this process and meeting these requirements is presented in Figure 2.5. This results in the selection of only a couple of thousands objects for 2014A and

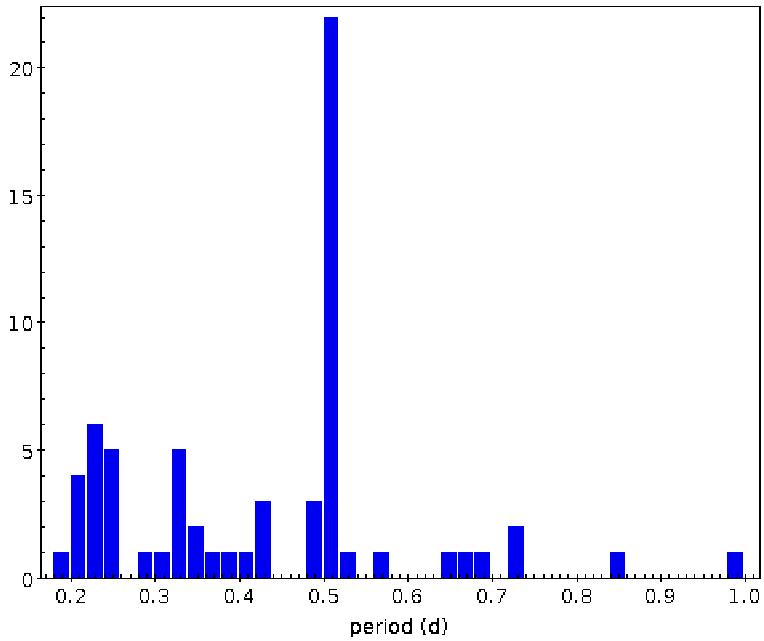

Figure 2.4 Distribution of periods of sources for Field 1, S13. This field/CCD has a large number of real variable sources, but a large number of spurious sources as well. Clear peaks associated to aliasing are evident in the distribution (0,33 and 0,50 d).

2015A.

2.3.2. Other Filters

In order to reduce the number of spurious variables and to select a definitive list of RRLs candidates, additional filters are needed. The criteria used for these selection cuts are explained in what follows.

(i) Color cuts: As explained in Chapter 1, RRLs are a particularly unique kind of pulsating stars, and the physics of the pulsations made them lie in specific regions of color-color diagrams. Therefore, meaningul information can be retrieved with the use of multiband photometry for the selection and characterization of RRLs, when available (Ivezić et al., 2005). In fact, most photometric RRL surveys use this information as a key filtering criteron to build their catalogs, reducing the number of false positives drastically.

    For this work, mean magnitudes in the $g-$ and the $r-$bands (for 2015A) are determined at this point of the analysis. Only objects with $-0{,}2 \leq g - r \leq 0{,}6$ where considered as potential RRLs candidates when analyzing data from HiTS 2015A. This window, somewhat large to be considered a big filter, ruled out objects with extreme colors while allowing offsets from the literature cutting values in case the mean g and r magnitudes do not refflect the real average magnitude of the RRLs. The difference between these mean magnitudes would be mainly given by the fact that RRLs do not change their brightness at a constant rate (in time) throughout their phases.

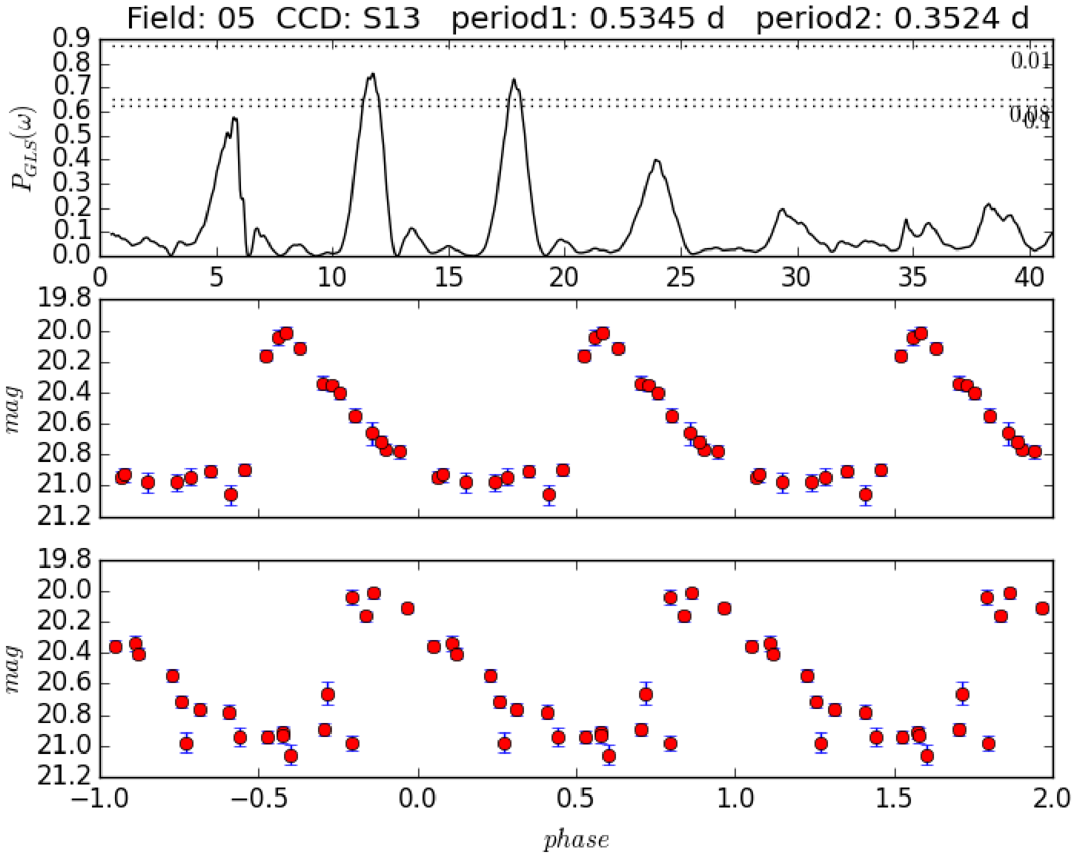

Figure 2.5 Typical output of the period detection analysis explained in Section 2.3.1, for a source with two significant periods identified. The object correspond to an RRLs from Field 5, S13. *top panel*: Power spectrum of the star, as given by the GLS software. Horizontal lines represent the 0,01, 0,05 and 0,08 significance levels. The light curve phased with the most significant period is shown in the *middle panel*, while the second most significant period is shown in the *bottom panel*.

Since the data from HiTS 2014A does not have observations in bands other than g, this filtering process is not applied for these data. A further analysis of the colors of the final list of RRL from 2014A is presented in Section 3.1.4.

(ii) Amplitude restriction: In Chapter 1, the typical amplitude of variation of RRLs is addressed. As mentioned in that Chapter, these amplitudes depend on the type of RRLs, and subsequently, the physics that trigger the pulsation itself. However, the amplitude of RRLs can be constrained to values within which most of these variables pulsate. Good approximation for the limits that could be chosen are $0{,}2 < A < 1{,}5$, where the RRLs with the biggest variations correspond to RRab.

Its important to note that the lower limit of this range is not clear for faint sources in which the mean uncertainties of the magnitude at different epochs could be of the order of the standard deviation of the magnitude. Because the observations that are used for the light-curves correspond to $g-$band data only in both the 2014A and the 2015A campaigns, a cut based on the amplitudes is applied to the data on this band solely. Variable objects with $\Delta g < 0{,}2$ are filtered out, where Δg is the magnitude difference between the brightest and faintest observations in the time-series. The amplitude restriction reduces the number of potential candidates to ~ 1000 for the data of each 2014A and 2015A.

(iii) Visual inspection: One of the main properties of RRLs is the characteristic shape their light curves have: saw-tooth shapes with a negative correlation between amplitudes and periods for RRab's, and sinusoidal light curves with smaller amplitudes and shorter periods for RRc's (Chapter 1).

The last step to create a definitive catalog of RRLs candidates is to visually inspect the folded light curves with the most significant periods detected by the GLS software. An example of a typical image inspected in this step is shown in Figure 2.5. These plots, which contain the periodograms and folded light curves, are analyzed looking for periods, amplitudes and light-curve shapes typical of RRLs. In addition, congruence is expected when comparing the period/amplitude of each star and the shape of the light curve. A careful visual inspection of the reference images for the faintest objects (in terms of mean magnitudes) is also performed, in order to reject artifacts and permit point sources only.

Applying all the filters mentioned above results in a final list of candidates comprised of only 173 RRLs candidates for 2014A and 159 for 2015A. These two catalogs are extensively detailed (in different levels) in Chapter 3 and Chapter 4, respectively.

2.4. Photometric Uncertainties

The estimation of the uncertainties associated to each RRL is an important step since it is usually the most significant for further RRLs characterization (among other propagated uncertainties). For example, the mean magnitude uncertainty for RRLs plays a major role in

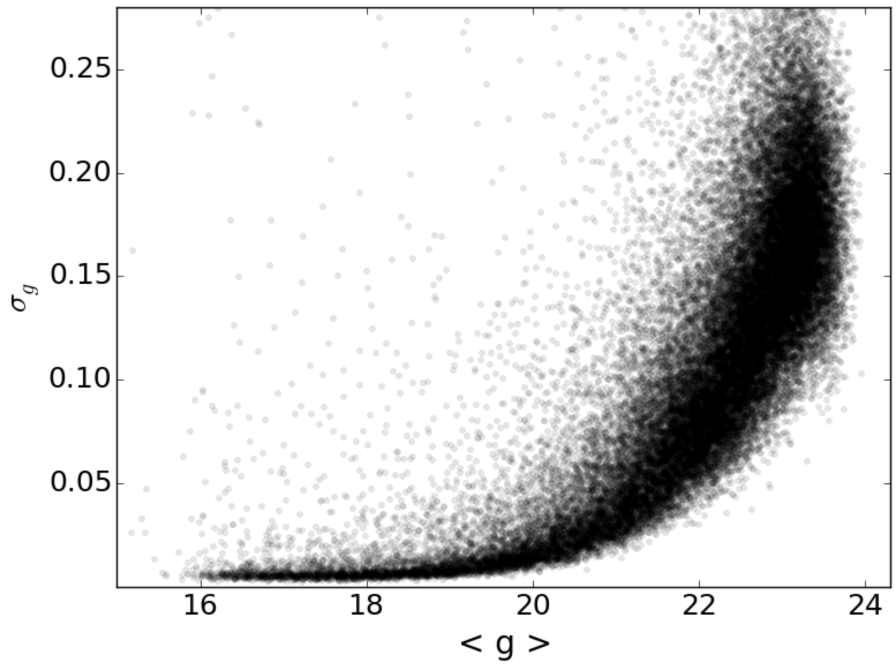

Figure 2.6 Variation of σ_g with the average magnitude for Field 8 (black dots). To generate a model, a cubic spline interpolation is applied to the sigma-clipped data.

their distance distribution.

To approximate an inherent value of this error it is not always recommended to rely on the flux errors of the individual observations given by the Sextractor software, and then to propagate to a mean magnitude error since they could be underestimated in the first place (Gawiser et al., 2006). For this reason it is necessary to assume magnitude uncertainties for each star by comparing with a non-parametric model of the standard deviation (σ_g) and mean magnitude ($< g >$) relation for all the stars in their respective fields. This is done by determining the mean magnitudes and standard deviation of all the stars in a field throughout the number of times that field was observed. As one could expect, the values of σ_g increase exponentially as the mean magnitude of the sources increases (see Figure 2.6). A cubic spline interpolation is applied to the data once it is sigma clipped. The value of the model for a star with a given mean magnitude in a HiTS field (σ_g) is expected to be then the mean magnitude uncertainty of that star.

2.5. Completeness Estimation

Having an estimation of how efficient is the method described above to detect RRLs is important in order to account for how many RRLs this study could be losing at a determined magnitude. In an ideal world, a method should be able to detect 100 % of the objects in the range of magnitude it covers, but that is far from the real situation. The efficiency in the detection depends on several factors, including the phase coverage the light curves have (number of epochs, cadence), how faint/bright the sources are, and how this relates to the

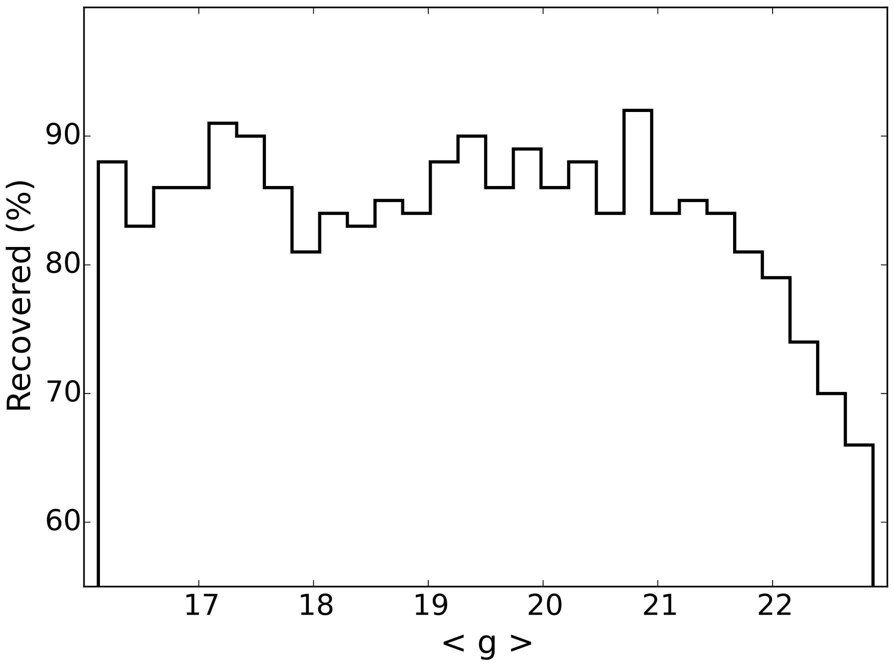

Figure 2.7 Recovery rates for the HiTS 2014 survey, and its mean magnitude dependance.

typical uncertainties of the magnitudes, among others.

To evaluate the completeness of the survey from the HiTS 2014 data, 5000 artificial light curves are studied. These light curves, generated by the astronomer Kathy Vivas, mimic the real cadence and typical photometric errors of the survey. Specifically, the number of observations per object were set equal to the ones of randomly selected RRLs in the survey. Thus, the number of epochs in the artificial light curves vary from 16 to 37. Each light curve was modelled using the parameters (amplitude in g, period and template) from the list of RRLs from SDSS in Sesar et al. (2010). A random initial phase was added to each simulated star. Finally, photometric errors were added to the template magnitudes according to the values of the main locus of stars seen in Figure 2.6. The artificial light curves are then processed by the pipeline and stars which pass all the criteria and have a period within 10 % of the real one are flagged as recovered.

Figure 2.7 shows the results of the process represented as a histogram where 0,25 magnitude bins are used. In the bright end, the followed methodology is able to recover $\sim 86\,\%$ of the full sample, and the rate ranges between 81 % and 92 % down to $g = 21{,}5$. Then, the completeness drops to less than 70 % for RRL fainter than $g = 22$.

The rates shown in Figure 2.7 represent the fraction of RRLs that pass the filters described above up to the step in which they are visually inspected. The completeness estimation of the RRLs detection does not take the photometric completeness of the survey into account.

2.6. Photometric Calibrations

So far, the selection and characterization of RRLs has been based on the instrumental magnitudes obtained in Section 2.2. This section describe the procedure that is used to calibrate the instrumental magnitudes obtained previously. These calibrations are made by comparing the instrumental magnitudes of stars in the reference frame with the values of g obtained by important previous surveys that cover large regions of the sky and overlap the HiTS field of view. By doing this correction, the magnitudes presented in the catalog of RRLs are "standarized".

The calibrations presented here are applied to the 2014A data only. The use of these techniques on the 2015A data is not presented in this thesis, and is briefly described in Appendix Section as part of the future work.

2.6.1. Sloan Digital Sky Survey Zeropoint

Since the SDSS is one of the most successful sky surveys with large coverage, a comparison of their catalogs is a natural extension of the work presented in this thesis. In spite of the overall brighter sources the SDSS catalogs have, the sky coverage of the survey (of over $14,000$ square degrees) made of SDSS the best option to compute calibration zeropoints before the PS1 became available. However, not all the HiTS fields/CCDs are present in the SDSS' footprint. This is shown in Figure 2.8. Here, the SDSS data release 10, which is part of SDSS-III (Ahn et al., 2014), is used.

To access the SDSS data, the Catalog Archive Server Jobs System (Casjobs) online tool is used. The casjobs service [2] is an online workbench that permits the users to perform large queries by using an SQL syntax. By using this tool, SDSS sources within 3° of the center of the 40 fields of HiTS 2014A are downloaded.

In order to compare the catalogs with the SDSS data, 40 files are created containing HiTS' data from the reference frame. Each one of these files contains information about the 60 available chips of the field and the stars within, with celestial coordinates (RA, DEC), magnitudes, and uncertainties.

Using the Starlink Tables Infrastructure Library Tool Set (STILTS; Taylor, 2006), an automated crossmatch between the 40 HiTS and SDSS catalogs is performed. STILTS is a command-line based package of tools designed for processing astronomical tabular data such as the catalogs here described. This Java package is an efficient and flexible program especially designed to deal with large datasets and to perform data calculations. It is the counter-part of the GUI table analysis tool TOPCAT (Taylor, 2005).

Once a crossmatch of sources within 2 arcseconds between catalogs is made, the comparison of the stars' magnitudes per field and CCD is carried out. Because of possible effects of the non-linearity of the detectors near the saturation limit, and the presence of artifacts for the

---

[2] `http://skyserver.sdss.org/casjobs/`

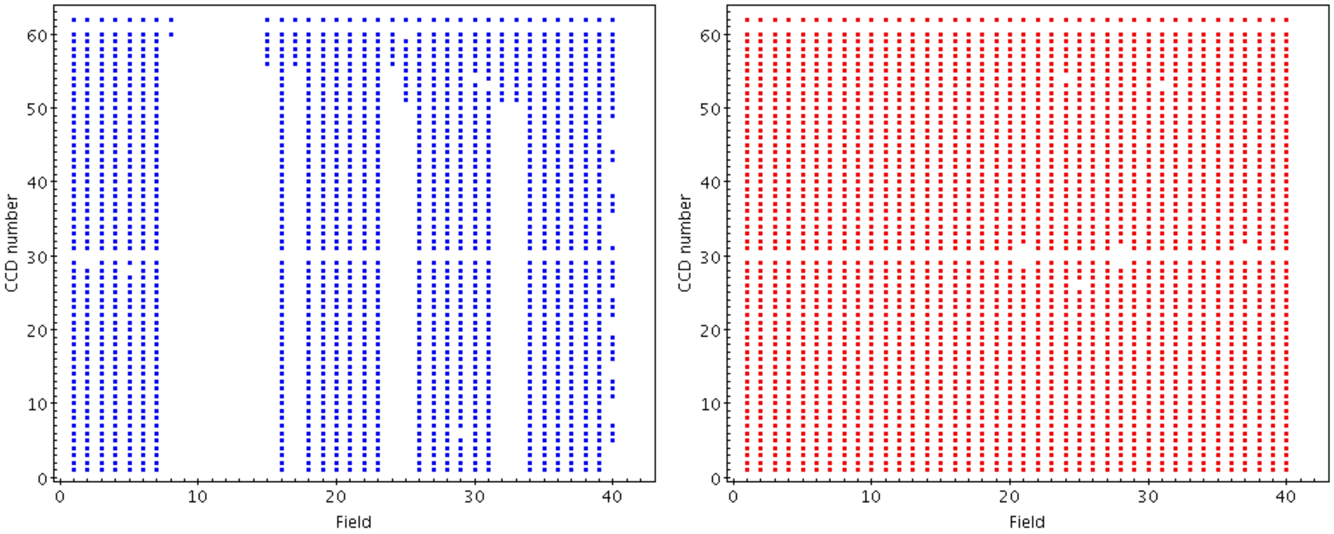

Figure 2.8 Overlap of two different large sky surveys with the HiTS 2014A data. The X-axis represent the field, while the Y-axis is the number of the CCD, from N1 to S31 (1-62). Note that the chips N30 and S30 are not available. *left panel*: HiTS' fields/CCDs with more than 15 common stars with the SDSS. Note that only $\sim$ 70 of the total number of fields/CCDs from HiTS are covered. *right panel*: Overlap of HiTS with PS1. Fields with more than 12 matches between both surveys are shown.

faint end of the HiTS magnitude distribution, only stars with $16{,}0 < g < 22{,}5$ from HiTS were considered for this calculation. For the sake of working with robust statistics, and to consider mostly non variable sources, this is only done if the number of common stars between HiTS and SDSS is greater than 15. This procedure yields 60 different zero-points for a given field, if complete overlap with SDSS is assumed. The results of the described method are shown in Figure 2.9. The zeropoints show a slight chip-to-chip variation, but behave in a stable manner when individual chips are considered.

A non negligible number of HiTS fields are not completely covered by the SDSS ($\sim 30\,\%$). In these cases, the small variations of the zeropoint for a given chip is assumed to reflect the effects of the different sky conditions over the CCDs, for the reference. For this reason, for the un-matched fields the mean values of the zero-points of individual CCDs is used as a good representation of its behavior. This consideration is valid since the fields are closely spaced and were observed consecutively within a short timespan. This is also represented in Figure 2.9.

The overall results, including all the fields/CCDs (matched and un-matched with the SDSS footprint) are shown in Figure 2.10 as a histogram. The mean value of the zeropoint is $-0{,}020\,\mathrm{mag}$, with a standard deviation of $0{,}085\,\mathrm{mag}$.

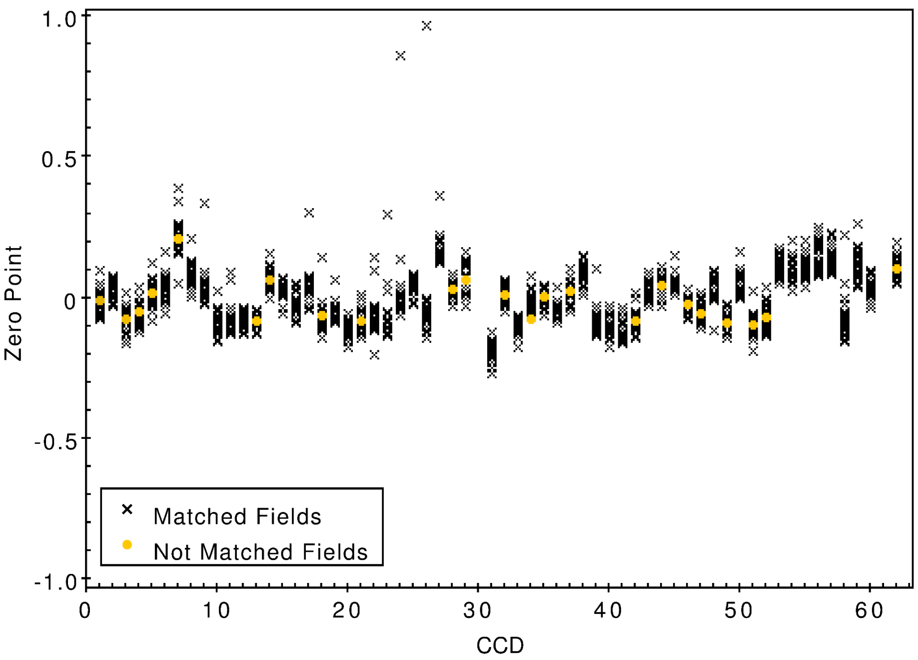

Figure 2.9 The zero point calibration values and their dependence on the chip. In theory, on each value of the CCD number there should be 40 datapoints in the Y-axis, representing the 40 fields. Black crosses represent the HiTS fields with a counterpart in the SDSS database. Filled circles (yellow) represents not-matched CCDs, for which the mean of the overall CCD behaviour is accounted.

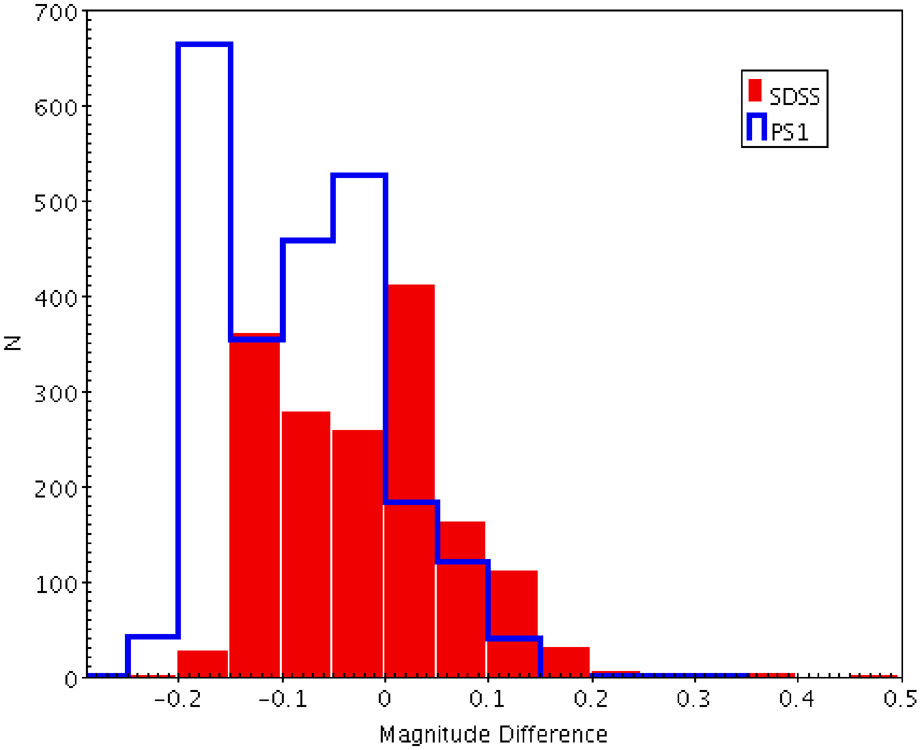

Figure 2.10 The distribution of the zeropoint values resulting after comparing the HiTS instrumental magnitudes with the SDSS and PS star catalogs. In this plot, the distribution represents fields and CCDs.

2.6.2. Pan-STARRS Zeropoint

The Pan-STARRS public catalogs can be used as a comparison for the determination of zeropoints just as the SDSS ones. In fact, this survey is a wide field survey as well, and covers most of the sky northern of declination $-30\,\deg$. One of the features that make the PS1 attracting for these purposes is the range of magnitudes it reaches for the g, r, i, z and y photometric bands. The saturation limit for the data of the PS1 is $12-14\,$mag, depending on the seeing, and their stacked images can reach a 5σ depth of $grizy < 23{,}3, 23{,}2, 23{,}1, 22{,}3, 21{,}3$.

When comparing the HiTS instrumental magnitudes with the PS1 public catalogs the methodology is similar to the described in the previous subsection. The main difference is that the coverage of the survey overlap almost entirely the HiTS footprint, permitting a direct comparison of both surveys for all the fields/CCDs observed in 2014A.

The distribution of zeropoint values (Figure 2.10) has a mean of $-0{,}083\,$mag with a standard deviation of 0,081, but is not as centered in zero as the obtained with the SDSS data. The PS1 correction is the one considered hereafter as the source of zeropoint calibration values.

2.7. Heliocentric Distance Determination

As explained in Chapter 1, period-luminosity relations for pulsating stars have been studied over a wide range of photometric filters and for different types of stellar populations. In the case of the low mass horizontal branch RRL, strong correlations between absolute magnitudes (hence distances) and periods have been found only for certain bandpasses (tigher toward the near infrared), owing to how the luminosity, temperature and periods are bonded for a given horizontal branch disposition (Catelan et al., 2004).

Unfortunately, according to Cáceres & Catelan (2008), there is not a tight PL relationship for RRLs in the $g-$band. In order to get accurate distances, other studies (Watkins et al., 2009; Vivas et al., 2016) have converted their g magnitudes into V using photometric transformations involving the $(g-r)$ color. This allows the use of the well known M_V for RRL (Cacciari & Clementini, 2003). For this thesis, there is no r magnitude available in the 2014A data to determine a color and therefore an alternative method has to be used to estimate a representative absolute magnitude for the halo RRLs in the $g-$band. The two methods used for the HiTS data are explained in the following subsections, after giving the details of the correction of the magnitudes by extinction.

2.7.1. Reddening Correction

Reddenning is an essential phenomenon to account for when the quantity of interest of an study is the intrinsic apparent magnitude rather than the uncorrected observable magnitude. The origin of the exctinction is the absorption and scattering of radiation by dust and gas located between the source and the observer. Since the bluer parts of the electromagnetic spectrum suffer a higher attenuation than the redder parts, objects appear to be redder in comparison with the originally emitted light. Therefore, since the reddening effect is associated with the amount of interestellar material between the source and the observer, it depends on the location of the sources in the galaxy. In the case of this work, correcting by exctinction is fundamental even when the field of view of HiTS is the Galactic halo. The explanation for this is that an RRL star of a certain uncorrected magnitude (g in the case of HiTS' RRLs) would look fainter (more distant) than it should.

In general, the reddening can be described by a color excess, which is the difference between the observed and intrinsic color index of the source:

$$E(B-V) = (B-V)_{\text{observed}} - (B-V)_{\text{intrinsic}}$$

where $E(B-V)$ is the color excess, and $(B-V)$ is the typical color used in the UBV photometric system. From this relation, the value of the exctinction factor A_V can be determined by $A_V = E(B-V) \cdot R(V)$, with $R(V)$ being a value correlated with the size of the dust grains.

The final apparent magnitudes used to determine distances includes exctinction corrections for which the dust maps of Schlafly & Finkbeiner (2011) are used. From that work, a list of $E(B-V)$ and A_V is given for the full list of RRL from HiTS 2014A (assuming $R(V) = 3{,}1$). The extinction values for the $g-$band were calculated using the relation $A_g = 3{,}303 \cdot E(B-V)$ from the same work. By doing this, the average A_g value of the RRLs in the HiTS fields is $\sim 0{,}14$, with a standard deviation of 0,03.

2.7.2. Anchoring Distances to the Catalina Survey's Data

To overcome the problem of the lack of a tight PL relation for RRLs in the $g-band$ a characteristic M_g for the complete RRLs sample is computed taking advantage of the common RRLs of the Catalina Surveys and the HiTS footprint. A complete comparison of these RRLs, and the missing ones, is presented in Section 3.1.3. For this estimation, 52 RRLs that appear in both surveys are considered. Since the Catalina catalog provides information about the mean V magnitude of their RRLs, heliocentric distances are calculated for them through distance modulus, by using $< M_V >= 0{,}55$ (Demarque et al., 2000). This value comes from the assumption of [Fe/H]$= -1{,}6$ as a representative metallicity for the halo. With the heliocentric distances calculated, and knowing the stars' g magnitudes, an average value for M_g can be determined. Following that idea, the absolute magnitude in g is:

$$< M_g >= 0{,}692 \pm 0{,}065$$

where the uncertainty corresponds to the dispersion of the resulting M_g values. This value of $< M_g >$ is a first approximation for the individual values of M_g, and could be considered an estimation of the representative value for the RRLs catalog presented in this thesis.

As the method for determining $< M_g >$ (and hence, distances) is not direct, it is expected for the distance uncertainties to be larger than usual.

2.7.3. Using Period-Luminosity-Metallicity Relations

Recently, Sesar et al. (2017a) obtained period-luminosity-metallicity (PLZ) relations for RRab stars in the PS1 bandpasses (g, r, i and z), based on the distance moduli of five globular clusters. Individual values of M_g can be computed for the RRLs presented in this work by using the PLZ relation for g from Sesar et al. (2017a). The use of these values of M_g provide precise distance determinations for the RRLs in PS1 even if the metallicity is unknown. This PLZ relation, of a shape resulting from theoretical and empirical studies (Catelan et al., 2004) is:

$$M = \alpha \; log_{10}(P/P_{\rm ref}) + \beta \; ([Fe/H] - [Fe/H]_{\rm ref}) + M_{\rm ref} + \varepsilon \tag{2.1}$$

where P is the period of pulsation of the RRL, $M_{\rm ref}$ is the absolute magnitude at the reference period $P_{\rm ref} = 0{,}6$ days and metallicity $[{\rm Fe/H}]_{\rm ref} = -1{,}5$ dex. The parameters α and β represent the dependence of the absolute magnitude on the period and metallicity, respectively. ε is a variable that models the scatter in the absolute magnitude when convolved with unaccounted measurement uncertainties.

Table 1 in Sesar et al. (2017a) set the values for α, β, $M_{\rm ref}$ and ε for the $g-$band as:

$$\alpha = -1{,}7 \pm 0{,}3 \text{ mag dex}^{-1}$$

$$\beta = 0{,}08 \pm 0{,}03 \text{ mag dex}^{-1}$$

$$M_{\rm ref} = 0{,}69 \pm 0{,}03 \text{ mag}$$

$$\varepsilon = 0{,}07 \pm 0{,}01 \text{ mag}$$

However, since there are no metallicities available for the HiTS RRLs, it is necessary to assume a value for the metallicity of the Galactic halo. A convenient assumption is to consider [Fe/H]$= -1{,}5$ as a good representation for the halo, which comes from known relations of the metallicity and the absolute magnitudes of RRLs in the halo (Demarque et al., 2000). In the case of a better estimation of [Fe/H] for some stars (as in Section 3.2), this procedure is repeated with more specific values of [Fe/H].

It is worth noticing that the previous PLZ relation is valid only for fundamental mode pulsators (RRab's). However, the use of the relation on RRc's could be justified if the periods of their pulsation are "fundamentalized". The latter can be understood as a shift in the period and luminosities of RRc's to match the valid relation of RRab's. For the RRc in the sample, the fundamentalized periods given by the following expression are used:

$$log(P_{\rm F}) = log(P) + 0{,}128 \tag{2.2}$$

where $P_{\rm F}$ is the fundamentalized period and P is the original (first overtone) period (Catelan, 2009).

If the metallicity considered is assumed to have an offset of ±0,5 dex from [Fe/H]= −1,5 (i.e., [Fe/H]= −1,0 or [Fe/H]= −2,0), the fractional difference in heliocentric distances would be of 1,8 %. This is, for the faintest RRLs, 4 kpc approximately. If the value of the offset is ±1,0 dex instead ([Fe/H]= −1,5 or [Fe/H]= −2,5), the fractional variation is ∼ 3,6 % with distances differences up to 8 kpc. The mean uncertainty in the distances obtained with this method is 5 %, which is consistent with the typical distance uncertainties of RRLs.

In Table 3.3 the distances obtained by this method are shown for the faintest (and hence farthest) candidates, while Figure 3.4 presents a radial plot for the entire list. The uncertainties in the distance estimates include the propagation of the errors associated to obtaining the absolute magnitudes and the photometric errors.

Chapter 3

RR Lyrae stars in HiTS 2014

In this chapter, details of the sample found in Chapter 2, with data from HiTS 2014, are given. A brief overview of the main properties of the full sample is provided in Section 3.1. The description of the RRLs from HiTS 2014A that belong to currently known dwarf spheroidal galaxies is given in Section 3.2. In Section 3.3 a characterization of the distant RRLs present in the sample is provided, while the analysis of number density profiles created with the full list is given in Section 3.4.

3.1. The sample

As described in the previous chapter, the search for RRLs in the data from HiTS 2014A results in a catalog composed of 173 stars, found in the ~ 120 square degrees area of that campaign. These RRLs have (corrected) mean magnitudes in g that range from 15,5 to 22,8 (Figure 3.1), and span over a region from 8,8 to 261 kpc (Figure 3.4). The complete list of RRLs is shown in Table 3.1, Table 3.2 and Table 3.3.

Identification names are given to the RRL based on their equatorial coordinates (RA, DEC), in a sexagesimal system. These names are given as a string value with the following format: "HiTS" + RA (hr:min:sec) + DEC (deg:arcmin:arcsec).

In the next subsections more specific properties of the RRLs list are analyzed.

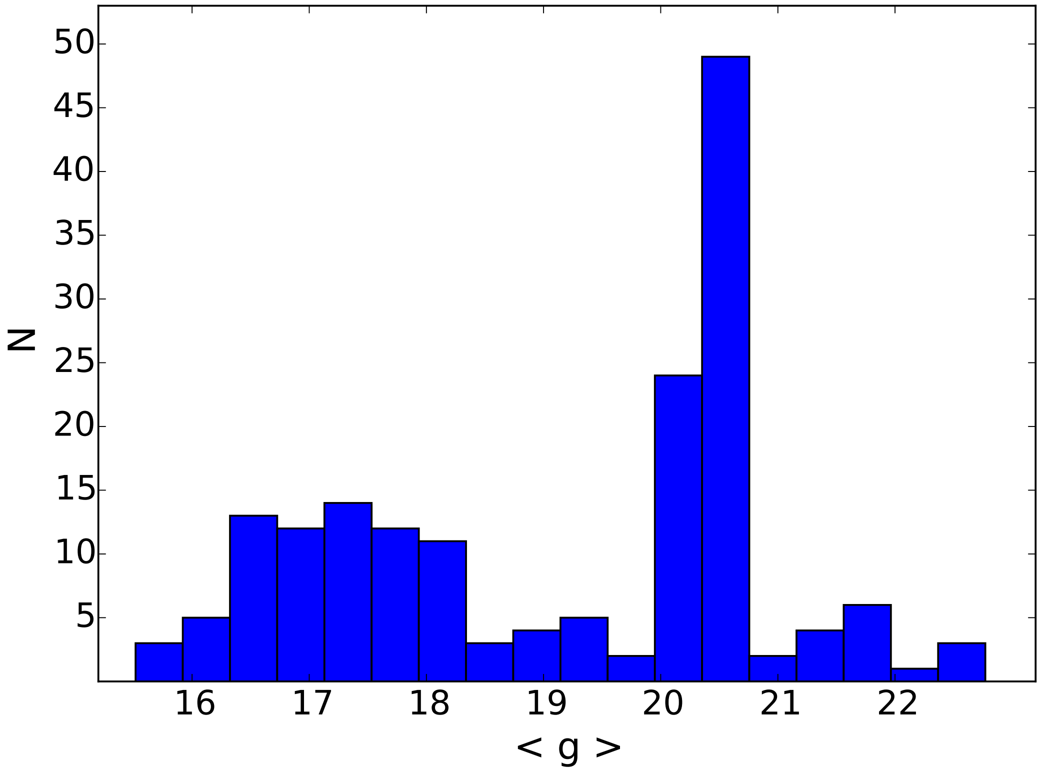

Figure 3.1 Distribution of the mean magnitudes g for the complete sample of RRLs from HiTS 2014.

Table 3.1. Full list of the RRLs presented in Chapter 3, excluding the candidates in the Sextans dSph galaxy. The table shows the main properties of the RRLs, as well as their number of observations (N).

ID	R.A. (deg)	DEC (deg)	$< g >$	Period (days)	Amplitude	d_H (kpc)	Type	N
HiTS095845+023118	149.68616	2.52172	17.9	0.6453	0.36	28	ab	18
HiTS100129+001100	150.37090	0.18338	16.4	0.6098	1.30	13	ab	21
HiTS100207+012232	150.52751	1.37554	16.5	0.7208	0.91	15	ab	16
HiTS100236+030023	150.64878	3.00649	16.1	0.6079	1.02	12	ab	20
HiTS100838-020312	152.15703	-2.05345	17.4	0.5799	1.28	20	ab	38
HiTS100843-041555	152.17745	-4.26539	17.9	0.6215	0.48	27	ab	21
HiTS100911-041232	152.29475	-4.20889	17.8	0.3754	0.65	26	c	21
HiTS100942+012903	152.42563	1.48407	19.3	0.4875	0.81	47	ab	20
HiTS100956+013212	152.48158	1.53665	20.4	0.6220	0.68	84	ab	20
HiTS101014-020114	152.55937	-2.02065	16.8	0.5574	1.08	15	ab	35
HiTS101057-033322	152.73691	-3.55624	19.8	0.6363	1.17	63	ab	21
HiTS101243+022118	153.17763	2.35503	20.6	0.5346	1.04	87	ab	20
HiTS101321-035610	153.33614	-3.93599	18.6	0.5871	0.97	36	ab	21
HiTS101336-013752	153.40203	-1.63120	18.8	0.6960	0.88	42	ab	20
HiTS101353-035021	153.46884	-3.83912	17.3	0.4162	0.23	22	c	21
HiTS101452-002635	153.71870	-0.44305	18.1	0.5803	0.96	28	ab	21
HiTS101529-012126	153.86970	-1.35711	20.1	0.4132	0.71	63	ab	21
HiTS101626-041658	154.10903	-4.28284	17.6	0.7404	0.58	24	ab	21
HiTS101750-020127	154.45848	-2.02430	16.5	0.3307	0.46	14	c	21
HiTS101936-012754	154.89982	-1.46512	17.1	0.6329	0.51	18	ab	21
HiTS101953-050553	154.97160	-5.09813	19.3	0.6865	0.82	50	ab	20
HiTS101957-020302	154.98816	-2.05048	19.5	0.4292	0.95	48	ab	21
HiTS102014-042354	155.05789	-4.39843	22.5	0.3841	0.37	233	c	19
HiTS102106-064439	155.27585	-6.74404	18.9	0.5985	0.94	41	ab	17
HiTS102306-080748	155.77552	-8.12994	17.4	0.4663	1.40	18	ab	21
HiTS102313-082435	155.80301	-8.40973	17.2	0.4632	1.30	17	ab	20
HiTS102344-064233	155.93215	-6.70930	18.2	0.6582	0.45	31	ab	17
HiTS102414-095518	156.05905	-9.92180	21.7	0.7641	0.54	161	ab	21
HiTS102610-083620	156.54047	-8.60557	16.2	0.3228	0.53	12	c	22
HiTS103015-050203	157.56265	-5.03403	17.1	0.3032	0.62	18	c	22
HiTS103601-015451	159.00456	-1.91422	21.7	0.4045	0.29	161	c	21
HiTS103626-014703	159.10785	-1.78424	16.1	0.5872	1.08	11	ab	19
HiTS103758-043930	159.49133	-4.65828	17.9	0.5836	0.89	25	ab	21
HiTS103931-034037	159.87731	-3.67708	17.1	0.5480	0.70	17	ab	21
HiTS103943-021726	159.93119	-2.29061	20.9	0.6956	0.44	108	ab	21
HiTS104009-063304	160.03895	-6.55105	20.8	0.6376	0.69	100	ab	21
HiTS104054-042827	160.22661	-4.47424	21.9	0.4650	0.34	183	c	20
HiTS104402-040641	161.00852	-4.11148	17.4	0.5705	1.04	20	ab	21
HiTS104407-035317	161.03109	-3.88797	18.0	0.6190	0.63	28	ab	21
HiTS104423+011722	161.09545	1.28950	16.4	0.3620	0.51	13	c	21
HiTS104427+024346	161.11385	2.72931	17.6	0.3198	0.40	23	c	18
HiTS104738+020627	161.90718	2.10746	22.8	0.3844	0.47	262	c	19
HiTS104924-023635	162.34954	-2.60969	17.5	0.5263	1.28	21	ab	20
HiTS105142+001611	162.92606	0.26978	16.5	0.6488	1.07	14	ab	20
HiTS105152+021339	162.96779	2.22743	16.1	0.5548	1.12	11	ab	20
HiTS105209-043942	163.03718	-4.66174	21.5	0.6036	0.46	136	ab	20

Table 3.1 (cont'd)

ID	R.A. (deg)	DEC (deg)	$< g >$	Period (days)	Amplitude	d_H (kpc)	Type	N
HiTS105213-043434	163.05435	-4.57609	17.3	0.3632	0.17	21	c	20
HiTS105226+022759	163.10707	2.46631	16.8	0.5584	1.07	16	ab	21
HiTS105311+015046	163.29669	1.84613	17.2	0.2893	0.28	18	c	20
HiTS105502-025906	163.75656	-2.98510	16.9	0.5797	0.94	16	ab	20
HiTS105537+022053	163.90258	2.34818	17.0	0.5476	0.90	17	ab	21
HiTS105545-013021	163.93648	-1.50583	16.5	0.4599	1.34	12	ab	20
HiTS105545-013440	163.93662	-1.57783	20.4	0.5219	1.01	76	ab	20
HiTS105549+023408	163.95249	2.56879	17.0	0.4496	1.44	15	ab	21
HiTS105613-015658	164.05547	-1.94939	18.1	0.7732	0.41	30	ab	20
HiTS105634+013335	164.14314	1.55986	18.1	0.3041	0.53	29	c	20
HiTS105726+024352	164.35679	2.73115	19.4	0.5843	1.02	53	ab	21
HiTS105738+001316	164.41037	0.22123	18.2	0.6421	0.53	30	ab	21
HiTS105754-002603	164.47577	-0.43403	20.5	0.3609	0.62	93	c	20
HiTS105843+023125	164.67737	2.52354	18.0	0.6988	0.71	29	ab	21
HiTS105933+020617	164.88765	2.10477	16.9	0.4653	1.31	15	ab	19
HiTS110117-035105	165.32027	-3.85142	19.9	0.4277	0.53	57	ab	18
HiTS110200+005324	165.49980	0.89006	17.6	0.5336	0.57	23	ab	21
HiTS110222-001624	165.59251	-0.27337	22.1	0.6118	0.51	180	ab	19
HiTS110243+014821	165.68036	1.80572	17.2	0.7910	0.55	21	ab	20
HiTS110254-003415	165.72515	-0.57075	17.4	0.3383	0.48	22	c	21
HiTS110456+015745	166.23204	1.96261	17.2	0.6505	0.93	20	ab	20
HiTS110510-022710	166.28982	-2.45282	22.4	0.7459	0.61	219	ab	19
HiTS110616+015120	166.56478	1.85545	16.4	0.3509	0.48	14	c	20
HiTS110739+012813	166.91383	1.47037	20.4	0.4359	0.24	93	c	20
HiTS110829+013851	167.11962	1.64753	16.5	0.5937	1.05	14	ab	20
HiTS111033-032936	167.63857	-3.49333	15.6	0.3439	0.49	9	c	22
HiTS111106-041718	167.77512	-4.28834	21.2	0.3034	0.62	113	c	22
HiTS111246-043641	168.19260	-4.61130	16.5	0.5258	1.13	13	ab	21
HiTS111311+025109	168.29469	2.85259	16.5	0.7284	0.67	15	ab	19
HiTS111342-021922	168.42638	-2.32288	17.3	0.3103	0.44	20	c	22
HiTS111420+024911	168.58268	2.81958	17.6	0.5540	1.10	22	ab	20
HiTS111522-025143	168.84248	-2.86206	18.0	0.6350	0.58	27	ab	21
HiTS111722+022620	169.33980	2.43886	17.2	0.6322	0.99	19	ab	20
HiTS111934-041741	169.89346	-4.29472	15.8	0.6413	0.37	10	ab	22
HiTS112000-003831	169.99881	-0.64205	16.6	0.4494	0.99	13	ab	20
HiTS112039-040702	170.16125	-4.11709	16.2	0.3906	0.55	13	c	22
HiTS112058-020326	170.23962	-2.05724	16.4	0.3516	0.49	14	c	22
HiTS112445+013726	171.18809	1.62395	18.1	0.5997	0.81	28	ab	20
HiTS112524-024348	171.35051	-2.72999	20.4	0.6373	0.43	83	ab	22
HiTS112549-041215	171.45363	-4.20410	15.5	0.6733	0.84	9	ab	20
HiTS112807-034733	172.03057	-3.79243	18.2	0.6359	1.14	29	ab	20
HiTS112820-000636	172.08521	-0.11014	19.3	0.6840	0.74	54	ab	20
HiTS112838-000112	172.15740	-0.02008	18.9	0.5699	1.10	40	ab	20
HiTS112859-034415	172.24634	-3.73761	20.4	0.3934	0.52	84	c	20
HiTS113006+001108	172.52405	0.18565	17.9	0.6584	0.28	28	ab	20
HiTS113057+021331	172.73946	2.22514	21.8	0.6453	0.72	172	ab	20

Table 3.1 (cont'd)

ID	R.A. (deg)	DEC (deg)	$< g >$	Period (days)	Amplitude	d_H (kpc)	Type	N
HiTS113105+021319	172.76936	2.22200	21.8	0.6574	1.40	172	ab	20
HiTS113107+023025	172.77770	2.50700	18.8	0.6626	0.90	41	ab	21
HiTS113107+021302	172.77796	2.21734	21.7	0.6442	1.02	163	ab	21
HiTS113217-035542	173.07262	-3.92844	17.9	0.7370	0.53	27	ab	20
HiTS113256-003329	173.23270	-0.55818	21.5	0.7146	0.78	156	ab	19
HiTS113259-003404	173.24674	-0.56770	21.5	0.6268	1.22	147	ab	18
HiTS113314+022239	173.30754	2.37736	17.6	0.6029	0.69	23	ab	20
HiTS113336-011012	173.39867	-1.17007	16.9	0.5125	1.21	16	ab	20
HiTS113353+010816	173.46942	1.13774	17.3	0.8128	0.83	23	ab	21
HiTS113400+024753	173.49853	2.79812	18.7	0.6703	0.86	39	ab	21
HiTS113600+021833	173.99975	2.30909	17.8	0.6626	0.61	27	ab	18
HiTS113609+025834	174.03651	2.97606	17.7	0.5505	1.01	24	ab	21
HiTS113634-012016	174.14059	-1.33785	18.7	0.6242	0.58	39	ab	20
HiTS113640-012516	174.16589	-1.42113	16.8	0.6507	0.60	17	ab	20
HiTS113653-024629	174.22135	-2.77481	16.7	0.2668	0.40	14	c	20
HiTS113748-021817	174.45040	-2.30472	16.8	0.5724	1.11	16	ab	20

3.1.1. Pulsational Properties and Classification

Throughout this work, the importance of the period and amplitude of the pulsation of RRLs has been recalled as fundamental parameters in terms of their characterization. By this point, the periods of the RRL correspond to the highest values in the periodogram that give a reasonable RRLs shape for the folded light curves. In the case of the amplitudes, they are just the difference between the extreme values of the magnitude in a light curve (Δg). However, Δg is not necessarily a good approximation of the intrinsic value of the amplitude, as a consequence of the low number of points used to sample the light curves.

To have a better estimation of these parameters, the parameters associated to adjusted templates of RRLs from a work based on SDSS Stripe 82 RRLs (Sesar et al., 2010) are used. In that study, a list of 23 templates is provided for the $g-$band, two of which are for RRc. The selection of the best fit for each candidate is not part of the work done for this thesis, and was based on χ^2 minimization. Also, the fitting process allowed small variations around the observed amplitude and maximum magnitude (0,2 magnitudes for each) as well as for the period and initial phase obtained through GLS (0,01 days and 0,2, respectively). The values of the periods and amplitudes obtained by this procedure are the ones used hereafter.

Regarding the classifications, the criteria used to distinguish between RRab's and RRc's is based on the period, amplitude and best template used to fit the light curve of the star. In this sense, RRLs with long periods and high amplitudes are most likely RRab's, alghough the classification is strongly dependent on the template fitted. The same situation applies to RRc's when the stars have short periods and low amplitudes.

The final classification of the 173 RRLs leads to 131 RRab's and 42 RRc's. Figure 3.2 shows the location of the RRLs in the Period-Amplitude space, color-coded by type.

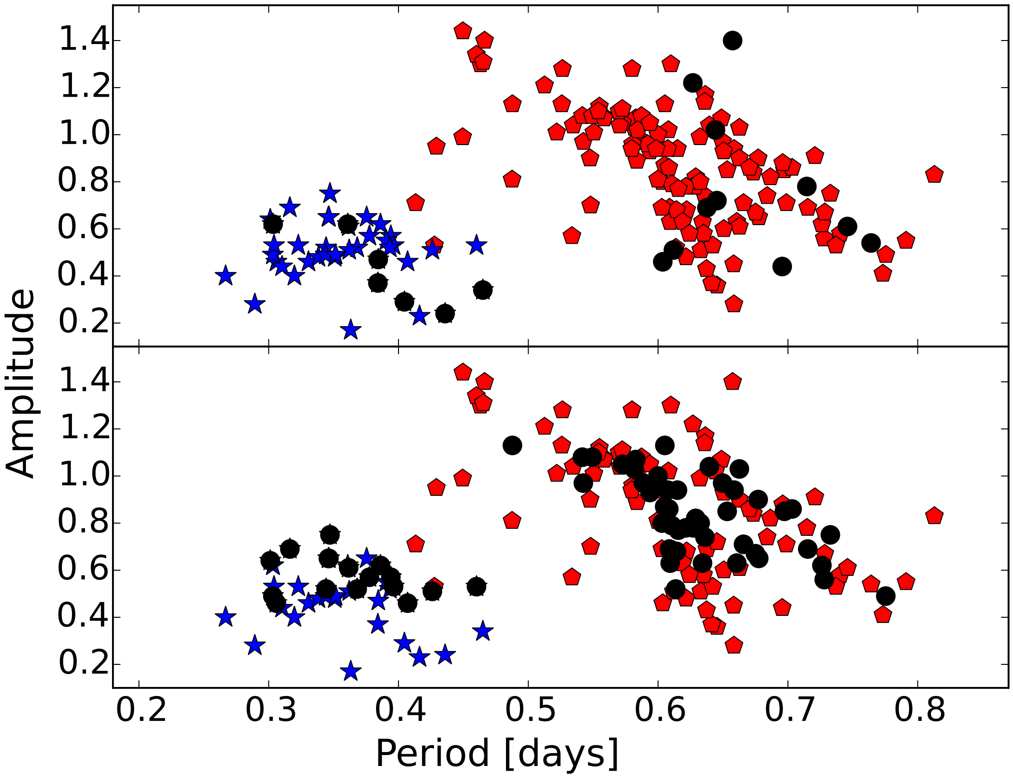

Figure 3.2 Period-Amplitude diagram of the complete sample of RR Lyrae stars. The blue hexagons represent RRc stars, while the RRab are plotted with red symbols. Black filled circles represent RRLs with $d_H > 90\,\text{kpc}$ (*top*) and RRLs members of the Sextans dSph galaxy (*bottom*).

The period-amplitude distribution of large samples of RRLs is important when understanding their possible origins. For example, $ab-$type RRLs that are members of globular clusters are separated in the distincted Oosterhoff groups (OoI and OoII; Oosterhoff, 1939), based on both their mean periods and their proportion compared with RRc's. Dwarf spheroidal galaxies of the MW do not show such dichotomy and many of them have been classified as Oo-Intermediate systems (Catelan, 2009; Catelan & Smith, 2015). Most of the ultra-faint dwarf satellites, on the other hand, despite their low number of stars, have been classified as Oo-II systems (Clementini, 2014), with typical mean periods of $\sim 0{,}65$ days. In Figure 3.2, the sequences of the Oo groups are clearly visible, specially for the halo RRab at distances < 90 kpc.

3.1.2. Spatial Distribution

Once equatorial coordinates and distances are determined for the sample of RRLs, a natural thing to do for the scope of this study is to analyze how these stars are populating this region of the halo. This exercise is particularly interesting when trying to associate groups of RRLs with currently known or undiscovered features. The sort of features that can be visible from studying the spatial distribution of RRLs go from substructures like simple stellar overdensities, streams, and tidal debris, to other stellar systems like globular clusters or satellite galaxies. This kind of information is crucial since it can give clues of the history of interactions of the Milky Way with systems with RRLs and the old stellar populations they represent.

Figure 3.3 exhibits the distribution of the 173 RRLs in the sky, as well as the HiTS footprint for 2014A. This figure also shows an auxiliar axis representing the heliocentric distances (color coded) obtained by following the methodology explained in Chapter 2.

The plot shows that the HiTS RRLs are mostly uniformly distributed along the fields, in right ascension, declination, and distance, with a few exceptions. Figure 3.4 display almost the same information from a different perspective. In the latter (a radial plot) the distribution of distances in kilo–parsecs as a function of the right ascension is shown. In spite of the overall uniformity on the location of the stars, from Figure 3.3, Figure 3.4, and Table 3.3 three groups of RRLs are evident. These overdensities coincide with the heliocentric distance and sky positions of three previously known dwarf satellite galaxies of the Milky Way. The RRLs in these systems are described in another section (see Section 3.2).

3.1.3. Comparison with previous surveys

Another way to investigate how many real RRLs are being missed by following the procedure described in the preceding chapter is to compare the resulting catalog with recent large-area surveys that covered the same portion of the sky as HiTS. In this subsection, data from the Catalina Survey data release 1 is used(Drake et al. 2013a, 2014), as well as the RRLs catalog from the La Silla-QUEST (LSQ) survey (Zinn et al., 2014) and from the Pan-STARRS 3π survey (PS1). The first two works are well known as $V-$band RRL star

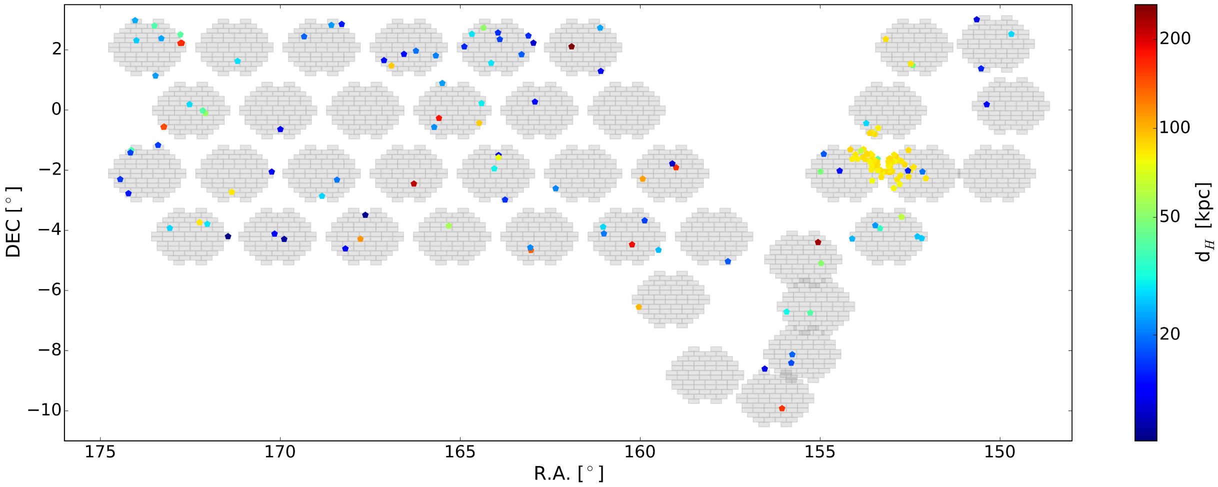

Figure 3.3 Color coded plot of the distribution of the 173 RRLs stars from HiTS 2014 in the sky, with the colors representing their heliocentric distances. An approximation of the HiTS footprint is shown in grey in the background as a reference.

databases, while PS1 is a large database in the *grizy* filters.

Drake et al. (2013a) present a catalog of $\sim$ 15000 fundamental mode pulsators. A more complete periodic variable catalog was given later with the classification of more than 47000 stars in 17 independent categories (Drake et al., 2014). That includes a differentiation between pulsational objects (e.g., RR Lyrae, Cepheids, high and low amplitude δ Scutis) and eclipsing variables (e.g., contact binaries, detached/semi detached systems). The Drake et al. (2014) catalog contains roughly 14000 known CSS RRab's and 150 Blazhko types from Drake et al. (2013a) (from a,b), and adds to the list $\sim$ 2400 new RRab's, $\sim$ 5400 RRc's, as well as $\sim$ 500 RRd's and $\sim$ 70 new Blazhko's long term modulators. These variables were found distributed along the same region of the sky observed in Drake et al. (2013a).

When compared with Drake et al. (2014), 93 RRL (76 RRab and 17 RRc) fall into the fields observed by HiTS with magnitudes fainter than 16 (near HiTS' saturation limit) that should have been detected at least 13 times. Of these 93, 69 matched up with HiTS' list within 2 arcseconds (74 %), and 74 within 2,5 arcseconds (80 %). In terms of percentages, 74 % (79 % for 2,5 arcsecs) of the ab types and 76 % (82 %) of the RRc's are recovered. There are no differences in the classifications they give to the RRLs and what is found in this work. The periods obtained for the HiTS' sample are in good agreement with the periods for the stars in common, with a mean discrepancy of $2 \times 10^{-3} \pm 2 \times 10^{-2}$ days.

If the position in the CCDs of the 24 (19) missing RRLs is considered, it is evident that at least 7 of them fall near the edges of the chip for the reference frame and therefore were not cleanly detected by the procedure. The previous number depends on how "proximity to the edges" is defined. The lower and upper positions of each CCD can be approximated by the area within the borders and $\approx$ 30 pixels away, but the effects of these areas in the CCD's can extend up to $\approx$ 100 pixels away from the borders. That correspond as well, more or less, to the variations on the position of the stars in the CCD's near the edges due to pointing fluctuations (there were no pointing corrections before any HiTS observation).

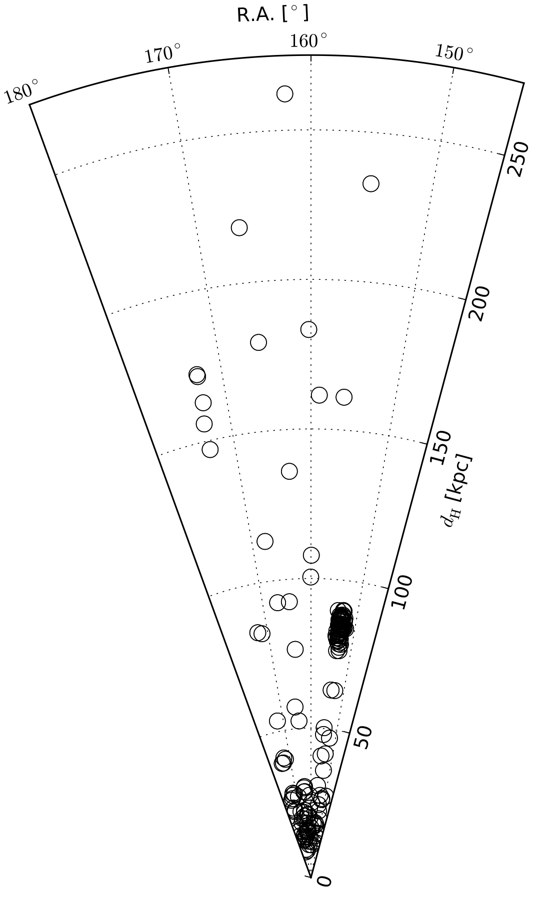

Figure 3.4 Radial plot with distances measured in kilo–parsecs (kpc) and with the equatorial right ascension (R.A.) marked on the top. The overdensity located at $\sim 80\,\mathrm{kpc}$ is the Sextans dSph. The RRL stars from Leo IV and Leo V, as well as other distant RRL, can also be distinguished.

Removing these 7 stars from the list of potential matches with Drake et al. (2014) increases the rate of recovery to 80 % (84 %) which is closer to the numbers obtained for the theoretical recovery rate computation. In general, the missed RRLs are relatively bright sources ($V < 19$, $\mathrm{d}_H < 40\,\mathrm{kpc}$), with $\langle V \rangle \sim 17$ and enough phase coverage to perform a good characterization in the Catalina survey ($N > 180$).

The HiTS' RRLs detection procedure classify as RRL stars 103 sources that were not present neither in Drake et al. (2013a) nor Drake et al. (2014). These stars may have been missed by these surveys for different reasons, but the most likely is attributable to the different depths of our surveys. Both Drake et al. (2013a) and Drake et al. (2014) have shallower limiting magnitudes, and have high completeness levels until $V_{\mathrm{CSS}} \sim 19{,}5$. The HiTS' analysis led to 74 new RRab, and 29 new RRc, compared to those works. More than half of these sources (63 %) are grouped together and seem to be part of the Sextans dwarf spheroidal galaxy (as described in Section 3.2.1), while from the remaining objects 22 have $g > 20$, i.e., faint enough to be beyond detection by the Catalina survey.

In the case of LSQ, which has 43 RRab and 7 RRc fainter than $g = 16$, the comparison yielded 44 stars recovered (88 %; five RRc and 39 RRab). In general, the periods seem to coincide with an absolute mean difference of $4{,}7 \times 10^{-2}$ days. However, there is one star with a significantly different period (HiTS101413-004502). If HiTS101413-004502 is not included in the comparison, the period discrepancy turns out to be $|\Delta P| \sim 5 \times 10^{-4}$. For that star, HiTS' most likely period is 0,386 days, while LSQ gives 0,628 days. However, the latter corresponds to the second most probable period according to our procedure. Since LSQ has 87 observations for that star and HiTS only have 21, their period is likely more reliable. This discrepant period determination led us to a misclassification of that RRL (from a RRab to a RRc). In Table 3.2, the period obtained with the methodology described in Chapter 2 is presented.

Of the RRL stars missed by our selection method, four are ab type and two are RRc. Nevertheless, one RRab (LSQ250) fell relatively close to the edges of its CCD, following the criteria applied in the comparison with the CRTS. Rejecting LSQ250, the recovery rate rises up to $\sim 90\,\%$.

As in the case of the comparison with the Catalina survey, this thesis report numerous RRL that do not appear in the LSQ list. A total of 93 new variables are found in the common regions (70 ab's and 23 c's) most of which seem to be associated, again, to the Sextans dSph RRLs overdensity (65 %).

The PS1 public RRLs catalog was built based on machine learning techniques and has a total of $\sim 24{,}000$ RRLs (Sesar et al., 2017a), with 298 falling into the HiTS fields. Based on their calculations, an RRab/RRc score is given in their selection for which values higher than 0,90 gives a purity of 0,97/0,94 and a completeness of 0,88/0,57 for $r < 18{,}5$. If only RRLs with scores higher than 0,90 are considered, the number of PS1 RRLs in the HiTS fields with mean magnitudes in g fainter than 16 is 110. A comparison of this group with HiTS RRLs yields 87 matches within 2 arcseconds (75 ab's, 12 c's), i.e., 80 % of the intersecting PS1 sample is recovered. The mean period difference is 0,001 d, with 0,07 d as the most significant discrepancy, and the mean magnitude difference is 0,09. The faintest common RRL, HiTS101243+022118, has $g = 20{,}61$ (87 kpc) in the HiTS catalog, and $g = 20{,}79$ in PS1. The classifications of all the stars in this subsample of the PS1 catalog are in agreement with the classifications presented in this work.

It is worth noticing that five of the RRLs in PS1 that are not detected in this work fall near the edges of the CCDs for the reference frame. If those RRLs are not taken into account, the recovery rate go as high as 83 %, in agreement with the estimations. The rest of the undetected RRL correspond to relatively bright sources, with a mean value of g of 18,3.

Of the 86 RRLs that are not clearly detected by PS1, 28 have $g < 20$ (18 ab's, 10 c's), which corresponds to $\mathrm{d_H} \lesssim 70\,\mathrm{kpc}$. The rest of the stars not present in the PS1 catalog are mostly *ab*−type (65 %), and include the entire sample of faint RRLs described in Section 3.3.

3.1.4. Color-color distribution

Meaningful information can be taken from large public catalogs (SDSS, PS1) as they may provide additional constraints for the selection/characterization criteria of RRLs in HiTS' data. Color information, in particular, plays a major role when it comes to building extensive RRLs databases from wide-area surveys since RRLs are found in specific regions of the color-color diagram (Ivezić et al., 2005).

Given that not all the fields observed by HiTS during 2014A overlap with the SDSS footprint, plus their relatively bright limiting magnitude, color information cannot be obtained for the entire HiTS' RRLs sample. In Figure 3.5 the SDSS DR10 colors of the 139 common RRLs is shown. The figure shows how most candidates have $0{,}9 < u - g < 1{,}8$ and $-0{,}1 < g - r < 0{,}3$. The location of these stars is in agreement with the classification as RRLs. However, two objects (HiTS104738+020627; HiTS110510-022710) fall far from the others in $g - r$ and they correspond to two of the faintest in the sample, with colors 1,36 and 0,79. The case is similar for the three bluest objects in $u - g$, being the u SDSS magnitudes the main difference. These RRLs are HiTS101312-021412, HiTS100815-021625 and HiTS101127-021833, from left to right in the plot, and have $u = 23{,}85, 25{,}53$ and 25,27, respectively. The offset in their position in the color-color diagram might be attributable to the large uncertainties of the SDSS u−band magnitude that typically reach ∼ 1 mag at those faint limits. Thus, conclusions cannot be firmly drawn about the stars' nature based on their SDSS colors only.

Regarding the PS1, 161 of the HiTS' RRLs have colors in the PS1 photometry, with only 10 being fainter than $g = 20{,}9$ ($\sim 90\,\mathrm{kpc}$). The PS1 catalogs do not have observations in the u−band to allow building a color-color plot that involves $u - g$, but it is possible to get data for $g - r$, $r - \mathrm{i}$ and $\mathrm{i} - z$. Figure 3.6 shows the color-color diagrams built with the information from PS1. For these colors, the common RRL have $-0{,}83 < g - r < 0{,}94$, $-0{,}52 < r - \mathrm{i} < 0{,}56$ and $-0{,}47 < \mathrm{i} - z < 0{,}35$, meeting the expectations with their classification as RRLs (see Chapter 1).

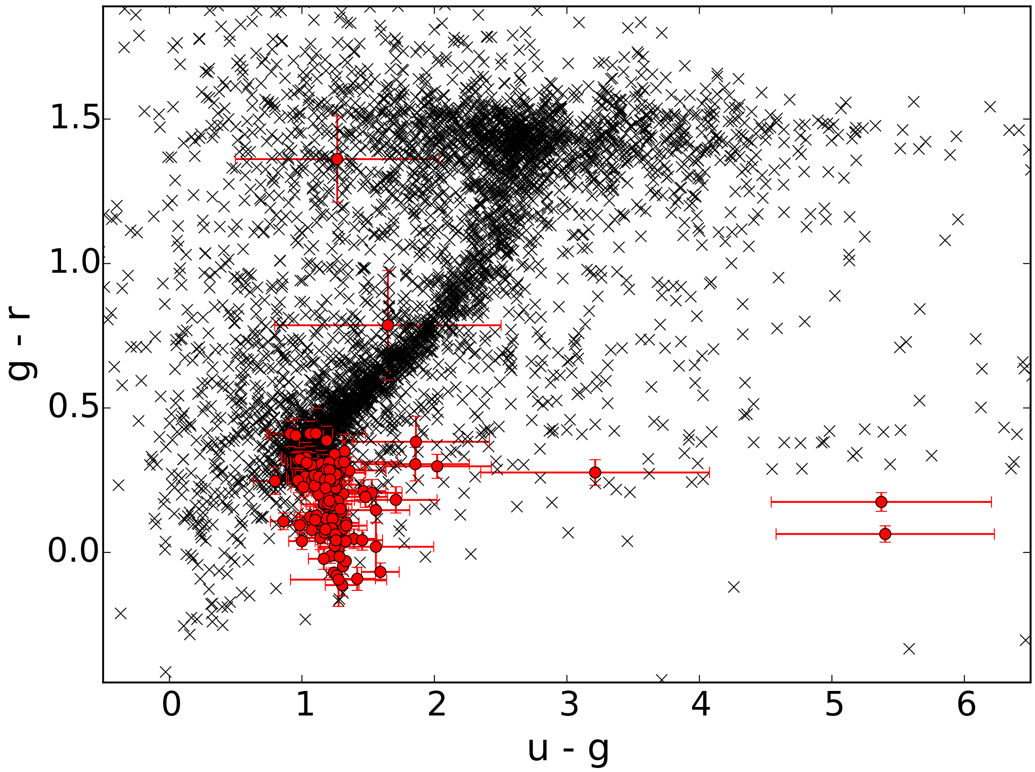

Figure 3.5 Color-color diagram of the 139 stars in common with the SDSS. Both axis show the magnitudes corresponding to the SDSS DR10. These 139 stars are plotted as red circles, while stars from the field are represented by black crosses.

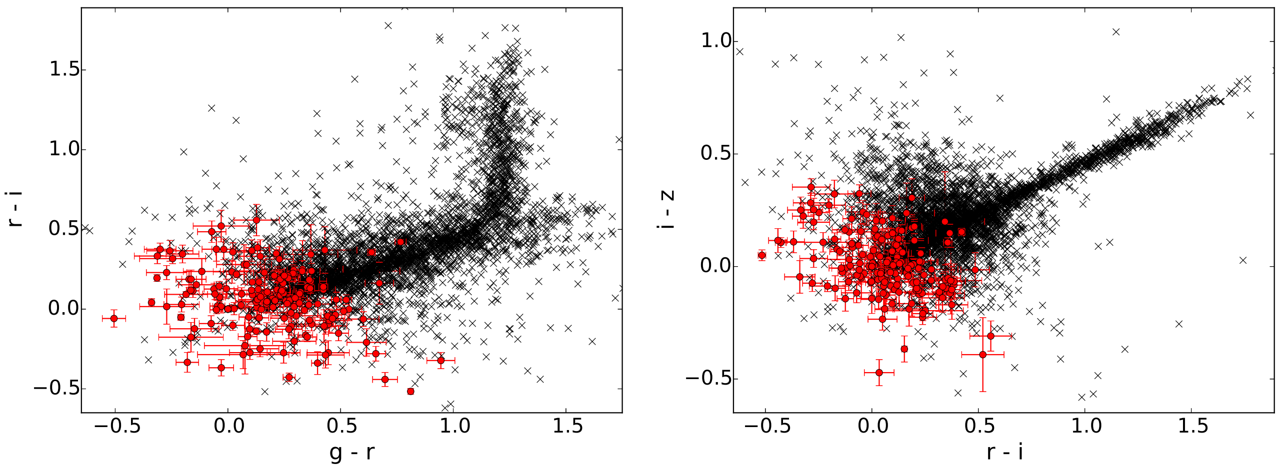

Figure 3.6 Color-color diagrams of the 161 stars in common with the PS1 3π survey. In the plots, both axis show the colors corresponding to the magnitude difference from PS1. These matched stars are plotted as red circles, while stars from the field are represented by black crosses. The position of the RRLs is in rough agreement with the expectations.

3.2. RR Lyrae Stars in Known Dwarf Spheroidal Galaxies

Based on the position of the full list of RRLs, both in the sky distribution and heliocentric distances, clear overdensities and close pairs of stars are closely analyzed. This work is performed with special emphasis in the outer regions of the halo, looking for stars with small angular separation as well as similar distances.

The potential relation of these stars with known or previously undiscovered globular clusters or dwarf galaxies is the focus of this section.

A big overdensity was clearly visible in the distribution. That clump of stars is associated with the Sextans dwarf spheroidal galaxy (dSph), and is described in Section 3.2.1. A pair and a triplet are obvious in the data as well, in both cases with angular distances smaller than one degree and a heliocentric distance difference no larger than 10 kpc; one of these groups seems to coincide with the position and published distance of the Leo IV dSph, and the other to the Leo V dSph. The analysis of these groups is explained in Section 3.2.2 and Section 3.2.3.

3.2.1. Sextans dSph

As seen in Figure 3.3, there is an overdensity of stars centered at RA $\simeq$ 153,2570°, DEC $\simeq -1{,}7408°$, $d_H \simeq 80\,\mathrm{kpc}$. The position of these stars, both in equatorial coordinates and distance, matches the location of the Sextans dSph (R.A. = 153,2512°, DEC = $-1{,}6147°$, $d_H = 86 \pm 4\,\mathrm{kpc}$, McConnachie, 2012). Sextans is a MW satellite discovered by Irwin et al. (1990) with an absolute magnitude of $M_V = -9{,}3$. The system is characterized by a relatively old and metal poor population (age=12 Gyr; [Fe/H]=$-1{,}9$), as described by Mateo et al. (1991) and Kirby et al. (2011), respectively. The Sextans dwarf is a relatively extended satellite with a half-light radius r_h of 695 pc (Irwin & Hatzidimitriou, 1995) and a surface brightness of $\sim 28\ \mathrm{mag\,arcsec^{-2}}$, typical of Local Group dSph galaxies. A recent study of Sextans carried out by Roderick et al. (2016) analysed its structural parameters using wide-field photometric data in order to investigate its kinematics and stellar structures. According to their results, the dSph has a halo-like substructure extended up to 82 arcminutes from its center, with several overdensities detected at statistically high significance levels.

From the HiTS sample, 65 RRLs candidates are located within 1,75 degrees of Sextans, and between distances of 76 and 90 kpc. Their distribution, as well as the position of the HiTS fields are shown in Figure 3.7 and Figure 3.3, in different scales. The plot also shows an ellipse marking the tidal radius from a King profile of the galaxy (Roderick et al., 2016) and variable star candidates from Lee et al. (2003). As can be seen in the figure, the HiTS fields do not cover the center of Sextans but the outskirts of the dwarf. The distribution of the RRL along the fields does not show any particular kind of structure or shape and are contained within the galaxy's known King limiting radius. The latter can be used as a tentative indication of the lack of evidence of a tidal disruption feature, according to the position of the RRL. That hypothesis is in agreement with previous studies (e.g. Roderick et al. (2016)) which suggest that Sextans actually does not have clear features related to a

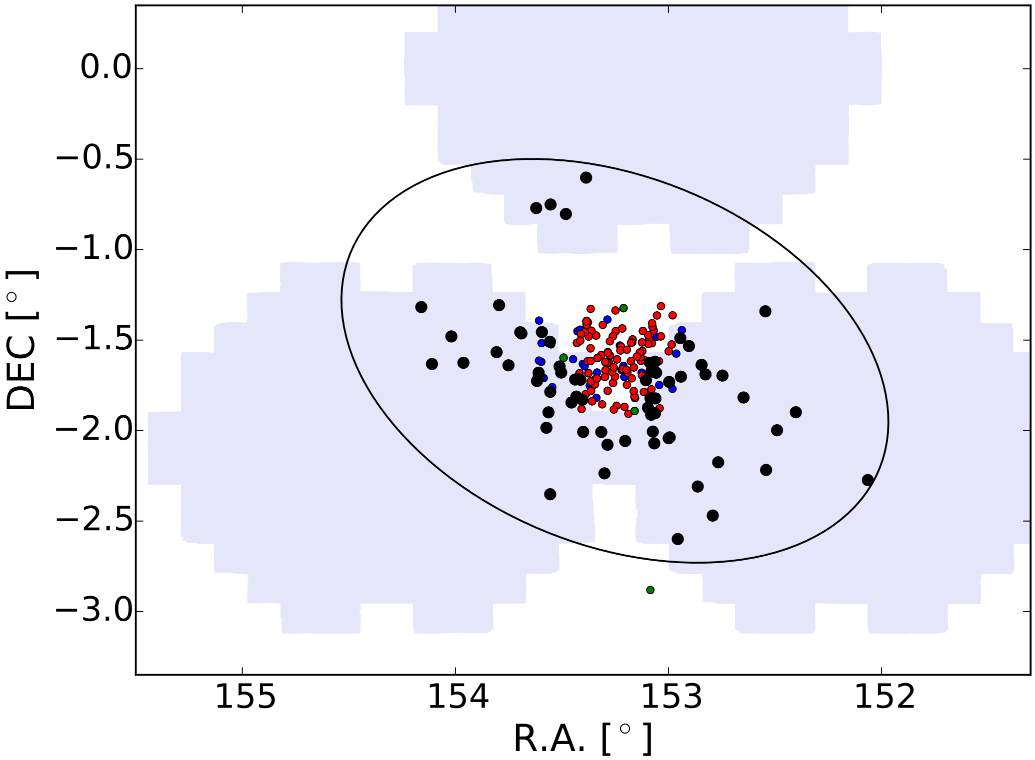

Figure 3.7 Positions in the sky of RRLs found by this work in Sextans dSph (black dots). These RRL cover a range of magnitudes from 20,03 to 20,57 in the $g-$band. Variable stars in the center of Sextans, from Lee et al. (2003), Amigo et al. (2012) and Zinn et al. (2014), are shown as blue, red, and green dots, respectively. From Lee et al. (2003), only horizontal branch variables ($19{,}0 < V < 21{,}6$) are plotted. The HiTS footprint is plotted in grey in the background. An ellipse centered in (RA,DEC) = ($153{,}2512^o, -1{,}6147^o$) (Irwin et al., 1990) is shown as a reference of the approximate tidal radius ($r_t = 83{,}2'$), orientation ($\theta = 56{,}7°$) and ellipticity ($\varepsilon = 0{,}29$) of the dSph (Roderick et al., 2016).

strong interaction with the Milky Way.

The distances for the Sextans dSph RRLs were re-calculated given the availability of values for the metallicity of the system in the literature, and these values are not necessarily close to the original assumption for the Halo ([Fe/H]= $-1{,}5$). For doing this, [Fe/H]= $-1{,}93 \pm 0{,}01$ from Kirby et al. (2011) is adpoted. The new distances are computed by using Equation 2.1, followed by the distance modulus equation (Equation 1.2).

Based on the subsample of RRLs associated with Sextans (both $ab-$ and $c-$types), a first estimation of the mean heliocentric distance to the satellite is $81{,}4 \pm 5{,}7$ kpc. However, a clear offset between the mean distance obtained with only RRab and only RRc (84,2 and 74,5 kpc, respectively) is noticeable. This discrepancy (13 %) is mainly due to the different behaviour of the period-luminosity relations for these stars, and the PLZ relations used are exclusive for RRab. As it is not expected for the different populations to be located at different distances, a correction (by this number) is applied to the distances of the RRc from the entire sample . By doing this, the derived mean heliocentric distance of the dwarf is $84{,}2 \pm 3{,}3$ kpc.

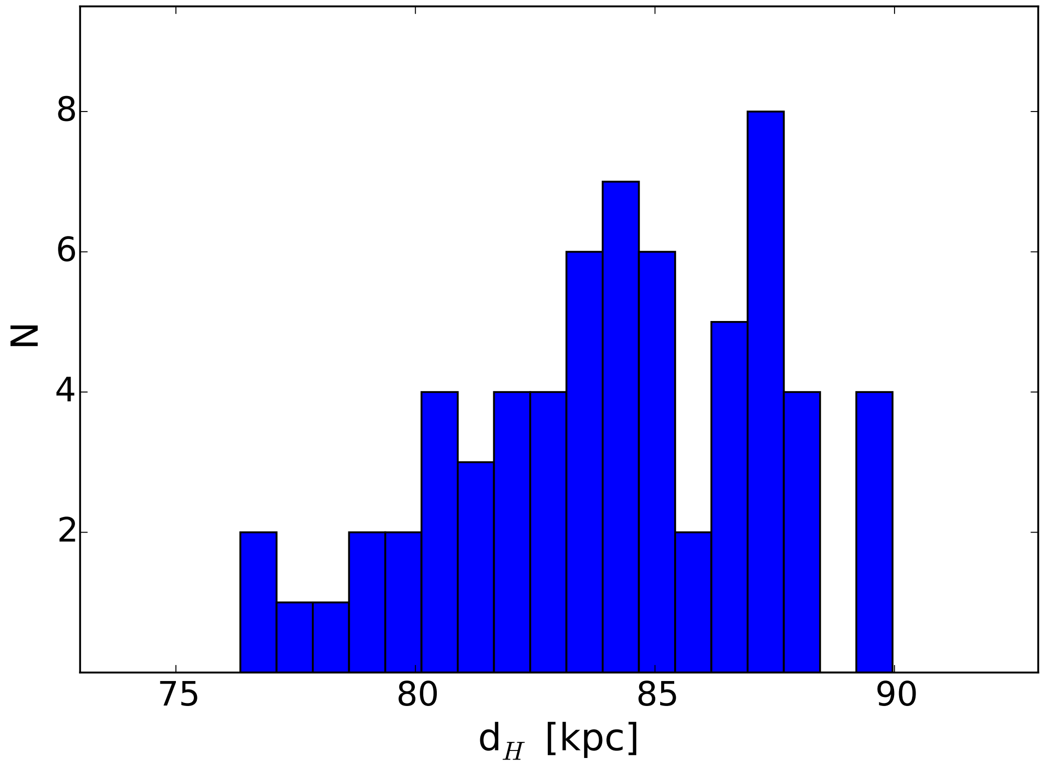

Figure 3.8 Distribution of heliocentric distances of the RRLs in the Sextans dSph, after changing the original values of the distances by considering [Fe/H]$= -1{,}93 \pm 0{,}01$ (Kirby et al., 2011) and after the correction of RRc's by a 13 % factor.

This estimation is in agreement with previous results in the literature. Lee et al. (2009), for instance, obtained $\mathrm{d_H} = 86 \pm 4\,\mathrm{kpc}$ as the mean distance to the dwarf by comparing observational and synthetic color-magnitude diagrams. Some works have estimated similar and slightly larger distances (86 ± 6 kpc by Mateo et al. 1995, 95 ± 2 kpc by Lee et al. 2009). A histogram of the resulting distance distribution of HiTS is shown in Figure 3.8. With the distance obtained in this work, it is possible to estimate physical distances from the dwarf's center for the subsample. Stars out to 1,90 kpc (1,30°) are found, which is in agreement with the results of Roderick et al. (2016), who found the Sextans halo overdensities to be as far as 2 kpc from the center. It should be noted that, from Figure 3.7, it is possible to claim that there is no clear evidence of extra-tidal RRLs based on our sample. Extending the search for RRLs in Sextans to the contiguous HiTS fields does not change this statement, even if a significantly larger radius is considered (e.g. $r_t = 90'$; Irwin et al., 1990). Comparing the mean heliocentric distance of our sample of Sextans' RRLs (4,1 kpc) and the standard deviation of the distribution (3,3 kpc), it is seen that the line-of-sight depth of the dwarf is consistent with its size (~ 700 pc; Irwin & Hatzidimitriou, 1995).

Compared with LSQ and the Catalina surveys, the list of RRLs presented in this thesis contains 63 new Sextans RRLs. This result is not surprising considering that the mean magnitude of the RRL in Sextans are close to the limiting magnitude of their detections. The three matching RRLs, for instance, are only present in the LSQ catalogue and have $V \sim 20$. When comparing HiTS' sample with the variable star candidates that lie near the dwarf center presented in Lee et al. (2003), only four are classified by both studies as RRL (within 2 arcseconds). These four variables are classified as three RRab and one RRc by both their and this study. In Lee et al. (2003), the authors do not provide individual distances for their RRLs. In the HiTS' table, these stars are identified as HiTS101339-014310 (RRc, $d_H =$ 85 kpc), HiTS101344-014845 (RRab,d_H = 83 kpc), HiTS101345-014305(RRab,d_H = 87 kpc) and HiTS101401-014046 (RRab, d_H = 82 kpc). There are also 14 variables un-flagged by them that match with the position of HiTS' RRLs. In Table 3.2, the full list of Sextans RRLs found in this work is presented, with their respective identification names from the surveys mentioned above (in case of a match).

In the doctoral thesis work done by Amigo et al. (2012), a list of 114 RRLs covering the inner regions of Sextans is presented, including the ones from Mateo et al. (1995). This catalog contains a large number of new discoveries (ranging from $V = 20{,}06$ to $V = 20{,}50$), and recovers most of the RRLs presented in Lee et al. (2003) (81 %). If the full table presented by Lee et al. (2003) is considered, including the unflagged objects, the number of matches increases to 77. Since Amigo et al. (2012) covers the central region of the dwarf, the overlap with HiTS' fields is not significant. However, there are 16 stars in common between HiTS and that work, with highly similar periods ($|\Delta P| \sim 2 \times 10^{-4}$) and same classifications.

In the case of the PS1 catalog, a large number of RRLs is located in the vicinity of Sextans (over 200 based on their sky positions), covering both the inner and outer regions of the galaxy. Comparing the Sextans sample presented in this work with PS1, 62 matches (47 RRab, 15 RRc) are found. From these, most of the classifications match as well, with the exception of HiTS101010-021303, HiTS101159-014352, and HiTS101349-015042, as described in Section 3.1.3. The mean period discrepancy of the 62 RRLs in common is $|\Delta P| \sim 1 \times 10^{-2}$. The stars detected by HiTS that are not in the PS1 RRLs catalog are HiTS101219-015445, HiTS101356-004811, HiTS101429-004613, and HiTS101500-013822. These stars are fainter than the estimation of the mean g magnitude of Sextans given here, and have distances of 85, 87, 87, 85 kpc, respectively.

Regarding the position of the Sextans RRLs in the Bailey-diagram (Figure 3.2, bottom panel) and their periods (Table 3.2), they can be placed close to the nominal Oo II group, with a mean period of the RRab of 0,63 d. However, they distribution do not follow a single sequence of Oo groups. Mateo et al. (1995) established Sextans as a Oo-intermediate system, based on 34 stars in the inner part of the galaxy. Therefore, this work confirms the Oo-intermediate nature of this dwarf.

Folded light-curves for the full Sextans RRLs sample are shown in from Figure 4.4 to Figure 4.6.

Table 3.2. Sextans RR Lyrae stars found by HiTS in 2014. Previous ID's with prefixes V and MV are from Mateo et al.'s work, while stars with C come from Amigo et al. 's. Prefixes VV and VI are from Lee et al.'s catalog, and LSQ are from Zinn et al.'s.

ID	R.A. (deg)	DEC (deg)	$< g >$	Period (days)	Amplitude	d$_H$ (kpc)	Type	N	Previous ID
HiTS100815-021625	152.06402	-2.27369	20.3	0.6973	0.85	84	ab	30	-
HiTS100936-015356	152.40198	-1.89876	20.4	0.346	0.65	84	c	38	-
HiTS100958-015954	152.49002	-1.99832	20.4	0.6497	0.97	84	ab	36	-
HiTS101010-021303	152.54151	-2.21761	20.4	0.6775	0.65	87	ab	37	-
HiTS101011-012028	152.54492	-1.34107	20.4	0.675	0.67	86	ab	38	-
HiTS101035-014902	152.64737	-1.81732	20.4	0.728	0.56	87	ab	38	-
HiTS101059-014146	152.74635	-1.69613	20.4	0.60505	0.87	85	ab	37	-
HiTS101104-021031	152.76652	-2.17535	20.4	0.5939	0.94	84	ab	37	-
HiTS101110-022812	152.79187	-2.46998	20.3	0.3059	0.46	79	c	35	-
HiTS101118-014123	152.82598	-1.68969	20.4	0.6088	0.69	85	ab	33	-
HiTS101123-013813	152.84444	-1.63696	20.4	0.6031	0.8	83	ab	38	-
HiTS101127-021833	152.86234	-2.30928	20.3	0.7153	0.69	85	ab	37	-
HiTS101137-013159	152.90356	-1.53294	20.4	0.3941	0.57	90	c	37	-
HiTS101146-014207	152.94133	-1.70199	20.2	0.3163	0.69	76	c	38	VV23
HiTS101147-012921	152.94423	-1.48912	20.5	0.3012	0.64	83	c	37	VI02
HiTS101149-023558	152.95618	-2.59951	20.2	0.6395	1.04	79	ab	20	-
HiTS101159-020215	152.99415	-2.03763	20.0	0.4601	0.53	80	c	37	-
HiTS101159-014352	152.99676	-1.73099	20.4	0.3472	0.75	84	c	38	C5
HiTS101200-020233	152.99877	-2.04241	20.5	0.5999	1.0	87	ab	37	-
HiTS101214-014048	153.05782	-1.68014	20.5	0.6093	0.63	87	ab	38	C13,VI47
HiTS101215-014921	153.06118	-1.82237	20.4	0.66581	0.71	86	ab	38	C14,VV26
HiTS101215-015415	153.06268	-1.90417	20.3	0.4261	0.51	90	c	38	C15
HiTS101215-013710	153.06378	-1.61944	20.6	0.629	0.82	90	ab	38	C16,VI46
HiTS101216-020415	153.06648	-2.07081	20.5	0.6532	0.85	88	ab	37	-
HiTS101218-020021	153.07314	-2.00582	20.3	0.73271	0.75	83	ab	37	LSQ27
HiTS101219-014025	153.07974	-1.67363	20.4	0.5937	0.93	83	ab	38	C21,VI44
HiTS101219-015445	153.08119	-1.91262	20.3	0.3776	0.57	85	c	33	-
HiTS101220-014915	153.08398	-1.82097	20.3	0.5817	1.03	78	ab	38	C23
HiTS101221-013733	153.08562	-1.62578	20.4	0.7032	0.86	88	ab	38	C24,VI45
HiTS101223-015225	153.09601	-1.87375	20.4	0.5828	1.07	81	ab	37	C30
HiTS101225-014319	153.10533	-1.72193	20.5	0.5726	1.05	84	ab	37	C33,VI49
HiTS101249-020327	153.20288	-2.05756	20.5	0.6361	0.74	87	ab	37	-
HiTS101309-020442	153.28603	-2.07826	20.2	0.6606	0.63	79	ab	20	LSQ33
HiTS101312-021412	153.30010	-2.23653	20.4	0.627	0.78	84	ab	21	-
HiTS101316-020029	153.31510	-2.00796	20.5	0.6105	0.79	87	ab	21	-
HiTS101333-003607	153.38637	-0.60196	20.2	0.6626	1.03	81	ab	21	-
HiTS101336-020026	153.40018	-2.00731	20.3	0.6052	1.13	80	ab	21	-
HiTS101337-014947	153.40393	-1.82963	20.5	0.6285	0.78	88	ab	21	C102,VI78
HiTS101339-014310	153.41355	-1.71934	20.4	0.3464	0.65	85	c	20	V22,VV35(RRL)
HiTS101344-014845	153.43204	-1.81237	20.4	0.5887	0.97	83	ab	21	V25,VI75(RRL)
HiTS101345-014305	153.43776	-1.71792	20.5	0.6215	0.78	87	ab	20	V26,VI80(RRL)
HiTS101349-015042	153.45497	-1.84497	20.3	0.3962	0.53	87	c	21	VI77
HiTS101356-004811	153.48130	-0.80309	20.4	0.3616	0.61	88	c	21	-
HiTS101401-014046	153.50327	-1.67939	20.5	0.48777	1.13	82	ab	20	V42,MV09(RRL)
HiTS101403-013845	153.51083	-1.64578	20.4	0.5417	1.08	82	ab	20	V43
HiTS101413-004502	153.55313	-0.75058	20.2	0.3861	0.62	84	c	21	LSQ39

Table 3.2 (cont'd)

ID	R.A. (deg)	DEC (deg)	$< g >$	Period (days)	Amplitude	d_H (kpc)	Type	N	Previous ID
HiTS101413-014709	153.55455	-1.78591	20.4	0.6149	0.94	84	ab	21	VI81
HiTS101413-022107	153.55496	-2.35185	20.2	0.3032	0.49	76	c	21	-
HiTS101414-013033	153.55636	-1.50920	20.4	0.6342	0.63	85	ab	20	VV21
HiTS101415-015358	153.56291	-1.89934	20.3	0.6141	0.68	81	ab	21	-
HiTS101417-015904	153.57276	-1.98455	20.4	0.5919	0.96	82	ab	21	-
HiTS101423-012721	153.59391	-1.45573	20.3	0.3442	0.52	82	c	21	-
HiTS101426-014200	153.60822	-1.69990	20.4	0.5424	0.97	82	ab	20	VI83
HiTS101426-014048	153.60920	-1.68002	20.5	0.6156	0.77	87	ab	20	VI84
HiTS101428-014334	153.61674	-1.72623	20.4	0.54928	1.08	79	ab	20	-
HiTS101429-004613	153.62042	-0.77035	20.5	0.6324	0.8	87	ab	21	-
HiTS101446-012748	153.69002	-1.46334	20.5	0.6074	0.94	86	ab	21	-
HiTS101447-012724	153.69536	-1.45670	20.4	0.3682	0.52	88	c	21	-
HiTS101500-013822	153.75073	-1.63955	20.3	0.7754	0.49	85	ab	21	-
HiTS101511-011825	153.79493	-1.30695	20.3	0.7262	0.62	85	ab	21	-
HiTS101514-013400	153.80651	-1.56672	20.5	0.60825	0.86	87	ab	21	-
HiTS101551-013732	153.96215	-1.62542	20.2	0.6771	0.9	81	ab	21	-
HiTS101605-012847	154.01876	-1.47980	20.4	0.6136	0.52	83	ab	21	-
HiTS101626-013756	154.10991	-1.63218	20.3	0.6585	0.94	81	ab	21	-
HiTS101638-011903	154.15994	-1.31752	20.4	0.407	0.46	90	c	21	-

3.2.2. Leo IV Ultra-Faint dSph

In addition to the RRLs associated to the Sextans dSph, other two distant (> 90 kpc) groups of stars are found with both small angular separations and similar heliocentric distances.

One of these cases coincide with the position on the sky and distance of the ultra-faint galaxies Leo IV. Two stars are members of Leo IV, HiTS113256-003329 and HiTS113259-003404, both RRab with periods of 0,7146 and 0,6268 days, and amplitudes of 0,78 and 1,22 mag, respectively. These are two of the three RRLs previously discovered by Moretti et al. (2009) in this ultra-faint system. The pulsation periods found for these stars (V2 and V1 in Moretti et al. 2009), are roughly in agreement with the values reported by those authors (0,7096 and 0,61895 days, respectively). The non-detection of the third RRL (called V3 by Moretti et al. 2009) is consistent with the completeness values expected for RRLs of these magnitudes, according to the estimations (see Section 2.5).

In a recent paper (Medina et al., 2017), the distances of the HiTS RRLs in Leo IV are anchored to the value of the distance from the literature ($d_H = 145$ kpc; Moretti et al., 2009), since that dwarf is significantly more metal poor than the mean halo metallicity. Nevertheless, if the metallicity of Leo IV is known, it is possible to get a better estimation of the distances by using the previously discussed Equation 2.1. Assuming $[Fe/H] = -2{,}31$ for this dwarf (Simon & Geha, 2007), a mean heliocentric distance of $151{,}4 \pm 4{,}4$ kpc is obtained ($d_H = 155{,}8 \pm 7{,}5$ kpc for HiTS113256-003329, and $d_H = 147{,}0 \pm 6{,}9$ kpc for HiTS113259-003404). This number is in agreement with the estimation made by Moretti et al. (2009)

(154 ± 5 kpc).

3.2.3. Leo V Ultra-Faint dSph

A triplet of RRLs is identified as member of the Leo V ultra-faint dwarf galaxy. These stars are HiTS113057+021331, HiTS113105+021319, and HiTS113107+021302, all being new discoveries (Medina et al., 2017). The periods measured for these RRLs, classified as fundamental-mode pulsators, are 0,6453, 0,6573, and 0,6451 days, respectively, with amplitudes of 0,72, 1,34 and 0,99 mag.

Other RRLs that lie spatially close to Leo V but at closer distances are also inspected, with the purpose of checking whether possible anomalous Cepheids had been misclassified as RRLs. Additionally, the region bridging Leo IV and Leo V was examined, considering that there is a potential association between the two ultra-faint systems (de Jong et al., 2010; Blaña et al., 2012; Jin et al., 2012). No other RRLs were found within a radius of 15 arcmin from the center of Leo V, or connecting both dwarfs. The closest star is HiTS113107+023025, at 17,4 arcmin but ~ 3 mag brighter than the HB of the galaxy and hence too bright for being an anomalous Cepheid in the galaxy. Also, it is located in the opposite direction to Leo IV, and thus not in the possible bridge.

As Leo V has a metallicity of [Fe/H]$= -2{,}48$ (Collins et al., 2016), which similar to Leo IV, it is significantly more metal poor than the Galactic halo. Therefore, the first approximation to the distance of these RRLs is not completely valid. In Medina et al. (2017), as a result of anchoring the distances to the one of Leo IV (Moretti et al., 2009) (valid approximation since both system have similar metallicities), the individual heliocentric distances for the triplet are 176 ± 9 kpc, 176 ± 9 kpc, and 167 ± 8 kpc. This yields an average distance to Leo V of 173 ± 5 kpc.

If the absolute magnitudes for these three stars are re-calculated using Equation 2.1, a more reliable value of the distances can be obtained. Doing this (using [Fe/H]$= -2{,}48$) gives individual values of 171,7 ± 9,4 kpc, 172,4 ± 9,4 kpc and 162,8 ± 8,6 kpc for HiTS113057+021331, HiTS113105+021319, and HiTS113107+021302, respectively. Therefore, the mean distance to Leo V is 169,0 ± 4,4 kpc. The latter agrees with the numbers obtained by Medina et al. (2017). While consistent within the uncertainties, this value lies on the low side of previously published values. In their discovery paper, Belokurov et al. (2008) used data from the 2,5−m INT telescope and estimated a distance of 180 ± 10 kpc to Leo V. de Jong et al. (2010) obtained deep photometry of the Leo IV and V pair with the Calar Alto 3,5−m telescope and determined a heliocentric distance of 175 ± 9 kpc. Sand et al. (2012), on the other hand, based on images taken with the Clay Magellan telescope, derived a much larger distance of 196 ± 15 kpc. The relatively large uncertainties associated to all these measurements are understandable given the sparsely populated Leo V's blue horizontal branch (BHB). These stars are commonly used as distance indicators and do not require time-series observations, but they lack precision compared to RRLs estimations when the BHB is poorly populated and not well defined, as it is the case for the literature data for Leo V.

The pulsational properties of the RRLs in Leo V locate them towards the locus of the

Oo-II group, with a mean period of 0,65 days. Thus, Leo V can classified as an Oosterhoff II type system, similar to most of the other ultra-faint dwarf galaxies. Unfortunately, the lack of detected c-type RRLs in this system does not allow verification of this classification based on the proportion between both type of stars. This hypothesis supports the idea that building blocks like the ultra-faint galaxies contribute to the Oo-II tail of the MW's halo population, but more massive galaxies, with mostly an Oo-I population, are needed to reproduce the present-day population of RRLs in the halo (Zinn et al., 2014; Fiorentino et al., 2015; Vivas et al., 2016).

In the context of the specific number of RRLs in dSphs as a function of magnitude, Leo V is broadly consistent with what has been seen in other ultra-faint dwarfs (Baker & Willman, 2015; Vivas et al., 2016). However, due to the large dispersion in this correlation, no further conclusions can be drawn just from this additional data.

3.3. Distant RR Lyrae Stars

Very distant RRL are found within the final list of RRLs in the HiTS 2014A database. From the full sample, a total of 18 distant RRLs have $\langle g \rangle \geq 20{,}5$, which correspond to distances $\mathrm{d_H} > 90\,\mathrm{kpc}$. Hereafter, these stars are named "distant RRLs". Two recent works, Drake et al. (2013b) and Sesar et al. (2017b), have reported some of the most distant Galactic RRLs known to date, located at $\sim 120\,\mathrm{kpc}$ and $\sim 130\,\mathrm{kpc}$, respectively, and no more very distant RRL have been reported in the literature since. Within the HiTS' RRLs 13 with $\mathrm{d}_H > 130\,\mathrm{kpc}$ are found; i.e., beyond the most distant previously known MW RR Lyrae. Based on the distance determination method described in Section 2.7.3, the distant RRL span a range from $\sim 92\,\mathrm{kpc}$ ($\langle g \rangle \sim 20{,}5$) to beyond 200 kpc (up to $\langle g \rangle \sim 22{,}8$). In Table 3.3 the main properties of these distant stars are presented. The uncertainties in the distance determinations shown in Table 3.3 include the photometric errors and the propagation of the uncertainties from the calculation of M_g.

With respect to their classifications, 11 RRL (61 %) from this faint subsample correspond to RRab, while five were classified as RRc (Table 3.3), roughly consistent with the observed ratio of the rest of the sample and the expected proportion. It is worth noting that the three most distant RRLs are $c-$type. Given their lower intrinsic amplitude and the large photometric uncertainties of the individual observations near the detection limit of our survey, their classification should be considered as tentative; the most distant RRab is at $\mathrm{d_H} = 219 \pm 15\,\mathrm{kpc}$.

Figure 3.2 shows that the distribution of distant RRab's seems to be different than the one from nearby RRab's. The distant RRab sample is roughly located towards the OoII locus. Since RRLs in ultra-faint dwarf galaxies are mostly OoII (Clementini, 2014), and the mean period of the distant RRab (0,668 d) is particularly similar to the one from these galaxies (0,667 d; Vivas et al., 2016) this suggests that the main contributor to the outer halo population may come from ultra-faint dwarf galaxies.

The folded light curves of the distant candidates are shown in Figure 3.9.

Table 3.3 Most distant RR Lyrae stars found in the data from HiTS 2014.

ID	R.A. (deg)	DEC (deg)	$< g >$	d_H (kpc)	Type	N
HiTS105754-002603	164.47577	-0.43403	20.5	$92{,}5 \pm 6{,}8$	c	20
HiTS110739+012813	166.91383	1.47037	20.4	$92{,}6 \pm 6{,}6$	c	20
HiTS104009-063304	160.03895	-6.55105	20.8	$100{,}5 \pm 4{,}0$	ab	21
HiTS103943-021726	159.93119	-2.29061	20.9	$107{,}8 \pm 4{,}5$	ab	21
HiTS111106-041718	167.77512	-4.28834	21.2	$113{,}4 \pm 8{,}8$	c	22
HiTS105209-043942	163.03718	-4.66174	21.5	$136{,}0 \pm 5{,}7$	ab	20
HiTS113259-003404	173.24674	-0.56770	21.5	$147{,}0 \pm 6{,}9$	ab	18
HiTS113256-003329	173.23270	-0.55818	21.5	$155{,}8 \pm 7{,}5$	ab	19
HiTS102414-095518	156.05905	-9.92180	21.7	$161{,}0 \pm 8{,}0$	ab	21
HiTS103601-015451	159.00456	-1.91422	21.7	$161{,}3 \pm 12{,}9$	c	21
HiTS113107+021302	172.77796	2.21734	21.7	$162{,}8 \pm 8{,}6$	ab	21
HiTS113057+021331	172.73946	2.22514	21.8	$171{,}7 \pm 9{,}4$	ab	20
HiTS113105+021319	172.76936	2.22200	21.8	$172{,}4 \pm 9{,}4$	ab	20
HiTS110222-001624	165.59251	-0.27337	22.1	$179{,}8 \pm 10{,}3$	ab	19
HiTS104054-042827	160.22661	-4.47424	21.9	$183{,}2 \pm 14{,}8$	c	20
HiTS110510-022710	166.28982	-2.45282	22.4	$218{,}6 \pm 14{,}6$	ab	19
HiTS102014-042354	155.05789	-4.39843	22.5	$232{,}9 \pm 21{,}9$	c	19
HiTS104738+020627	161.90718	2.10746	22.8	$262{,}2 \pm 24{,}3$	c	19

As mentioned in Section 3.1.2, Figure 3.3 shows the location of the distant RRLs color coded by distance. The remote stars do not seem to be concentrated in contiguous fields but they are homogeneously distributed throughout the covered area, which makes a possible hypothesis regarding a common origin (of the RRLs not bound to known systems) unlikely.

3.4. Number Density Profiles

The density profile of halo tracers contains important clues to understand the accretion history of the Milky Way (Bullock & Johnston, 2005; Cooper et al., 2013). Since RRLs are excellent distance indicators (see Chapter 1) they are particularly useful for the construction of number density profiles $\rho(R)$, i.e., the variation in the number of RRLs per unit volume ($\#$ kpc^{-3}) where R is the distance to the center of the galaxy. Note that this distance is different than the heliocentric distance, since the latter refers to the separation between the source and the Sun (i.e., they are equivalent if the sun were in the center of the Galaxy). Recent works regarding the halo density profile had studied catalogs of RRL sufficiently large that allowed them to examine the variation of the number density with direction (Zinn et al., 2014). In the case of HiTS' RRLs, the sample is made up of only ~ 100 RRLs (excluding stars from known dSph galaxies) spread over an area of $\sim 120\,\mathrm{deg}^{-2}$. Therefore, working with sub-samples located in different directions of the halo would not be statistically meaningful. For this reason, the data from all 40 HiTS 2014A fields is used to build a single number density profile. Since HiTS' fields span from 39 to 60 deg in Galactic latitude, and from 236 to 269 deg in longitude, this can be considered a single line of sight in the Galaxy. For the selection of the distance bins and the number density calculation, the distance from the galactic center R_{GC} is calculated for each star in the sample. R_{GC} can be obtained from

$$R_{\mathrm{GC}}^2 = (R_\odot - \mathrm{d_H} \cos b \cos l)^2 + \mathrm{d_H^2} \sin^2 b + \mathrm{d_H^2} \cos^2 b \sin^2 l, \tag{3.1}$$

where $\mathrm{d_H}$ is the heliocentric distance, b and l are the Galactic latitude and longitude of each star, respectively, and $R_\odot$ is the distance from the sun to the Galactic center. For this work $R_\odot$ is assumed to be 8 kpc. The bins are created evenly-spaced on a log scale.

When trying to place the Milky Way into context with external galaxies and model stellar halos a decision has to be made whether to include stars from small overdensities (2-3 stars) or not. Excluding the stars belonging to overdensities has the benefit of permitting a clean view (with no contamination) of the stars in the field of the halo. However, this may not be a realistic way of approaching the problem, since the presence (or not) of stars from unknown systems in the observations is hard to probe. On the other hand, including the stars from these groups is beneficial for the analysis given that in the typical datasets such overdensities may not be indentified. In this work both calculations are made (with and without stars from Leo IV and Leo V), always removing the RRLs from the classical Sextans dSph. The fits described in the following sections are virtually unchanged by the inclusion/exclusion of the Leo IV/V RRLs.

Two halo models are used to fit the data: a spherical halo model as well as an ellipsoidal one with a flattening parameter $q = 0{,}7$ adopted from Sesar et al. (2011). The adopted model is an exponential one, given by $\rho(R) = \rho_\odot(R/R_\odot)^n$, where $\rho_\odot$ is the number density of RR Lyrae stars in the vicinity of the Sun. The fit is performed to the logarithmic form of the previous equation:

$$\log(\rho(R)) = A + n \ \log(R/R_\odot) \tag{3.2}$$

where $A = \log(\rho_\odot)$. A bayesian approach for the parameter estimation is followed to describe the fits. The python MCMC routine *emcee* (Foreman-Mackey et al., 2013) is chosen to find posterior distributions for the parameters of the model.

Simulations suggest that there should be a clear difference in the behaviour of the inner and outer halo number density profiles, probably driven by different formation processes (Bullock & Johnston, 2005). In this sense, the inner halo is thought to contain both accreted and formed in-situ populations, while the stellar component of the outer halo seems to be formed mainly by accretion events (Zinn, 1993; Bullock & Johnston, 2005; Carollo et al., 2007; Abadi et al., 2006; Zolotov et al., 2009). There is possible evidence for the different formation pathways of the inner/outer halo in the form of a break in the radial number density profile of MW stars near 25 kpc from the Galactic center (Saha, 1985; Watkins et al., 2009; Deason et al., 2011; Sesar et al., 2011). Here, fits of a simple power law (SPL) and a broken power law (BPL) profile are studied to describe the number densities. For the latter, the break radius is considered to be a free parameter, as well as the inner and outer slopes.

In the case of the BPL profile, the equations used are:

$$\begin{aligned} \log(\rho(R)) &= A1 + n_1 \ \log(R/R_{\odot}) \\ \log(\rho(R)) &= A2 + n_2 \ \log(R/R_{\odot}) \\ A1 + n_1 \ \log(R_{break}/R_{\odot}) &= A2 + n_2 \ \log(R_{break}/R_{\odot}) \end{aligned} \tag{3.3}$$

The values of A are constrained to within 0,05 and 1,1, and 0,1 and 3 for $A2$ (after the break). The slope is constrained to be between -7 and -1 for the SPL. For the BPL, the constraining values are set to between -10 and 5, and -14 and 15 for the inner and outer slopes, respectively. The break radius is constrained to within 15 and 70 kpc. An initial guess for the value of each parameter is provided to the routine, based on the result of following a non-linear least squares methodology (using the Levenberg-Marquardt algorithm from *scipy).*

The left/right panels of Figure 3.10 and Figure 3.11 show the fitted models to the data under different considerations. In the *left* panels the model to the RRLs within 145 kpc is fitted, which corresponds to the upper limit based on completeness considerations (this study is $\sim 85\,\%$ complete down to $g = 21{,}5$). In this case, the more distant ($R_{\rm GC} > 145$ kpc) bins are shown for comparison with extrapolations of the fits to large radii. In the *right* panels, the models shown are fitted to the entire sample, after correcting for completeness as calculated in Figure 2.7.

In both cases the first bin, which includes the closest RRL, is removed from the plots and the analysis because these bins suffer incompleteness due to saturation of bright stars. The corner plots with the resulting posterior distributions from the fits are shown in the Figures 3.12 and 3.13.

It is important to notice that, according to Equation 3.1, the Galactic latitude and longitude are required to determine $R_{\rm GC}$ from $\rm d_H$. Given the wide area covered by the survey, it is not possible to transform the completeness values per apparent magnitude bin to a unique Galactocentric distance and subsequently to unique ellipsoidal distance. If the mean latitude and longitude of the area observed by the survey is used ($b \sim 46°$, $l \sim 250°$), the difference in distance, between heliocentric and Galactocentric, is of up to 5 kpc. The completeness correction is considered still valid in this case, since the size of the bins is in general > 5 kpc. In the case of the ellipsoidal distances, this distance difference reaches up to 70 kpc, which makes the correction less accurate for the further bins. The *left*/*right* panel of the plots in Figure 3.10/Figure 3.11 are provided only to show the approximate effect to the density profile if a completeness correction is or is not considered. For this reason, the best-fit parameters in Table 3.4 and the posterior analysis are only given for the corrected/uncorrected (by completeness) data.

3.4.1. Spherical Halo Model

In this case $R^2 = R^2_{\rm GC} = X^2 + Y^2 + Z^2$, where X and Y are the cartesian coordinates in the Galactic plane, and Z is the axis perpendicular to it. These values are given by:

Table 3.4. Parameters for the different power law models described in Section 3.4, with RRLs from Leo IV and Leo V.

Model	A1	A2	n1	n2 (kpc)	R_b (kpc)	χ^2_ν
sph SPL	$1{,}16^{+0{,}12}_{-0{,}12}$	–	$-4{,}18^{+0{,}18}_{-0{,}19}$	–	–	2,659
sph BPL	$0{,}91^{+0{,}51}_{-0{,}75}$	$1{,}21^{+0{,}16}_{-0{,}25}$	$-3{,}47^{+2{,}26}_{-1{,}32}$	$-4{,}23^{+0{,}33}_{-0{,}25}$	$19{,}34^{+10{,}66}_{-3{,}16}$	3,203
ell SPL	$1{,}14^{+0{,}15}_{-0{,}16}$	–	$-4{,}15^{+0{,}23}_{-0{,}25}$	–	–	3,181
ell BPL	$0{,}48^{+0{,}73}_{-0{,}66}$	$1{,}29^{+0{,}33}_{-0{,}23}$	$-2{,}40^{+1{,}59}_{-1{,}91}$	$-4{,}36^{+0{,}33}_{-0{,}44}$	$22{,}38^{+7{,}97}_{-5{,}75}$	4,006

$$\begin{aligned} x &= R_\odot - \mathrm{d_H}\ \cos b\ \cos l \\ y &= \mathrm{d_H}\ \cos b\ \sin l \\ z &= \mathrm{d_H}\ \sin b \end{aligned} \tag{3.4}$$

Figure 3.10 shows the density profiles as described above. Table 3.4 summarizes the parameters found for the spherical halo (sph) SPL and BPL, when the data is corrected by completeness. Based on these results, the best fit for the data corresponds to the SPL model, with a slope of $n = -4{,}18^{+0{,}18}_{-0{,}19}$. In the case of the broken power law model, a break at $R_b = 19{,}34^{+10{,}66}_{-3{,}16}$ kpc is found, with inner and outer slopes of $n_1 = -3{,}47^{+2{,}26}_{-1{,}32}$ and $n_2 = -4{,}23^{+0{,}33}_{-0{,}25}$, respectively.

From Figure 3.10 one can infer that the presence of the break at ~ 20 kpc is mostly due to the relatively-high density of the point at $R_{GC} \sim 26$ kpc. The larger uncertainties in the determination of the BPL parameters, compared with the ones for the SPL, support the low probability of that model. For completeness, a broken power law with two breaks (double broken power law; DBPL) is also fitted to account for a potential different behavior of the profile at large radii, ruled by the interaction of the MW halo with further large massive galaxies (mostly M31), for example. Table 3.4 does not include these parameters, given the large uncertainties associated and the difficulty to assess a physical meaning to this fit.

3.4.2. Ellipsoidal Halo Model

For an oblate halo with a flattening parameter $q = 0{,}7$, the semi-major axis of the ellipsoid is $R_{\mathrm{el}}^2 = X^2 + Y^2 + (Z/0{,}7)^2$ which replaces R in Equation 3.2. The results of the fit are shown in Table 3.4. As in the previous case, the best fit corresponds to the SPL model (based on χ^2_ν), in which $n = -4{,}15^{+0{,}23}_{-0{,}25}$. The density profile (Figure 3.11) displays a clear break only if the RR Lyrae with $R_{el} < 60$ kpc are considered, as described by Zinn et al. (2014). As in the case of the spherical halo model, the distant bins make the difference when looking for a change in the slope. In the case of a BPL, the fits give $R_{el} \sim 22{,}38^{+7{,}97}_{-5{,}75}$ kpc as the most likely value for the break radius, with inner and outer slopes of $n_1 = -2{,}40^{+1{,}59}_{-1{,}91}$ and $n_2 = -4{,}36^{+0{,}33}_{-0{,}44}$. The values of the breaks for the DBPL are ~ 25 kpc and ~ 85 kpc, with large uncertainties. For the latter, overfitting is much more likely to have happened than in the spherical halo model.

Table 3.5. Parameters for the different power law models described in Section 3.4, without Leo IV and Leo V.

Model	A1	A2	n1	n2 (kpc)	R_b (kpc)	χ^2_ν
sph SPL	$1,18^{+0,12}_{-0,12}$	–	$-4,22^{+0,18}_{-0,19}$	–	–	2,131
sph BPL	$0,78^{+0,64}_{-0,61}$	$1,24^{+0,18}_{-0,19}$	$-3,06^{+1,66}_{-1,73}$	$-4,30^{+0,26}_{-0,27}$	$19,30^{+6,90}_{-3,09}$	2,573
ell SPL	$1,14^{+0,15}_{-0,15}$	–	$-4,15^{+0,22}_{-0,25}$	–	–	2,509
ell BPL	$0,50^{+0,80}_{-0,78}$	$1,28^{+0,29}_{-0,21}$	$-2,44^{+1,88}_{-2,02}$	$-4,35^{+0,30}_{-0,39}$	$21,93^{+6,76}_{-5,33}$	3,080

Overall, based on a reduced χ^2 criterion the spherical halo model provides a better fit to the halo than the ellipsoidal model with $q = 0{,}7$. The results of using samples that include/exclude the RRLs in the UFD Leo IV and Leo V are the same, within the erros, indicating that small galaxies do not affect the general behaviour of the density profile of the halo.

The fits of the models do not support the presence of a clear break in the profiles. However, this result might be biased by the fact that, due to the saturation limit of HiTS' photometry, the data only have $\sim 1-2$ bins within the radius where a break is typically identified. Thus, the fits may not be sensitive to a significant break in the inner halo.

The slopes of the power-laws and the position of a potential break are broadly consistent with previous studies (Table 3.6). This agreement might represent a possible real feature of the Galactic halo, even when the sample used for those studies are located at different positions. However, it is not clear that the data favor a certain model over the other. Here, a less likely double broken power law (a power law with two breaks) is fitted to the profile as well, but it was not considered for further analysis due to the lack of a strong physical meaning, big uncertainties and possible overfitting.

Table 3.6 Parameters of number density profiles of the halo from previous works, when power laws are considered. This Table only includes works with upper limits in distance > 25 kpc.

Model	Slope	R_b (kpc)	Inner Slope	Outer slope	Range (kpc)	Tracer Used	Paper
SPL							
	$-3{,}034 \pm 0{,}08$	–	–	–	1–80	RRLs	Wetterer & McGraw 1996
	$\sim -2{,}8$	–	–	–	4–60	RRLs	Vivas & Zinn 2006
	$-3{,}0$	–	–	–	5–40	MSTO stars	Bell et al. 2008
	$-2{,}5 \pm 0{,}2$	–	–	–	10–90	BHB stars	De Propris et al. 2010
	$-2{,}7 \pm 0{,}5$	–	–	–	1–40	BHB and BS stars	Deason et al. 2011
	$-2{,}42 \pm 0{,}13$	–	–	–	5–30	($ab-$type) RRLs	Sesar et al. 2013
	< -6	–	–	–	50–100	A-type stars	Deason et al. 2014
	$-3{,}8 \pm 0{,}3$	–	–	–	50–100	($ab-$type) RRLs	Cohen et al. 2015
	$-3{,}4 \pm 0{,}1$	–	–	–	10–80	K giants	Xue et al. 2015
	$-3{,}5 \pm 0{,}2$	–	–	–	30–90	Giant stars	Slater et al. 2016
	$-2{,}96 \pm 0{,}05$	–	–	–	1–28	RRLs	Iorio et al. 2017
	$-4{,}18^{+0{,}18}_{-0{,}19}$	–	–	–	17–145	RRLs	This work
BPL							
	–	23	$-2{,}4$	$-4{,}5$	5–100	RRLs	Watkins et al. 2009
	–	27 ± 1	$-2{,}3 \pm 0{,}1$	$-4{,}6^{+0{,}2}_{-0{,}1}$	1–40	BHB and BS stars	Deason et al. 2011
	–	28	$-2{,}6 \pm 0{,}04$	$-3{,}8 \pm 0{,}1$	12–40	near MSTO stars	Sesar et al. 2011
	–	24	$-2{,}8 \pm 0{,}5$	$-5{,}4 \pm 0{,}5$	5–60	RRLs	Zinn et al. 2014
	–	20	$-2{,}5 \pm 0{,}4$	$-4{,}9 \pm 0{,}4$	10–60	F-type stars	Pila-Díez et al. 2015
	–	18 ± 1	$-2{,}1 \pm 0{,}3$	$-3{,}8 \pm 0{,}1$	10–80	K giants	Xue et al. 2015
	–	$29{,}87^{+2{,}80}_{-3{,}55}$	$-3{,}61^{+0{,}15}_{-0{,}16}$	$-4{,}75^{+0{,}30}_{-0{,}28}$	10–70	BHB stars	Das et al. 2016
	–	$19{,}34^{+10{,}66}_{-3{,}16}$	$-3{,}47^{+2{,}26}_{-1{,}32}$	$-4{,}23^{+0{,}33}_{-0{,}25}$	17–145	RRLs	This work

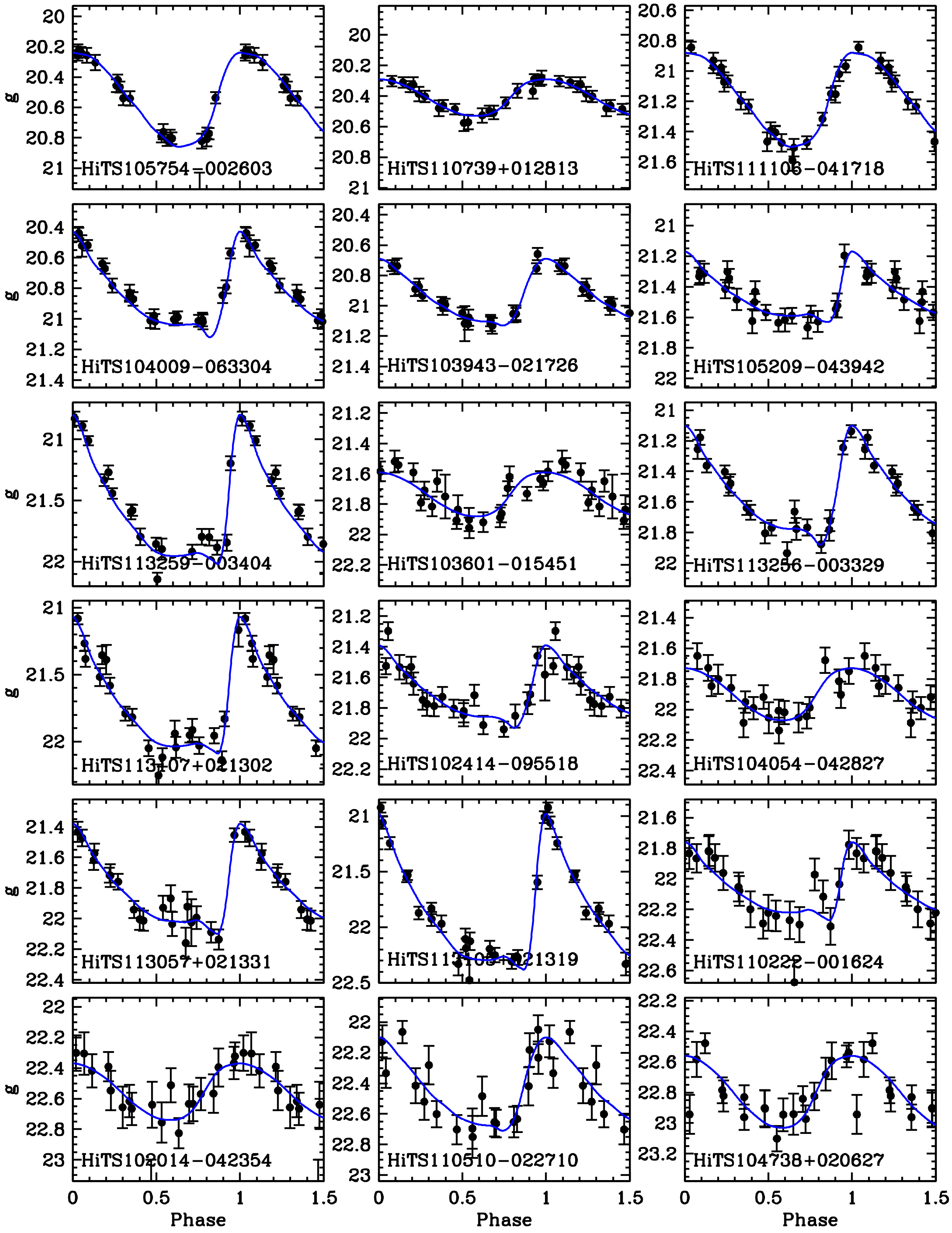

Figure 3.9 Folded light curves of the distant RR Lyrae stars listed in Table 3.3.

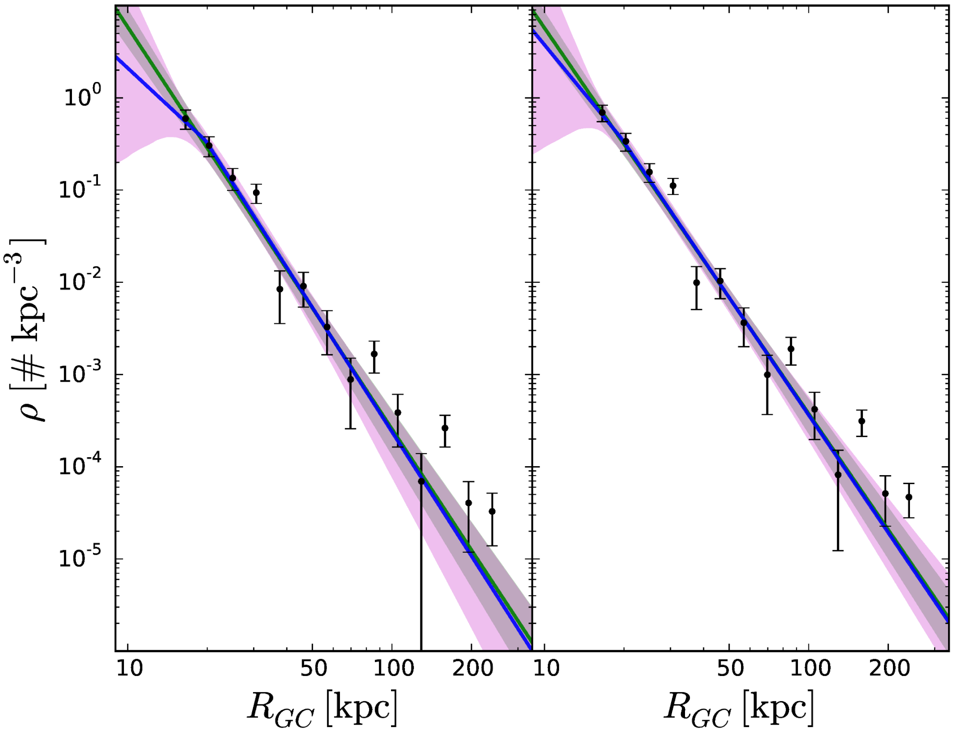

Figure 3.10 Number density versus Galactocentric distance R_{GC}, excluding RR Lyrae stars from the Sextans dwarf galaxy, assuming a spherical halo. Density profiles built without and with considering completeness values (see Figure 2.7) are shown in the *left* and *right* panels, respectively. A simple power-law (green) and a broken power-law model (blue) are fitted to the corrected data; the corresponding fit parameters are listed in Table 3.4, and the fits overlaid as solid lines in both panels. The shaded regions show the 3σ confidence levels determined via MCMC methods.

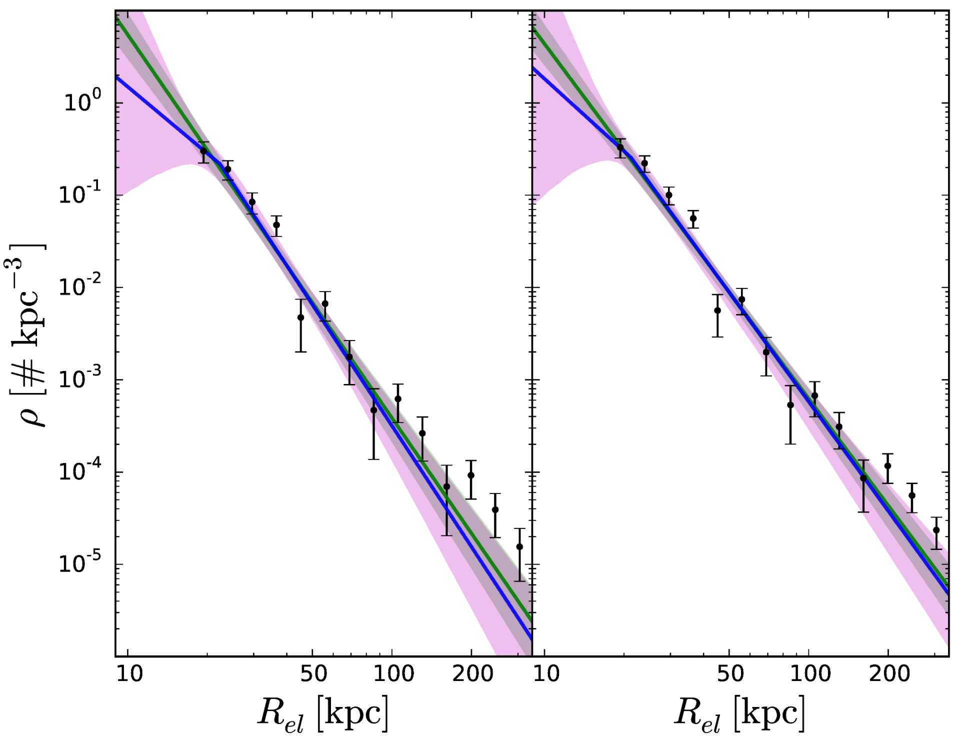

Figure 3.11 Number density as a function of radius in an elliptical halo, R_{el}, assuming an oblate halo with $q = 0{,}7$. As in Figure 3.10, RR Lyrae stars from the Sextans dSph are excluded. Density profiles built without and with considering completeness values (see Figure 2.7) are shown in the *left* and *right* panels, respectively. A simple power-law (green) and a broken power-law model (blue) are fitted to the uncorrected data at $R_{\mathrm{GC}} < 145\,\mathrm{kpc}$; the corresponding fit parameters are listed in Table 3.4, and the fits overlaid as solid lines in both panels. The shaded regions show the 3σ confidence levels determined via MCMC methods.

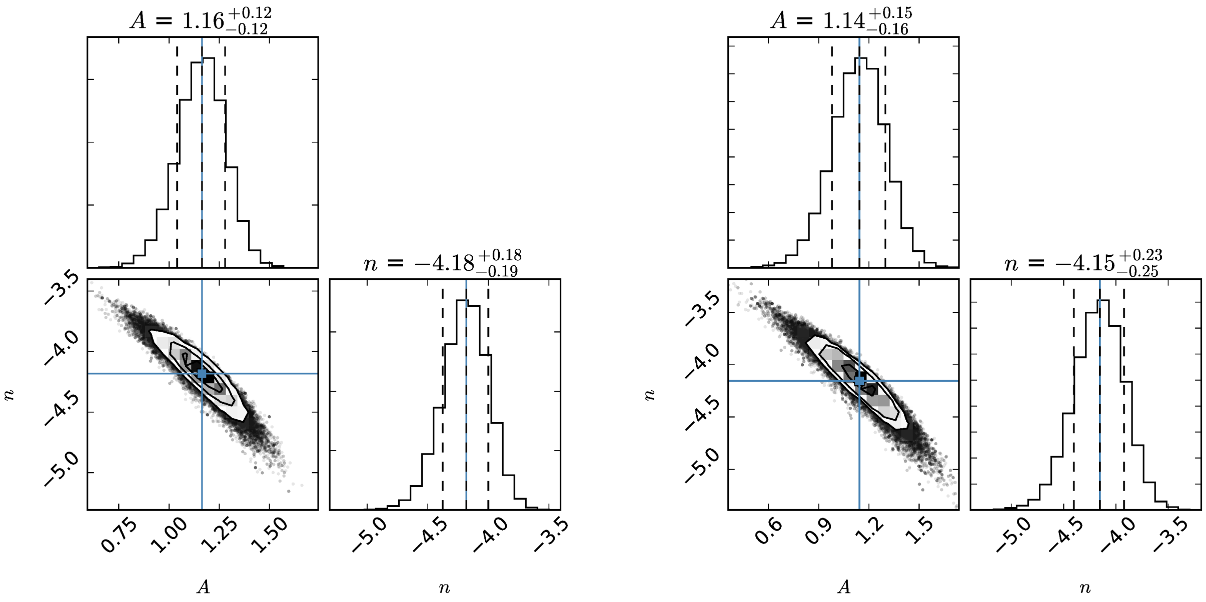

Figure 3.12 Corner plot showing the posterior joint probability distribution of the parameters of a simple power law number density profile, for a spherical Halo model (*left*) and an ellipsoidal one (*right*). The parameters used for this model are the logarithm form of the number density in the solar neighborhood (A) and the power law index of the model (n).

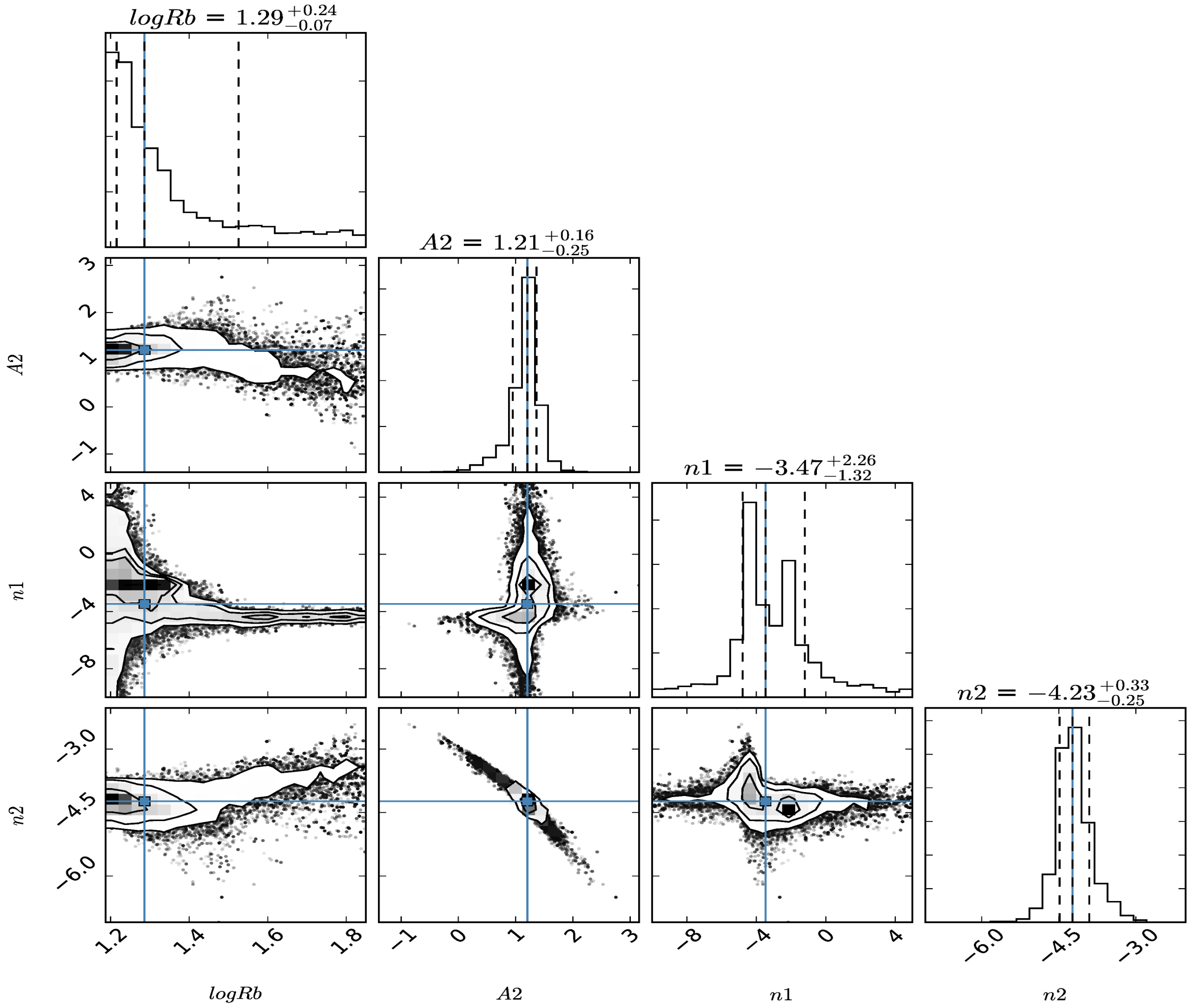

Figure 3.13 Posterior joint probability distribution of the parameters of a broken power law number density profile. The parameters shown are the logarithm of the break radius ($logRb$), the logarithm of the number density in the solar neighborhood (after the break; A_2) and the power law index before and after the break (n_1 and n_2, respectively).

Chapter 4

RR Lyrae stars from HiTS 2015

The motivation for this chapter is to introduce and describe the preliminar list of RRLs found in the data from HiTS 2015A. An overview of the main features of the full 2015' sample is given in Section 4.1. This section specifies the common RRLs between HiTS 2014 and 2015, and the number of candidates that are exclusive from 2015. Also, the pulsational properties of these RRLs is presented, as well as their classifications and spatial distribution, following an analysis similar to the one made in Chapter 3.

A key aspect to be considered for this chapter is that the selection process of the catalog from 2015, and its respective analysis, is not complete yet. Therefore, the procedure of construction of the RRLs catalog presented here has to be refined still and the results are, in consequence, tentative.

Section 4.2 briefly places the preliminar detection of these stars in HITS 2015A into context to recall the scientific value of finding/not finding RRLs in the Galactic halo. In Appendix A, the ongoing work and expected continuation of this study is summarized.

4.1. The sample

A total of 159 RRLs constitute the preliminary list of RRLs resulting from the selection procedure described in Chapter 2, including color cuts (that are not applied to the data from HiTS 2014). This catalog is made up of stars with uncorrected magnitudes (by zeropoint), and their periods and amplitudes are rough estimations of the real values, as explained in the following subsections. These RRLs candidates cover a range of $15{,}7 - 23{,}1$ in g magnitude, and from $-0{,}14$ to $0{,}59$ in $g - r$.

It is important to mention that 14 of the fields that are part of the HiTS 2015A footprint overlay fields from 2014A. Therefore, a significant number of RRLs are present in both selections. Since the footprint of the third campaign of HiTS overlaps the ones from the second campaign, only 102 of the 159 RRLs are exclusive from this search. The other 57 are mostly from the Sextans dSph (see Section 4.1.3), and can be used as a confirmation of the

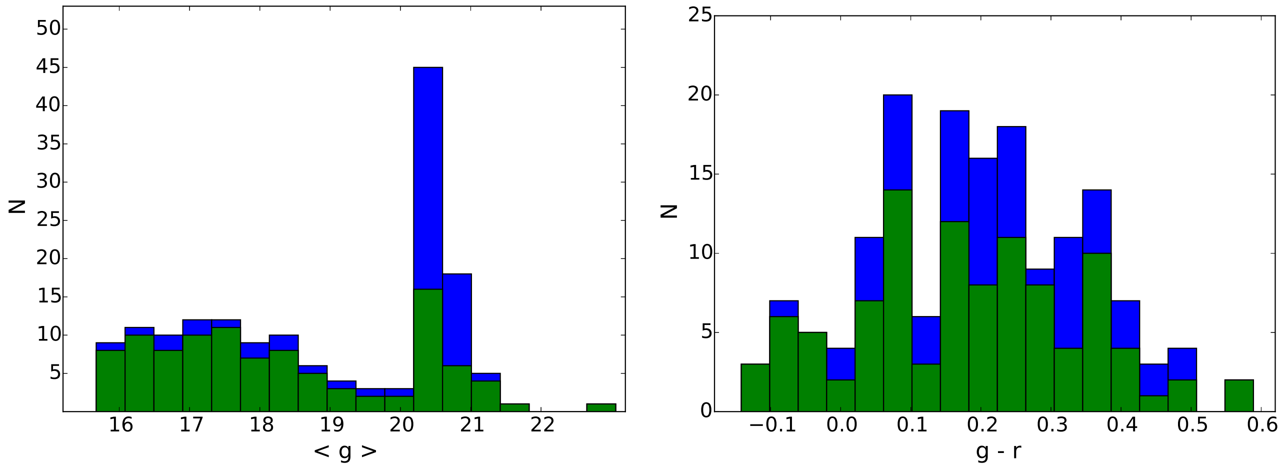

Figure 4.1 *left panel*: Distribution of the mean magnitudes g for the complete sample of RRLs from HiTS 2015 (blue) and for the candidates from 2015 only (green). *right panel*: Distribution of colors $(g - r)$ for the samples.

nature of these variable stars as RRLs, given that the data from 2015 also includes colors.

The 102 exclusive candidates have magnitudes in the range of 15,7 to 23,1 in g. Figure 4.1 (left panel) shows the uncorrected mean magnitude of the list of RRLs with and without considering the repeated candidates from 2014. A histogram of the color distribution of these stars is shown in the right panel of Figure 4.1. The sample comprised of the faintest candidates is presented in Section 4.1.4.

The following subsections focus on the 102 RRLs that do not match in position in the sky with HiTS 2014.

Table 4.1. List of the HiTS 2015-exclusive RRLs presented in Chapter 4.

ID	R.A. (deg)	DEC (deg)	$< g_{ref} >$[1]	Color	Period (days)	Amplitude	Type	N
HiTS090839-003849	137.162	-0.6469	17.22	-0.01	0.3689	0.48	c	25
HiTS091013-050321	137.5523	-5.0557	15.79	0.08	0.5412	1.24	ab	26
HiTS091047+015033	137.695	1.8424	18.56	0.36	0.6021	0.94	ab	27
HiTS091050-055917	137.7094	-5.988	19.69	0.22	0.6468	0.47	ab	28
HiTS091110-062237	137.7899	-6.377	18.50	0.19	0.5713	0.85	ab	28
HiTS091139-003904	137.9134	-0.6512	16.70	-0.08	0.4742	1.33	ab	25
HiTS091156+022530	137.9831	2.4249	16.46	0.30	0.6021	1.32	ab	27
HiTS091510-052952	138.7914	-5.4979	20.67	0.16	0.6199	0.97	ab	28
HiTS091512+021915	138.8009	2.3208	17.78	-0.03	0.2855	0.65	c	28
HiTS091528-041929	138.866	-4.3246	16.57	-0.04	0.3872	0.62	c	24
HiTS091558-062404	138.9911	-6.4012	16.74	-0.10	0.4865	1.48	ab	28
HiTS091924-063037	139.8499	-6.5102	18.37	0.09	0.3593	0.67	c	24
HiTS091945-000157	139.9373	-0.0324	16.26	0.27	0.6111	1.05	ab	27
HiTS091947+011016	139.946	1.171	16.70	0.21	0.6575	1.14	ab	26
HiTS091948+021041	139.9482	2.1781	16.75	-0.04	0.2942	0.60	c	26
HiTS092035-042137	140.1449	-4.3604	17.21	0.13	0.2556	0.43	c	24
HiTS092103+014538	140.2619	1.7606	17.00	0.09	0.6177	0.82	ab	26
HiTS092442-062442	141.1765	-6.4118	17.67	-0.09	0.3044	0.52	c	24
HiTS092505+015005	141.2725	1.8347	18.17	0.12	0.3445	0.53	c	26
HiTS092521+015542	141.3365	1.9283	18.49	0.17	0.2706	0.77	c	26
HiTS092916-033445	142.3177	-3.5791	18.58	-0.03	0.2864	0.44	c	26
HiTS092927-055440	142.3618	-5.9112	21.19	0.18	0.5779	1.05	ab	25
HiTS093042-022248	142.6742	-2.38	17.74	0.25	0.5886	1.13	ab	26
HiTS093056+015751	142.7353	1.9642	18.45	0.39	0.592	0.86	ab	26
HiTS093310-000612	143.2934	-0.1034	17.53	0.23	0.6249	1.20	ab	25
HiTS093357-005409	143.4893	-0.9026	18.19	0.37	0.6826	0.21	ab	25
HiTS093431-034020	143.6291	-3.6722	19.29	0.28	0.5615	1.10	ab	27
HiTS093704-042224	144.2661	-4.3732	17.70	0.24	0.5909	0.89	ab	27
HiTS093707-000425	144.2785	-0.0737	18.73	0.27	0.5975	0.77	ab	25
HiTS093807+002518	144.5282	0.4217	19.59	0.04	0.3458	0.77	c	25
HiTS093807-005552	144.5289	-0.9311	20.96	0.10	0.6109	0.83	ab	25
HiTS093847-060049	144.6965	-6.0135	20.99	0.35	0.5895	0.85	ab	28
HiTS093851+000703	144.7113	0.1176	19.13	0.35	0.3804	0.82	c	25
HiTS093902-010035	144.7573	-1.0096	16.15	-0.08	0.5968	1.11	ab	25
HiTS093913-061915	144.8035	-6.3208	17.33	0.32	0.5268	1.23	ab	28
HiTS093950-012236	144.9578	-1.3768	15.94	0.04	0.5442	0.64	ab	25
HiTS094023-025937	145.0973	-2.9936	20.89	0.48	0.8484	0.41	ab	26
HiTS094027-065219	145.1136	-6.872	17.10	0.35	0.631	0.69	ab	28
HiTS094032+021012	145.1344	2.1699	17.53	0.17	0.5956	0.71	ab	24
HiTS094109+013118	145.2862	1.5216	17.06	0.07	0.3097	0.34	c	24
HiTS094118-065433	145.3251	-6.9093	16.13	0.17	0.4845	1.44	ab	27
HiTS094242+015605	145.6766	1.9347	18.71	0.15	0.5221	1.00	ab	24
HiTS094304-060042	145.7677	-6.0118	17.27	0.31	0.5374	1.28	ab	28
HiTS094339-070105	145.9124	-7.018	16.79	0.36	0.5488	1.17	ab	28
HiTS094637-034213	146.6542	-3.7036	17.32	0.06	0.3921	0.59	c	26
HiTS094710-044627	146.7904	-4.7742	17.35	0.38	0.6622	0.68	ab	26

Table 4.1 (cont'd)

ID	R.A. (deg)	DEC (deg)	$< g_{ref} >$ [1]	Color	Period (days)	Amplitude	Type	N
HiTS094714+000300	146.8096	0.05	16.54	0.43	0.5425	0.48	ab	27
HiTS094842-042035	147.1767	-4.3431	16.68	0.41	0.6685	1.14	ab	26
HiTS095009-064914	147.5395	-6.8206	19.34	0.22	0.3721	0.60	c	28
HiTS095017-061952	147.5721	-6.3312	17.98	0.09	0.2621	0.44	c	28
HiTS095123-065416	147.8465	-6.9045	16.47	0.33	0.4855	1.24	ab	28
HiTS095209-014404	148.0385	-1.7344	16.91	0.13	0.527	1.20	ab	27
HiTS095253-014305	148.2227	-1.718	21.40	-0.12	0.3523	0.83	c	27
HiTS095351-062142	148.4621	-6.3616	16.37	0.23	0.5642	1.08	ab	28
HiTS100145-024303	150.4366	-2.7176	18.40	0.03	0.7786	0.50	ab	28
HiTS100507-032355	151.2805	-3.3987	17.67	0.09	0.5126	0.91	ab	26
HiTS100527-050335	151.361	-5.0597	20.18	0.22	0.6125	0.69	ab	26
HiTS100752-020827	151.965	-2.1407	20.52	0.56	0.4808	0.29	c	20
HiTS100809-053823	152.0363	-5.6396	18.08	0.09	0.5483	1.10	ab	29
HiTS100918+023801	152.3247	2.6335	18.72	0.08	0.5961	0.73	ab	28
HiTS101057-033318	152.7361	-3.555	19.99	0.17	0.643	0.76	ab	26
HiTS101128-013921	152.8668	-1.6557	20.37	0.48	0.3884	0.80	c	28
HiTS101128-013643	152.8674	-1.612	20.57	0.16	0.5945	0.99	ab	27
HiTS101227-013643	153.1106	-1.612	20.50	0.23	0.5871	1.10	ab	27
HiTS101228-014711	153.1147	-1.7865	20.49	0.16	0.632	0.85	ab	28
HiTS101253-004020	153.2195	-0.6721	20.29	0.23	0.6468	1.05	ab	28
HiTS101337-014952	153.4045	-1.8311	20.73	0.41	0.6289	0.93	ab	28
HiTS101338-015258	153.4079	-1.8828	20.34	0.06	0.4353	0.66	c	28
HiTS101342-021246	153.4233	-2.2128	20.43	0.19	0.3999	0.57	c	27
HiTS101344-014848	153.4325	-1.8134	20.65	0.42	0.5855	1.05	ab	28
HiTS101449+000709	153.7033	0.1192	17.06	0.08	0.5153	1.44	ab	27
HiTS101453+001915	153.7197	0.3209	23.06	0.59	0.6169	1.75	ab	23
HiTS101456-022025	153.7342	-2.3403	20.39	-0.02	0.489	0.76	c	28
HiTS101511-012700	153.7954	-1.45	20.60	0.26	0.6073	1.02	ab	28
HiTS101516-011649	153.8151	-1.2804	20.45	0.18	0.7302	1.29	ab	26
HiTS101527-011655	153.8643	-1.2819	20.42	0.23	0.5723	0.88	ab	27
HiTS101531-011841	153.8796	-1.3115	20.26	0.23	0.4373	0.52	c	28
HiTS101538+022342	153.9073	2.3949	15.84	0.22	0.3111	0.64	c	26
HiTS101551-015619	153.9606	-1.9385	20.31	0.03	0.3232	0.62	c	27
HiTS101653-013750	154.2188	-1.6305	16.06	0.29	0.5761	1.02	ab	27
HiTS101700+023314	154.2481	2.554	16.18	0.08	0.5677	0.70	ab	26
HiTS101734+001322	154.3912	0.2228	20.51	0.01	0.3716	0.61	c	26
HiTS101945-012651	154.9373	-1.4474	20.51	0.24	0.722	0.87	ab	26
HiTS102007-061151	155.0288	-6.1975	18.36	0.29	0.6199	0.80	ab	25
HiTS102041+012207	155.1729	1.3685	17.31	-0.08	0.4637	1.42	ab	26
HiTS102052-035820	155.2185	-3.9723	17.51	0.08	0.3022	0.39	c	26
HiTS102241+005948	155.6709	0.9967	16.40	-0.13	0.3478	0.58	c	26
HiTS102351-054146	155.9623	-5.696	15.90	-0.09	0.6457	0.96	ab	27
HiTS102820-063614	157.0841	-6.6039	17.10	0.29	0.5603	1.21	ab	26
HiTS102858+023759	157.2405	2.6331	21.74	0.38	0.4047	1.44	ab	22
HiTS102910+000310	157.2918	0.0528	17.83	0.07	0.6406	0.63	ab	27
HiTS102941-025613	157.4188	-2.9369	17.66	0.38	0.6438	0.35	ab	27

Table 4.1 (cont'd)

ID	R.A. (deg)	DEC (deg)	$< g_{ref} >$ [1]	Color	Period (days)	Amplitude	Type	N
HiTS103003-044803	157.5108	-4.8008	16.41	0.37	0.5585	1.13	ab	27
HiTS103140-005140	157.9172	-0.861	17.60	0.18	0.2933	0.60	c	26
HiTS103258-063715	158.2403	-6.6209	15.67	0.16	0.6167	1.07	ab	27
HiTS103258-063715	158.2404	-6.6209	15.85	0.05	0.613	0.99	ab	21
HiTS103325+014710	158.3561	1.7861	18.04	0.29	0.6776	0.86	ab	25
HiTS103402-062058	158.5085	-6.3495	15.76	-0.14	0.5506	0.96	ab	25
HiTS103455+005814	158.728	0.9705	17.88	0.22	0.4542	1.48	ab	25
HiTS103644-065357	159.1832	-6.8993	21.19	0.05	0.2698	1.00	ab	22
HiTS103721+015616	159.3392	1.9378	16.19	0.34	0.6544	1.10	ab	25
HiTS103945-021802	159.9369	-2.3005	21.23	0.24	0.7088	0.68	ab	24

[1] These magnitudes are not calibrated.

4.1.1. Pulsational Properties and Classification

As in the case of the sample obtained with data from 2014A, the period and amplitude of the 102 RRLs from 2015 are obtained from the first estimations made by the GLS periodograms and the difference between the extreme values of the g magnitude in the time series, respectively. In this section the values of these parameters without further analysis (template fitting, for instance) are presented.

Figure 4.2 displays the position of the RRLs in the Period-Amplitude diagram. The figure, as well as Figure 3.2, highlights potential members of the Sextans dSph. From the figure, it is noticeable that a large number of RRLs have large amplitudes ($\Delta g > 1{,}0\,\mathrm{mag}$), which could be explained by the way Δg is calculated, in addition to the fact that the magnitudes are not corrected.

In order to perform a preliminary classification, the values of the periods and amplitudes are used to discriminate between RRab's and RRc's. In Figure 4.2 the two types of RRLs are color coded. From the RRLs that are exclusive from HiTS 2015, 73 are RRab's and 29 are RRc's.

4.1.2. Spatial distribution

Since the overall stellar properties of the RRLs presented in this chapter are not very well defined, from this point the distances to these RRLs are not going to be given directly. Although, a rough approximation of them will be provided by estimating distances from assuming typical values for the absolute magnitude of RRLs in the halo ($M_g = 0{,}69$, for example).

In Figure 3.3, the spatial distribution of this sample is shown, as well as their position

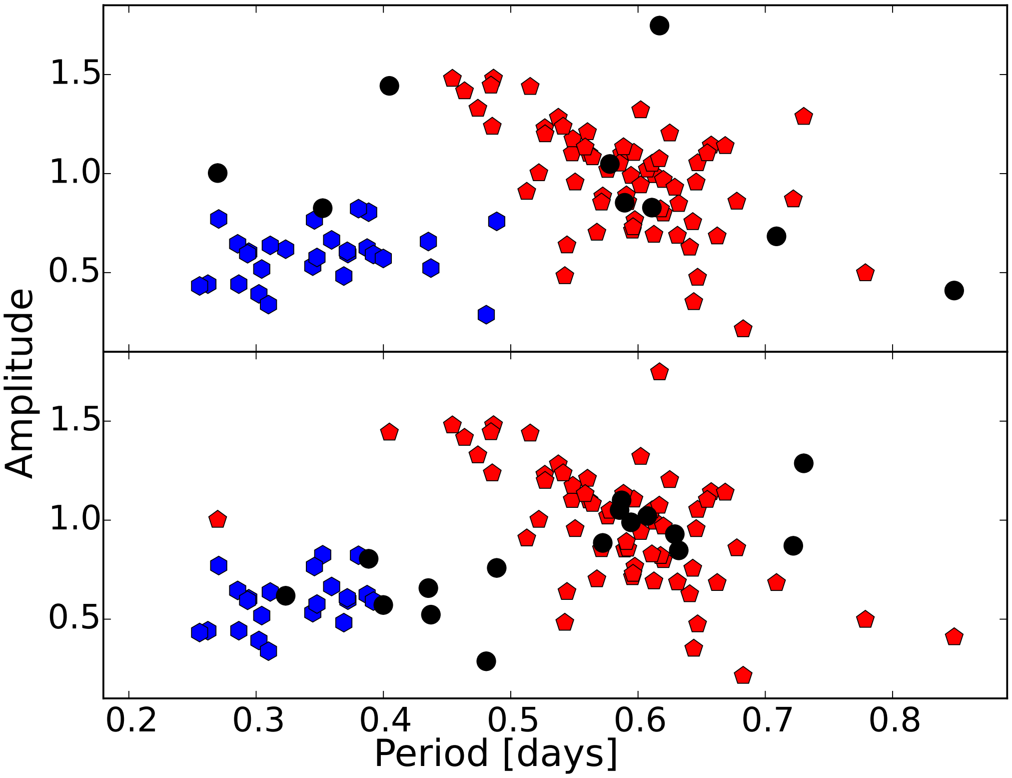

Figure 4.2 Period-Amplitude diagram of the sample of RRLs from 2015 (exclusives). The blue hexagons represent RRc stars, while the RRab are plotted with red symbols. Black filled circles represent RRLs with an uncorrected g magnitude $> 20{,}85$ (*top*) and potential RRLs members of the Sextans dSph galaxy (*bottom*).

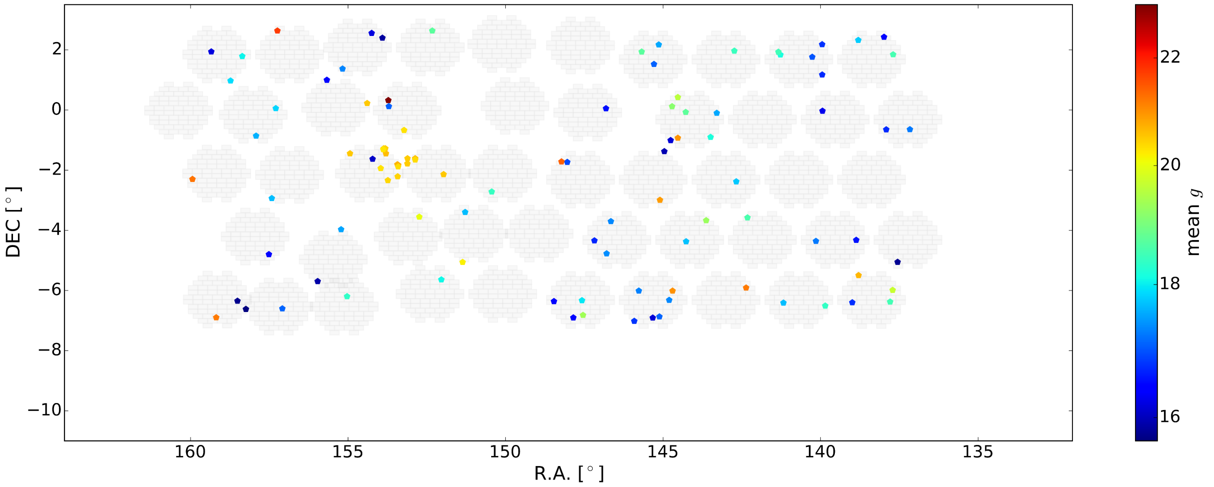

Figure 4.3 Color coded plot of the distribution of our 102 RRLs stars from HiTS 2015, with the colors representing their uncorrected mean magnitudes. An approximation of the HiTS footprint is shown in grey in the background as a reference.

in the HiTS 2015 footprint. The figure displays the position of the RRLs color coded by the mean g magnitude of the stars. The latter can be used as a proxy of the corresponding heliocentric distances.

The figure displays an approximated uniform distribution, although it is clear that the sample is very incomplete at this level. In any case, as the a region of the field of view overlaps with the footprint from 2014, RRLs from the Sextans dSph can be inmediately identified. These RRLs are described in the following section.

4.1.3. RR Lyrae Stars in the Sextans dSph

Since the footprint of both HiTS' campaigns overlap in their extremes (see Figure 2.2), it is expected for some of the RRLs described in Section 3.2.1 to be detected in the sample presented here. Using the data from HiTS 2015A, only 16 RRLs of a total 57 potential members of Sextans are new discoveries. Because of the lack of reliable distant estimations for the HiTS 2015's sample, the likelihood of RRLs in the region to be possible members of the dwarf is determined by, again, their angular separation from the dwarf and the mean apparent magnitude of the RRLs. The $< g >$ window chosen for the selection is between 20,0 and 20,8 (~ 70 and $\sim 100\,\mathrm{kpc}$, respectively), and the values of the selected stars range from 20,3 to 20,7. As the RRLs selection method with this data is not refined yet, as mentioned above, it is expected that a high number of RRLs from HiTS 2014 are missed. In fact, 26 members of the latter are missed.

4.1.4. Faint RR Lyrae Stars

Although there are no reliable heliocentric distances for the stars in this sample, their mean magnitudes can be used as an indicator of distance. If a mean magnitude of 20,8 is assumed to represent an heliocentric distance of $\sim 100\,\mathrm{kpc}$, a total of 9 RRLs lie above that threshold (from the sample of 102 stars). From that group, 8 are preliminary classified as RRab's, while only one is RRc. A possible connection between these stars is not easily detectable, since they do not overlay the HiTS fields in contiguous regions. Table 4.1 summarize the main properties of these RRLs candidates.

4.2. Importance of the Sample in an Astrophysical Context

Even when not detailed information can be taken out from the sample presented in this chapter, there are some facts that is good to point out. One of these is the important role that HiTS 2015' data could play when confirming RRLs in the common region between both campaigns of the survey, because of the use of colors.

Also, and even more important than the latter in the context of this work, is that a significant number of RRLs is found at distances greater than $\sim 100\,\mathrm{kpc}$, as in the case of HiTS 2014. In terms of the presence of remote individual RRLs or groups of them, this fact is remarkable since, a priori, one could consider the findings presented in the previous chapter as the result of observing a particular region of the Galactic halo. However, in this chapter the existence of faint RRLs in a different (but adjacent) region is shown, which seems to be consistent with a halo with more or less the same characteristics, and in line with theoretical estimations about the distributions of these old stars with distance (Pillepich et al., 2014). In Appendix A, a summary of the planned way to proceed with the data from 2015 is given.

Conclusions

By examining the 40 fields observed by HiTS during 2014, a methodology was designed to identify RR Lyrae stars in the halo, focusing the work on the outermost regions of the Galaxy. As a result, 173 RR Lyrae stars were detected. The built catalog includes 61 stars that do not appear in previous public surveys overlapping the same sky region, most of which have $< g >> 20$ ($\sim 90\,\%$), corresponding to $\mathrm{d_H} \gtrsim 60\,\mathrm{kpc}$. Additionally, a significant number of these stars (18) have $\mathrm{d_H} \gtrsim 90\,\mathrm{kpc}$, and therefore fall into the category of "distant RR Lyrae stars". The surveyed region overlaps with the position of currently known satellite galaxies of the Milky Way: the dwarf galaxies Sextans, Leo IV, and Leo V, in which 66, 2 and 3 RR Lyrae were detected, respectively. Most of the stars in the Sextans dSph (70 %) and the three from Leo V are new discoveries.

With respect to the distant RRLs in HiTS 2014, they are mostly located toward the locus of the Oo II group, although a large dispersion is observed. However, the mean period of the distant RRab stars is $0{,}668 \pm 0{,}05\,\mathrm{d}$, which is significantly different to the one from nearby RRab's, $0{,}600 \pm 0{,}09\,\mathrm{d}$. It is worth noticing that the mean period of the distant RRLs is remarkably similar to the mean period of the RRLs in the ultra-faint dwarf satellites of the Milky Way, 0,667 d (Vivas et al., 2016), which suggests that these galaxies may be the main contributors of the outermost regions of the halo.

Regarding the RR Lyrae found in Leo IV and the discoveries in Leo V, the idea of using these stars as lightposts when looking for ultra-low luminosity, low surface brightness satellites in the halo came up as a proof-of-concept of ideas recently discussed in the literature. Baker & Willman (2015) argued that groups of two or more closely spaced RRLs in the halo can reveal the presence of a Galactic satellite beyond 50 kpc, since RR Lyrae stars lie in a region of the color-magnitude diagram with little contamination from foreground sources, plus their particular pulsational properties. In the data from HiTS 2014, there is no clear evidence of additional groups of 2–3 RRLs with similar positions that might suggest the presence of new satellites. Does this mean that other faint satellites are not being detected due to the detection efficiency of the survey? Or is it that there are no other faint systems in the field of view, in contrast with the ΛCDM models predictions? Unfortunately, no further conclusions can be drawn giving the limitations of the HiTS and the current surveys.

The possibility of using RRLs to detect new dwarfs becomes even more relevant when looking ahead to projects like the Large Synoptic Survey Telescope (LSST Science Collaboration et al., 2009); the traditional method for detecting ultra-faint systems based on detecting their major CMD sequences will suffer from significant contamination at the faint end, especially arising from unresolved galaxies, a problem that progressively worsens as we explore the outer regions of the Milky Way halo. Thus, RRLs will be with no doubt of much valuable help in the efforts to obtain a complete census of Galactic satellites up to distances of $\sim 400\,\mathrm{kpc}$ (Ivezić et al., 2008; Oluseyi et al., 2012), and to clarify cosmological inconsistencies like the missing satellites problem.

Using the catalog of RR Lyrae stars from HiTS 2014, number density profiles were built, and models of the form $\rho(R) = \rho_\odot(R/R_\odot)^n$ were fitted for a spherical halo and an ellipsoidal one with a flattening parameter $q = 0{,}7$. Simple power laws and broken power laws were considered. The fits described in Chapter 3 do not support the presence of a clear break in the profiles. However, due to the saturation limit of HiTS' photometry there are only $\sim 1-2$ bins within the radius where a break is typically identified, so our data may not be sensitive to the presence of a break. In fact, the data are well represented by a simple power law with a slope of $-4{,}18$ for the spherical halo, and $n = -4{,}15$ for the elliptical case. If a broken power law is considered, the profile (for a spherical halo) exhibits a break at $R_b = 19{,}34\,\mathrm{kpc}$, with inner and outer slopes of $n_1 = -3{,}47$ and $n_2 = -4{,}23$, respectively. In any case, the position of the break and the values of the power-law indices are broadly consistent with previous studies.

The sample of RRLs presented in this work is an unprecedented probe of the outer Galactic halo, since all but three of the bins in stellar density are at distances beyond $30\,\mathrm{kpc}$. Thus, comparing the results of the fits obtained here with other studies of the density in the outer halo is worth being mentioned. In the literature, the existence of a break in the halo density profile at $R_{\mathrm{GC}} \sim 20-30\,\mathrm{kpc}$ is typically argued to represent a transition between predominantly in-situ formed halo stars in the inner halo and an accretion-dominated outer halo (e.g., Bullock & Johnston, 2005; Abadi et al., 2006). Deason et al. (2013) fit broken power-laws to the density profiles of 11 accretion-only models, and found a mean outer halo slope of $\langle n\rangle = -4{,}4$, with values ranging from $-2{,}5 > n > -6{,}5$, and median break radius of $26\,\mathrm{kpc}$. Cooper et al. (2010) also predicts slightly steeper slopes (all with $n < -4{,}4$) for the outer halos of model galaxies formed by the tidal disruption of dwarf satellites. The rough agreement of the power-law fits of HiTS (both the SPL with $n = -4{,}18$, and the BPL with $n_2 = -4{,}23$, $R_b = 19\,\mathrm{kpc}$) with these predictions from halos made entirely of accreted satellites suggests, again, that the outer MW halo may be made up completely of accreted stars.

Also, 159 RR Lyrae variables were found in the preliminar analysis of data from HiTS 2015, most of which are exclusive from the region covered by that campaign. From this sample, nine stars seem to be distant objects. Even when the analysis of this catalog is not completed, the numbers are congruent with the findings of the 2014 data. In spite of that, the data presented here cover only a small field of view in the Galactic halo, not enough to take out a definitive conclusion in a broader context. With a handful of ~ 200 deg^2 field surveys such as that presented in this work, the examination of the fraction of stars in substructures as a function of position would be possible, as well as the variation of density profiles with line of sight. The deep, ~ 20000 deg^2, time-domain LSST will recover a nearly complete sample of RR Lyrae out to $\gtrsim 350$ kpc by the completion of the 10-year survey (Ivezić et al., 2008; Oluseyi et al., 2012; VanderPlas & Ivezić, 2015). The HiTS results presented here are part of the larger ongoing LSST precursor observing programs with which the mapping of the outer limits of the Galactic halo with RR Lyrae stars will continue. This will permit the development of tools that lay the groundwork for exploiting the huge samples of RR Lyrae stars in the LSST era.

Appendix A : Future Work

As explained in Chapter 2, the High cadence Transient Survey has an exceptional potential as a wide-field database to search for distant RRLs in the Galactic halo. In Chapter 3, a detailed examination of the data from the second campaign of the survey is presented. However, the data from HiTS 2015 have not been fully exploited yet, and only preliminary results are available (Chapter 4). In order to perform a complete analysis of these data, the same methodology used to preprocess and analyze the data from HiTS 2014 is going to be adopted. This can be summarized as follows:

(i) Select a definitive catalog of RRLs based on color cuts, periods and their statistical significance, amplitudes, light curve shapes, shape of their point-spread functions, among others.

(ii) Obtain typical photometric uncertainties per field/chip, for HiTS 2015.

(iii) Estimate the detection efficiency of the algorithm.

(iv) Perform a photometric calibration by comparing the magnitudes of the non variable sources in the catalogs with the PS1 database.

(v) Apply a reddening correction to the sample. Then, estimate heliocentric distances following the PLZ relation from Sesar et al. (2017a).

(vi) Examine the spatial distribution of the RRLs. Look for overdensities and groups of stars, in angular and heliocentric distances. Can they be associated to known/undiscovered substructures?

(vii) Analyze the distribution of the stars in the Bailey diagram. See what this can reveal about the origin of the RRLs and their overall distribution in the halo.

(viii) Bin the data and study the number density profiles based on different models and assumptions. Are these results similar to the ones from HiTS 2014?

(ix) Make comparisons with the overall conclusions from HiTS 2014 and other studies, in a cosmological context.

Appendix B : Light Curves

Appendix C : Medina et al. (2017a)

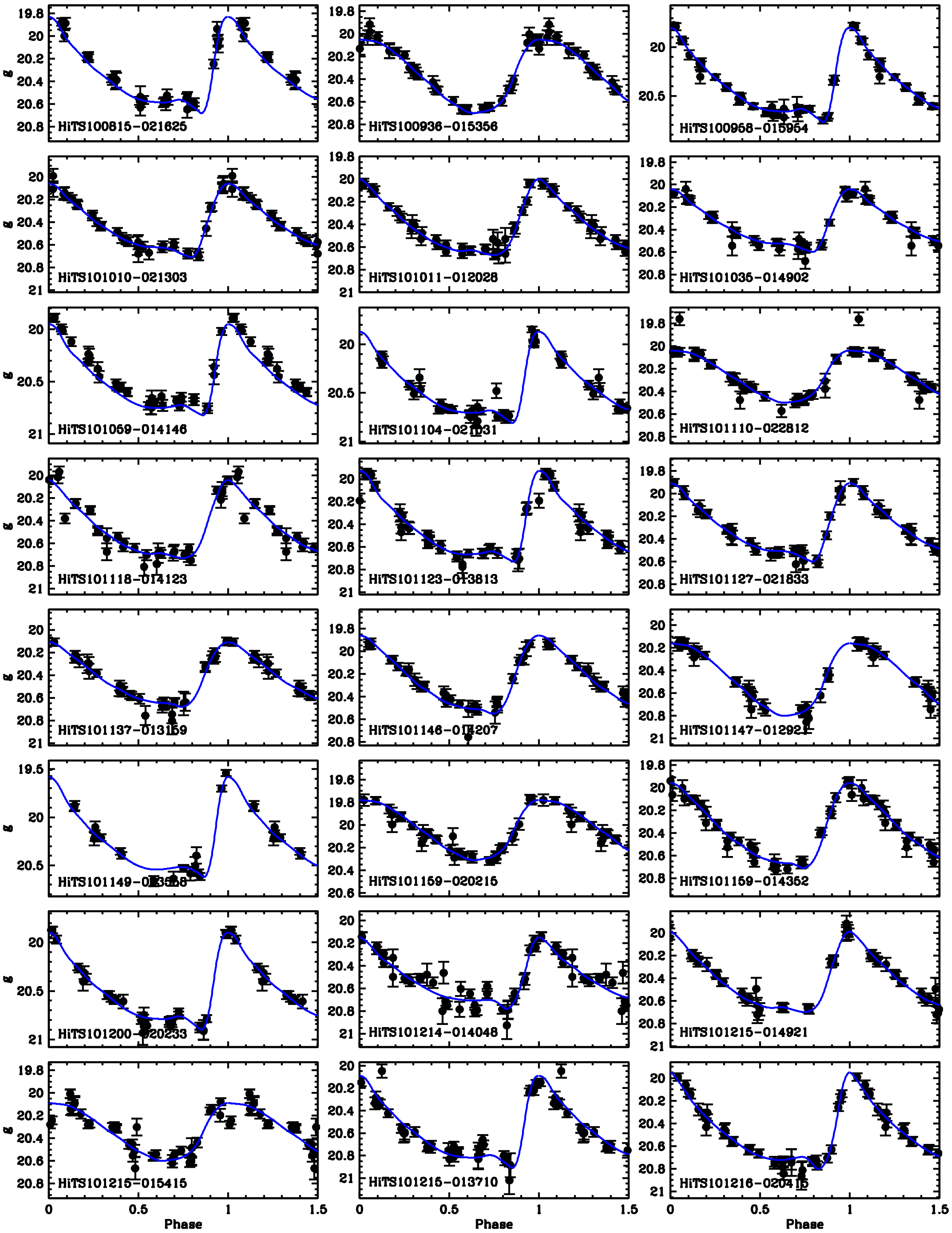

Figure 4.4 Phased lightcurves of RR Lyrae stars in the Sextans dwarf spheroidal galaxy, from HiTS 2014 (1/3).

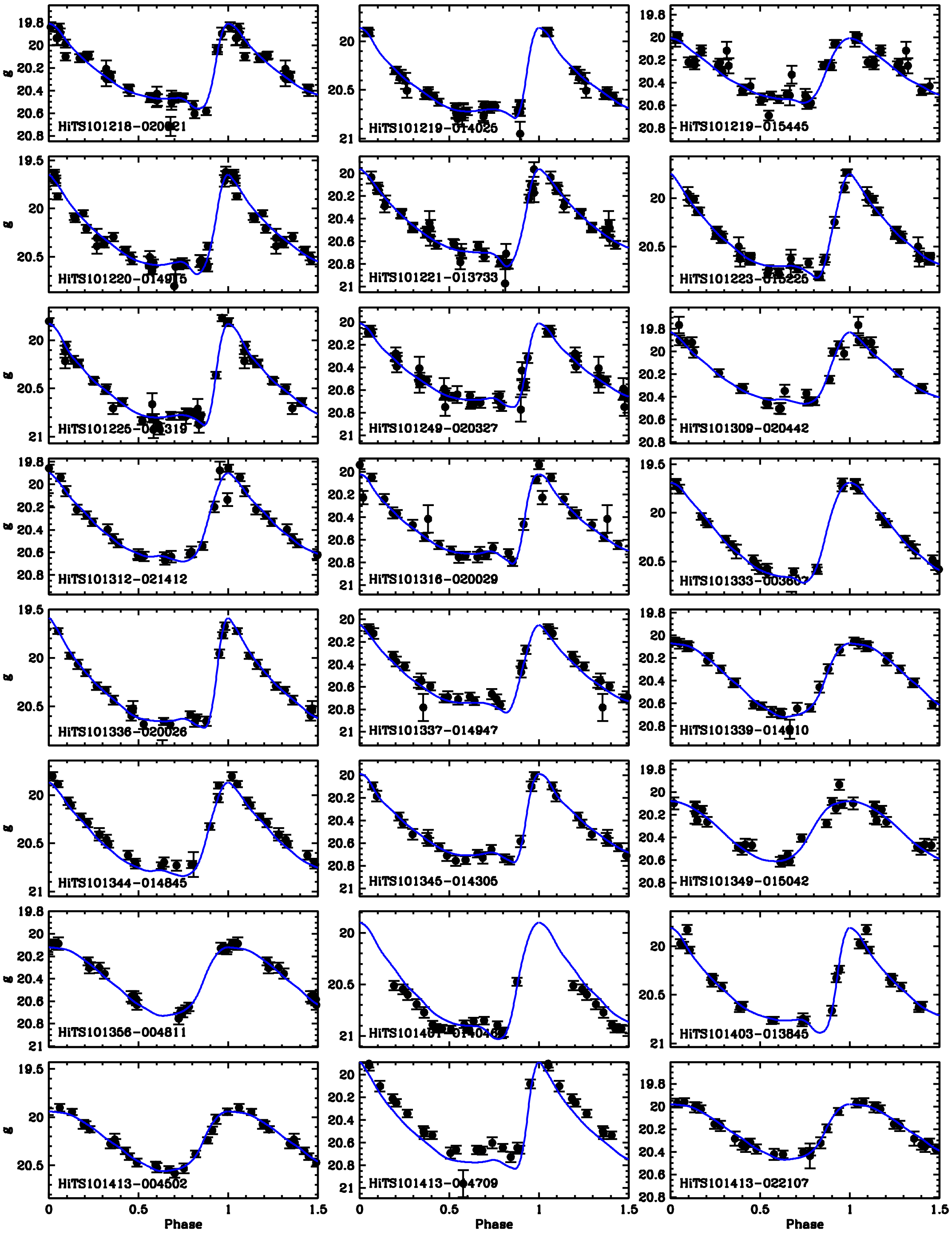

Figure 4.5 Phased lightcurves of RR Lyrae stars in the Sextans dwarf spheroidal galaxy, from HiTS 2014 (2/3).

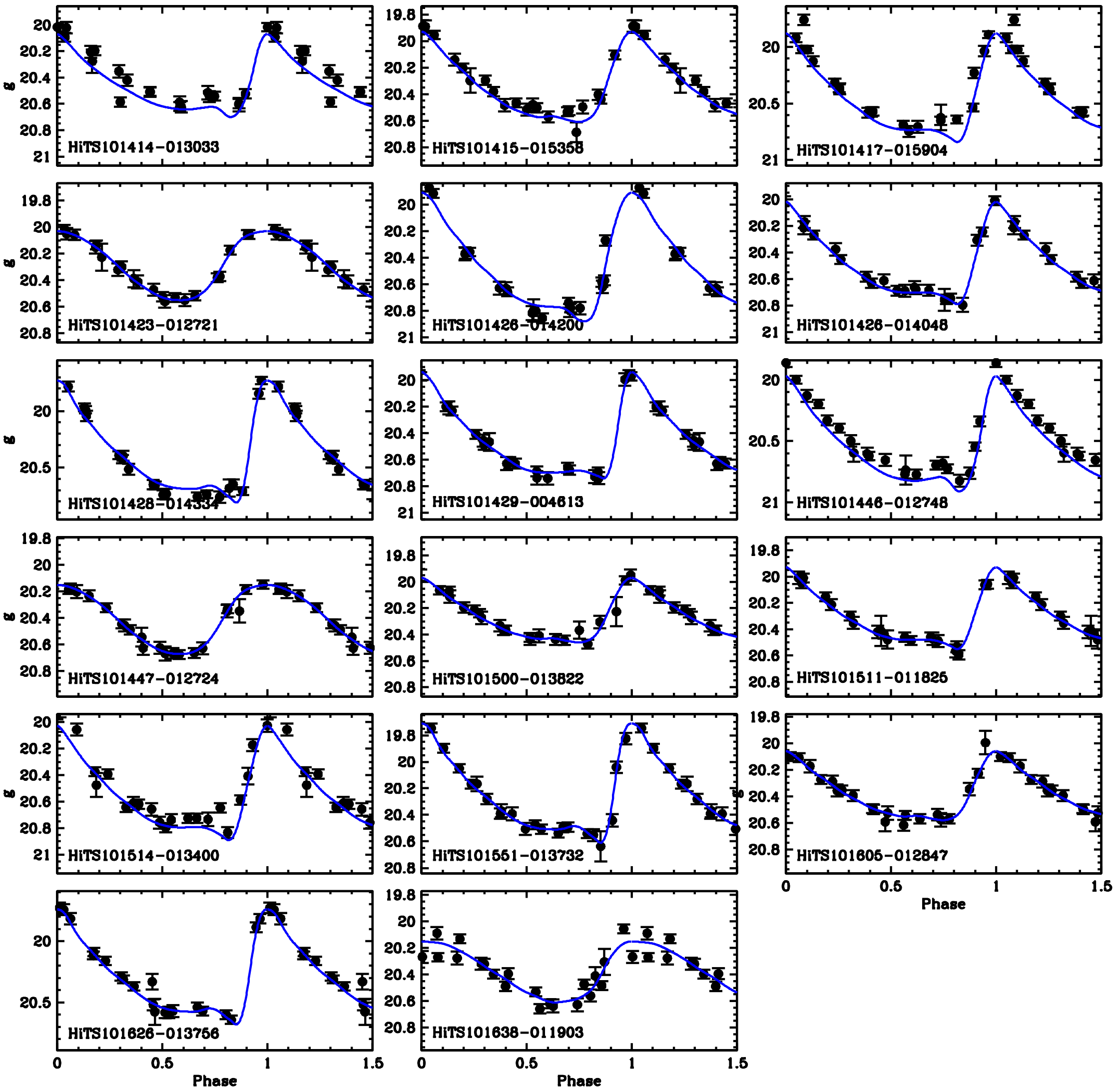

Figure 4.6 Phased lightcurves of RR Lyrae stars in the Sextans dwarf spheroidal galaxy, from HiTS 2014 (3/3).

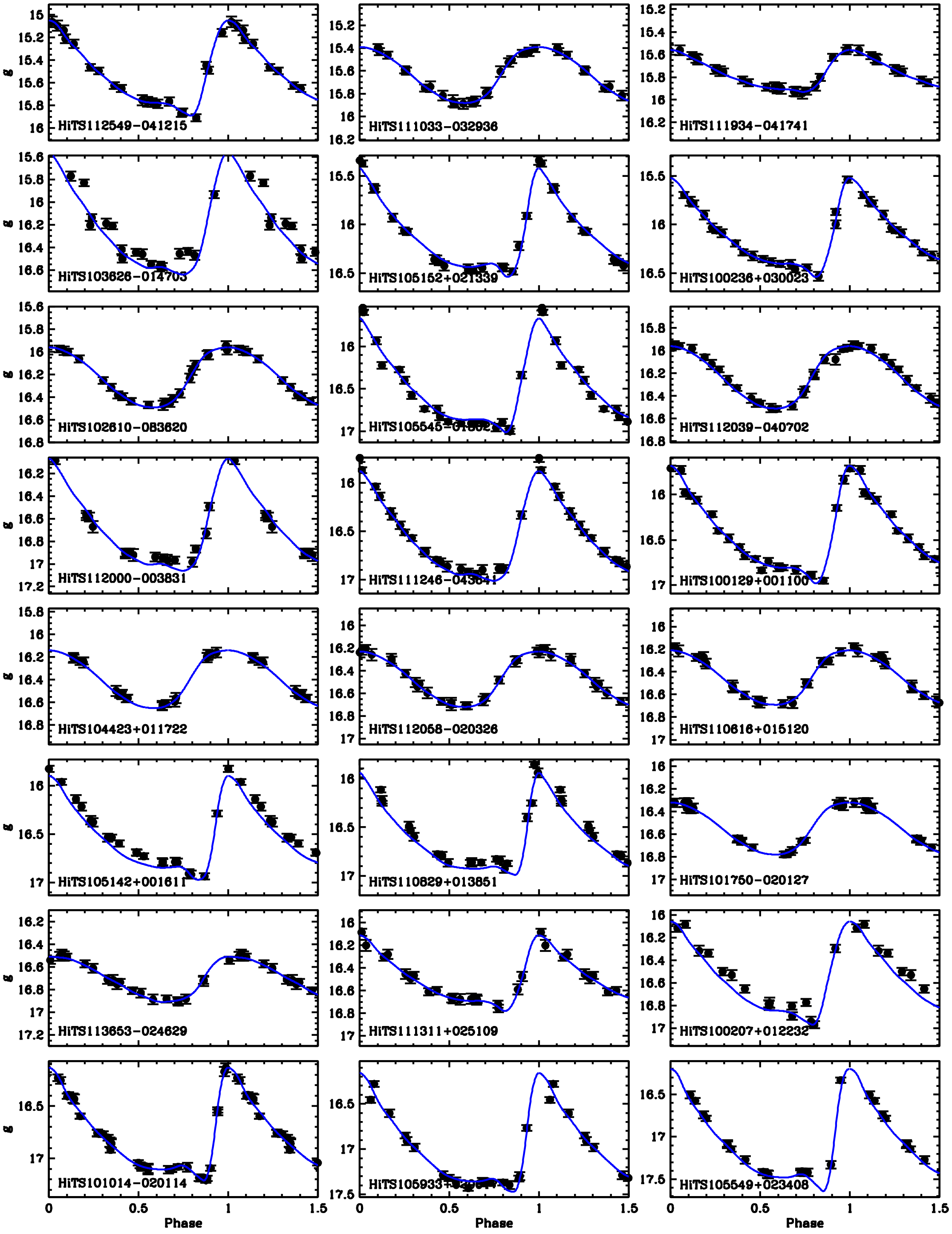

Figure 4.7 Phased lightcurves of nearby (< 90 kpc) RR Lyrae stars in the field, from HiTS 2014 (1/4).

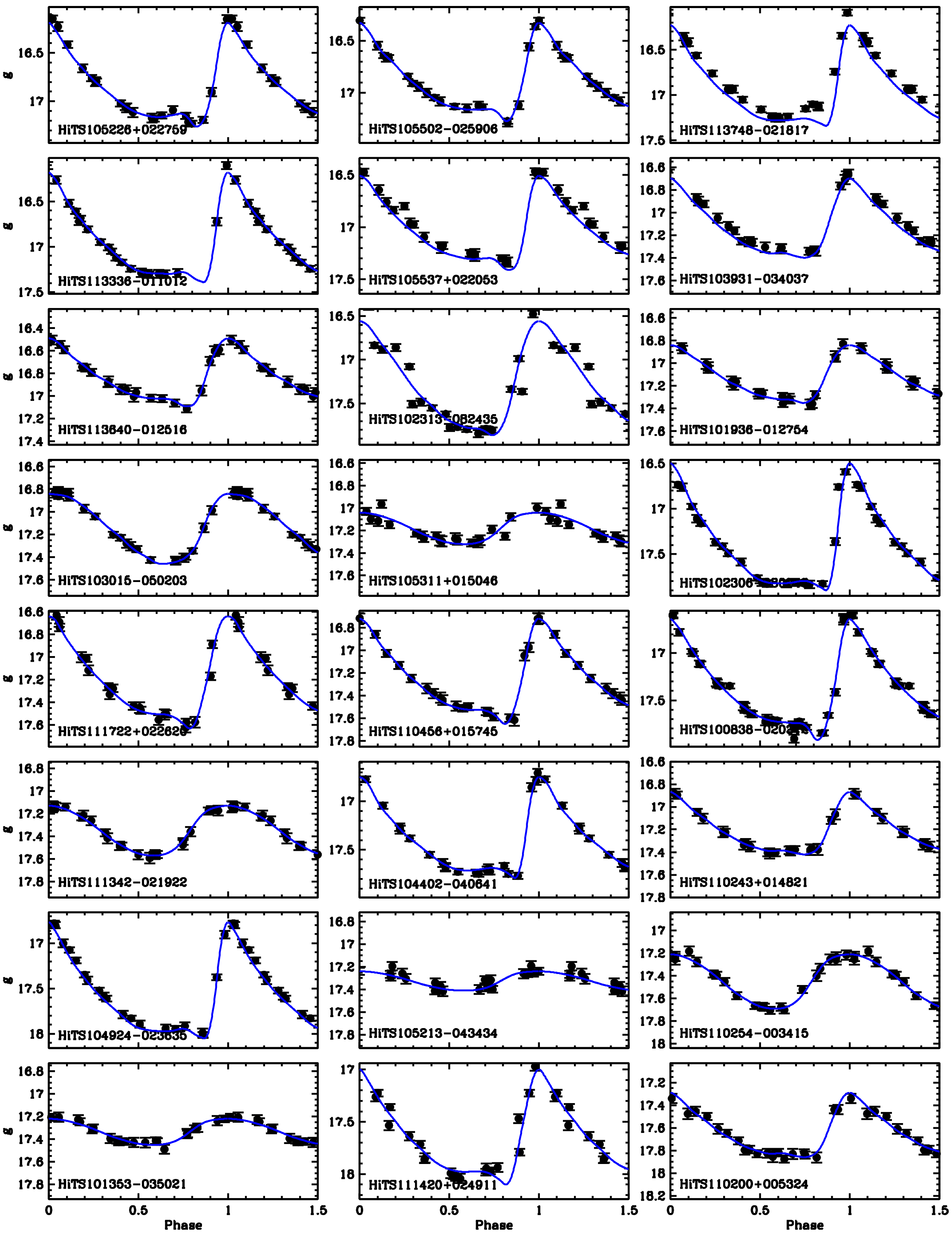

Figure 4.8 Phased lightcurves of nearby (< 90 kpc) RR Lyrae stars in the field, from HiTS 2014 (2/4).

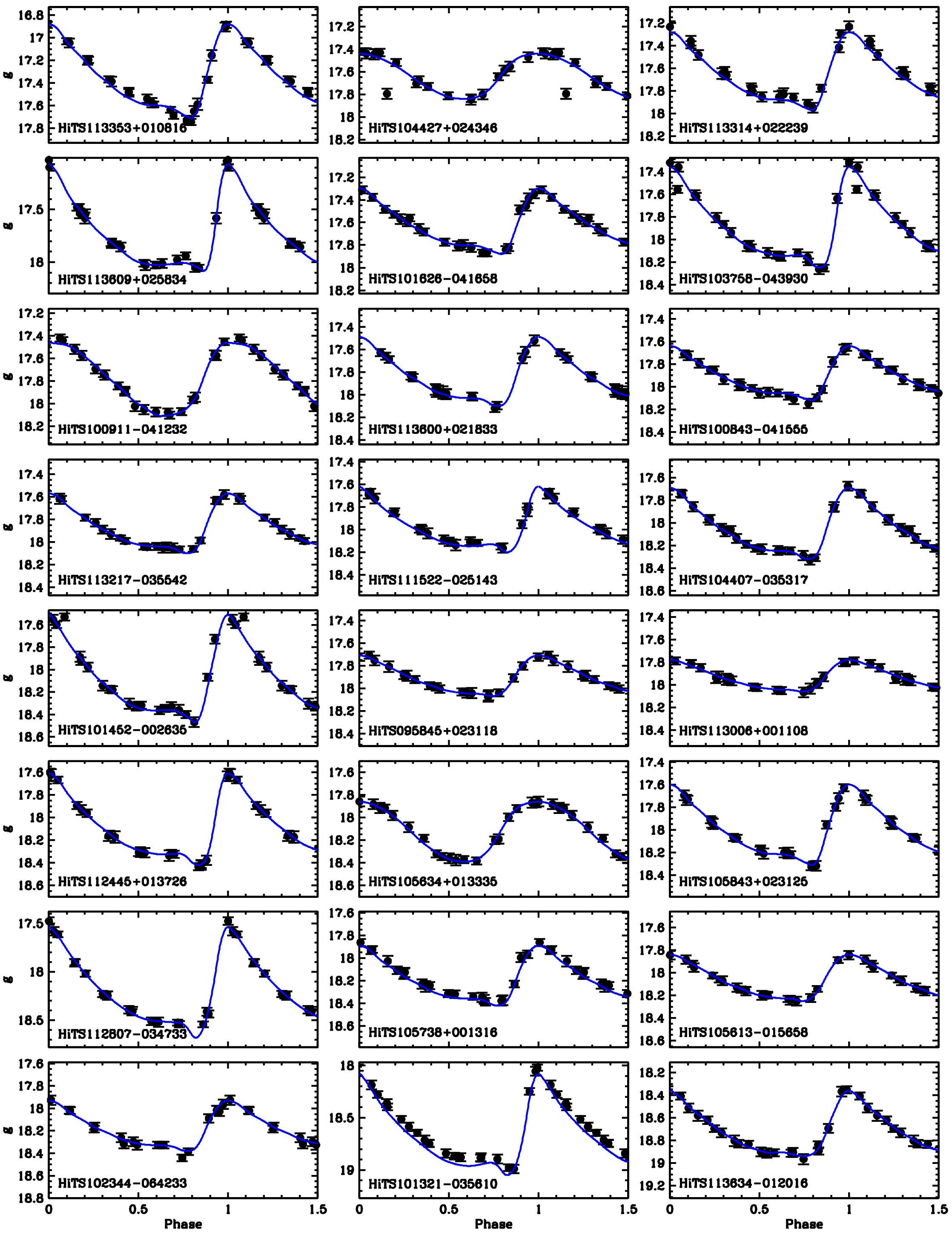

Figure 4.9 Phased lightcurves of nearby (< 90 kpc) RR Lyrae stars in the field, from HiTS 2014 (3/4).

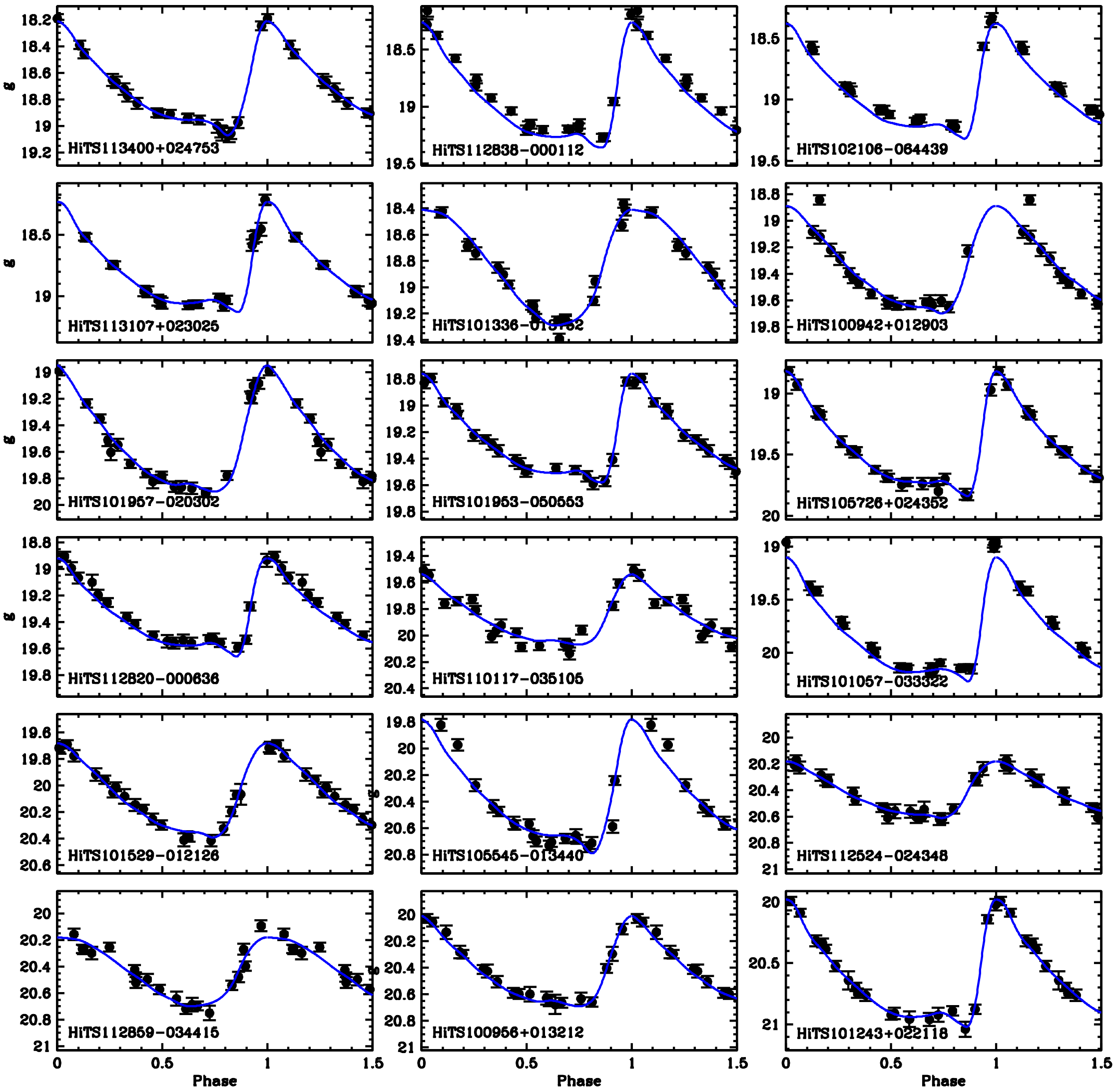

Figure 4.10 Phased lightcurves of nearby (< 90 kpc) RR Lyrae stars in the field, from HiTS 2014 (4/4).

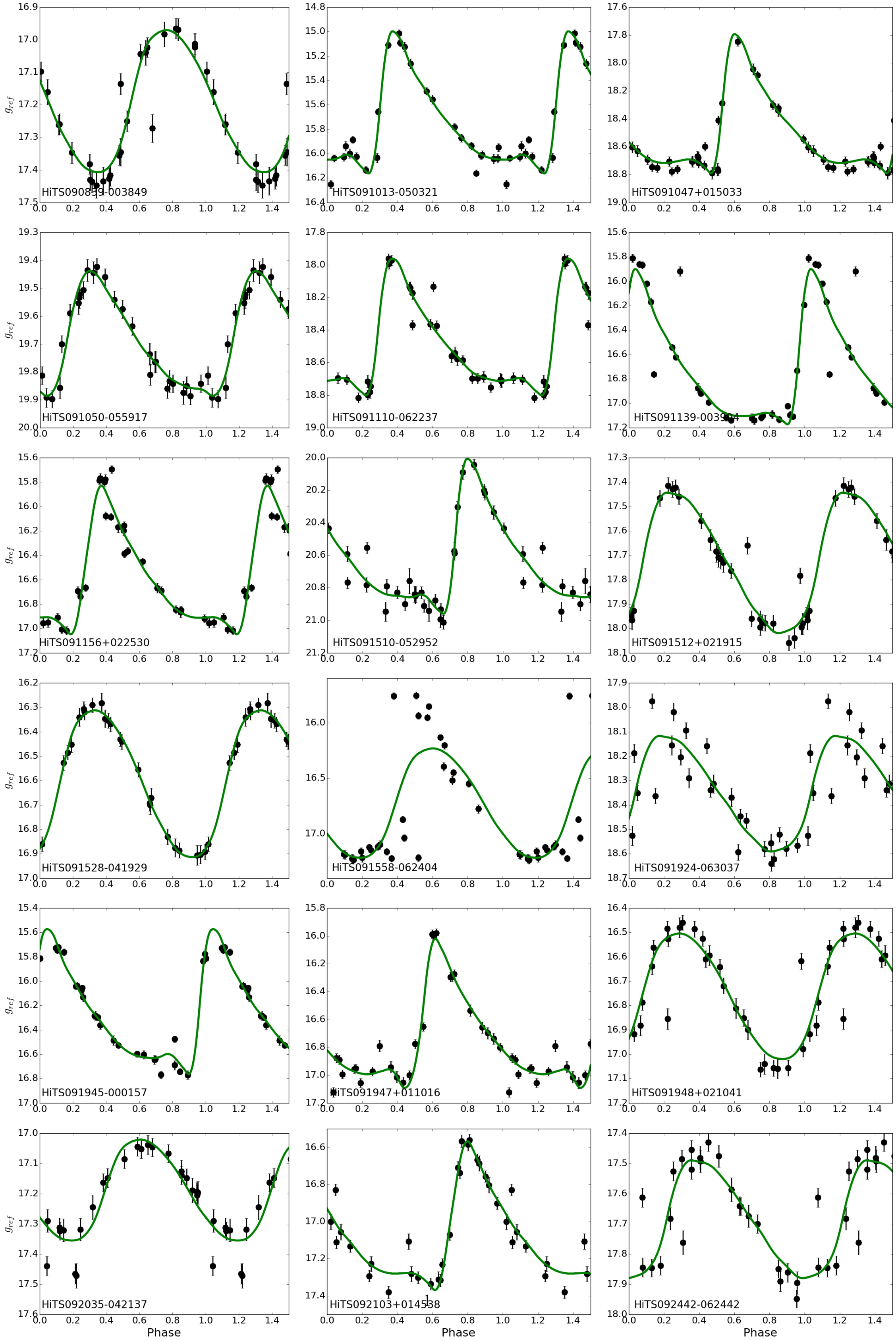

Figure 4.11 Phased lightcurves of RR Lyrae stars from HiTS 2015 exclusively (1/6).

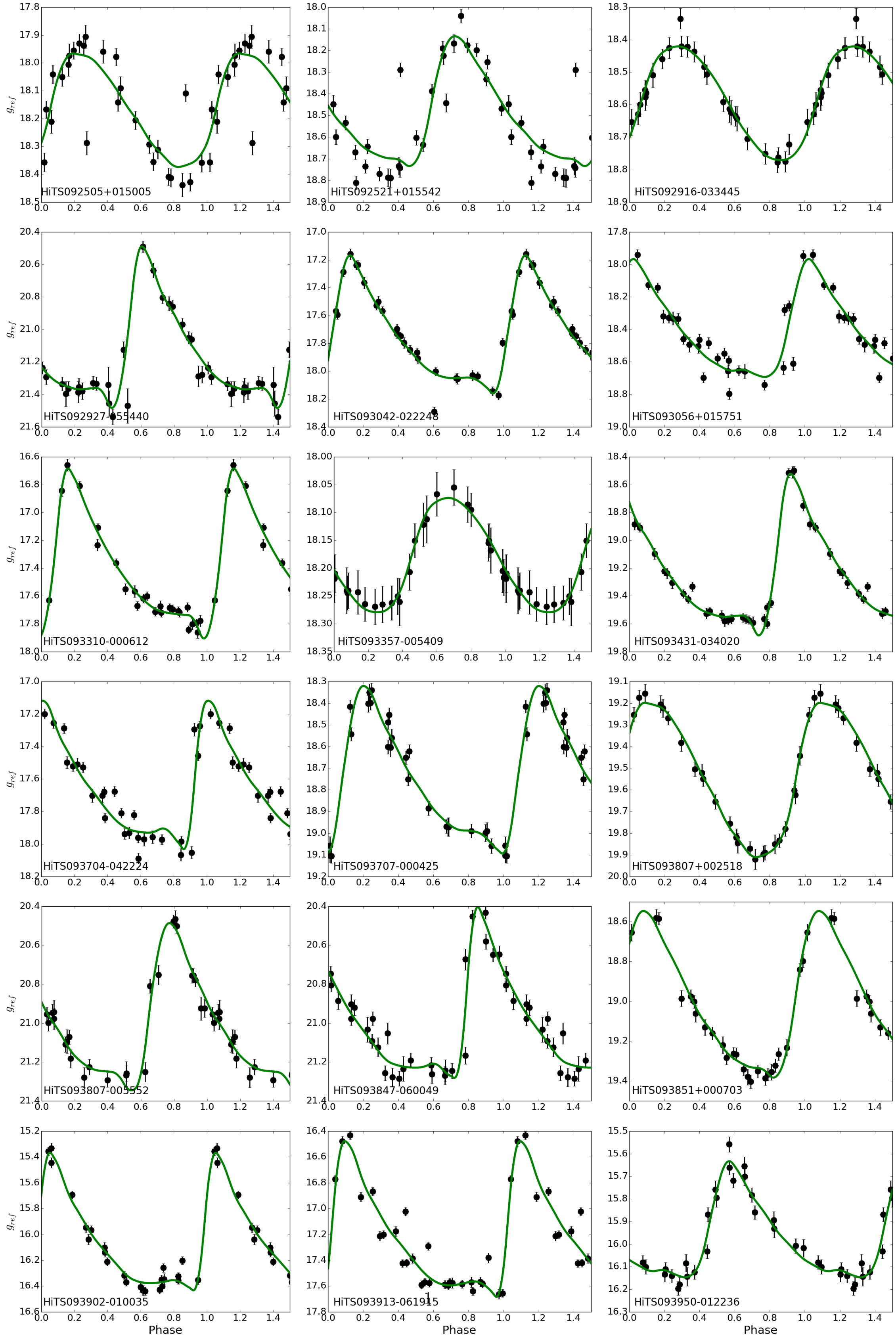

Figure 4.12 Phased lightcurves of RR Lyrae stars from HiTS 2015 exclusively (2/6).

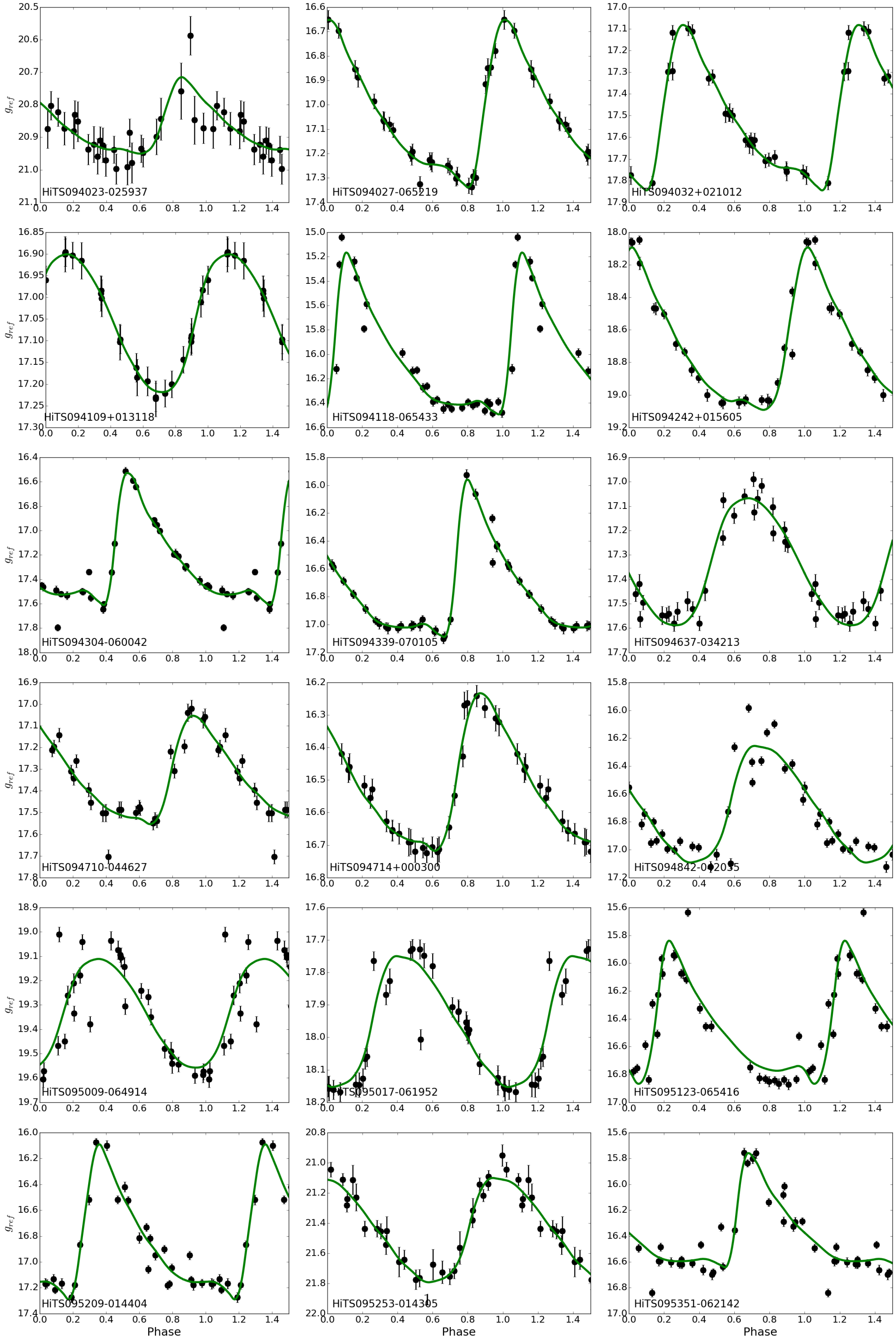

Figure 4.13 Phased lightcurves of RR Lyrae stars from HiTS 2015 exclusively (3/6).

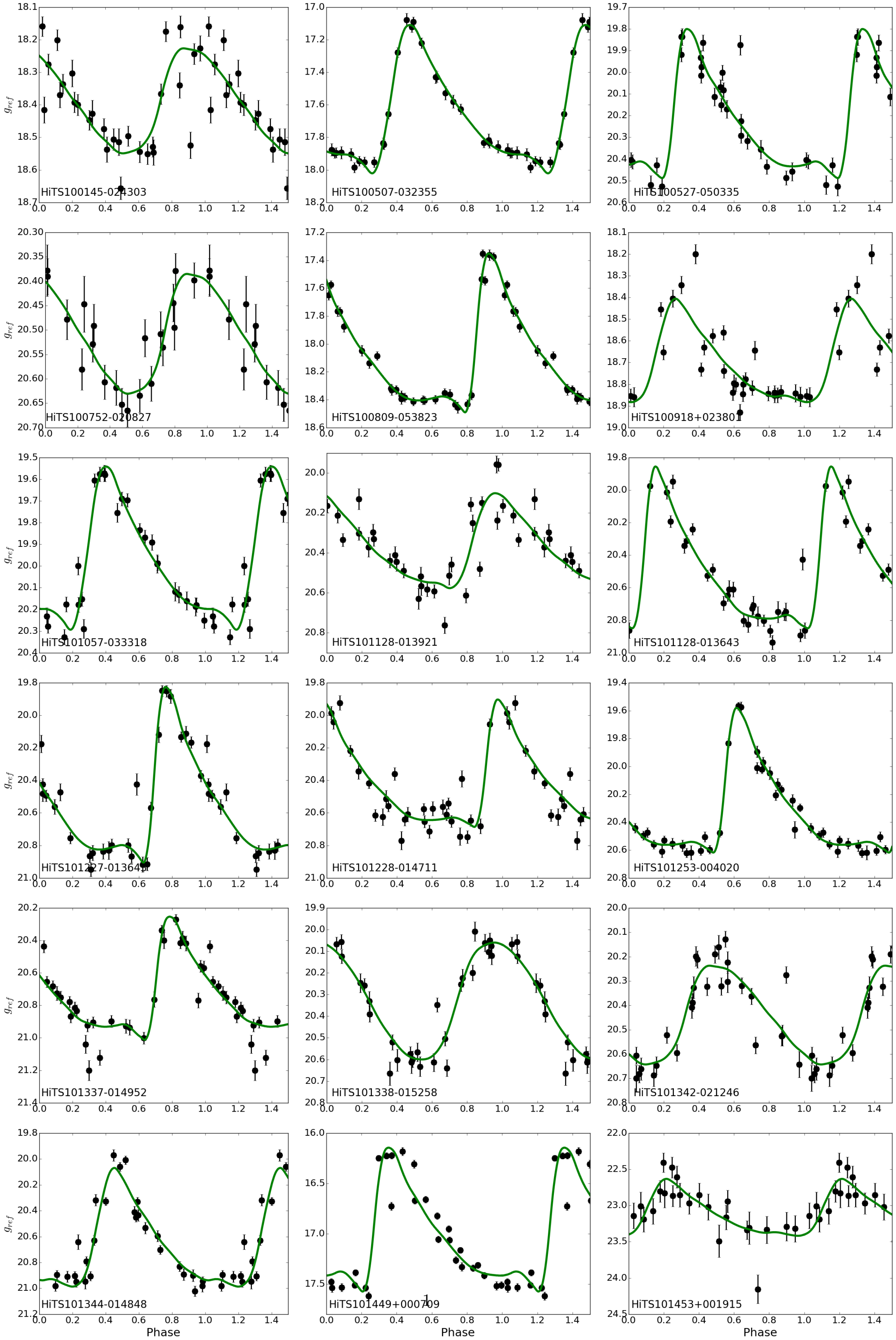

Figure 4.14 Phased lightcurves of RR Lyrae stars from HiTS 2015 exclusively (4/6).

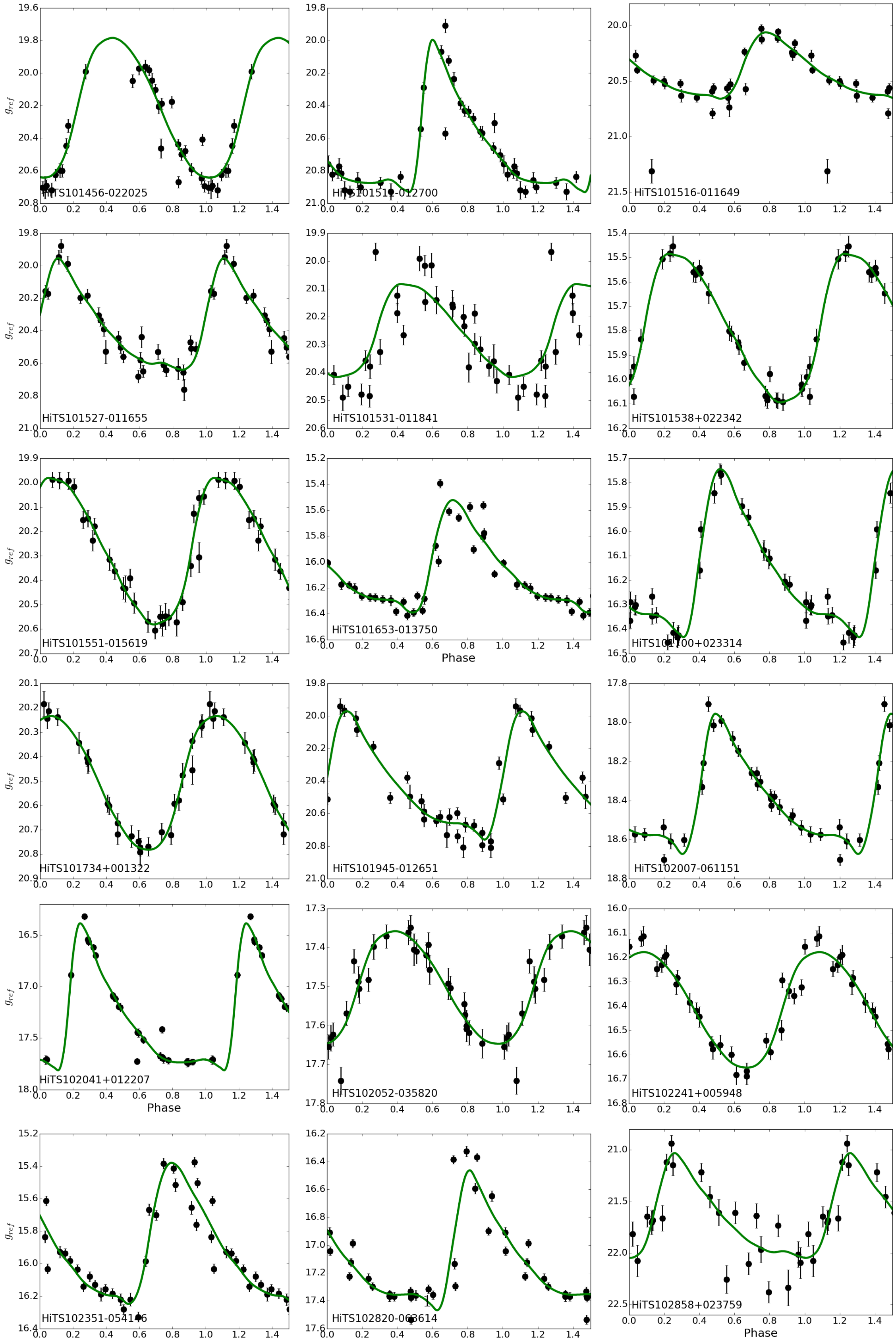

Figure 4.15 Phased lightcurves of RR Lyrae stars from HiTS 2015 exclusively (5/6).

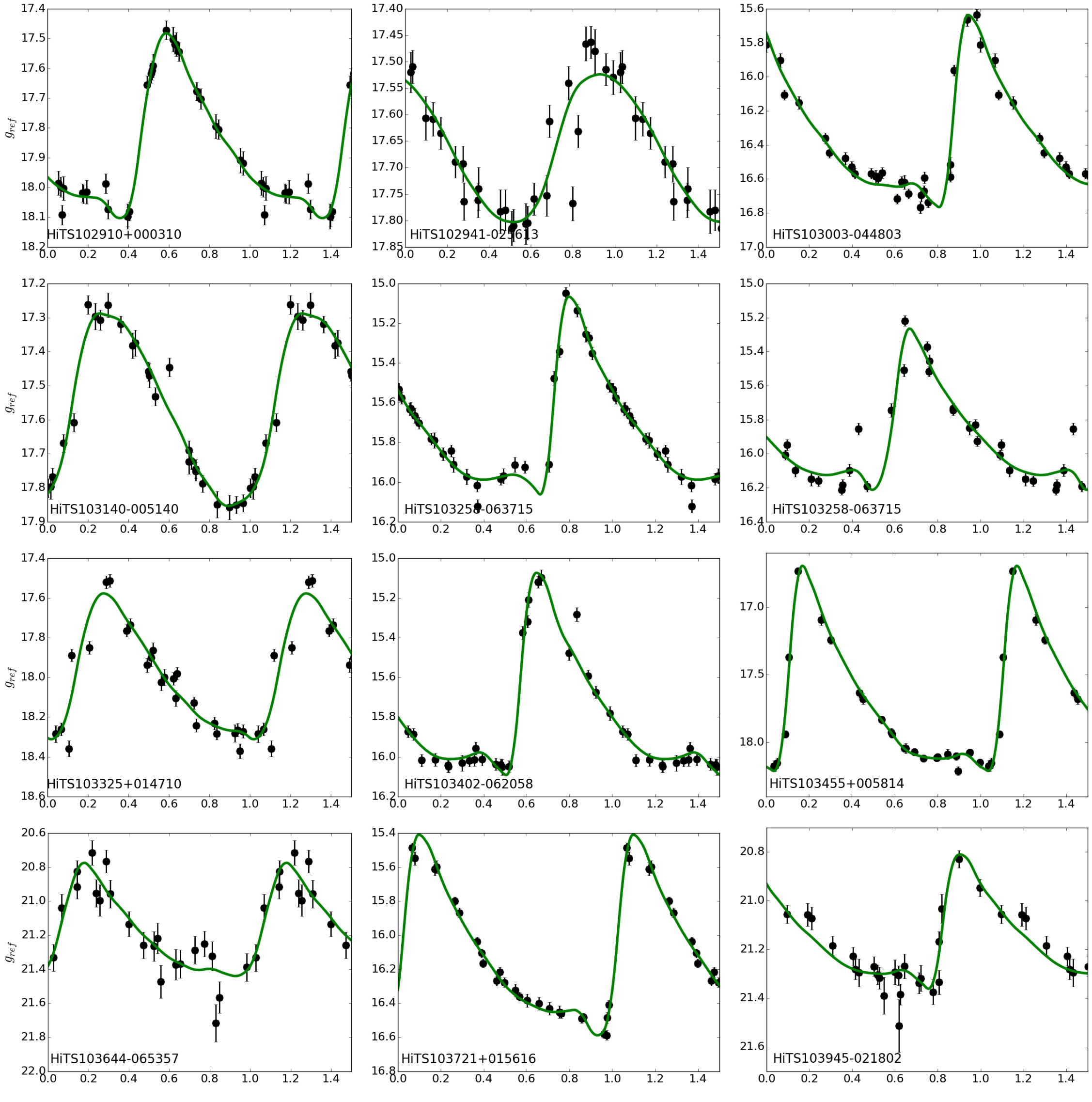

1

Figure 4.16 Phased lightcurves of RR Lyrae stars from HiTS 2015 exclusively (6/6).

Draft version August 2, 2017
Preprint typeset using LaTeX style emulateapj v. 12/16/11

SERENDIPITOUS DISCOVERY OF RR LYRAE STARS IN THE LEO V ULTRA-FAINT GALAXY

Gustavo E. Medina[1,3], Ricardo R. Muñoz[1], A. Katherina Vivas [2], Francisco Förster[3,4], Jeffrey L. Carlin[5], Jorge Martinez[1,4,3], Lluis Galbany[7], Santiago González-Gaitán[4,3], Mario Hamuy[1,3], Thomas de Jaeger[6,3,1], Juan Carlos Maureira[4], Jaime San Martín[4]

Draft version August 2, 2017

ABSTRACT

During the analysis of RR Lyrae stars discovered in the High cadence Transient Survey (HiTS) taken with the Dark Energy Camera at the 4−m telescope at Cerro Tololo Inter-American Observatory, we found a group of three very distant, fundamental mode pulsator RR Lyrae (type *ab*). The location of these stars agrees with them belonging to the Leo V ultra-faint satellite galaxy, for which no variable stars have been reported to date. The heliocentric distance derived for Leo V based on these stars is 173 ± 5 kpc. The pulsational properties (amplitudes and periods) of these stars locate them within the locus of the Oosterhoff II group, similar to most other ultra-faint galaxies with known RR Lyrae stars. This serendipitous discovery shows that distant RR Lyrae stars may be used to search for unknown faint stellar systems in the outskirts of the Milky Way.

Keywords: Galaxy: halo - stars: variables: RR Lyrae - galaxies: individual (Leo V) - Local Group

1. INTRODUCTION

With the advent of large, optical sky surveys like the Sloan Digital Sky Survey (SDSS; York et al. 2000), the Panoramic Survey Telescope And Rapid Response System (Pan-STARSS−1, Chambers et al. 2016) or the Dark Energy Survey (DES; Abbott et al. 2015), over the last decade and a half, a flurry of new Milky Way (MW) satellites have been discovered (e.g., Willman et al. 2005; Belokurov et al. 2006a,b, 2008, 2010; Zucker et al. 2006a,b; Irwin et al. 2007; Bechtol et al. 2015; Koposov et al. 2015; Drlica-Wagner et al. 2015, 2016; Martin et al. 2015). These discoveries are of particular relevance since they allow us to probe the faint end of the galaxy luminosity function and shed new light into known discrepancies between predictions from cosmological simulations and observations. Among these stands the well-known "missing satellites problem" present in ΛCDM models (e.g., Kauffmann et al. 1993; Klypin et al. 1999; Moore et al. 1999; Simon & Geha 2007) wherein hundreds to thousands of low mass subhalos should orbit around the MW but only a few dozen actual dwarf satellites are known. In this context, a reliable census of satellite galaxies, particularly at the faint end, is essential to make progress toward solving these inconsistencies. This has led to focused efforts to discover dwarf galaxies and extremely low luminosity sub-halos, and finding new ways to use the data available from wide and deep field surveys in an efficient way (e.g., Bechtol et al. 2015; Koposov et al. 2015; Baker & Willman 2015).

The detection of variable stars in dwarf satellites has played a major role in the study of their properties and populations. The case of the pulsating RR Lyrae stars (RRLs) is particularly interesting since they are old stars (> 10 Gyr) easily identifiable by the shape of their light curves. In fact, historically the discovery of RRLs in dwarf spheroidal (dSph) galaxies was the first confirmation that these systems contained old, population II stars (e.g., Baade & Hubble 1939; Saha et al. 1986; Siegel 2006). Additionally, these type of variable stars play an important role since they are considered well-known standard candles and therefore provide reliable distances to their host dwarf satellites. In this context, at least one RRL has been reported in every Milky Way's satellite classified as a dwarf galaxy that has been searched for them (see compilation in Vivas et al. 2016), including systems with extremely low luminosity and surface brightness like Segue 1 (Simon et al. 2011) and Segue 2 (Boettcher et al. 2013). This fact has brought forth the idea that RRL can actually be used to discover new stellar systems in the outer halo (Sesar et al. 2014; Baker & Willman 2015; Sanderson et al. 2016), as well as to study the properties of halo substructures (Vivas et al. 2001; Sesar et al. 2013; Drake et al. 2013; Torrealba et al. 2015). Since distant RRLs are rare, these works suggest that they can trace the existence of faint stellar systems (as the light of the lighthouse). In particular, Baker & Willman (2015) suggested that groups of two or more RRLs at heliocentric distances > 50 kpc could reveal stellar systems as faint as $M_V = -3.2$.

In this Letter we describe the serendipitous discovery of variable stars in the Leo V ultra-faint galaxy while studying a sample of distant RRLs from the High cadence Transient Survey (HiTS; Förster et al. 2016). Following Baker & Willman's idea, two close groups of RRLs were recognized in these data. The locations of these groups agreed with the locations of the dwarf satellites Leo IV and Leo V. Variable stars in Leo IV have been identified before by Moretti et al. (2009), but no search so far has been reported in Leo V.

[1] Departamento de Astronomía, Universidad de Chile, Casilla 36-D, Santiago, Chile.
[2] Cerro Tololo Inter-American Observatory, Casilla 603, La Serena, Chile.
[3] Millenium Institute of Astrophysics MAS.
[4] Center for Mathematical Modelling, Universidad de Chile, Av. Blanco Encalada 2120 Piso 7, Santiago, Chile.
[5] LSST, 933 North Cherry Avenue, Tucson, AZ 85721, USA.
[6] Department of Astronomy, University of California, Berkeley, CA 94720-3411, USA
[7] PITT PACC, Department of Physics and Astronomy, University of Pittsburgh, Pittsburgh, PA 15260, USA

Leo V was discovered in SDSS data by Belokurov et al. (2008). It is a faint system, $M_V = -4.4$ (Sand et al. 2012), composed of an old, metal-poor ([Fe/H]$= -2.48$; Collins et al. 2016) stellar population. Based on the observed horizontal branch (HB), the estimates of the distance to Leo V have been set between 175 to 195 kpc (Belokurov et al. 2008; de Jong et al. 2010; Sand et al. 2012). Its closeness with Leo IV in both location in the sky and radial velocity has suggested a possible common origin for both galaxies (Belokurov et al. 2008; de Jong et al. 2010; Blaña et al. 2012). It has also been suggested that the galaxy is undergoing tidal disruption (Belokurov et al. 2008; de Jong et al. 2010; Collins et al. 2016) although Sand et al. (2012) did not find evidence for extra-tidal features in their data. In any case, the detection of RRLs in this work allows the determination of a precise distance to this galaxy which will be useful for future dynamical works to understand the origin of this system and its possible interaction with Leo IV and/or the Milky Way.

The structure of this article is as follows: In §2 the details of the HiTS observations are presented. Properties of the RRLs discovered in Leo V are presented in §3 and finally, a summary and final discussion are addressed in §4. The details of the methodology and analysis of the complete list of distant RR Lyrae stars in the HiTS survey is the topic of a separate paper (Medina et al., in preparation).

2. OBSERVATIONS AND DATA ANALYSIS

The data used in this article were collected between UT 2014 February 28 and UT 2014 March 4 with the Dark Energy Camera (DECam, Flaugher et al. 2015), a prime focus CCD imager installed at the Blanco 4−m telescope at Cerro Tololo Inter-American Observatory (CTIO), as part of the High cadence Transient Survey (HiTS, Förster et al. 2016, hereinafter F16). The survey is focused on the detection of young supernovae with emphasis in the early stages of the explosions. Despite being designed for other purposes, the data can be mined for the study of optical transients in general.

HiTS observed 40 blindly selected fields in 2014 at high Galactic latitudes, covering a total of ∼ 120 square degrees from 150° to 175° in RA and −10° to 3° in DEC (see Figure 4 in F16). These fields were observed on the g SDSS photometric system filter with exposure times varying from 160 seconds (83% of the total) to 174 seconds (14%), and a cadence of two hours. That resulted in a total of 20 epochs for most of the fields, with a limiting apparent magnitude of $23 - 24.5$ (F16). The mean seeing of the survey was 1.5 arcsec. Details on the survey strategy can be found in F16, while the search for RRLs will be detailed in an upcoming paper (Medina et al. in preparation). Here we summarize the most relevant asteps.

The data processing was carried out using the DECam community pipeline (Valdes et al. 2014). Point source photometry was done with the SExtractor photometry software (Bertin & Arnouts 1996). To generate time series, we performed an alignment in x, y position of the SExtractor outputs. Using our second epoch as reference, we compared the instrumental magnitudes of all stars and calculated a zero point offset ($\Delta_{\rm rel}$) on a chip-by-chip basis. Then, the reference scan was calibrated (only by zero point) using overlapping SDSS photometry from DR10 (Ahn et al. 2014). To correct for extinction, we used the re-calibrated dust maps of Schlafly & Finkbeiner (2011), and calculated the extinction values following $A_g = 3.303\, E(B-V)$.

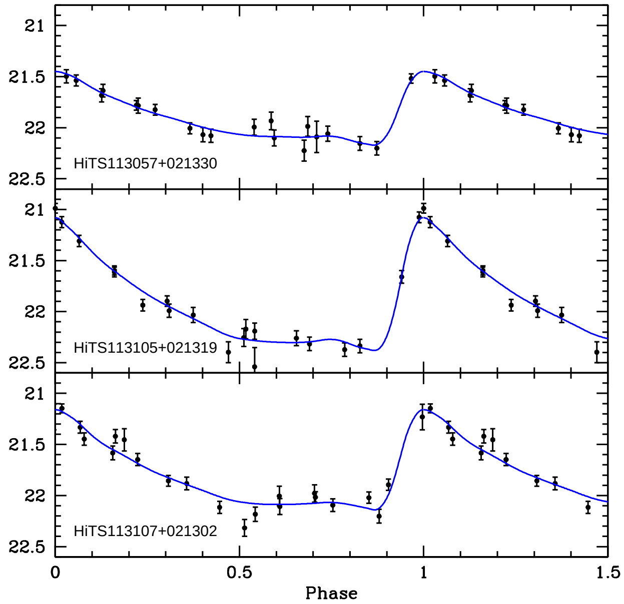

Figure 1. Folded light curves for the three RRLs found in Leo V. The solid blue line is the best fitted template from the library of Sesar et al. (2010). The pulsational properties and distance of these variables are shown in Table 1.

For the detection of RRLs, we filtered out objects with less than five observations, and also stars with low variation in brightness compared with the typical magnitude errors. After that we performed a period search using the Generalized Lomb-Scargle technique (GLS; Zechmeister & Kürster 2009) using an astroML python module developed by VanderPlas et al. (2012). Pre-candidates were selected based on the periods found, where objects with periods shorter than 4.8 hours and longer than 21.6 hours were rejected for being outside the typical pulsation window of RRLs. In this process, we did not consider periods within 0.1 days around 0.33 and 0.50 days to avoid spurious detection attributable to aliasing. Another filter was applied based on the level of significance of the period detection computed by the python module (statistical significance < 0.08 were left out). Following these criteria, we accepted the two most significant periods (if applicable). Finally, the candidates with a difference in magnitude between the brightest and faintest observation larger than 0.2 were visually inspected to make the final catalogue. The pulsation parameters of the light curves were obtained by adjusting RRLs templates from SDSS Stripe 82 (Sesar et al. 2010). For this fitting, small variations around the observed amplitude and GLS period were allowed. We selected the best fit based on a χ^2 minimization criterion. The mean magnitudes of the RRLs were calculated by integrating the transformed fitted template, in intensity units, and transforming back to magnitudes the mean.

We examined the best two periods because aliasing can produce reasonable lightcurves for different peri-

Table 1
Identification number and main properties of the three Leo V's RRL presented in this work.

ID	R.A. (deg)	DEC (deg)	$< g >$	A_g	d_H ([Fe/H]$= -1.6$) (kpc)	d_H ([Fe/H]$= -2.31$) (kpc)	Period (days)	Amplitude g	Type	N
HiTS113057+021330	172.73946	2.22514	21.79 ± 0.08	0.09	166 ± 8	176 ± 9	0.6453	0.72	ab	20
HiTS113105+021319	172.76936	2.22200	21.79 ± 0.08	0.09	166 ± 8	176 ± 9	0.6573	1.34	ab	20
HiTS113107+021302	172.77796	2.21734	21.68 ± 0.08	0.09	158 ± 7	167 ± 8	0.6451	0.99	ab	21

ods. This was indeed the case for one RRL found in Leo V, HiTS113105, for which the second best period, 0.657 days, produced a light curve almost indistinguishable from the main period (a 1-day alias), 1.955 days. We took the 0.657 days period as the correct one as it agrees better with the expectations for RRL stars.

3. RR LYRAE STARS IN LEO V

Theoretical calibrations for the absolute magnitude of RRL stars in the SDSS $g-$band exist in the literature (Marconi et al. 2006; Cáceres & Catelan 2008), but they require knowledge of color information which is not available from our single-band survey. For the same reason, we do not have data to calculate a Johnson V magnitude using known transformation equations like the ones derived by R. Lupton[8]. Thus, we estimated preliminary M_g for our stars by comparing our complete sample of RRL with the ones in the Catalina surveys (Drake et al. 2013, 2014). Distances were computed for the RRLs in the Catalina survey using their mean V magnitudes (corrected by extinction) and assuming [Fe/H]$= -1.6$ as the metallicity for the halo, which yields $< M_V >= 0.55$ (Demarque et al. 2000). We found ~ 50 stars in common between our catalogs and from the known apparent g magnitudes of the stars in our sample, we determined an average absolute g magnitude of $< M_g >= 0.69 \pm 0.06$. We validated this method by comparing the results for a sub-sample of the HiTS RRL stars which belong to the Sextans dSph galaxy. Using the M_g above, we obtained a distance of $d_H = 83 \pm 4$ kpc for this galaxy which agrees well with literature values (e.g., Lee et al. 2009).

From the list of distances obtained for the RRLs detected in the HiTS data we closely analyzed stars beyond 100 kpc with special attention to potential close pairs or groups on the sky, i.e., stars with small angular separation as well as similar distances. A pair and a triplet were obvious in the data, in both cases with angular distances smaller than one degree and a heliocentric distance difference no larger than 10 kpc; one of these groups seemed to coincide with the position and published distance of the Leo V dSph. The stars are identified as HiTS113057+021330, HiTS113105+021319 and HiTS113107+021302 (hereafter HiTS113057, HiTS113105 and HiTS113107). Figure 1 shows the light curves of the three RRLs. No search for variable stars in this galaxy has been reported to date, and thus these are the first RRLs detected in this ultra-faint galaxy.

Figure 2 (*right panel*) shows that, at 0.75 arcmin from the center, only HiTS113107 lies within one half-light radius of the dwarf galaxy (with r_h=1 arcmin, according to Muñoz et al., in preparation). The other two stars lie at 1.26 and 3.05 arcmin (HiTS113057 and HiTS113105 respectively). Although not as centrally located, they are still close enough to be associated with Leo V. Figure 2 (*left panel*) shows a color-magnitude diagram (CMD) of Leo V using data from the Megacam survey by Muñoz et al. (in preparation). The RRLs fall redward of the predominantly blue and sparsely populated blue horizontal branch (BHB), as expected. For reference, a 13 Gyr old, [Fe/H]$= -2.2$ Padova isochrone (Girardi et al. 2004; Bertelli et al. 2008) was visually matched to the blue horizontal branch (BHB) at a distance of 175.4 kpc. We note that in our single-epoch CMD, the three RRLs are located below the BHB, at magnitudes of $g = 22.07, 22.24$ and 22.16, respectively, consistent given their amplitudes with having been observed at fainter phases in their light curves (see Fig. 1). Table 1 summarizes the main properties of the triplet.

We detected another close group, this time of two RRLs, in addition to Leo V. This pair matched the position of the Leo IV dwarf galaxy. In fact, these two RRLs had been previously discovered by Moretti et al. (2009). These authors identified three RRLs in the Leo IV region. It is worth noting that in Medina et al. (in preparation) we estimated the completeness for detecting RRL at these magnitudes to be $\sim 60\%$, which is consistent with the fact that we detected only two of the three RRLs in Moretti et al. (2009).

We looked for other RRL in our sample that lie spatially close to Leo V but at closer distances, with the purpose of checking whether possible anomalous Cepheids have been misclassified as RRLs. We also looked in the region bridging Leo IV and Leo V considering that there is a potential association between the two ultra-faint systems (de Jong et al. 2010; Blaña et al. 2012; Jin et al. 2012). We did not find any other RRL within a radius of $15'$ from the center of Leo V, or connecting both dwarf galaxies. The closest star was HiTS113107+023025, at $17.'4$ but ~ 3 magnitudes brighter than the HB of the galaxy and hence too bright for being an anomalous Cepheid in the galaxy. Also, it is located in the opposite direction to Leo IV, and thus, not in the possible bridge. Stars lying close to the three RRL in the CMD of Leo V shown in Figure 2 (*left panel*) were also inspected, resulting in no additional RRL candidates.

We estimated the distance to the Leo V RRLs in two ways. As mentioned above, using the mean metallicity of the Galactic halo ([Fe/H]$= -1.6$) as a representative value for our sample, we found a mean $g-$band absolute magnitude of $< M_g >= 0.69$. With this value we obtain a mean distance to Leo V of 163 ± 4 kpc. However, it is known that Leo V is significantly more metal-poor than this value. For this reason, a more appropriate estimation should assume a lower metallicity for the RRLs. To address this issue, we re-estimate the mean absolute mag-

[8] `http://www.sdss.org/dr12/algorithms/sdssUBVRITransform/#Lupton2005`

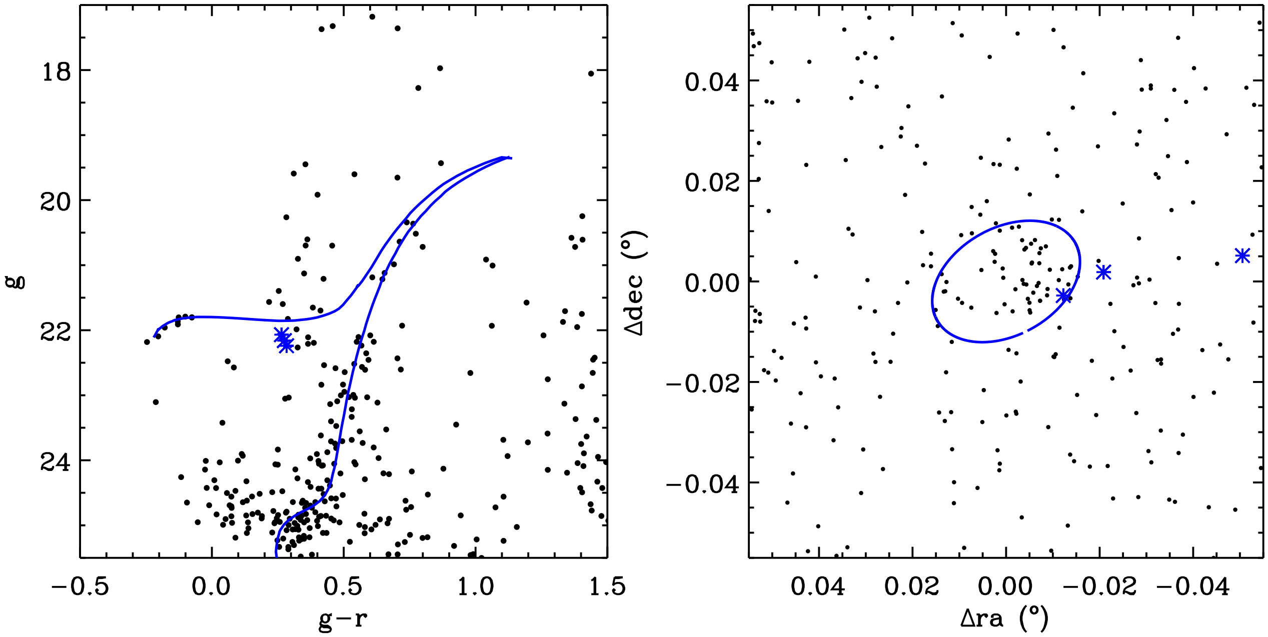

Figure 2. *left panel:* Color-magnitude diagram of the inner five arcmin of Leo V. The blue stars mark the position of the three RRLs. Overplotted is a 13 Gyr old isochrone with [Fe/H]= −2.2, visually matched to the BHB stars at a distance of 175.4 kpc, consistent with the mean distance of 173 ± 5 kpc from the RRLs. *right panel:* Spatial distribution of stars near the center of Leo V. The location of the three RRLs is marked. The ellipse marks the position of Leo V's effective radius (Muñoz et al. in preparation).

nitude of our RRLs using as reference the Leo IV stars in common with Moretti et al. (2009), and assuming their derived distance of 154 ± 5 kpc. Leo IV has a metallicity of [Fe/H]= −2.31 (Simon & Geha 2007), which is very close to the recent value of [Fe/H]= −2.48 found for Leo V by Collins et al. (2016). In this case, we derived $< M_g >= 0.57 \pm 0.07$, which results in a mean heliocentric distance to Leo V of 173 ± 5 kpc. The individual values for the distances are shown in Table 1.

4. DISCUSSION AND CONCLUSIONS

We have used data from the High cadence Transient Survey in the $g-$band and identified the first three RR Lyrae stars known to date in the Leo V ultra-faint galaxy. From the shape and properties of their light curves, we classified these three RRL, HiTS113057+021330, HiTS113105+021319 and HiTS113107+021302, as fundamental mode pulsators ($ab-$type RRL). The periods found for them are 0.6453, 0.6573 and 0.6451 days, respectively, and the amplitudes, according to fitted models, are 0.72, 1.34 and 0.99 mag.

Globular clusters in the MW separate in two groups, (the Oosterhoff, Oo, groups; Oosterhoff 1939), based on both the mean period of their RR Lyrae stars and the proportion between $ab-$type and $c-$type stars. Dwarf spheroidal satellites of the MW do not show such dichotomy and many of them have been classified as Oo-Intermediate systems (Catelan 2009; Catelan & Smith 2015). Most of the ultra-faint dwarf satellites, on the other hand, despite their low number of stars, have been classified as Oo-II systems (Clementini 2014, and references therein), and Leo V seems to follow that behavior based on the mean period of 0.65 days for the three RRLs. Unfortunately, the lack of detected $c-$type RRL in this system does not allow verification of this classification based on the proportion between both type of stars. The properties of the RR Lyrae stars in Leo V supports the view that building blocks like the ultra-faint galaxies contribute to the Oo-II tail of the MW's halo population, but more massive galaxies, with mostly Oo-I population, are needed to reproduce the present day population of RRLs in the halo (Zinn et al. 2014; Fiorentino et al. 2015; Vivas et al. 2016).

In the context of the specific number of RRL in dSphs as a function of magnitude (see Figure 3 from Baker & Willman 2015), we find that Leo V is broadly consistent with what has been seen in other ultra faints (Vivas et al. 2016). However, due to the large dispersion in this correlation, no further conclusions can be drawn just from this additional data.

To derive the distance to Leo IV we anchored our measured $g-$band magnitudes to a known distance to thus calibrate $< M_g >$. In particular, we used data from the low metallicity ultra-faint system Leo IV, similar in metallicity to Leo V. Anchoring our measurements to the RRL stars in Leo IV (Moretti et al. 2009) we obtained a mean heliocentric distance to Leo V of 173 ± 5 kpc. While consistent within the uncertainties, our value lies on the low side of previously published values. In their discovery paper, Belokurov et al. (2008) used data from the 2.5−m INT telescope and estimated a distance of 180 ± 10 kpc to Leo V. de Jong et al. (2010) obtained deep photometry of the Leo IV and V pair with the Calar Alto 3.5−m telescope and determined a heliocentric distance of 175 ± 9 kpc. Sand et al. (2012), on the other hand, based on images taken with the Clay Magellan telescope, derived a much larger distance of 196±15 kpc. The relatively large uncertainties associated to all these measurements are understandable given the sparsely populated Leo V's BHB. These stars are commonly used as distance indicators and do not require time-series observations, but they lack precision compared to RRLs estimations when the BHB is poorly populated and not well defined, as it is the case for the literature data for Leo V.

Baker & Willman (2015) argued that groups of two or more closely spaced RRLs in the halo can reveal the presence of a Galactic satellite beyond 50 kpc. The serendipitous discovery of three RRLs beyond 100 kpc coinciding with the position of the Leo V ultra-faint dwarf is a proof-of-concept for their proposal and opens up the exciting possibility of searching for distant ultra-low luminosity, low surface brightness Milky Way satellites. This possibility becomes even more relevant when looking ahead to projects like the Large Synoptic Survey Telescope (LSST; LSST Science Collaboration et al. 2009); the traditional method for detecting ultra-faint systems based on detecting their major CMD sequences will suffer from significant contamination at the faint end, especially arising from unresolved galaxies, a problem that progressively worsens as we explore the outer regions of the Milky Way halo. Since RRLs lie in a region of the CMD less contaminated by foreground sources, and particularly due to their identification as pulsational sources, the use of these variables as lightposts for ultra-faint systems will be with no doubt of much valuable help in the efforts to obtain a complete census of Galactic satellites up to distances of ~ 400 kpc (Ivezic et al. 2008; Oluseyi et al. 2012).

We thank an anonymous referee for his/her careful reading of this article that helped improve the manuscript. G.M. and F.F. acknowledges support from the Ministry of Economy, Development, and Tourism's Millennium Science Initiative through grant IC120009, awarded to The Millennium Institute of Astrophysics (MAS), and from Conicyt through the Fondecyt Initiation into Research project No. 11130228. G.M. acknowledges CONICYT-PCHA/MagísterNacional/2016-22162353. R. R. M. acknowledges partial support from BASAL Project PFB-06 as well as FONDECYT project N°1170364. F.F. acknowledges support from BASAL Project PFB–03 and through the Programme of International Cooperation project DPI20140090. L.G. was supported in part by the US National Science Foundation under Grant AST-1311862. SGG also acknowledges support from the Ministry of Economy, Development, and Tourisms Millennium Science Initiative through grant IC120009, awarded to The Millennium Institute of Astrophysics (MAS). We acknowledge support from Conicyt through the infrastructure Quimal project No. 140003. Powered@NLHPC: this research was partially supported by the supercomputing infrastructure of the NLHPC (ECM-02). This project used data obtained with the Dark Energy Camera (DECam), which was constructed by the Dark Energy Survey (DES) collaboration. Funding for the DES Projects has been provided by the DOE and NSF (USA), MISE (Spain), STFC (UK), HEFCE (UK). NCSA (UIUC), KICP (U. Chicago), CCAPP (Ohio State), MIFPA (Texas A&M), CNPQ, FAPERJ, FINEP (Brazil), MINECO (Spain), DFG (Germany) and the collaborating institutions in the Dark Energy Survey, which are Argonne Lab, UC Santa Cruz, University of Cambridge, CIEMAT-Madrid, University of Chicago, University College London, DES-Brazil Consortium, University of Edinburgh, ETH Zurich, Fermilab, University of Illinois, ICE (IEEC-CSIC), IFAE Barcelona, Lawrence Berkeley Lab, LMU Munchen and the associated Excellence Cluster Universe, University of Michigan, NOAO, University of Nottingham, Ohio State University, University of Pennsylvania, University of Portsmouth, SLAC National Lab, Stanford University, University of Sussex, and Texas A&M University.

REFERENCES

Abbott, T., Abdalla, F. B., Alleksic, J. et al. 2016, MNRAS, 460, 1270
Ahn, C. P., Alexandroff, R., Allende Prieto, C., et al. 2014, ApJS, 211, 17
Baade, W. & Hubble, E. 1939, PASP, 51, 40
Baker, M., & Willman, B. 2015, AJ, 150, 160
Bechtol, K., Drlica-Wagner, A., Balbinot, E., et al. 2015, ApJ, 807, 50
Belokurov, V., Zucker, D. B., Evans, N. W., et al. 2006, ApJ, 647, L111
Belokurov, V., Zucker, D. B., Evans, N. W., et al. 2006, ApJ, 642, L137
Belokurov, V., Walker, M. G., Evans, N. W., et al. 2008, ApJ, 686, L83
Belokurov, V., Walker, M. G., Evans, N. W., et al. 2010, ApJ, 712, L103
Bertelli G., Girardi L., Marigo P., et al. 2008, A&A, 484, 815
Bertin, E., & Arnouts, S. 1996, A&AS, 117, 393
Blaña, M., Fellhauer, M., & Smith, R. 2012, A&A, 542, A61
Boettcher, E., Willman, B., Fadely, R., et al. 2013, AJ, 146, 94
Cacciari, C., & Clementini, G. 2003, in Stellar Candles for the Extragalactic Distance Scale, ed. D. Alloin & W. Gieren (Lecture Notes in Physics, Vol. 635; Berlin: Springer), 105
Cáceres, C., & Catelan, M. 2008, ApJS, 179, 242
Catelan, M. 2009, Ap&SS, 320, 261
Catelan, M., & Smith, H. A. 2015, Pulsating Stars (New York: Wiley, VCH)
Chambers, K. C., Magnier, E. A., Metcalfe, N., et al. 2016, arXiv:1612.05560
Clementini, G. 2010, in Variable Stars, the Galactic Halo and Galaxy Formation, ed. C. Sterken, N. Samus, & L. Szabados (Russia: Sternberg Astronomical Institute of Moscow Univ.), 107
Clementini, G. 2014, in Proc. IAU Symp. 301, Precision Asteroseismology,ed. J. A. Guzik et al. (Cambridge: Cambridge Univ. Press), 129
Collins, M. L. M., Tollerud, E. J., Sand, D. J., et al. 2016, arXiv:1608.05710
de Jong, J. T. A., Martin, N. F., Rix, H.-W., et al. 2010, ApJ, 710, 1664
Demarque, P., Zinn, R., Lee, Y.-W., et al. 2000, AJ, 119, 1398
Diehl, H. T., Abbott, T. M. C., Annis, J., et al. 2014, Proc. SPIE, 9149, 0
Drake, A. J., Catelan, M., Djorgovski, S. G., et al. 2013, ApJ, 763, 32
Drake, A. J., Catelan, M., Djorgovski, S. G., et al. 2013, ApJ, 765, 154
Drake, A. J., Graham, M. J., Djorgovski, S. G., et al. 2014, ApJS, 213, 9
Drlica-Wagner, A., Bechtol, K., Rykoff, E. S., et al. 2015, ApJ, 813, 109
Drlica-Wagner, A., Bechtol, K., Allam, S., et al. 2016, ApJ, 833, L5
Fiorentino, G., Bono, G., Monelli, M., et al. 2015, ApJ, 798, L12
Flaugher, B., Diehl, H. T., Honscheid, K., et al. 2015, AJ, 150, 150
Förster, F., Maureira, J. C., San Martín, J., et al. 2016, ApJ, 832, 155
Girardi, L., Grebel, E. K., Odenkirchen, M., et al. 2004, A&A, 422, 205
Irwin, M. J., Belokurov, V., Evans, N. W., et al. 2007, ApJ, 656, L13
Ivezic, Z., Tyson, J. A., Abel, B., et al. 2008, arXiv:0805.2366
Jin, S., Martin, N., de Jong, J., et al. 2012, in ASP Conf. Ser. 458, Galactic Archaeology: Near-Field Cosmology and the Formation of the Milky Way, ed. W. Aoki, M. Ishigaki, T. Suda, T. Tsujimoto, & N. Arimoto (San Francisco, CA: ASP), 153

Kauffmann, G., White, S. D. M., & Guiderdoni, B. 1993, MNRAS, 264, 201

Klypin, A., Kravtsov, A. V., Valenzuela, O., et al. 1999, ApJ, 522, 82

Koposov, S.E., Belokurov, V., Torrealba, G., et al. 2015a, ApJ, 805, 130

Lee, M. G., Yuk, I.-S., Park, H. S., et al. 2009, ApJ, 703, 692

Lomb, N. R. 1976, Ap&SS, 39, 447

LSST Science Collaboration, Abell, P. A., Allison, J., et al. 2009, arXiv:0912.0201

Marconi, M., Cignoni, M., Di Criscienzo, M., et al. 2006, MNRAS, 371, 1503

Martin, N. F., Nidever, D. L., Besla, G., et al. 2015, ApJ, 804, L5

Molnár, L., Pál, A., Plachy, E., et al. 2015, ApJ, 812, 2

Moore, B., Ghigna, S., Governato, F., et al. 1999, ApJ, 524, L19

Moretti, M. I., Dall'Ora, M., Ripepi, V., et al. 2009, ApJ, 699, L125

Oluseyi, H. M., Becker, A. C., Culliton, C., et al. 2012, AJ, 144, 9

Oosterhoff, P. T. 1939, The Observatory, 62, 104

Saha, A., Monet, D. G., & Seitzer, P. 1986, AJ, 92, 302

Sand, D. J., Strader, J., Willman, B., et al. 2012, ApJ, 756, 79

Sanderson, R. E., Secunda, A., Johnston, K. V., et al. 2016, arXiv:1609.06406

Scargle, J. D. 1982, ApJ, 263, 835

Schlafly, E. F., & Finkbeiner, D. P. 2011, ApJ, 737, 103

Schlegel, D. J., Finkbeiner, D. P., & Davis, M. 1998, ApJ, 500, 525

Sesar, B., Ivezić, Ž., Grammer, S. H., et al. 2010, ApJ, 708, 717

Sesar, B., Ivezić, Ž., Stuart, J. S., et al. 2013, AJ, 146, 21

Sesar, B., Banholzer, S. R., Cohen, J. G., et al. 2014, ApJ, 793, 135

Siegel, M. H. 2006, ApJ, 648, L83

Simon, J. D., & Geha, M. 2007, ApJ, 670, 313

Simon, J. D., Geha, M., Minor, Q. E., et al. 2011, ApJ, 733, 46

Torrealba, G., Catelan, M., Drake, A. J., et al. 2015, MNRAS, 446, 2251

Valdes, F., Gruendl, R., & DES Project. 2014, in ASP Conf. Ser. 485, Astronomical Data Analysis Software and Systems XXIII, ed. N. Manset, & P. Forshay (San Francisco, CA: ASP), 379

VanderPlas, J., Connolly, A. J., Ivezic, Z., et al. 2012, in Proc. Conf. Intelligent Data Understanding (CIDU), ed. K. Das, N. V. Chawla, & A. N. Srivastava (Boulder, CO: NCAR), 47

Vivas, A. K., Zinn, R., Andrews, P., et al. 2001, ApJ, 554, L33

Vivas, A. K., Olsen, K., Blum, R., et al. 2016, AJ, 151, 118

Walker, M. G., Mateo, M., & Olszewski, E. W. 2009, AJ, 137, 3100

Willman, B., Blanton, M. R., West, A. A., et al. 2005, AJ, 129, 2692

York, D. G., Adelman, J., Anderson, J. E., Jr., et al. 2000, AJ, 120, 1579

Zechmeister, M., Kürster, M. 2009, A&A, 496, 577

Zinn, R., Horowitz, B., Vivas, A. K., et al. 2014, ApJ, 781, 22

Zucker, D. B., Belokurov, V., Evans, N. W., et al. 2006, ApJ, 643, L103

Zucker, D. B., Belokurov, V., Evans, N. W., et al. 2006, ApJ, 650, L41

Appendix D : Medina et al. (2017b), submitted

Draft version December 13, 2017
Preprint typeset using LATEX style emulateapj v. 12/16/11

DISCOVERY OF DISTANT RR LYRAE STARS IN THE MILKY WAY USING DECAM

Gustavo E. Medina[1,2], Ricardo R. Muñoz[1], A. Katherina Vivas [3], Jeffrey L. Carlin[4], F. Förster[2,5], J. Martínez[1,5,2], L. Galbany[6], S. González-Gaitán[5,3,7], M. Hamuy[1,2], Th. de Jaeger[8,2,1], J.C. Maureira[5], J. San Martín[5]

Draft version December 13, 2017

ABSTRACT

We report the discovery of distant RR Lyrae stars, including the most distant known in the Milky Way, using data taken with the Dark Energy Camera as part of the High cadence Transient Survey (HiTS; 2014 campaign). The search was carried out in the $g-$band and we detect a total of 173 RR Lyrae stars over a $\sim 120\,\mathrm{deg}^2$ area, which includes both known RR Lyrae stars and new detections. The heliocentric distances d_H of the full sample range from 9 to > 200 kpc, with 18 of them beyond 90 kpc. We identify three sub-groups of RR Lyrae as members of known systems: one corresponding to the Sextans dwarf spheroidal galaxy, for which we report 46 new discoveries, and two groups related to the ultra-faint dwarf galaxies Leo IV and Leo V, respectively. Using the full sample and a Markov Chain Monte Carlo analysis, we fit spherical and ellipsoidal profiles of the form $\rho(R) \sim R^n$ to the radial density distribution in the Galactic halo up to ~ 145 kpc from the Sun. The best fit was obtained in the spherical case, for which we obtain a simple power-law index of $n = -4.17^{+0.18}_{-0.20}$, in agreement with previous results made with samples covering shorter distances. The pulsational properties of the outermost RR Lyrae stars in the sample ($d_h > 90$ kpc) differ from the ones in the halo population at closer distances. The distribution of the stars in a Period-Amplitude diagram suggest they belong to Oosterhoff intermediate or Oosterhoff II groups, similar to what is found in the ultra faint dwarf satellites around the Milky Way. The new distant stars discovered represent an important addition to the few existing tracers of the Milky Way potential in the outer halo.

Keywords: Galaxy: halo - Galaxy: stellar content - Galaxy: structure - stars: variables: RR Lyrae

1. INTRODUCTION

The outermost regions of the Milky Way (MW) halo are key probes of the recent assembly history of our Galaxy. Models suggest that stars in the outer halo (beyond Galactocentric radii of $R_\mathrm{GC} \gtrsim 100$ kpc) likely originated in relatively recently-accreted satellite galaxies (e.g., Bullock & Johnston 2005; Zolotov et al. 2009). While current models of galaxy formation generate specific predictions of the amount of stellar substructure in the outermost part of the halo, these have been hard to explore because of the lack of deep, large area surveys of tracers with reliable distance estimates. Because RR Lyrae pulsational variable stars (RRLs) are easily identified in time-series data, are intrinsically bright, and follow well-known period-luminosity relations, they provide a means of mapping the distant halo at distances beyond $d \gtrsim 100$ kpc. Sanderson et al. (2017) predicted that different accretion histories of 12 synthetic halos (from Bullock & Johnston 2005) yield populations of $2,000 - 10,000$ RRLs between $100 < d < 300$ kpc in the MW halo, with roughly half of these in intact dwarf galaxies, and half unbound from their parent satellite.

The accreted dwarfs that are expected to have contributed their stellar populations to the MW halo imprint evidence of the MW's accretion history in the radial stellar density profile. Studies of the halo density profile with various tracers (e.g. Saha 1985; Vivas & Zinn 2006; Watkins et al. 2009; Deason et al. 2011; Sesar et al. 2011; Akhter et al. 2012, summarized later in Table 4) have found widely varying stellar density slopes at large radii, making it difficult to place the MW in a broader context. The discrepancies may be due in part to small samples, especially at large distances from the Galactic center. The addition of outer halo stars is vital to anchor density profile fits in regions of the Galaxy where recent accretion should dominate, and where long dynamical times preserve a record of the accretion events. Simulations also suggest that there is a clear difference in the behavior of the inner and outer halo number density profiles, probably driven by different formation processes (see e.g., Bullock & Johnston 2005). The inner halo is thought to contain both accreted and formed in-situ populations, while the stellar component of the outer halo seems to be formed mainly by accretion events (Zinn 1993; Bullock & Johnston 2005; Carollo et al. 2007; Abadi et al. 2006; Zolotov et al. 2009). There is possible evidence for the different formation pathways of the inner/outer halo in the form of a break in the radial number density profile of MW stars near 25 kpc from the Galactic center (see e.g., Saha 1985; Watkins et al. 2009; Deason et al. 2011; Sesar et al. 2011). However, the behavior of the MW's radial density profile at Galactocentric distances

---

[1] Departamento de Astronomía, Universidad de Chile, Casilla 36-D, Santiago, Chile.
[2] Millenium Institute of Astrophysics MAS.
[3] Cerro Tololo Inter-American Observatory, National Optical Astronomy Observatory, Casilla 603, La Serena, Chile.
[4] LSST, 950 North Cherry Avenue, Tucson, AZ 85719, USA.
[5] Center for Mathematical Modelling, Universidad de Chile, Av. Blanco Encalada 2120 Piso 7, Santiago, Chile.
[6] PITT PACC, Department of Physics and Astronomy, University of Pittsburgh, Pittsburgh, PA 15260, USA.
[7] CENTRA, Instituto Superio Técnico, Universidade de Lisboa, Portugal
[8] Department of Astronomy, University of California, Berkeley, CA 94720-3411, USA.

($R_{\rm GC}$) beyond 80 kpc is a subject that has not been covered with similar depth, mainly due to incompleteness in current surveys at large distances.

Furthermore, the most distant stars are vital tracers for the estimation of the total mass of the MW. Detailed predictions (e.g., the number and luminosity function of satellites) for MW-like galaxies extracted from cosmological models for comparison with observations are highly sensitive to the total mass of the host halo (e.g., Geha et al. 2017); thus, determining a reliable total mass for our Galaxy becomes essential if one wishes to use it as a cosmological laboratory. Unfortunately, the total mass of the MW within 150 kpc is known only within a factor of two (e.g., Eadie & Harris 2016; Ablimit & Zhao 2017). Mass modeling of the MW halo is most strongly constrained by tracers in the outermost regions; RRLs are thus valuable probes of the Galactic potential because they can be found at large distances, and their distances can be determined to better than $\sim$ 10% with ground-based data.

Regarding remote Milky Way stars, only a small number has been detected at heliocentric distances ($d_{\rm H}$) larger than 100 kpc. A summary can be found in Bochanski et al. (2014). In that study the authors reported the discovery of the two most distant MW stars known to date, with estimated distances larger than 200 kpc and classified as M giants. These stars are intrinsically bright which makes them good tracers of halo structure at large distances, but the distance estimations suffer from significant uncertainties (Bochanski et al. 2014 adopted 25% distance uncertainties). Other distance tracers such as pulsational variables have been commonly used to map the Galactic halo over a wide range of distances. RR Lyrae stars, for example, have been identified from a few parsecs to beyond 100 kpc (e.g., Watkins et al. 2009; Drake et al. 2013b; Sesar et al. 2017b, reaching $d_{\rm H} \sim 115$ kpc). RRLs are old, metal-poor pulsating variables that are considered standard candles in the same way but not as luminous as Cepheids. The light curves of these variables have very characteristic shapes and they are usually classified into two main groups: *ab* and *c*-type RRLs. The first class (RRab) are fundamental mode pulsators, with saw-tooth shaped light curves and a negative correlation between their amplitudes and periods, which are known to be of the order of 0.6 days. RRc, on the other hand, pulsate on the first overtone and display more sinusoidal light curves. The later have in general shorter periods ($\sim$ 0.35 days) and smaller amplitudes compared to RRab.

The discovery of groups of RRLs at medium to large distances has become particularly important for the physical description of substructures in the inner and outer halo. Some examples are the discovery and characterization of the Sagittarius stellar tidal stream (Vivas et al. 2001; Vivas & Zinn 2006; Prior et al. 2009; Watkins et al. 2009; Sesar et al. 2010, 2017b; Drake et al. 2013a; Zinn et al. 2014), the Virgo stellar stream (Duffau et al. 2006; Vivas et al. 2016; Sesar et al. 2017b), the Pisces overdensity (Sesar et al. 2010), or the Gemini stream that extends beyond 100 kpc (Drake et al. 2013b), among others. However, the discovery of very distant, isolated stars in the halo brings out questions related to the understanding of their origin. Since they are not expected to have formed in the outskirts of the halo, the origin of distant stars is generally thought to be either the gravitational interaction between the Milky Way and its satellites or the ejection from the center (or disk) of the Galaxy (Bullock & Johnston 2005; Brown et al. 2005; Zolotov et al. 2009). Simulations suggest that it is possible to reproduce important stellar halo properties (the break in the density profiles for instance) taking only accretion events into consideration (Deason et al. 2013). In this context, an interesting suggestion regarding the origin of distant RRL comes from evidence that all known Milky Way's dwarf galaxies have at least one RRL (Boettcher et al. 2013; Vivas et al. 2016). This would make RRL potential tracers of faint satellite systems in the outer halo. Indeed, based on the data presented in this work, Medina et al. (2017) recognized the presence of the ultra faint dwarf galaxies Leo IV and Leo V based on compact groups of distant RRLs.

To date, large RRLs catalogs have been constructed using data from different variability surveys that map different parts of the halo. Among them, the Quasar Equatorial Survey Team (QUEST) RRL catalog (Vivas et al. 2004) contains 457 objects with $V < 19.5$, and subsequently with La Silla QUEST Southern Hemisphere Variability Survey (LSQ) came the discovery of 1013 RRab and 359 RRc distributed across $\sim$ 840 deg^2 of the sky in the range $150^\circ < \rm RA < 210^\circ$ and $-10^\circ < \rm Dec < 10^\circ$ (Zinn et al. 2014). The latter contains stars with $d_{\rm H}$ between 5 and 80 kpc. More recently, the Catalina Surveys identified $\sim 43,500$ RRLs over $\sim 30,000$ sq degrees of the sky up to heliocentric distances of $\sim 60-110$ kpc (Drake et al. 2017). The Pan-STARRS1 (PS1) 3π survey has proven to be also an excellent source for RRLs, despite its poor temporal sampling, by identifying a sample of $\sim 45,000$ RRLs up to ~ 130 kpc from the Sun with a 90% purity (Sesar et al. 2017a). All these surveys have found several distant RRLs, but the surveys' low completenesses at faint magnitudes limit the depth of the findings.

In this contribution, we use data from the High Cadence Transient Survey (HiTS; Förster et al. 2016) to search for distant RRL (beyond 100 kpc). HiTS is a survey designed for the detection of young supernovae events with a total sky coverage of $\sim$ 350 square degrees and a limiting g magnitude that varies between 23 and 24.5 (Förster et al. 2016). Since the cadence and observing strategy of the survey are well matched for RRL detection, it should allow us to find distant RRL in the observed region, if present. Here we discuss results from $\sim$ 120 deg^2 of HiTS survey data, corresponding to the second campaign which was held during semester 2014A.

The structure of this paper is organized as follows: In section 2 an overview of the observation context of this work is given, including details of HiTS. In §3 the candidates selection and characterization process is described, as well as the distance determination. The analysis of the sample, including the presence of substructures in our data like the Sextans dwarf spheroidal galaxy and the description of the most distant candidates is presented in §4 and §5, respectively. In §6 we use our sample to construct radial density profiles of the halo and compare them with previous studies. Finally, in §7 our main results are summarized.

2. OBSERVATIONS

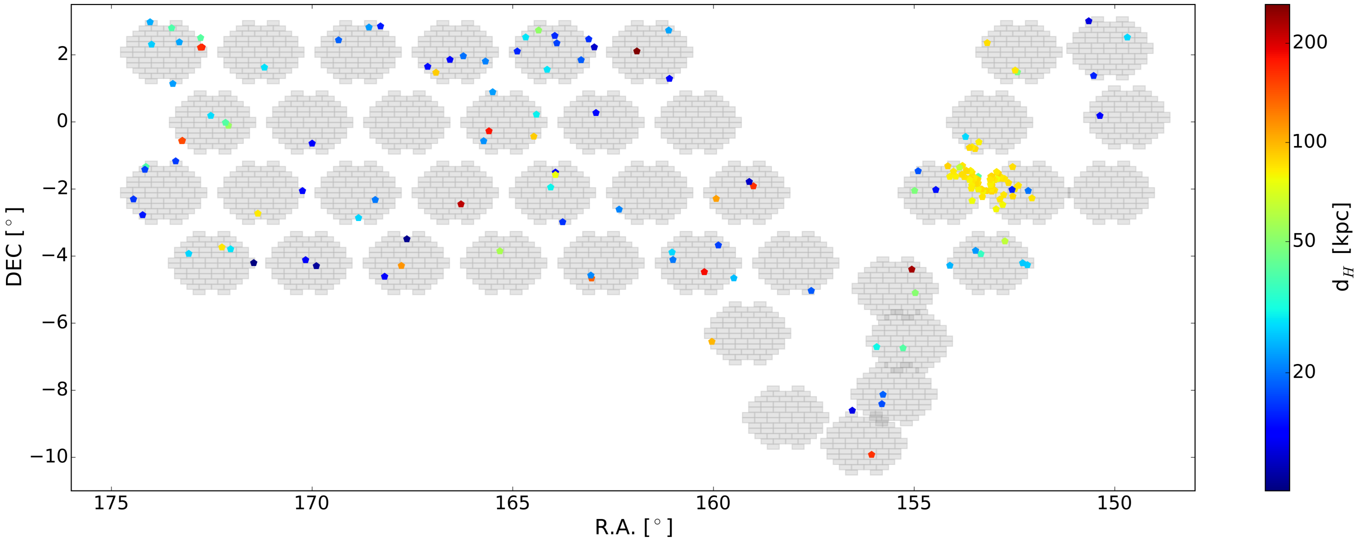

Figure 1. Color coded plot of the distribution of our 173 RRL stars in the sky, with the colors representing their heliocentric distances. An approximation of the HiTS footprint is shown in grey in the background as a reference.

HiTS is a deep optical campaign carried out with the Dark Energy Camera (DECam, Flaugher et al. 2015) mounted at the prime focus of the Blanco 4 m telescope at Cerro Tololo Inter-American Observatory (CTIO). The camera contains 62 CCDs with 520 megapixels and generates three square degree images. It is currently the largest etendue camera in operation in the southern hemisphere, and it will remain so until the Large Synoptic Survey Telescope (LSST) begins operations in 2022.

One of the main goals of HiTS is the detection of optical transient objects, in particular young supernovae events mainly in the g SDSS photometric system filter (~ 4000 to 5500 Å) in the search for empirical evidence of the shock breakout phenomena. The fact that the survey can detect transient objects with characteristic timescales of hours make HiTS suitable for RRLs studies as well.

The observations used for the current work took place between UT 2014 February 28 and March 4 (five consecutive nights). Forty fields were observed with a cadence of two hours, four times per night on the $g-$band and the exposure times varied from 160 seconds (83% of the observations) to 173 and 174 seconds (3% and 14% respectively). This translates into 20 epochs per field, with the exception of one field (centered in 151.5° RA, −2° DEC), which has 37 (see Förster et al. (2016) for detailed field positions). The sky was clear during all nights, with typical seeing values around 1.5 arcseconds.

The fields observed by HiTS were selected almost entirely blindly, covering ~ 120 square degrees in the sky region from $150° < \mathrm{RA} < 175°$ and $-10° < \mathrm{Dec} < 3°$ (see Figure 1). The only requirement for the fields was the observing availability during the entire night. Six of the fields were chosen for being known cluster fields and two for being SuperCOSMOS fields. The data obtained were stored on the National Laboratory for High Performance Computing (NLHPC) cluster at the Center for Mathematical Modeling (CMM) of Universidad de Chile and then analyzed using the HiTS pipeline.

The HiTS pipeline is based on a basic calibration, image substraction, candidate filtering and visualization (Förster et al. 2016). The instrumental signature removal steps were performed using the DECam community pipeline (Valdes et al. 2014). For this work, we generated catalogs using the SExtractor photometry software (Bertin & Arnouts 1996), with a limiting apparent magnitude of 23–24.5 (Förster et al. 2016).

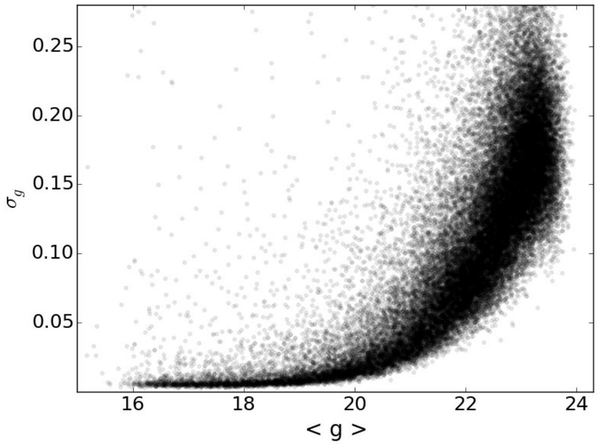

Figure 2. Variation of σ_g with the average magnitude for one of the HiTS fields (black dots). To model the data, a cubic spline interpolation was applied to the sigma-clipped data.

3. SEARCH AND CHARACTERIZATION OF RRLS

3.1. *Photometric Calibration*

In order to select periodic variables we need to define a common x, y pixel coordinate system using the output catalogs generated by SExtractor, a process we call alignment. We select the second epoch observation as the reference frame for having the best observing conditions. The scaling constants needed to do the alignment were found by the HiTS pipeline (Förster et al. 2016). Subsequently, we performed a cross-match between the aligned catalogs and rejected as possible candidates sources with fewer than five detections. Sources whose mean flux uncertainties are larger than two times the flux standard deviation were also filtered out. Pixel coordinates were transformed into equatorial coordinates following the procedure described in Förster et al. (2016).

To account for the effects of the atmospheric conditions over the different epochs, we calculated a relative zero-point associated with the reference. This was performed comparing the instrumental magnitudes given by

$$g_{\text{inst}} = -2.5 \log \left(\frac{\text{counts}}{s} \right) - a_g - k_g\, A \qquad (1)$$

where A is the airmass, a_g is the photometric zero-point in the $g-$band (one for each CCD) and k_g is the first-order extinction in g[9]. Then, the g magnitude was calculated as following:

$$\begin{aligned} g_{\text{ref}} &= g_{\text{inst}} + \Delta_{\text{rel}} \\ g &= g_{\text{ref}} + \Delta_{\text{PS}} \end{aligned} \qquad (2)$$

In the previous equation, Δ_{rel} refers to the relative zero-point between the different epochs and the reference, which was calculated in a chip-by-chip basis, and Δ_{PS} is a calibration zero point respect to the PS1 DR1 public catalog. To obtain the PS1 zero-points, we compared the instrumental magnitudes for all the stars in a given chip (corrected by Δ_{rel}) with the corresponding magnitudes listed in the PS1 database. This yields 60 different zero-points for a given field. We repeated this procedure for all fields in the PS1 footprint.

To estimate the photometric uncertainties, we assume that the uncertainties for each star magnitude can be obtained using a non-parametric model of the standard deviation and mean magnitude relation for all the stars in their respective fields, as can be seen in Figure 2. We do not use the flux errors given by SExtractor since they are, in general, underestimated (Gawiser et al. 2006; Martínez et al. 2017) and therefore are not reliable when accounting for the photometric uncertainties. The photometric uncertainties reach ~ 0.10 mag at $g \sim 22$ and ~ 0.15 mag at $g \sim 23$.

The final magnitudes include extinction corrections for which the re-calibrated dust maps of Schlafly & Finkbeiner (2011) were used. The extinction values for the $g-$band were calculated using the relation $A_g = 3.303 \cdot E(B-V)$ from the mentioned work. Following this, the average A_g of the RRLs in the HiTS fields is ~ 0.14 mag, with a standard deviation of 0.03 mag.

3.2. *Selection of RRLs*

For period determination, we ran the generalized version of the Lomb-Scargle periodogram (GLS; Zechmeister & Kürster 2009), which provides more accurate frequencies and is less susceptible to aliasing than the Standard Lomb-Scargle (LS; Lomb 1976; Scargle 1982) periodogram analysis. We selected as pre-candidates objects with periods greater than 4.8 hours (0.2 days) and less than 21.6 hours (0.9 days), and with a GLS statistical level detection of < 0.08. The statistics were computed by using the GLS tool from the astroML python module (VanderPlas et al. 2012). In spite of the reduction in the aliasing by the GLS near certain problematic periods (0.33 and 0.50 d) compared with the standard LS, we considered reasonable to filter out objects with periods between 0.32 and 0.34 days, and within 0.49 and 0.51 to reduce the number of spurious variables. In the case where two or more significant periods met the requirements discussed above, we allowed the two most significant to be selected. This results in the selection of 2434 objects.

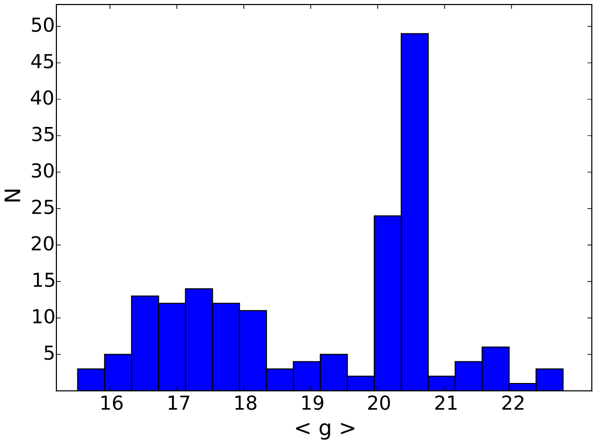

Figure 3. Distribution of the mean magnitudes g for the complete sample of RRLs.

Finally, objects with Δ mag < 0.2 were filtered out and we use visual inspection of the phased light curves (looking for periods, amplitudes and light-curve shapes typical of RRLs) to obtain our final list of RRLs comprised of only 173 objects ($\sim 7\%$). A small number of stars look clearly periodic but they do not have the correct amplitude, period or shape for being considered RRLs and they are not further discussed here. An additional visual inspection of the reference images for each of the RRLs was performed to reject possible extended objects.

Color information provides additional constraints at the moment of selecting/confirming RRLs (see e.g. Ivezić et al. 2005). Unfortunately, HiTS observations were done only in the g band. Not all our stars have a counterpart in SDSS because some of our fields are outside the footprint of that survey, and our limiting magnitude is significantly fainter than SDSS. However, 139 of our RRLs have a counterpart in SDSS DR12 and the ones with small photometric errors in SDSS are constrained within $0.9 < u-g < 1.8$ and $-0.1 < g-r < 0.3$, as expected for RRLs. We also look at the colors in PS1 which completely covers our region although again, does not go as deep as HiTS. In this case we found a match for 161 RRLs and all of them have colors $g-r$, $r-i$ and $i-z$ consistent with RRLs, and confirming our selection criteria based on the g light curves is good enough to isolate RRLs.

To have a more robust method for the estimation of the light curve parameters we adjusted templates of RRLs from the work by Sesar et al. (2010), which was based on SDSS Stripe 82 RRLs. In that study, a list of 23 templates is provided for the $g-$band, two of which are for RRc. The selection of the best fit for each candidate was based on χ^2 minimization. For the fitting we allowed small variations around the observed amplitude and maximum magnitude (0.2 magnitudes for each) as well as for the period and initial phase obtained through GLS (0.01 days and 0.2, respectively).

---

[9] `http://www.ctio.noao.edu/noao/content/Mean-Photometric-Standard-Star-Module-PSM-Solutions-mean-zeropoints-color-terms-extinctions`

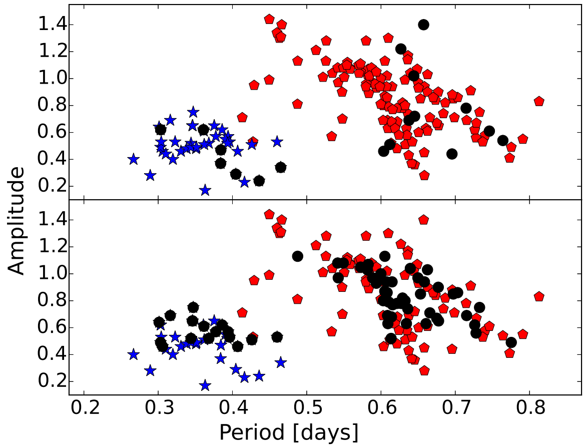

Figure 4. Period-Amplitude diagram of the complete sample of RRLs. The blue stars symbols represent RRc stars, while the RRab are plotted with red pentagons. Black filled circles represent RRLs with $d_{\rm H} > 90\,{\rm kpc}$ (*top*) and RRLs members of the Sextans dSph galaxy (*bottom*).

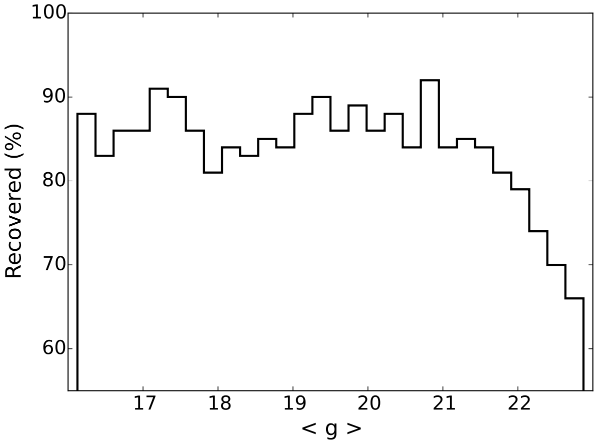

Figure 5. Recovery rates as a function of mean g magnitude of synthetic RRLs.
2

The 173 RRLs (131 RRab and 42 RRc) have mean magnitudes between 15.5 and 22.7. Figure 3 shows the distribution of the mean g magnitude for the full sample. The strong peak seen at $g \sim 20.5$ correspond to stars associated with the Sextans dSph galaxy and are further discussed in §4. Surprisingly, there is a non-negligible number of RRLs with $g > 21$ which correspond to very distant halo object. Folded light curves and tables with the properties of the RRLS are shown in §5 (for the very distant stars) and in the Appendix material (for the rest of the stars).

Figure 4 shows the location of the RRLs in the Period-Amplitude diagram. As expected, the sequences of the Oosterhoff (Oo) groups I and II (Oosterhoff 1939; Catelan & Smith 2015) are clearly visible in this plot, specially for the halo RRab at distances < 90 kpc (red symbols in Figure 4). This is reassuring that our methodology is correctly recovering properties of RRLs. We discuss implications of the location in this diagram of the newly found RRLs later in the article.

3.3. *Detection Efficiency*

To estimate the detection efficiency of our survey we generated 5000 artificial light curves of RRLs mimicking our real cadence and photometric errors. Specifically, the number of observations per object were set equal to the ones of randomly selected stars in our survey. Thus, the number of epochs in the artificial light curves vary from 16 to 37. Each light curve was modeled using the parameters (amplitude in g, period, template) from the list of SDSS RRLs in Sesar et al. (2010). A random initial phase was added to each simulated star. Finally, photometric errors were added to the template magnitudes according to the values of the main locus of stars seen in Figure 2. The artificial light curves were then processed by our software and stars which pass all our criteria and have a period within 10% of the real one were flagged as recovered.

Figure 5 shows the results of the process represented as a histogram where 0.25 magnitude bins were used. In the bright end, our method is able to recover $\sim 86\%$ of the full sample, and the rate ranges between 81% and 92% down to $g = 21.5$. The detection efficiency drops to less than 70% for RRL fainter than $g = 22$. The estimation of the RRLs detection efficiency does not take the photometric completeness of the survey into account. A detailed analysis of the photometric completeness of HiTS can be found in Förster et al. (2016).

3.4. *Comparison with previous surveys*

Another way to investigate how many RRLs we are missing in our survey is to compare our results with recent large-area surveys that covered the same portion of the sky as HiTS. In this work we compare with data from the Catalina Real-Time Transient Survey (CRTS) data release 1 (Drake et al. 2013a, 2014), from the La Silla-QUEST (LSQ) survey (Zinn et al. 2014) (both have complete time series in the $V-$band) and from PS1 (*grizy* filters but only a few epochs in each band).

When compared with Drake et al. (2014), 93 RRL (76 RRab and 17 RRc) fall into the fields observed by HiTS with magnitudes fainter than 16 (near our saturation limit) that we should have been able to detect. Of these 93, 69 matched up with our list within 2 arcseconds (74%), and 74 within 2.5 arcseconds (80%). In terms of percentages, 74% (79% for 2.5 arcsecs) of the ab types and 76% (82%) of the RRc's were recovered. There are no differences in the classifications they give to the RRLs and what we find in this work. The periods obtained for our sample are in good agreement with the periods for the stars in common, with a mean discrepancy of $2 \times 10^{-3} \pm 2 \times 10^{-2}$ days. We considered the position of the 24 (19) missing RRLs in the CCDs and found that at least 7 of them fell near the edges for the reference frame and therefore were not cleanly detected by our procedure. Removing these 7 stars from the list of potential matches with Drake et al. (2014) increases the rate of recovery to 80% (84%) which is closer to the numbers obtained for the theoretical recovery rate computation. In general, the missed RRLs are relatively bright sources ($V < 19$, $d_{\rm H} < 40\,{\rm kpc}$), with $\langle V \rangle \sim 17$ and enough phase coverage to perform a good characterization in the CRTS ($N > 180$). In our sample we classified as RRLs 103 sources that were not present in Drake et al. (2013a) or Drake et al. (2014); 74 of them are RRab, and the remaining 29 are RRc. These stars may have been missed by these surveys for different reasons, but the most likely is attributable to the different depths of our surveys. Both Drake et al. (2013a) and Drake et al. (2014) have shallower limiting magnitudes, and have high completeness levels until $V_{\rm CSS} \sim 19.5$. More than a half of the new RRLs ($\sim 60\%$) are grouped together and seem to be part of the Sextans dwarf spheroidal galaxy (as described in section §5), while from the remaining objects, 22 have magnitudes $g > 20$, mostly beyond the detection limits of the CRTS.

In the case of LSQ, which has 43 RRab and 7 RRc fainter than $g = 16$, the comparison yielded 44 stars recovered (88%; 5 RRc and 39 RRab). In general, the periods seem to coincide with an absolute mean difference of 4.7×10^{-2} days. However, there is one star with a significantly different period (HiTS101413-004502). If we do not include HiTS101413-004502 in the comparison, the period discrepancy turns out to be $|\Delta P| \sim 5 \times 10^{-4}$. For that star we found a period of 0.386 days as the most likely period, while LSQ gives 0.628 days. However, the latter corresponds to the second most probable period according to our procedure. Since LSQ has 87 observations for that star and we only have 21, their period is likely more reliable. This discrepant period determination led us to a misclassification of that RRL (from a RRab to a RRc). In Table 5, the period obtained with our methodology is presented. Of the RRLs we missed, 4 are RRab and 2 are RRc. Nevertheless, one RRab (LSQ250) fell relatively close to the edges of its CCD, following the criteria applied in the comparison with the CRTS. Rejecting LSQ250, the recovery rate rises up to $\sim 90\%$. As in the case of the comparison with CRTS, we report numerous RRLs that do not appear in the LSQ catalog. We found 93 new variables in the common regions (70 ab's and 23 c's) most of which seem to be related, again, to the Sextans dSph RRLs overdensity (65%).

The PS1 public catalog has $\sim 24,000$ RRLs and was built based on machine learning techniques (Sesar et al. 2017a). From this sample, 298 fall into the HiTS fields. Based on their calculations, an RRab/RRc score in their selection higher than 0.90 gives a purity of 0.97/0.94 and a completeness of 0.88/0.57 for $r < 18.5$. If only RRLs with scores higher than 0.90 are considered, the number of PS1 RRLs in the HiTS fields with mean magnitudes in g fainter than 16 is 110. A comparison of this group with HiTS RRLs yields 87 matches within 2 arcseconds (75 ab's, 12 c's), i.e., we recover 80% of the intersecting PS1 sample. The mean period difference is 0.001 d, with 0.07 d as the most significant discrepancy, and the mean magnitude difference is 0.09. The faintest common RRL, HiTS101243+022118, has $g = 20.61$ (87 kpc) in the HiTS catalog, and $g = 20.79$ in PS1. The classifications of all the stars in this subsample of the PS1 catalog are in agreement with the classifications presented in this work.

It is worth noticing that five of the RRLs in PS1 that were not detected by us fall near the edges of the CCDs for the reference frame. If we do not take into account these RRLs, our recovery rate go as high as 83%, in agreement with our estimations. The rest of the undetected RRL correspond to relatively bright sources, with a mean value of g of 18.3.

Of the 86 RRLs that are not clearly detected by PS1, 28 have $g < 20$ (18 ab's, 10 c's), which corresponds to $d_{\rm H} \lesssim 70$ kpc. The rest of the stars not present in the PS1 catalog are mostly $ab-$type (65%), and include the entire sample of faint RRLs described in Section 5.

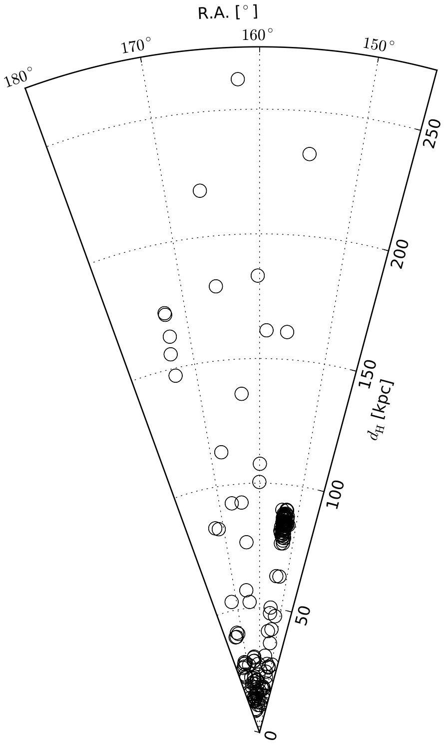

Figure 6. Radial plot of heliocentric distances as a function of right ascension (R.A.). The overdensity located at ~ 80 kpc corresponds to the Sextans dSph galaxy. Sixteen RRLs have distances > 100 kpc.

3.5. *Heliocentric distance determination*

RR Lyrae stars are known to follow a period-luminosity-metallicity (PLZ) relationship that makes them useful as distance indicators. We used Sesar et al. (2017a) PLZ relations to compute individual values of M_g, and subsequently heliocentric distances through distance modulus. For deriving the absolute magnitudes, we used the values from Table 1 in Sesar et al. (2017a) and assumed [Fe/H]$= -1.5$ as a representative value of the metallicity of the Galactic halo, given our lack of individual metallicities. It is worth noticing that the PLZ relationship is valid for RRc only when their periods are "fundamentalized". For the RRc in our sample, we used the periods given by

$$\log(P_F) = \log(P) + 0.128 \tag{3}$$

where P_F is the fundamentalized period and P is the pulsational period of the RRc stars (Catelan 2009).

The dependence of the absolute magnitude on metallicity is weak. Considering a mean metallicity offset of ± 0.5 dex from [Fe/H]$= -1.5$ dex for the entire sample would lead to fractional difference in heliocentric distances of 1.8%, being these differences as high as 4 kpc (for the faintest RRL). If the metallicity offset is ± 1.0 dex

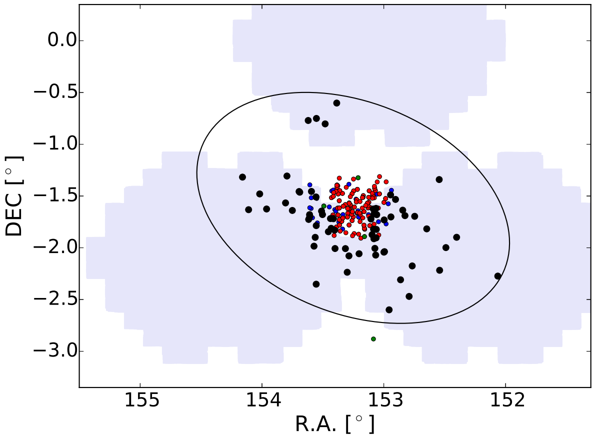

Figure 7. Positions in the sky of RRLs found by this work near the Sextans dSph galaxy (black dots). These RRLs cover a range of magnitudes from 19.89 to 20.39 in the $g-$band. Known RRLs from Amigo et al. (2012) and Zinn et al. (2014), are shown as red and green dots, respectively. In addition, variable star candidates at the level of the Horizontal Branch ($19.0 < V < 21.6$) from Lee et al. (2003) are plotted with blue dots. The HiTS footprint is plotted in grey in the background. An ellipse centered in (RA,DEC) = $(153.2512^o, -1.6147^o)$ (Irwin et al. 1990) is shown as a reference of the tidal radius ($r_t = 83.2'$), orientation ($\theta = 56.7°$) and ellipticity ($\epsilon = 0.29$) of the dSph as determined by Roderick et al. (2016).

instead, these values vary ∼ 3.6% and with distances up to 8 kpc. Hence, the lack of individual metallicities should not introduce large discrepancies in our distance estimates. In Table 1 the distances obtained by this method are shown for the faintest (and hence farthest) candidates. Distances obtained for the remaining sample are reported in Tables 5 and 6 in the Appendix section. The uncertainties in the distance estimates include the propagation of the errors associated to not only the photometric errors but also the errors associated with M_g. Figure 6 presents a radial plot for the entire list. The HiTS RRLs are located between 9 and 262 kpc from the Sun, including many stars at heliocentric distances > 100 kpc, which we discuss in §5. There is also a significant overdensity of stars near $d_{\rm H} \sim 80$ kpc, which corresponds to RRLs in the Sextans dSph galaxy (see also Figure 1) that are discussed in the next section.

4. SEXTANS DSPH RRL POPULATION

Figures 1 and 6 show an overdensity of stars centered at RA ≃ 153.3°, DEC ≃ −1.7° and $d_{\rm H} \simeq 80$ kpc. The position of these stars, both in equatorial coordinates and distance, matches the location of the Sextans dwarf spheroidal galaxy (R.A. = 153.2512°, DEC = −1.6147°, $d_{\rm H} = 86 \pm 4$ kpc, McConnachie 2012). Sextans is a Milky Way satellite discovered by Irwin et al. (1990) with an absolute magnitude of $M_V = -9.3$. The system is characterized by a relatively old and metal poor population (age=12 Gyr; [Fe/H]=−1.9), as described by Mateo et al. (1991) and Kirby et al. (2011), respectively. The Sextans dwarf is a relatively extended satellite with a half-light radius r_h of 695 pc (Irwin & Hatzidimitriou 1995; Roderick et al. 2016) and a surface brightness of ∼ 28 mag arcsec^{-2}, typical of Local Group dSph galaxies. A recent study of Sextans carried out by Roderick et al. (2016) analysed its structural parameters using wide-field photometric data in order to investigate its kinematics and stellar structures. According to their results, the dSph has a halo-like substructure extended up to 82′ from its center, with several overdensities detected at statistically high significance levels.

From our sample, 65 of the RRL candidates are located within 1.75 degrees of Sextans, and between heliocentric distances of 76 and 90 kpc (48 ab's, 17 c's). Their distribution, as well as the position of the HiTS fields are shown in Figure 7 and Figure 1, in different scales. Figure 7 also shows an ellipse marking the tidal radius from a King profile of the galaxy (Roderick et al. 2016) and known RRLs in the galaxy from the literature. As can be seen in the figure, the HiTS fields do not cover the center of Sextans but only the outskirts of the dwarf. However, none of the previous surveys of RRLs in this galaxy were able to cover the full extension of Sextans. Thus, HiTS is providing for the first time information on the outermost RRLs in Sextans. The distribution of the RRLs along the fields does not show any particular kind of structure or shape and all are contained within the galaxy's known King limiting radius.

The distances for the Sextans dSph RRLs were recalculated since values for the metallicity of the galaxy are available in the literature, and they are not necessarily close to our assumption for the Halo ([Fe/H]= −1.5). For the Sextans RRLs, we adopted [Fe/H]= -1.93 ± 0.01 from Kirby et al. (2011).

Based on our subsample of RRLs associated to Sextans (both *ab* and $c-$types), in principle we estimated a mean heliocentric distance to the satellite of 81.4 ± 5.7 kpc. We noted, however, a clear offset between the mean distance obtained with only RRab and only RRc (84.2 and 74.5 kpc, respectively). This discrepancy (13%) may be due to the different behavior of the period-luminosity relations for these stars (see for example Vivas et al. 2017), and we are using PLZ relations that are exclusive for RRab (Sesar et al. 2017a). As we do not expect the different populations to be located at different distances, we corrected the RRc from our entire sample by this number, including all type c stars outside Sextans. By doing this, the re-derived mean heliocentric distance of the dSph is 84.2 ± 3.3 kpc, which is in agreement with the distance of 86 ± 4 kpc obtained by (Mateo et al. 1995) based as well on RRLs.

Knowing the distance we can estimate the physical distances of our Sextans RRLs to the dwarf's center. We find stars out to 1.9 kpc (1.30°) which is in agreement with the results of Roderick et al. (2016), who found Sextans halo overdensities to be as far as 2 kpc from the center.

RRLs have been used as a mean to detect extra-tidal material around satellite galaxies and globular clusters (eg. Fernández-Trincado et al. 2015; Garling et al. 2017). From Figure 7 it is possible to claim that there is no clear evidence of extra-tidal RRLs based on our sample. Extending the search for RRLs in Sextans to the contiguous HiTS fields does not change this statement, even if a significantly larger radius is considered (e.g. $r_t = 90'$; Irwin et al. 1990). One of the RRLs from the LSQ survey lies outside Roderick et al.'s tidal radius (see Figure 7), but inside the estimate by Irwin et al. (1990). Thus, it is not strong evidence of extra tidal material. Regarding hypothetical internal substructures in the galaxy, it is not possible to measure any given the mean uncertainty of the distance of our sample of Sextans' RRLs (4.1 kpc),

Table 1
Most distant RR Lyrae stars ($d_{\rm H} > 90\,{\rm kpc}$).

ID	R.A. (deg)	DEC (deg)	$\langle g\rangle$	$d_{\rm H}$ (kpc)	Type	N
HiTS105754-002603	164.47577	-0.43403	20.5	92.5 ± 6.8	c	20
HiTS110739+012813	166.91383	1.47037	20.4	92.6 ± 6.6	c	20
HiTS104009-063304	160.03895	-6.55105	20.8	100.5 ± 4.0	ab	21
HiTS103943-021726	159.93119	-2.29061	20.9	107.8 ± 4.5	ab	21
HiTS111106-041718	167.77512	-4.28834	21.2	113.4 ± 8.8	c	22
HiTS105209-043942	163.03718	-4.66174	21.5	136.0 ± 5.7	ab	20
HiTS113259-003404	173.24674	-0.56770	21.5	147.0 ± 6.9	ab	18
HiTS113256-003329	173.23270	-0.55818	21.5	155.8 ± 7.5	ab	19
HiTS102414-095518	156.05905	-9.92180	21.7	161.0 ± 8.0	ab	21
HiTS103601-015451	159.00456	-1.91422	21.7	161.3 ± 12.9	c	21
HiTS113107+021302	172.77796	2.21734	21.7	162.8 ± 8.6	ab	21
HiTS113057+021331	172.73946	2.22514	21.8	171.7 ± 9.4	ab	20
HiTS113105+021319	172.76936	2.22200	21.8	172.4 ± 9.4	ab	20
HiTS110222-001624	165.59251	-0.27337	22.1	179.8 ± 10.3	ab	19
HiTS104054-042827	160.22661	-4.47424	21.9	183.2 ± 14.8	c	20
HiTS110510-022710	166.28982	-2.45282	22.4	218.6 ± 14.6	ab	19
HiTS102014-042354	155.05789	-4.39843	22.5	232.9 ± 21.9	c	19
HiTS104738+020627	161.90718	2.10746	22.8	262.2 ± 24.3	c	19

the standard deviation of the distribution (3.3 kpc), and its size ($\sim 700\,{\rm pc}$; Irwin & Hatzidimitriou 1995; Roderick et al. 2016).

In Amigo et al. (2012), a list of 114 RRLs covering the inner regions of Sextans is presented, including 37 identified earlier by Mateo et al. (1995). This catalog contains a large number of new discoveries (ranging from $V = 20.06$ to $V = 20.50$), and recovers as RRLs most of the variable star candidates presented in Lee et al. (2003). Since Amigo et al. (2012) covers the central region of the dwarf, the overlap with HiTS' fields is not significant. However, there are 16 stars in common between HiTS and that work, with highly similar periods ($|\Delta P| \sim 2 \times 10^{-4}$) and same classifications. In addition, Zinn et al. (2014) recognized seven RRLs in the galaxy, four of which are not contained in the catalog of Amigo et al. (2012). Thus, there are 46 new RRLs discovered by HiTS in Sextans, seven of which are not flagged as RRLs by Lee et al. (2003). This brings the total number of RRLs in this galaxy to 165.

Folded light-curves for the HiTS Sextans RRLs sample are shown in the appendix section (Figure 12 to Figure 14). Table 5 contains the information of these stars. The mean period of the RRab is 0.63 d which is close to the nominal Oo II group. However, the distribution of the 65 RRLs in Sextans in the Period-Amplitude diagram (Figure 4) clearly shows that the stars do not follow a single sequence of Oo groups. Thus, HiTS confirms the Oo-intermediate nature of this dSph which was already established by Mateo et al. (1995) based in 34 stars in the inner part of the galaxy. Following the Milky Way satellites (except the massive galaxies of Sagittarius and the Magellanic Clouds) our extended sample confirms that Sextans does not contain High Amplitude Short Period (HASP) stars, which have been interpreted by Fiorentino et al. (2015) as coming from populations more metal rich than [Fe/H]~ -1.5.

5. RR LYRAE STARS BEYOND 90 KPC

We find 18 distant RRLs within our list of candidates that are located at $d_{\rm H} > 90\,{\rm kpc}$ (hereafter distant RRLs); this corresponds to mean magnitudes $\langle g\rangle \geq 20.5$. Two recent works, Drake et al. (2013b) and Sesar et al. (2017b), have reported some of the most distant Galactic RRLs known to date, located at $\sim 120\,{\rm kpc}$ and $\sim 130\,{\rm kpc}$, respectively. Among our distant RRLs sample there are 13 with $d_{\rm H} > 130\,{\rm kpc}$; i.e., beyond the most distant previously known MW RRLs. The distant RRLs group span a range from $\sim 92\,{\rm kpc}$ ($\langle g\rangle \sim 20.5$) to beyond 200 kpc (up to $\langle g\rangle \sim 22.8$). In Table 1 the main properties of these distant stars are presented (full info is presented in Table 6 in the Appendix section), and Figure 8 shows the folded light curves for this group.

Regarding their classification, 11 RRL (61%) from this faint subsample correspond to RRab, while seven were classified as RRc (Table 1), roughly consistent with the observed ratio in the rest of the sample. We note that three of the four most distant RRLs are $c-$type. Given their lower intrinsic amplitude and the large photometric uncertainties of the individual observations near the detection limit of our survey, we regard their classification as tentative; the most distant RRab, which has a secure classification, is at $d_{\rm H} = 219 \pm 15\,{\rm kpc}$. In the Period-Amplitude diagram (Figure 4, top panel) these stars are mostly located toward the locus of the Oo II group, although a large dispersion is observed. However, the distribution looks significantly different compared with the one from nearby stars ($d_{\rm H} < 90\,{\rm kpc}$). The mean period of the sample of 11 distant RRab stars is $0.668 \pm 0.05\,{\rm d}$, which is significantly different to the mean period of the RRab with $d_{\rm H} < 90\,{\rm kpc}$, $0.600 \pm 0.09\,{\rm d}$. The mean period of the distant RRLs is remarkably similar to the mean period of the ensemble of RRLs in the ultra-faint dwarf (UFD) satellites of the Milky Way, 0.667 d (Vivas et al. 2016), suggesting that these galaxies may be the main contributors of the outermost regions of the halo. As Sextans, the distant RRLs sample does not contain HASP stars.

In Figure 1 we showed the spatial distribution of the

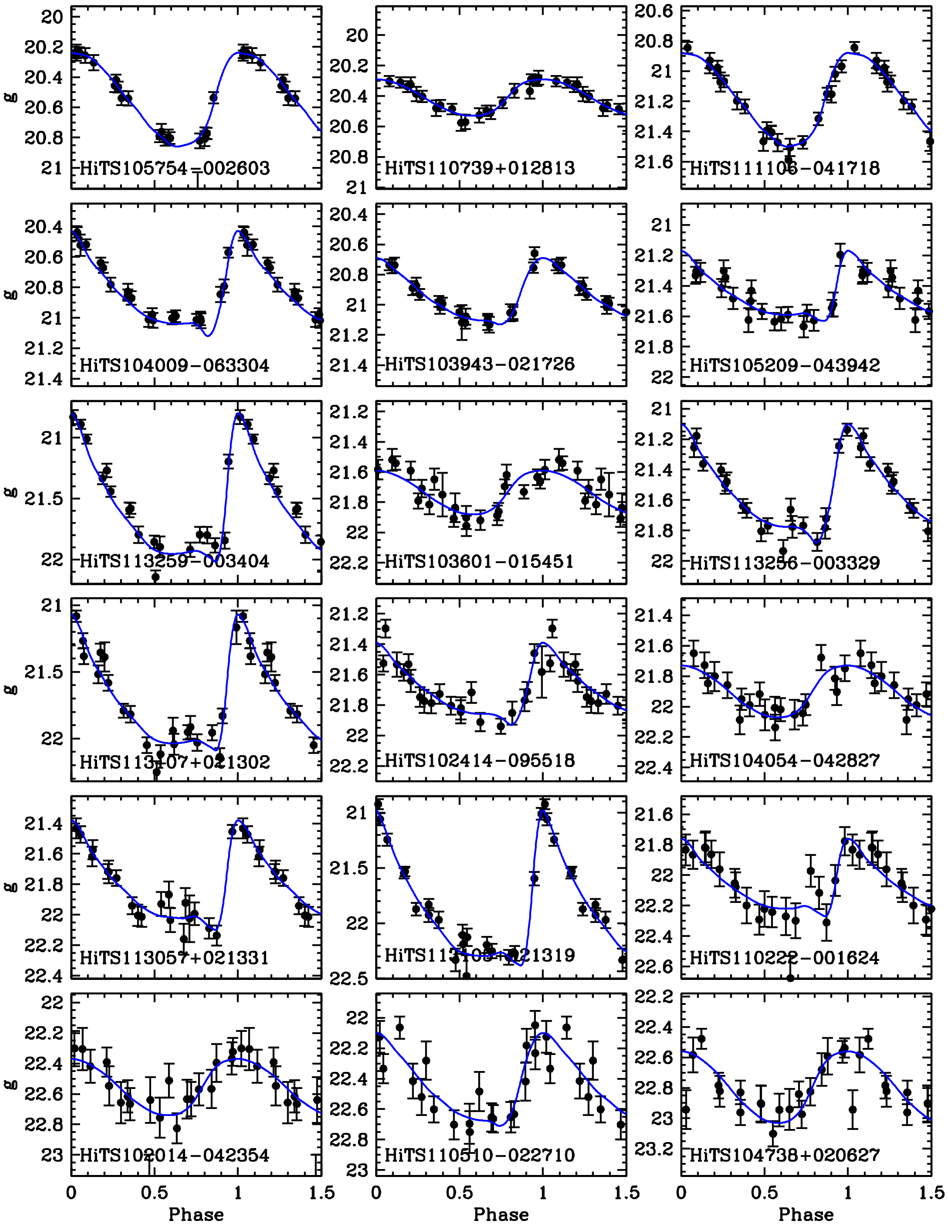

Figure 8. Folded light curves of the distant RR Lyrae stars listed in Table 1.

distant RRLs, color coded by their heliocentric distance. The distant RRLs look randomly distributed in the sky except for two compact groups, with two and three RRLs respectively, whose stars are very close together in the sky. We discuss those groups in the next sub-section.

5.1. *Leo IV and Leo V*

Among the sample of distant RRLs, we found two distant groups of closely spaced RRL both in angular separation and heliocentric distances. In these cases, they coincide with the position on the sky and distance of the ultra-faint galaxies Leo IV and Leo V. In Medina et al. (2017) we separately reported the discovery of the RRLs in Leo V since that galaxy had not been explored before for variability. Medina et al. (2017) also argues the importance of groups of distant RRLs as a mean to discover previously unknown satellites or substructure in the halo. Since the properties of the RRLs in Leo IV and Leo V were already discussed in Medina et al. (2017), here we only present a summary and update the distance estimates.

Out of the three known RRLs in Leo IV (Moretti et al. 2009), we detected two stars, HiTS113256-003329 and HiTS113259-003404, both RRab. The non-detection of the third RRLs (called V3 by Moretti et al. 2009) is consistent with the detection efficiency expected for RRLs of these magnitudes, according to our results (Section 3). Three RRLs were identified as members of Leo V, HiTS113057+021331, HiTS113105+021319, and HiTS113107+021302, all being new discoveries.

In Medina et al. (2017), the distances of the Leo IV and Leo V RRLs were anchored to the known distance to Leo IV (Moretti et al. 2009). Here, we obtain revised distances for those RRLs since metallicities for both systems are available in the literature and we can use them in the PLZ relation given by Sesar et al. (2017a), which was not available at the time of writing Medina et al. (2017). Using [Fe/H]= -2.31 for Leo IV (Simon & Geha 2007), we get a mean heliocentric distance of 151.4 ± 4.4 kpc. This number is in agreement with the estimation made by Moretti et al. (2009) (154 ± 5 kpc). For Leo V, assuming [Fe/H]= -2.48 (Collins et al. 2016) gives us a mean distance of 169.0 ± 4.4 kpc, which is still consistent with our earlier results.

6. SPACE DENSITY DISTRIBUTION

The density profile of halo tracers contains important clues of the accretion history of the Milky Way (Bullock & Johnston 2005; Cooper et al. 2013). Since RRLs are excellent distance indicators they are particularly useful for the construction of number density profiles $\rho(R)$, i.e., the variation in the number of RRLs per unit volume (# kpc^{-3}) where R is the distance to the center of the Galaxy. Recent studies have worked with catalogs of RRLs sufficiently large that allowed them to study the variation of the number density with direction in the sky (see for example Zinn et al. 2014). In our case, the sample is made up of only ~ 100 RRLs (excluding stars from known dSph galaxies) spread over an area of $\sim 120\,\mathrm{deg}^{-2}$. Therefore, working with sub-samples located in different directions would not be statistically meaningful. For this reason, we use the data from all 40 fields to build a single number density profile. Since HiTS' fields span from 39 to 60 deg in Galactic latitude, and from 236 to 269 deg in longitude, this can be considered a single line of sight in the Galaxy. For the selection of the distance bins and the number density calculation, the distance from the Galactic center R_{gc} was calculated for each star in our sample. R_{gc} can be obtained from

$$R_{\mathrm{GC}}^2 = (R_\odot - d_{\mathrm{H}} \cos b \cos l)^2 + d_{\mathrm{H}}^2 \sin^2 b + d_{\mathrm{H}}^2 \cos^2 b \sin^2 l, \tag{4}$$

where d_{H} is the heliocentric distance, b and l are the Galactic latitude and longitude of each star, respectively, and $R_\odot$ is the distance from the sun to the Galactic center. For this work we assumed $R_\odot$ to be 8 kpc. The bins were created evenly-spaced on a log scale.

We are interested in placing the Milky Way into context with external galaxies and model stellar halos. Given that in typical data sets, small overdensities of 2-3 stars, such as what we found in Leo IV and Leo V, may not have been identified with known galaxies, we first performed density profile fits including the RRLs in the UFD, but leaving out the RRLs from the larger Sextans dSph. We repeated the fits with the Leo IV/V stars removed, in order to test the effect of these ultra-faint dwarfs on the profile; the fits are virtually unchanged by the inclusion/exclusion of the Leo IV/V RRLs.

Two halo models were used to fit the data: a spherical (sph) halo model and an ellipsoidal (ell) one with a flattening parameter $q = 0.7$ adopted from Sesar et al. (2011). The adopted model was $\rho(R) = \rho_\odot (R/R_\odot)^n$, where $\rho_\odot$ is the local (solar circle) number density of RRLs. The fit was done using the logarithmic form of the previous equation:

$$\log(\rho(R)) = A + n \ \log(R/R_\odot) \tag{5}$$

where $A = \log(\rho_\odot)$. We used the Markov Chain Monte Carlo routine *emcee* (Foreman-Mackey et al. 2013) to find distributions for the parameters of this model of a simple power law (SPL), A and n.

Although our main interest is to study the behaviour of the density profile at large distances from the Sun, we also explored a model with a broken power law which has been observed in multiple works (Saha 1985; Watkins et al. 2009; Deason et al. 2011; Sesar et al. 2011) at ~ 25 kpc. For the broken power law model (BPL), the break radius was considered a free parameter, as well as the inner and outer slopes. In the case of the BPL profile, the equations used are:

$$\begin{gathered}\log(\rho(R)) = A1 + n_1 \ \log(R/R_\odot) \\ \log(\rho(R)) = A2 + n_2 \ \log(R/R_\odot) \\ A1 + n_1 \ \log(R_{break}/R_\odot) = A2 + n_2 \ \log(R_{break}/R_\odot)\end{gathered} \tag{6}$$

The values of A were constrained to within 0.20 and 1.75, and -5 and 5 for $A2$ (after the break). The slope was constrained to be between -7 and -1 for the SPL. For the BPL, the constraining values were set to between -10 and 5, and -14 and 15 for the inner and outer slopes, respectively. The break radius was constrained to within 15 and 70 kpc. An initial guess for the value of each parameter was given, based on the result of following a non-linear least squares methodology (using the Levenberg-Marquardt algorithm from *scipy).*

The left/right panels of Figure 9 and Figure 10 show the fitted models to the data, with sph and ell halos respectively, under different considerations. In the *left* panels we fit the model to the RRLs within 145 kpc, which corresponds to the upper limit based on completeness considerations (we are $\sim 85\%$ complete down to $g = 21.5$). In this case, the more distant ($R > 145$ kpc) bins are shown for comparison with extrapolations of the fits to large radii. In the *right* panels, we show fits to the entire sample, after correcting for detection efficiency as calculated in Figure 5.

In both cases the first bin, which includes the closest RRL, was removed from the plots and the analysis because these bins suffer incompleteness due to saturation of bright stars, which was not considered in our detection efficiency calculations. The corner plot with the resulting posterior distributions from our fits are shown in (Figure 11). Tables 2 and 3 shows the results of the fitting for the different models assumed and with the samples with/without the RRLs in Leo IV and V, respectively.

It is important to notice that, according to Equation 4, the Galactic latitude and longitude are required to

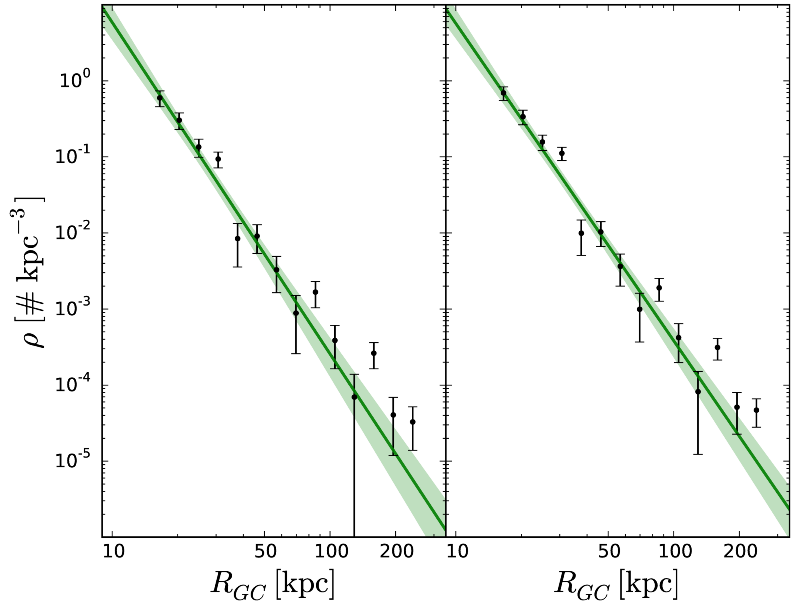

Figure 9. Number density versus Galactocentric distance R_{GC}, excluding RR Lyrae stars from the Sextans dwarf galaxy, assuming a spherical halo. Density profiles built without and with considering our detection efficiency (see Figure 5) are shown in the *left* and *right* panels, respectively. We fit a simple power-law model to the corrected data; the corresponding fit parameters are listed in Table 2, and the fits overlaid as solid lines in both panels. The shaded regions show the 3σ confidence levels determined via MCMC methods.

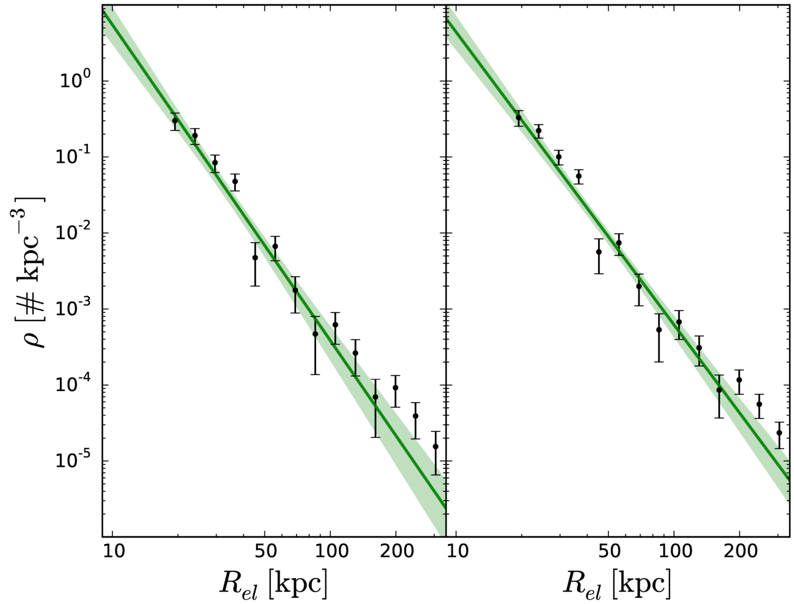

Figure 10. Number density as a function of radius in an elliptical halo, R_{el}, assuming an oblate halo with $q = 0.7$. As in Figure 9, we exclude RRLs from the Sextans dSph. Density profiles built without and with considering our detection efficiency (see Figure 5) are shown in the *left* and *right* panels, respectively. We fit a simple power-law model to the data at uncorrected $R_{\mathrm{el}} < 145$ kpc; the corresponding fit parameters are listed in Table 2, and the fits overlaid as solid lines in both panels. The shaded regions show the 3σ confidence levels determined via MCMC methods.

determine R_{GC} from d_{H}. Given the wide area covered by the survey, it is not possible to transform the detection efficiency per apparent magnitude bin to a unique Galactocentric distance and subsequently to unique ellipsoidal distance. If the mean latitude and longitude of the area observed by the survey is used ($b \sim 46°$, $l \sim 250°$), the difference in distance, between heliocentric and Galactocentric, is of up to 5 kpc. We consider the detection efficiency correction still valid in this case, since the size of the bins is in general > 5 kpc. In the

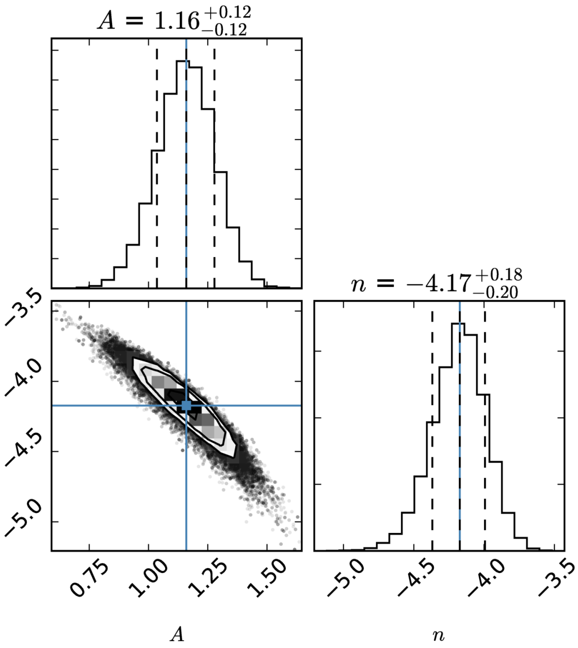

Figure 11. Corner plot showing the posterior joint probability distribution of the parameters of a simple power law number density profile, for a spherical Halo model. The parameters used for this model are the logarithm form of the number density in the solar neighborhood (A) and the power law index of the model (n).

case of the ellipsoidal distances, this distance difference reaches up to 70 kpc, which makes the correction less accurate for the more distant bins. The *left/right*panel of the plots in Figure 9/Figure 10 are provided only to show the approximate effect to the density profile if the detection efficiency is or is not considered. For this reason, the best-fit parameters in Tables 2 and 3 and the posterior analysis are only given for the corrected/uncorrected data, for the spheroidal/ellipsoidal model.

6.1. *Spherical Halo*

In this case $R^2 = R_{\rm GC}^2 = X^2 + Y^2 + Z^2$, where X and Y are the cartesian coordinates in the Galactic plane, and Z is the axis perpendicular to it. These values are given by:

$$\begin{aligned} x &= R_\odot - d_{\rm H}\ \cos b\ \cos l \\ y &= d_{\rm H}\ \cos b\ \sin l \\ z &= d_{\rm H}\ \sin b \end{aligned} \qquad (7)$$

Figure 9 shows the density profiles as described above. Table 2 summarizes the parameters found for the spherical halo SPL and BPL, when the data is corrected and not corrected by detection efficiency, respectively. Based on these results, the best fit for the data corresponds to the SPL model. From Figure 9 one can infer that the presence of the break at ~ 20 kpc is mostly due to the relatively-high density of the point at $R_{\rm GC} \sim 26$ kpc. The larger uncertainties in the determination of the BPL parameters, compared with the ones for the SPL, support the low probability of that model. The lack of stars at short distances in our sample may be part of the reason in finding a good fit to this model. For completeness, we also fit a broken power law with two breaks (double broken power law; DBPL) to account for a potential different behavior of the profile at large radii, ruled by the interaction of the Milky Way halo with farther large massive galaxies (mostly M31), for example. Table 2 does not include these parameters, given the large uncertainties associated and the difficulty to assess a physical meaning to this fit.

6.2. *Ellipsoidal Halo*

For an oblate halo with $q = 0.7$, the semi-major axis of the ellipsoid is $R_{\rm el}^2 = X^2 + Y^2 + (Z/0.7)^2$ which replaces R in Equation 5. The results of the fit are shown in Table 2 and Figure 10. As in the previous case, the best fit corresponds to the SPL model (based on χ^2_ν) but again, this may be due to the scarse bins at short distances in our dataset. As in the case of the spherical halo model, the distant bins make the difference when looking for a change in the slope. The fits give $R_{\rm el} \sim 22$ kpc as the most likely value for the break radius for the BPL, while for the DBPL these are ~ 25 kpc and ~ 80 kpc, with large uncertainties. For the latter, overfitting is much more likely to have happened than in the spherical halo model.

Overall, the spherical halo model provides a better fit to the halo than the ellipsoidal model with $q = 0.7$. The results of using samples that include/exclude the RRLs in the UFD Leo IV and Leo V are the same, within the erros, indicating that small galaxies do not affect the general behaviour of the density profile of the halo.

6.3. *Contribution from known substructures in the HiTS field of view*

The approach we have taken here best facilitates comparisons to model and external galaxy halos, where individual stellar streams and substructures may not be distinguished from the halo as a whole. However, we acknowledge that there are known MW substructures in the vicinity of the HiTS field of view. Here we briefly assess these substructures' contributions to the halo density profiles shown in Figures 9 and 10.

The Orphan tidal stream (Grillmair 2006; Belokurov et al. 2007) is a wide stellar stream that spans more than 100 degrees (Grillmair et al. 2015), tracing a roughly north-south path across (and extend southward beyond) the SDSS footprint. The distance to the stream ranges from ~ 55 kpc at its northernmost point, decreasing to ~ 20 kpc as the Orphan extends below the southern edge of the SDSS footprint (Sesar et al. 2013). We select Orphan RRLs candidates using the coordinate system defined by Newberg et al. (2010) to align with the stream and at distances between $20 < d_{\rm H} < 32$ kpc (consistent with the stream distances found in the region of the HiTS footprint by Hendel et al. 2017). We find 12(7) RRLs within 5°(3°) of the stream center and satisfying this distance cut. Newberg et al. (2010) showed that the Orphan stream is a $\sim 10\%$ excess of MSTO stars relative to the nearby field density; thus, we estimate that $\sim 1-2$ of the stars selected as Orphan candidates are actual members of the stream. Indeed, one of them (HiTS104924-023635) corresponds to "RR49" from Hendel et al. (2017), who measured a distance with Spitzer Space Telescope time-series data of 23.05 ± 0.58 kpc. This compares favorably

Table 2
Parameters for the different power law models described in section 6, with the Leo IV and Leo V RRLs.

Model	A1	A2	n1	n2 (kpc)	R_b (kpc)	χ^2_ν
sph SPL	$1.16^{+0.12}_{-0.12}$	–	$-4.17^{+0.18}_{-0.20}$	–	–	2.657
sph BPL	$0.91^{+0.56}_{-0.70}$	$1.20^{+0.17}_{-0.25}$	$-3.50^{+1.98}_{-1.46}$	$-4.22^{+0.32}_{-0.26}$	$19.52^{+9.90}_{-3.27}$	3.204
ell SPL	$1.14^{+0.15}_{-0.16}$	–	$-4.16^{+0.23}_{-0.25}$	–	–	3.184
ell BPL	$0.42^{+0.75}_{-0.74}$	$1.30^{+0.37}_{-0.24}$	$-2.23^{+1.77}_{-1.99}$	$-4.37^{+0.34}_{-0.50}$	$22.46^{+7.10}_{-5.50}$	3.962

Table 3
Parameters for the different power law models described in section 6, without Leo IV and Leo V.

Model	A1	A2	n1	n2 (kpc)	R_b (kpc)	χ^2_ν
sph SPL	$1.18^{+0.11}_{-0.12}$	–	$-4.22^{+0.18}_{-0.19}$	–	–	2.132
sph BPL	$0.75^{+0.66}_{-0.67}$	$1.24^{+0.16}_{-0.19}$	$-3.01^{+2.11}_{-1.77}$	$-4.30^{+0.28}_{-0.25}$	$18.85^{+7.76}_{-2.67}$	2.584
ell SPL	$1.14^{+0.16}_{-0.16}$	–	$-4.15^{+0.23}_{-0.25}$	–	–	2.497
ell BPL	$0.43^{+0.78}_{-0.88}$	$1.29^{+0.33}_{-0.23}$	$-2.29^{+2.18}_{-2.02}$	$-4.37^{+0.33}_{-0.45}$	$22.04^{+6.43}_{-5.26}$	3.131

to our estimate of $d_{\mathrm{H}} = 20.92 \pm 0.75$ kpc for the same star, especially given that if we instead adopted its metallicity of [Fe/H]$= -2.02$ as measured by Sesar et al. (2013), we would derive a slightly larger distance (by $\sim 2\%$).

Another possible contributor to the halo stellar populations in the HiTS field of view is the Sagittarius (Sgr) tidal stream. Sgr is a prominent stellar overdensity over much of the sky (see review in Law & Majewski 2016). Using the N-body model of Law & Majewski (2010), we select model Sgr stars within the footprint of our HiTS RRLs search, and that were stripped from the progenitor within the last ~ 5 Gyr (i.e., are part of the most recent leading debris tail). The model predicts that only the northeastern corner of the HiTS footprint should contain any Sgr debris. The mean distance of these model debris points is $\langle d \rangle = 42$ kpc, with a spread of $\sigma_{\mathrm{d}} \sim 6$ kpc. There are nine HiTS RRLs between $31 < d_{\mathrm{H}} < 49$ kpc, of which four are in the region occupied by Sgr model debris (i.e., $170° < 7\mathrm{RA} < 175°$, $-3° < \mathrm{Dec} < 3°$). Interestingly, these four stars are tightly clumped in distance, with a mean of $\langle d_{\mathrm{H}} \rangle = 40.0$ kpc and standard deviation of $\sigma_{\mathrm{d}} \sim 0.7$ kpc. Nonetheless, given that these four stars are $\sim 16.5 - 20°$ from the center of the Sgr stream (using the Sgr-aligned coordinate system of Majewski et al. 2003), we consider their association with Sgr tentative at best.

In conclusion, while there are likely stars from previously identified substructures in our sample of HiTS RRLs, it is unlikely that they have significantly biased our density profile fits, as each of the substructures would contribute only a small number of stars in our field of view.

7. DISCUSSION AND SUMMARY

We present the detection of 173 RRLs using observations from the 2014 campaign of the HiTS survey. The data cover ~ 120 square degrees of the sky and include from 20 to 37 epochs in the $g-$band. The photometric depth of the HiTS data enables us to build a catalog that includes a significant number of stars that do not appear in previous public surveys overlapping the same sky region (such as the CRTS). Most of the additional RRLs we contribute have $\langle g \rangle > 20$, corresponding to $d_{\mathrm{H}} \gtrsim 60$ kpc.

The surveyed region overlaps with the position of currently known satellite galaxies of the Milky Way. We detect 65 RRLs members of the Sextans dSph, 46 of them being new discoveries. This number includes seven stars that were not classified as RRLs by other works, but were already considered as members of the dwarf. Two additional dwarf galaxies, Leo IV and Leo V, were found within our RRLs catalog. A more detailed analysis of the RRLs in Leo V has been presented in a companion paper (Medina et al. 2017).

Regarding distant RRLs in our sample, we find 18 candidates with $d_{\mathrm{H}} > 90$ kpc, 11 of which are classified as *ab*-type, while seven are $c-$type. To understand the connection of this sub-sample with previously known/unknown systems, the period-amplitudes of the individual stars could play a major role. RRLs that are members of globular clusters are separated in the distincted Oosterhoff groups (OoI and OoII, Oosterhoff 1939). On the other hand, RRLs in ultra-faint dwarf galaxies are mostly OoII (Clementini 2014), while the halo general population (within a radius of ~ 80 kpc) presents stars in both locus, but the majority of them follow the locus of the Oo I group. This has been shown multiple times in the literature (e.g. Zinn et al. 2014; Catelan & Smith 2015) and it is also clearly seen in Figure 4. The distant sample of RRLs however does not follow the main trend of nearby field RRLs, suggesting that the main contributor to the outer halo may come from UFD galaxies.

We build number density radial profiles with our RRLs catalog (§ 5), then fit models of the form $\rho(R) = \rho_{\odot}(R/R_{\odot})^n$ for a spherical halo and an ellipsoidal one with a flattening parameter $q = 0.7$. The fits described in the previous section do not support the presence of a

Table 4
Parameters of number density profiles of the Halo from previous works, when power laws are considered. This Table only includes works with upper limits in distance > 25 kpc.

Model	Slope	R_b (kpc)	Inner Slope	Outer slope	Range (kpc)	Tracer Used	Paper
Simple Power Law							
	-3.034 ± 0.08	–	–	–	1–80	RRLs	Wetterer & McGraw 1996
	~ -2.8	–	–	–	4–60	RRLs	Vivas & Zinn 2006
	-3.0	–	–	–	5–40	MSTO stars	Bell et al. 2008
	-2.5 ± 0.2	–	–	–	10–90	BHB stars	De Propris et al. 2010
	-2.7 ± 0.5	–	–	–	1–40	BHB and BS stars	Deason et al. 2011
	-2.42 ± 0.13	–	–	–	5–30	(ab−type) RRLs	Sesar et al. 2013
	< -6	–	–	–	50–100	A-type stars	Deason et al. 2014
	-3.8 ± 0.3	–	–	–	50–100	(ab−type) RRLs	Cohen et al. 2015
	-3.4 ± 0.1	–	–	–	10–80	K giants	Xue et al. 2015
	-3.5 ± 0.2	–	–	–	30–90	Giant stars	Slater et al. 2016
	-2.96 ± 0.05	–	–	–	1–28	RRLs	Iorio et al. 2017
	$\mathbf{-4.17^{+0.18}_{-0.20}}$	–	–	–	**17–145**	**RRLs**	**This work**
Broken Power Law							
	–	23	-2.4	-4.5	5–100	RRLs	Watkins et al. 2009
	–	27 ± 1	-2.3 ± 0.1	$-4.6^{+0.2}_{-0.1}$	1–40	BHB and BS stars	Deason et al. 2011
	–	28	-2.6 ± 0.04	-3.8 ± 0.1	12–40	near MSTO stars	Sesar et al. 2011
	–	24	-2.8 ± 0.5	-5.4 ± 0.5	5–60	RRLs	Zinn et al. 2014
	–	20	-2.5 ± 0.4	-4.9 ± 0.4	10–60	F-type stars	Pila-Díez et al. 2015
	–	18 ± 1	-2.1 ± 0.3	-3.8 ± 0.1	10–80	K giants	Xue et al. 2015
	–	$29.87^{+2.80}_{-3.55}$	$-3.61^{+0.15}_{-0.16}$	$-4.75^{+0.30}_{-0.28}$	10–70	BHB stars	Das et al. 2016
	–	$\mathbf{19.52^{+9.90}_{-3.27}}$	$\mathbf{-3.50^{+1.98}_{-1.46}}$	$\mathbf{-4.22^{+0.32}_{-0.26}}$	**17–145**	**RRLs**	**This work**

clear break in the profiles. However, due to the saturation limit of our photometry we only have $\sim 1-2$ bins within the radius where a break is typically identified, so that our data may not be sensitive to the presence of a break. In fact, the data are well represented by a simple power law, with a slope of $-4.17^{+0.18}_{-0.20}$ for the spherical halo, and $n = -4.16^{+0.23}_{-0.25}$ for the elliptical case. If a broken power law is considered, the profile (for a spherical halo) exhibits a break at $R_b = 19.52^{+9.90}_{-3.27}$ kpc, with inner and outer slopes of $n_1 = -3.50^{+1.98}_{-1.46}$ and $n_2 = -4.22^{+0.32}_{-0.26}$, respectively. The position of the break and the values of the power-law indices are broadly consistent with previous studies. We summarize values from the literature for these parameters in Table 4. This agreement might represent a possible real feature of the Galactic halo, even when the sample used for those studies are located at different positions. However, it is not clear that the data favor a certain model over the other. We tried a less likely double broken power law (a power law with two breaks) profile as well, but it was not considered for further analysis due to the lack of a strong physical meaning, big uncertainties and possible overfitting.

Our sample of HiTS RR Lyrae is an unprecedented probe of the outer Galactic halo; all but three of our stellar density bins are at distances beyond 30 kpc. As illustrated in Table 4, the power-law slope of the outer MW halo is typically found to be rather steep, whether it is measured by fitting a single power-law to the outer halo ($R_{\rm GC} \gtrsim 50$ kpc), or a broken power-law with separate slopes for the inner/outer halo. The existence of a break in the halo density profile at $R_{\rm GC} \sim 20-30$ kpc is typically argued to represent a transition between predominantly *in situ* halo stars in the inner halo and an accretion-dominated outer halo (e.g., Bullock & Johnston 2005; Abadi et al. 2006). Deason et al. (2013) fit broken power-laws to the density profiles of synthetic, accretion-only models from Bullock & Johnston (2005), and found a mean from the 11 outer halo slopes of $\langle n \rangle = -4.4$, with values ranging from $-2.5 > n > -6.5$, and median break radius of 26 kpc. Because all but two of our radial profile bins are beyond this typical break, these predictions provide a valid comparison to even our single power-law fits. Cooper et al. (2010) also predicts slightly steeper (on average) slopes (all with $n < -4.4$) for the outer halos of Aquarius model galaxies formed by the tidal disruption of dwarf satellites. The rough agreement of our power-law fits (both the SPL with $n = -4.17$, and the BPL with $n_2 = -4.22, R_b = 19$ kpc) with these predictions from halos made entirely of accreted satellites suggests that the outer MW halo may be made up completely of accreted stars.

We can perhaps learn even more about our Galaxy's accretion history based on the density profile. Pillepich et al. (2014) fit the power-law stellar density profiles of ~ 5000 MW analogs from the Illustris simulation suite between radii of the stellar half-mass radius ($r_{1/2}; \sim 10$ kpc for a $10^{12} M_\odot$ galaxy) out to the virial radius. These slopes range from $3.5 < n < 5.5$, with more massive halos exhibiting shallower stellar density profiles. More recently-formed halos, those that had a recent minor/major merger, or those that accreted a larger fraction of their stellar mass from satellites, typically have shallower slopes; thus, the fact that the MW's outer slope is often found to be steep suggests a relatively quiescent recent accretion history. Our measured slope of $n = -4.17$ is remarkably consistent with Illustris model predictions for MW-mass galaxies (see Figure 6 of Pillepich et al. 2014).

With the addition of radial velocities for our outer halo RRLs, we can assess whether groups of stars which share similar radial velocities and 3D positions are part of physically associated, recently accreted tidal debris (e.g., Baker & Willman 2015; Vivas et al. 2016). If tidal debris structures in the outer halo can be linked to related structures at smaller Galactocentric radii, they provide a means of tracing the halo potential over the intervening distances (e.g., Johnston et al. 2012). Furthermore, the 13 RRLs we have discovered beyond 130 kpc in the Galaxy more than double the number of known stars at such distances in the MW. With spectroscopically-derived radial velocities, these stars will be vital tracers of the MW mass (e.g., Watkins et al. 2010; Sanderson 2016), which is currently known only to roughly a factor of two (e.g., Eadie & Harris 2016; Ablimit & Zhao 2017).

The data presented here cover only a small field of view in the Galactic halo, making interpretation within a global galaxy-formation context limited. Fully understanding our Galaxy's accretion history thus requires samples of tracers at $R_{\rm GC} > 100\,{\rm kpc}$ over many sky areas. Even with a handful of $\sim 100\,{\rm deg}^2$ fields such as that presented in this work, we could examine the fraction of stars in substructures as a function of position, and the variation of density profiles with line of sight, while also combining data sets to average over local variations. The deep, $\sim 20000\,{\rm deg}^2$, time-domain LSST survey (e.g., LSST Science Collaboration et al. 2009) will recover a nearly complete sample of RRLs out to $\gtrsim 350$ kpc by the completion of the 10-year survey (Ivezić et al. 2008; Oluseyi et al. 2012; VanderPlas & Ivezić 2015, see also Fig. 2 of Baker & Willman 2015). The HiTS results presented here are part of a larger ongoing LSST precursor observing program we are conducting, with which we will continue to map the outer limits of the Galactic halo with RR Lyrae variables, and develop tools for interpretation that lay the groundwork for exploiting the huge samples of RRLs in the LSST era.

G.M., F.F. and J.M. acknowledge support from the Ministry of Economy, Development, and Tourism's Millennium Science Initiative through grant IC120009, awarded to The Millennium Institute of Astrophysics (MAS), and from Conicyt through the Fondecyt Initiation into Research project No. 11130228. G.M. acknowledges CONICYT-PCHA/MagísterNacional/2016-22162353. R. R. M. acknowledges partial support from BASAL Project PFB-06 as well as FONDECYT project N°1170364. F.F. acknowledges support from BASAL Project PFB–03 and through the Programme of International Cooperation project DPI20140090. J.M. acknowledges the support from CONICYT Chile through CONICYT-PCHA/Doctorado-Nacional/2014-21140892, and Basal Project PFB-03, Centro de Modelamiento Matemico (CMM), Universidad de Chile. L.G. was supported in part by the US National Science Foundation under Grant AST-1311862. We acknowledge support from Conicyt through the infrastructure Quimal project No. 140003. Powered@NLHPC: this research was partially supported by the supercomputing infrastructure of the NLHPC (ECM-02). This project used data obtained with the Dark Energy Camera (DECam), which was constructed by the Dark Energy Survey (DES) collaboration. Funding for the DES Projects has been provided by the U.S. Department of Energy, the U.S. National Science Foundation, the Ministry of Science and Education of Spain, the Science and Technology Facilities Council of the United Kingdom, the Higher Education Funding Council for England, the National Center for Supercomputing Applications at the University of Illinois at Urbana-Champaign, the Kavli Institute of Cosmological Physics at the University of Chicago, Center for Cosmology and Astro-Particle Physics at the Ohio State University, the Mitchell Institute for Fundamental Physics and Astronomy at Texas A&M University, Financiadora de Estudos e Projetos, Fundação Carlos Chagas Filho de Amparo, Financiadora de Estudos e Projetos, Fundação Carlos Chagas Filho de Amparo à Pesquisa do Estado do Rio de Janeiro, Conselho Nacional de Desenvolvimento Científico e Tecnológico and the Ministério da Ciência, Tecnologia e Inovação, the Deutsche Forschungsgemeinschaft and the Collaborating Institutions in the Dark Energy Survey. The Collaborating Institutions are Argonne National Laboratory, the University of California at Santa Cruz, the University of Cambridge, Centro de Investigaciones Enérgeticas, Medioambientales y TecnológicasMadrid, the University of Chicago, University College London, the DES-Brazil Consortium, the University of Edinburgh, the Eidgenössische Technische Hochschule (ETH) Zürich, Fermi National Accelerator Laboratory, the University of Illinois at Urbana-Champaign, the Institut de Ciències de l'Espai (IEEC/CSIC), the Institut de Física d'Altes Energies, Lawrence Berkeley National Laboratory, the Ludwig-Maximilians Universität München and the associated Excellence Cluster Universe, the University of Michigan, the National Optical Astronomy Observatory, the University of Nottingham, the Ohio State University, the University of Pennsylvania, the University of Portsmouth, SLAC National Accelerator Laboratory, Stanford University, the University of Sussex, and Texas A&M University. R.R.M. acknowledges partial support from BASAL project PFB-06 as well as FONDECYT project N°1170364.

APPENDIX

TABLES AND LIGHTCURVES

In this section, we include tables with the main properties of the sample of RRLs found by HiTS, as well as phased light curves for the stars that are not shown in Figure 8. Table 5 displays information about the RRLs in the Sextans dSph, while Table 6 shows the information of the rest of the sample.

Table 5
RR Lyrae stars found in the Sextans dSph by HiTS. In the columun Previous ID, stars with prefixes V and C are taken from Amigo et al. (2012), with the former corresponding to detections made by Mateo et al. (1995). The RRLs with prefixes LSQ are stars from LSQ (Zinn et al. 2014), and the ones labeled as VV, VI and MV are from Lee et al. (2003). Stars with MV come from Mateo et al. (1995) as well. Note that only 4 of our RRLs are classified as RRLs in Lee et al. (2003).

ID	R.A. (deg)	DEC (deg)	$\langle g \rangle$	Period (days)	Amplitude	d_{H} (kpc)	Type	N	Previous ID
HiTS100815-021625	152.06402	-2.27369	20.3	0.6973	0.85	84	ab	30	-
HiTS100936-015356	152.40198	-1.89876	20.4	0.346	0.65	84	c	38	-
HiTS100958-015954	152.49002	-1.99832	20.4	0.6497	0.97	84	ab	36	-
HiTS101010-021303	152.54151	-2.21761	20.4	0.6775	0.65	87	ab	37	-
HiTS101011-012028	152.54492	-1.34107	20.4	0.675	0.67	86	ab	38	-

Note. — Table 5 is published in its entirety in the machine-readable format. A portion is shown here for guidance regarding its form and content.

Table 6
Full list of the RRLs presented in this work, excluding the candidates in the Sextans dSph galaxy.

ID	R.A. (deg)	DEC (deg)	$\langle g \rangle$	Period (days)	Amplitude	d_{H} (kpc)	Type	N
HiTS095845+023118	149.68616	2.52172	17.9	0.6453	0.36	28	ab	18
HiTS100129+001100	150.37090	0.18338	16.4	0.6098	1.30	13	ab	21
HiTS100207+012232	150.52751	1.37554	16.5	0.7208	0.91	15	ab	16
HiTS100236+030023	150.64878	3.00649	16.1	0.6079	1.02	12	ab	20
HiTS100838-020312	152.15703	-2.05345	17.4	0.5799	1.28	20	ab	38

Note. — Table 6 is published in its entirety in the machine-readable format. A portion is shown here for guidance regarding its form and content.

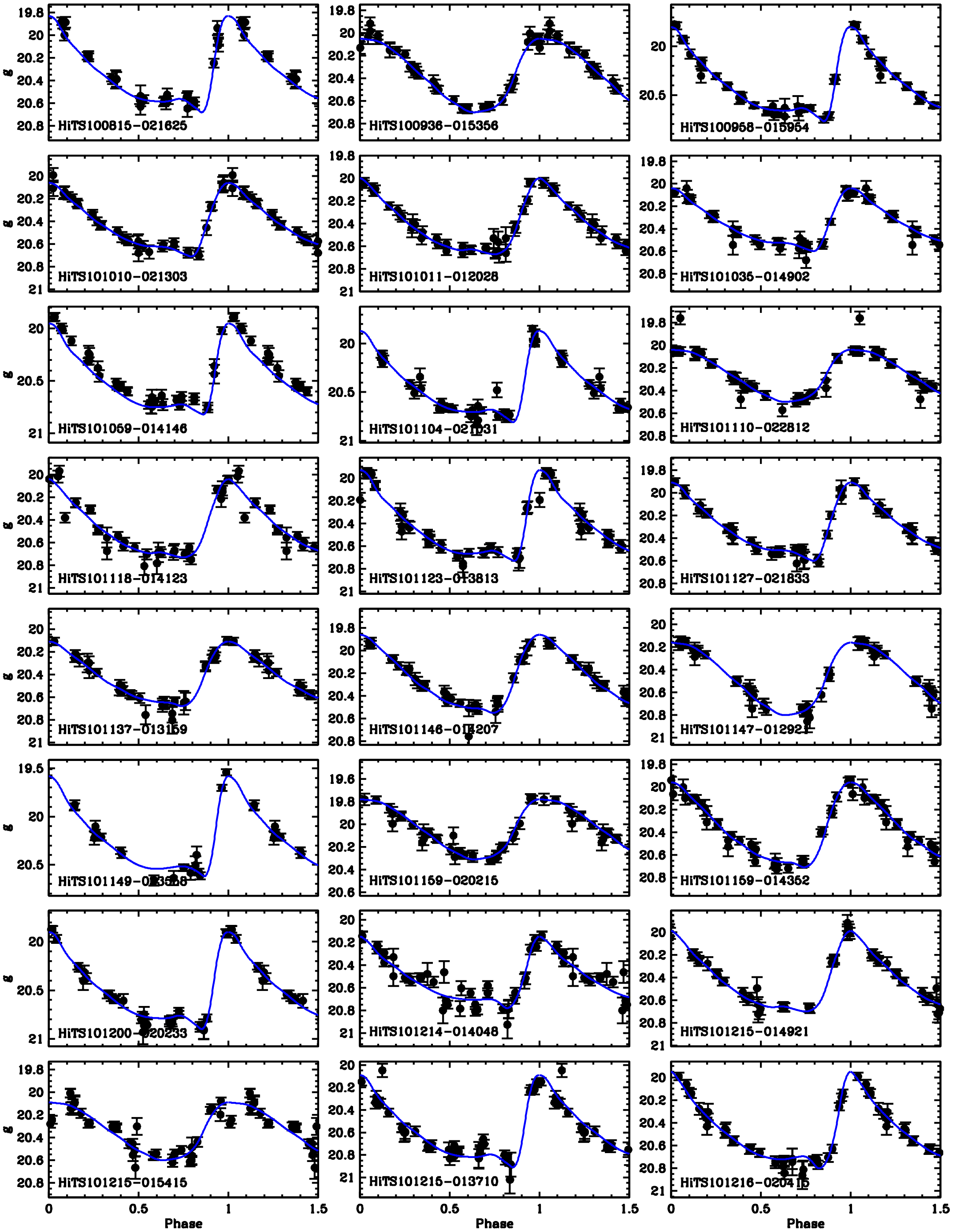

Figure 12. Phased light curves of RR Lyrae stars in the Sextans dwarf spheroidal galaxy (1/3).

Figures 12 to 14 display the phased light curves of the RR Lyrae stars in the Sextans dwarf spheroidal galaxy. On the other hand, Figures 15-18 show the light curves of the field RR Lyrae stars closer than 90 kpc.

REFERENCES

Abadi, M. G., Navarro, J. F., & Steinmetz, M. 2006, MNRAS, 365, 747

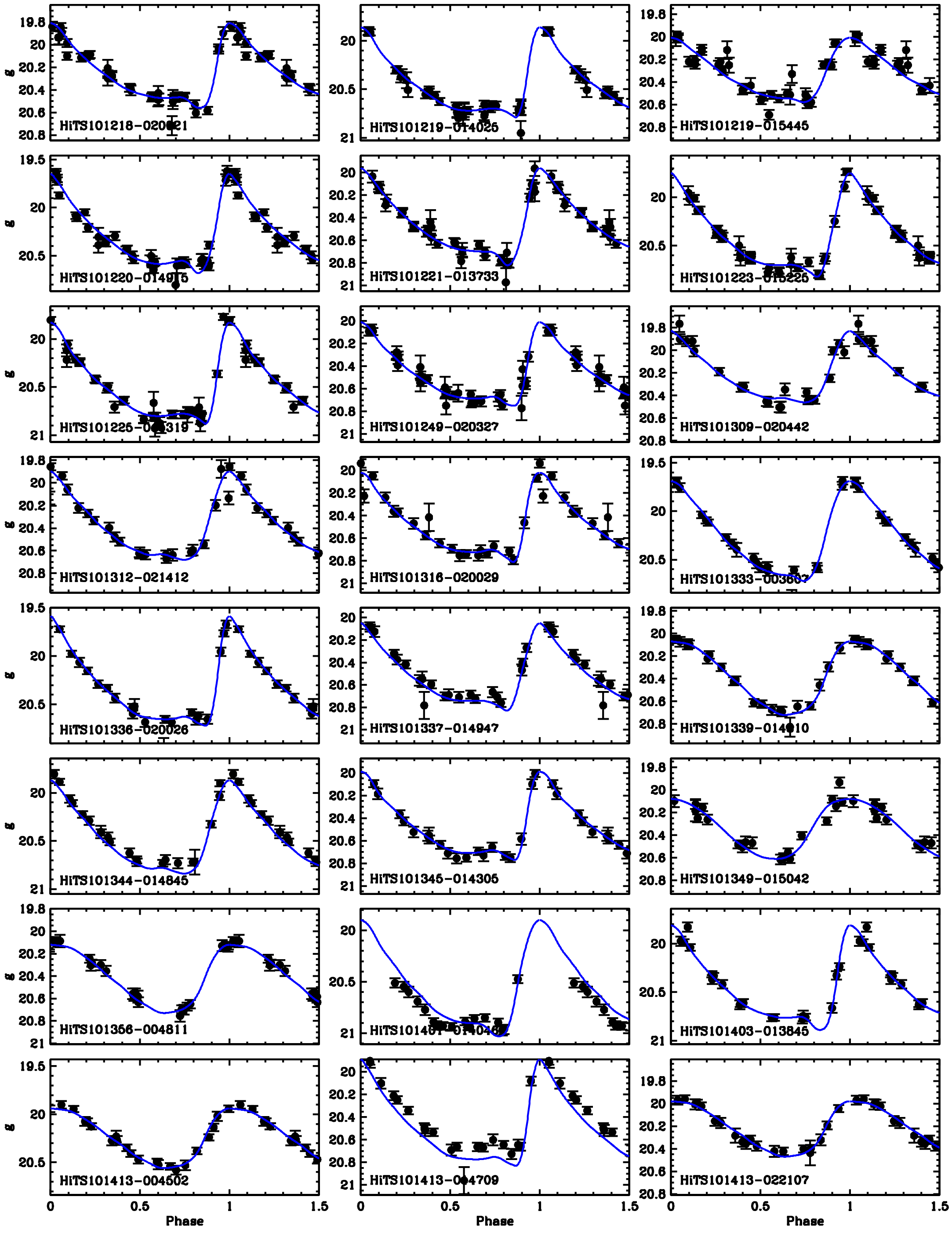

Figure 13. Phased light curves of RR Lyrae stars in the Sextans dwarf spheroidal galaxy (2/3).

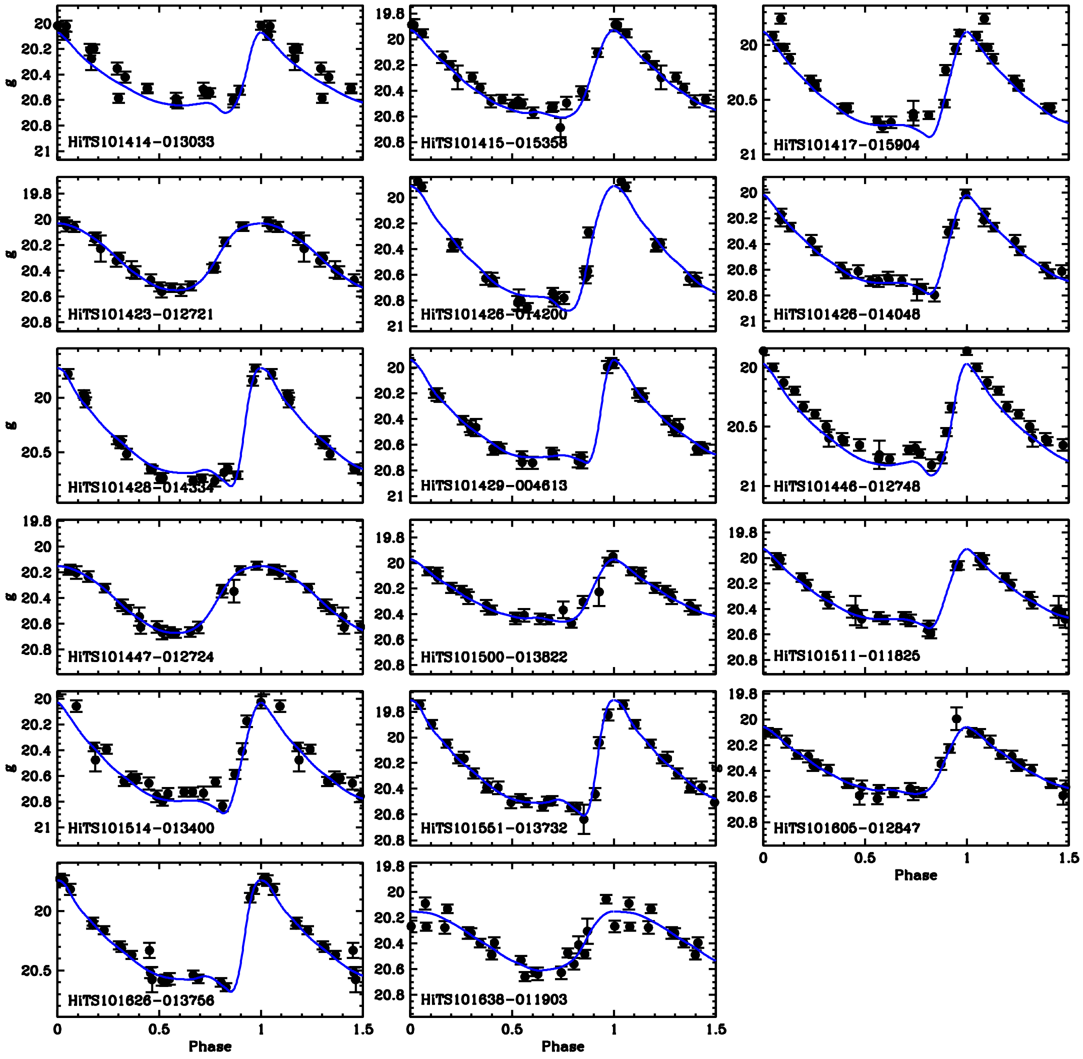

Figure 14. Phased light curves of RR Lyrae stars in the Sextans dwarf spheroidal galaxy (3/3).

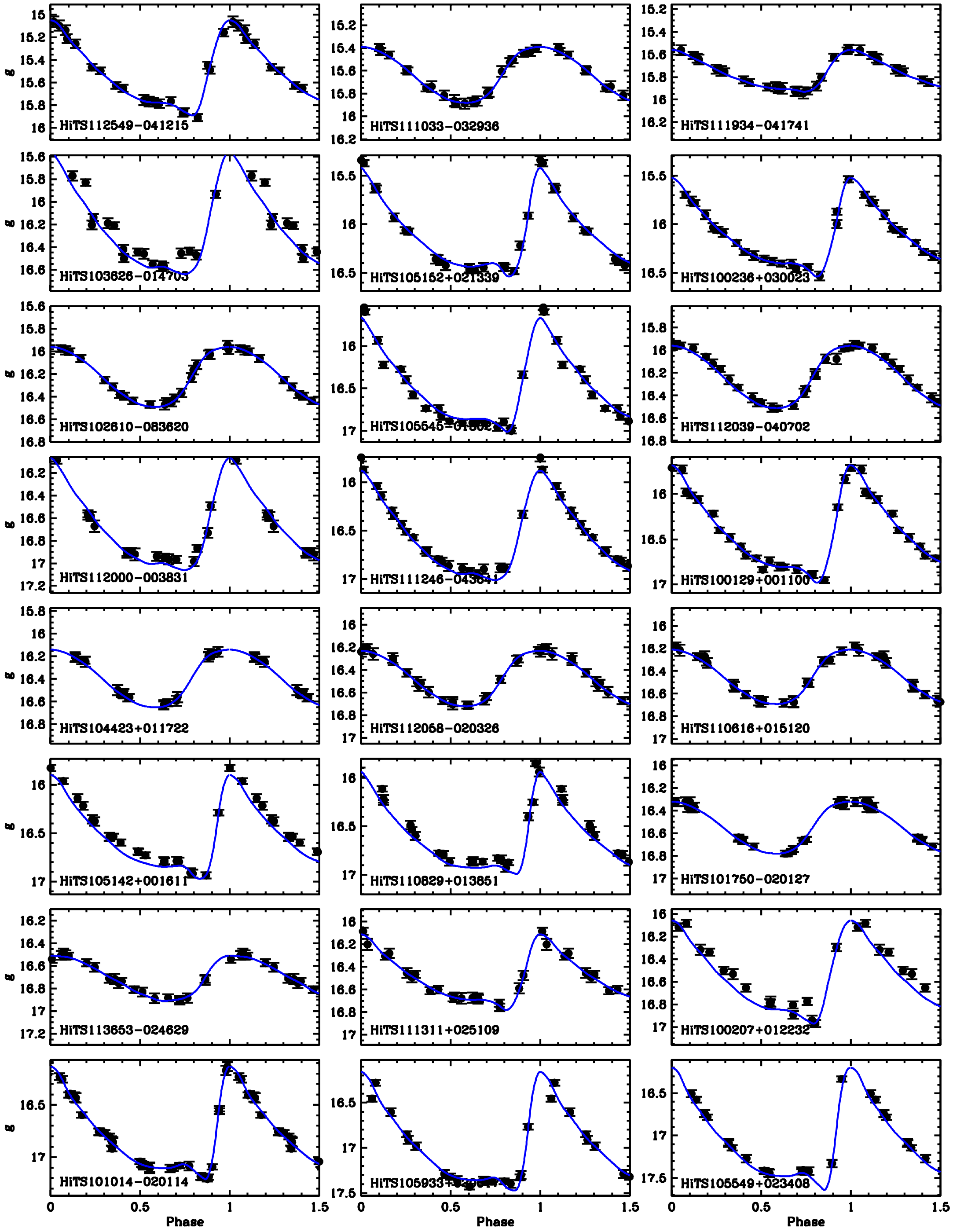

Figure 15. Phased light curves of nearby (< 90 kpc) RR Lyrae stars in the field (1/4).

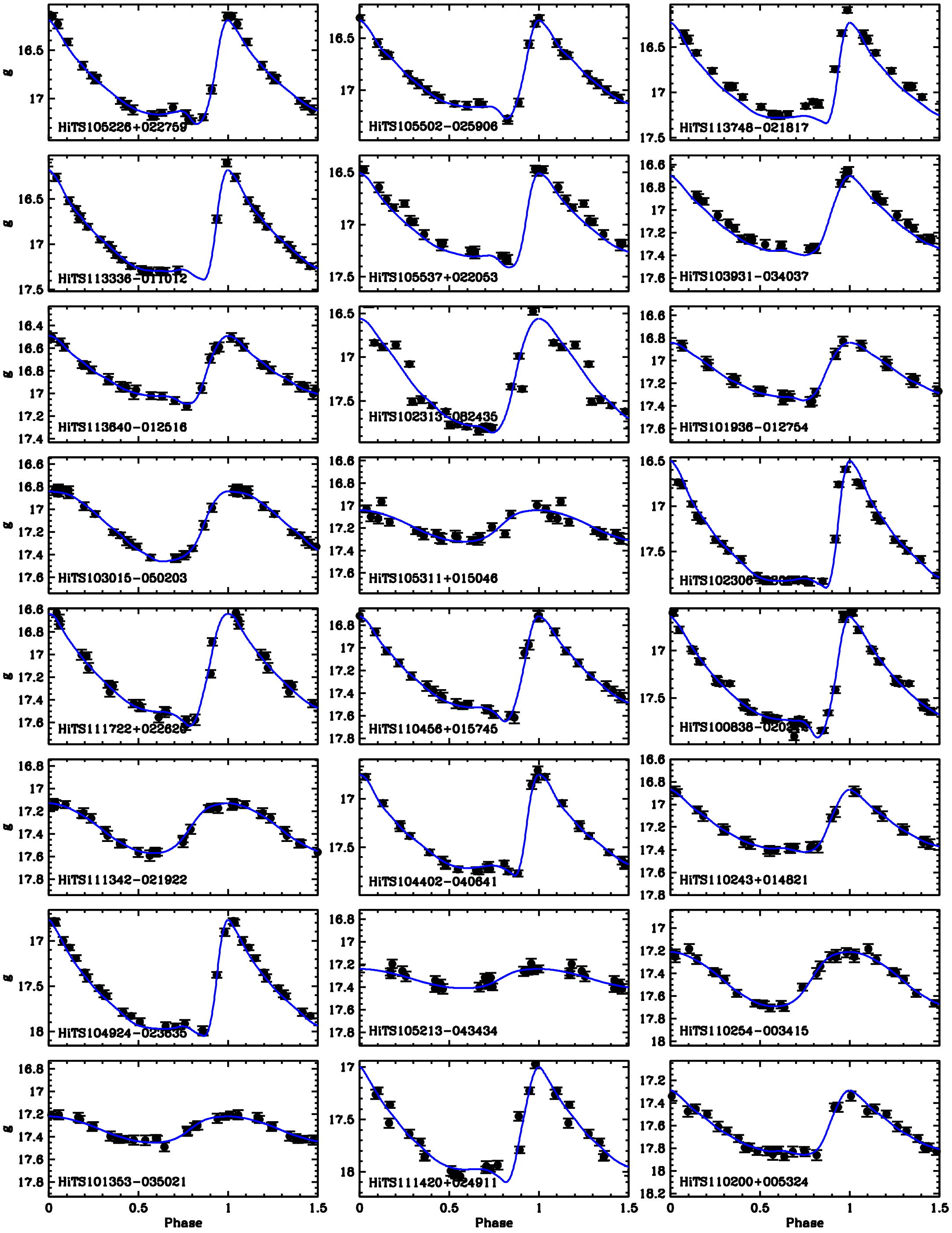

Figure 16. Phased light curves of nearby (< 90 kpc) RR Lyrae stars in the field (2/4).

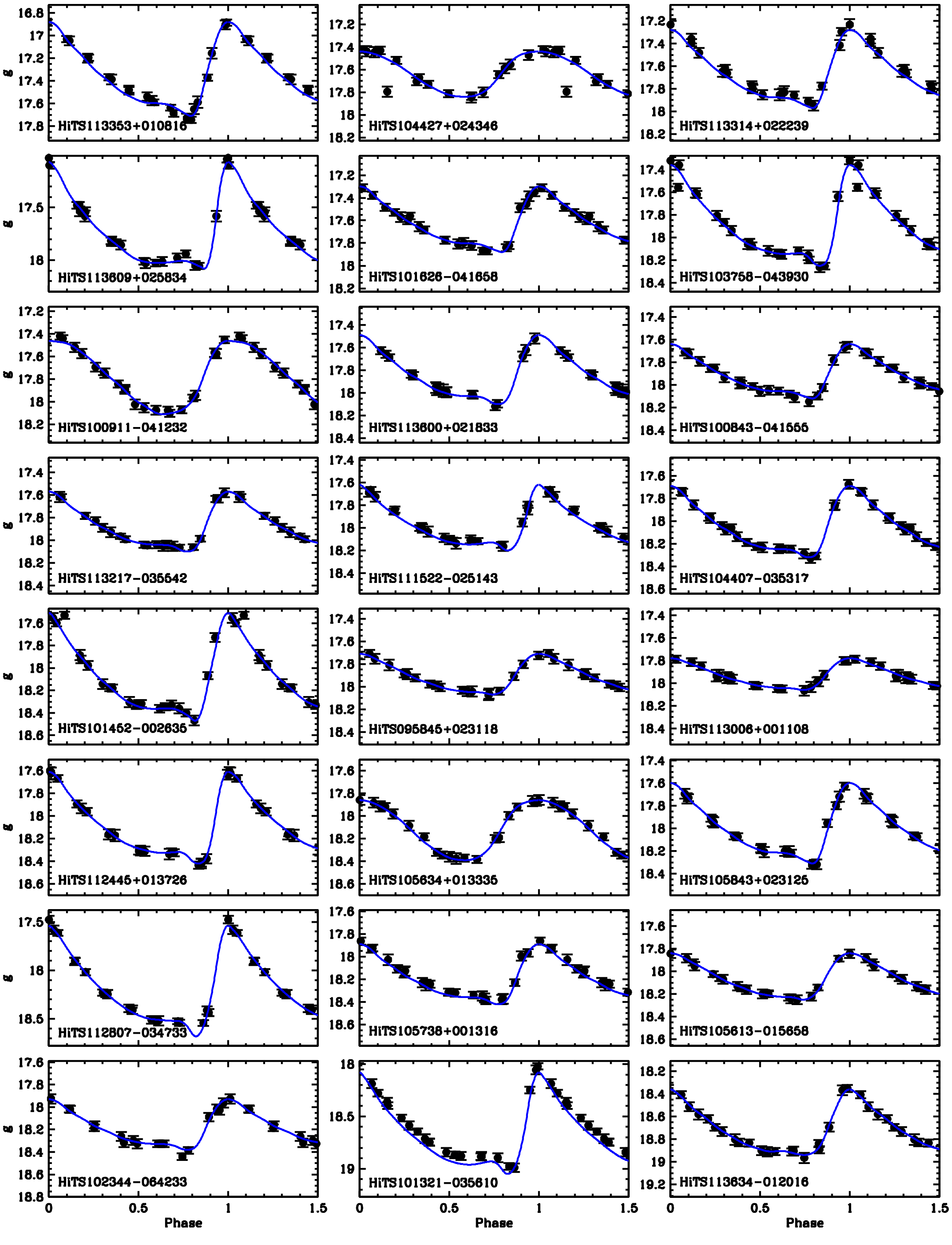

Figure 17. Phased light curves of nearby (< 90 kpc) RR Lyrae stars in the field (3/4).

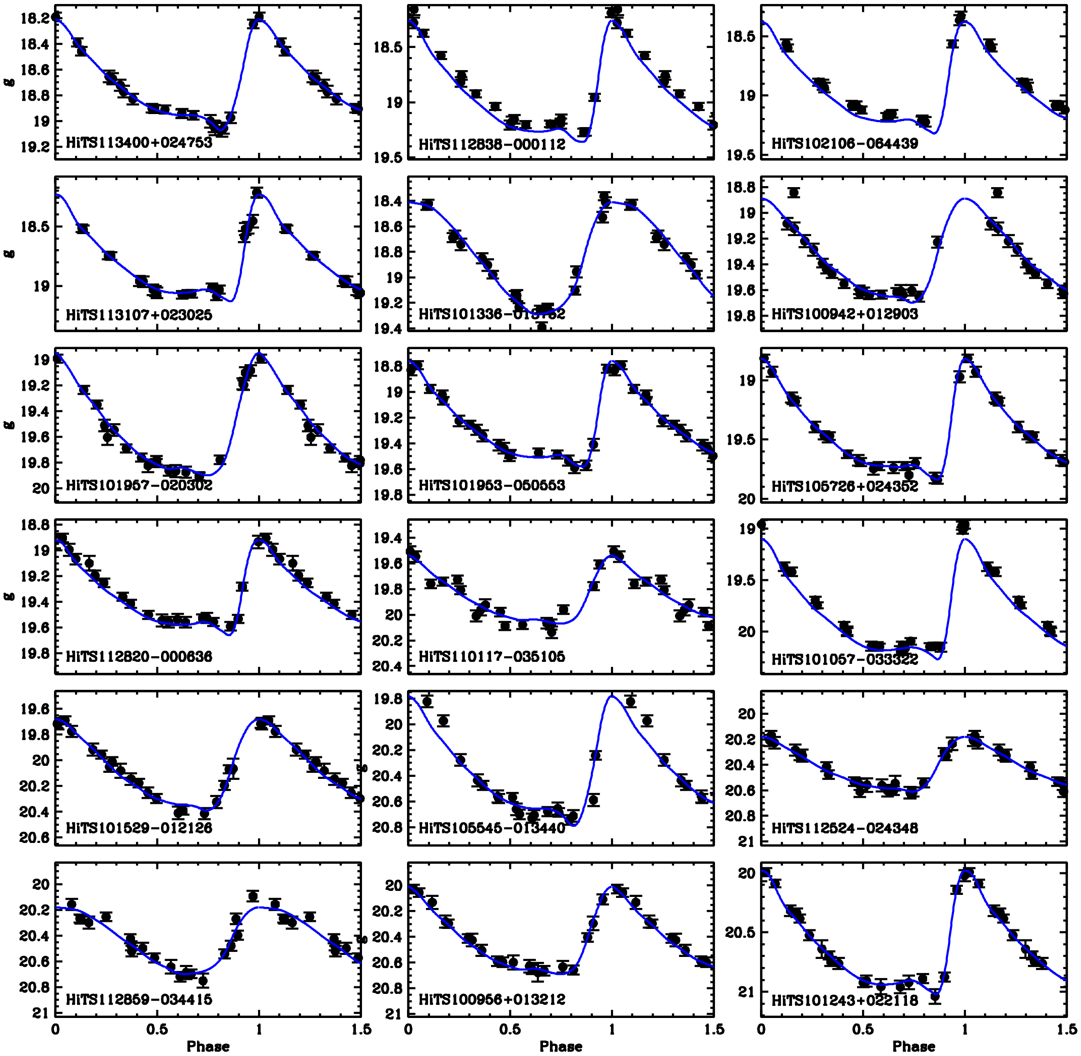

Figure 18. Phased light curves of nearby (< 90 kpc) RR Lyrae stars in the field (4/4).

Abbas, M. A., Grebel, E. K., Martin, N. F., et al. 2014, MNRAS, 441, 1230
Abbott, T., Abdalla, F. B., Alleksic, J. et al. 2016, MNRAS, 460, 1270
Ablimit, I., & Zhao, G. 2017, ApJ, 846, 10
Akhter, S., Da Costa, G. S., Keller, S. C., et al. 2012, ApJ, 756, 23
Amigo Fuentes, P., Catelan, M., Zoccali, M., & Pontificia Universidad Católica de Chile. Facultad de Física. The Milky Way in the making : . : Clues into the formation history of our galaxy from time-resolved photometry of globular clusters and dwarf satellite galaxies. Santiago, Chile, 2012.
Baker, M., & Willman, B. 2015, AJ, 150, 160
Bell, E. F., Zucker, D. B., Belokurov, V., et al. 2008, ApJ, 680, 295-311
Belokurov, V., Evans, N. W., Irwin, M. J., et al. 2007, ApJ, 658, 337
Bertin, E., & Arnouts, S. 1996, A&AS, 117, 393
Bochanski, J. J., Willman, B., Caldwell, N., et al. 2014, ApJ, 790, LL5
Boettcher, E., Willman, B., Fadely, R., et al. 2013, AJ, 146, 94
Bonaca, A., Jurić, M., Ivezić, Ž., et al. 2012, AJ, 143, 105
Boubert, D., Belokurov, V., Erkal, D., et al. 2017, arXiv:1711.07493
Brown, W. R., Geller, M. J., Kenyon, S. J., et al. 2005, ApJ, 622, L33
Bullock, J. S., & Johnston, K. V. 2005, ApJ, 635, 931
Cáceres, C., & Catelan, M. 2008, ApJS, 179, 242
Cacciari, C., & Clementini, G. 2003, in Stellar Candles for the Extragalactic Distance Scale, ed. D. Alloin & W. Gieren (Lecture Notes in Physics, Vol. 635; Berlin: Springer), 105
Carlin, J. L., Yam, W., Casetti-Dinescu, D. I., et al. 2012, ApJ, 753, 145
Carollo, D., Beers, T. C., Lee, Y. S., et al. 2007, Nature, 450, 1020
Catelan, M., Pritzl, B. J., & Smith, H. A. 2004, ApJS, 154, 633
Catelan, M., & Cortés, C. 2008, ApJ, 676, L135
Catelan, M. 2009, Ap&SS, 320, 261
Catelan, M., & Smith, H. A. 2015, Pulsating Stars (New York: Wiley, VCH)
Clementini, G. 2010, in Variable Stars, the Galactic Halo and Galaxy Formation, ed. C. Sterken, N. Samus, & L. Szabados (Russia: Sternberg Astronomical Institute of Moscow Univ.), 107
Clementini, G. 2014, in Proc. IAU Symp. 301, Precision Asteroseismology,ed. J. A. Guzik et al. (Cambridge: Cambridge Univ. Press), 129
Cohen, J. G., Sesar, B., Banholzer, S., et al. 2015, arXiv:1509.05997
Collins, M. L. M., Tollerud, E. J., Sand, D. J., et al. 2016, arXiv:1608.05710
Cooper, A. P., Cole, S., Frenk, C. S., et al. 2010, MNRAS, 406, 744
Cooper, A. P., D'Souza, R., Kauffmann, G., et al. 2013, MNRAS, 434, 3348
Cortés, C., & Catelan, M. 2008, ApJS, 177, 362-372
Das, P., Williams, A., & Binney, J. 2016, MNRAS, 463, 3169
De Propris, R., Harrison, C. D., & Mares, P. J. 2010, ApJ, 719, 1582
Deason, A. J., Belokurov, V., & Evans, N. W. 2011, MNRAS, 416, 2903
Deason, A. J., Belokurov, V., Evans, N. W., et al. 2013, ApJ, 763, 113
Deason, A. J., Belokurov, V., Koposov, S. E., et al. 2014, ApJ, 787, 30
Demarque, P., Zinn, R., Lee, Y.-W., et al. 2000, AJ, 119, 1398
Drake, A. J., Catelan, M., Djorgovski, S. G., et al. 2013, ApJ, 763, 32
Drake, A. J., Catelan, M., Djorgovski, S. G., et al. 2013, ApJ, 765, 154
Drake, A. J., Graham, M. J., Djorgovski, S. G., et al. 2014, ApJS, 213, 9
Drake, A. J., Djorgovski, S. G., Catelan, M., et al. 2017, MNRAS, 469, 3688
Duffau, S., Zinn, R., Vivas, A. K., et al. 2006, ApJ, 636, L97
Duffau, S., Vivas, A. K., Zinn, R., et al. 2014, A&A, 566, A118
Eadie, G. M., & Harris, W. E. 2016, ApJ, 829, 108
Fernández-Trincado, J. G., Vivas, A. K., Mateu, C. E., et al. 2015, A&A, 574, A15
Fiorentino, G., Bono, G., Monelli, M., et al. 2015, ApJ, 798, L12
Flaugher, B., Diehl, H. T., Honscheid, K., et al. 2015, AJ, 150, 150
Foreman-Mackey, D., Hogg, D. W., Lang, D., et al. 2013, PASP, 125, 306
Förster, F., Maureira, J. C., San Martín, J., et al. 2016, ApJ, 832, 155
Garling, C., Willman, B., Sand, D. J., et al. 2017, arXiv:1711.07469
Gawiser, E., van Dokkum, P. G., Herrera, D., et al. 2006, ApJS, 162, 1
Geha, M., Wechsler, R. H., Mao, Y.-Y., et al. 2017, ApJ, 847, 4
Grillmair, C. J. 2006, ApJ, 645, L37
Grillmair, C. J., & Carlin, J. L. 2016, Tidal Streams in the Local Group and Beyond, 420, 87
Grillmair, C. J., Hetherington, L., Carlberg, R. G., et al. 2015, ApJ, 812, L26
Hendel, D., Scowcroft, V., Johnston, K. V., et al. 2017, arXiv:1711.04663
Ibata, R., Irwin, M., Lewis, G. F., et al. 2001, ApJ, 547, L133
Iorio, G., Belokurov, V., Erkal, D., et al. 2017, arXiv:1707.03833
Irwin, M. J., Bunclark, P. S., Bridgeland, M. T., et al. 1990, MNRAS, 244, 16P
Irwin, M., & Hatzidimitriou, D. 1995, MNRAS, 277, 1354
Ivezić, Ž., Vivas, A. K., Lupton, R. H., et al. 2005, AJ, 129, 1096
Ivezić, Ž., Tyson, J. A., Abel, B., et al. 2008, arXiv:0805.2366
Johnston, K. V., Sheffield, A. A., Majewski, S. R., et al. 2012, ApJ, 760, 95
Jurić, M., Ivezić, Ž., Brooks, A., et al. 2008, ApJ, 673, 864-914
Keller, S. C., da Costa, G. S., & Prior, S. L. 2009, MNRAS, 394, 1045
Keller, S. C., Murphy, S., Prior, S., et al. 2008, ApJ, 678, 851-864
Kirby, E. N., Lanfranchi, G. A., Simon, J. D., et al. 2011, ApJ, 727, 78
Law, D. R., & Majewski, S. R. 2010, ApJ, 718, 1128
Law, D. R., & Majewski, S. R. 2016, Tidal Streams in the Local Group and Beyond, 420, 31
Lee, M. G., Park, H. S., Park, J.-H., et al. 2003, AJ, 126, 2840
Lomb, N. R. 1976, Ap&SS, 39, 447
Longmore, A. J., Fernley, J. A., & Jameson, R. F. 1986, MNRAS, 220, 279
LSST Science Collaboration, Abell, P. A., Allison, J., et al. 2009, arXiv:0912.0201
Majewski, S. R., Skrutskie, M. F., Weinberg, M. D., et al. 2003, ApJ, 599, 1082
Marconi, M. 2009, American Institute of Physics Conference Series, 1170, 223
Martínez, J., Förster, F., Protopapas, P., et al. 2017, ApJ, submitted
Mateo, M., Nemec, J., Irwin, M., et al. 1991, AJ, 101, 892
Mateo, M., Fischer, P., & Krzeminski, W. 1995, AJ, 110, 2166
Mateo, M. L. 1998, ARA&A, 36, 435
McConnachie, A. W. 2012, AJ, 144, 4
Medina, G. E., Muñoz, R. R., Vivas, A. K., et al. 2017, ApJ, 845, L10
Moretti, M. I., Dall'Ora, M., Ripepi, V., et al. 2009, ApJ, 699, L125
Newberg, H. J., Yanny, B., Rockosi, C., et al. 2002, ApJ, 569, 245
Newberg, H. J., Yanny, B., Cole, N., et al. 2007, ApJ, 668, 221
Newberg, H. J., Willett, B. A., Yanny, B., et al. 2010, ApJ, 711, 32
Oluseyi, H. M., Becker, A. C., Culliton, C., et al. 2012, AJ, 144, 9
Oosterhoff, P. T. 1939, The Observatory, 62, 104
Palaversa, L., Ivezić, Ž., Eyer, L., et al. 2013, AJ, 146, 101
Pila-Díez, B., de Jong, J. T. A., Kuijken, K., et al. 2015, A&A, 579, A38
Pillepich, A., Vogelsberger, M., Deason, A., et al. 2014, MNRAS, 444, 237
Prior, S. L., Da Costa, G. S., & Keller, S. C. 2009, ApJ, 704, 1327
Roderick, T. A., Jerjen, H., Da Costa, G. S., et al. 2016, MNRAS, 460, 30
Saha, A. 1985, ApJ, 289, 310
Sanderson, R. E. 2016, ApJ, 818, 41
Sanderson, R. E., Secunda, A., Johnston, K. V., et al. 2017, MNRAS, 470, 5014
Scargle, J. D. 1982, ApJ, 263, 835
Schlafly, E. F., & Finkbeiner, D. P. 2011, ApJ, 737, 103

Schlegel, D. J., Finkbeiner, D. P., & Davis, M. 1998, ApJ, 500, 525
Sesar, B., Ivezić, Ž., Lupton, R. H., et al. 2007, AJ, 134, 2236
Sesar, B., Ivezić, Ž., Grammer, S. H., et al. 2010, ApJ, 708, 717
Sesar, B., Jurić, M., & Ivezić, Ž. 2011, ApJ, 731, 4
Sesar, B., Ivezić, Ž., Stuart, J. S., et al. 2013, AJ, 146, 21
Sesar, B., Grillmair, C. J., Cohen, J. G., et al. 2013, ApJ, 776, 26
Sesar, B., Banholzer, S. R., Cohen, J. G., et al. 2014, ApJ, 793, 135
Sesar, B., Hernitschek, N., Mitrović, S., et al. 2017a, AJ, 153, 204
Sesar, B., Hernitschek, N., Dierickx, M. I. P., et al. 2017b, ApJ, 844, L4
Simon, J. D., & Geha, M. 2007, ApJ, 670, 313
Slater, C. T., Nidever, D. L., Munn, J. A., et al. 2016, ApJ, 832, 206
Tsujimoto, T., Miyamoto, M., & Yoshii, Y. 1997, Hipparcos - Venice '97, 402, 639
VanderPlas, J., Connolly, A. J., Ivezic, Z., et al. 2012, in Proc. Conf. Intelligent Data Understanding (CIDU), ed. K. Das, N.V. Chawla, & A. N. Srivastava (Boulder, CO: NCAR), 47
VanderPlas, J. T., & Ivezić, Ž. 2015, ApJ, 812, 18
Valdes, F., Gruendl, R., & DES Project 2014, Astronomical Data Analysis Software and Systems XXIII, 485, 379
Vivas, A. K., Zinn, R., Andrews, P., et al. 2001, ApJ, 554, L33
Vivas, A. K., Zinn, R., Abad, C., et al. 2004, AJ, 127, 1158
Vivas, A. K., & Zinn, R. 2006, AJ, 132, 714
Vivas, A. K., Olsen, K., Blum, R., et al. 2016, AJ, 151, 118
Vivas, A. K., Zinn, R., Farmer, J., et al. 2016, ApJ, 831, 165
Vivas, A. K., Saha, A., Olsen, K., et al. 2017, AJ, 154, 85
Watkins, L. L., Evans, N. W., Belokurov, V., et al. 2009, MNRAS, 398, 1757
Watkins, L. L., Evans, N. W., & An, J. H. 2010, MNRAS, 406, 264
Wetterer, C. J., & McGraw, J. T. 1996, AJ, 112, 1046
Xue, X.-X., Rix, H.-W., Ma, Z., et al. 2015, ApJ, 809, 144
Zechmeister, M., Kürster, M. 2009, A&A, 496, 577
Zinn, R. 1993, The Globular Cluster-Galaxy Connection, ASP Conference Series, Vol 48, 38
Zinn, R., Horowitz, B., Vivas, A. K., et al. 2014, ApJ, 781, 22
Zolotov, A., Willman, B., Brooks, A. M., et al. 2009, ApJ, 702, 1058

Bibliography

Abadi, M. G., Navarro, J. F., & Steinmetz, M. 2006, MNRAS, 365, 747

Abbas, M. A., Grebel, E. K., Martin, N. F., et al. 2014, MNRAS, 441, 1230

Abbott, T., Abdalla, F. B., Alleksic, J. et al. 2016, MNRAS, 460, 1270

Ablimit, I., & Zhao, G. 2017, ApJ, 846, 10

Ahn, C. P., Alexandroff, R., Allende Prieto, C., et al. 2014, ApJS, 211, 17

Akhter, S., Da Costa, G. S., Keller, S. C., & Schmidt, B. P. 2012, ApJ, 756, 23

Amigo Fuentes, P., Catelan, M., Zoccali, M., & Pontificia Universidad Católica de Chile. Facultad de Física. The Milky Way in the making : . : Clues into the formation history of our galaxy from time-resolved photometry of globular clusters and dwarf satellite galaxies. Santiago, Chile.

Baade, W. & Hubble, E. 1939, PASP, 51, 40

Bailey, S. I. 1902, Annals of Harvard College Observatory, 38,

Baker, M., & Willman, B. 2015, AJ, 150, 160

Bechtol, K., Drlica-Wagner, A., Balbinot, E., et al. 2015, ApJ, 807, 50

Bell, E. F., Zucker, D. B., Belokurov, V., et al. 2008, ApJ, 680, 295-311

Belokurov, V., Zucker, D. B., Evans, N. W., et al. 2006, ApJ, 647, L111

Belokurov, V., Zucker, D. B., Evans, N. W., et al. 2006, ApJ, 642, L137

Belokurov, V., Evans, N. W., Irwin, M. J., et al. 2007, ApJ, 658, 337

Belokurov, V., Walker, M. G., Evans, N. W., et al. 2008, ApJ, 686, L83

Belokurov, V., Walker, M. G., Evans, N. W., et al. 2010, ApJ, 712, L103

Benedict, G. F., McArthur, B. E., Feast, M. W., et al. 2011, AJ, 142, 187

Bertelli G., Girardi L., Marigo P., et al. 2008, A&A, 484, 815

Bertin, E., & Arnouts, S. 1996, A&AS, 117, 393

Blaña, M., Fellhauer, M., & Smith, R. 2012, A&A, 542, A61

Blažko, S. 1907, Astronomische Nachrichten, 175, 327

Bochanski, J. J., Willman, B., Caldwell, N., et al. 2014, ApJ, 790, LL5

Boettcher, E., Willman, B., Fadely, R., et al. 2013, AJ, 146, 94

Bonaca, A., Jurić, M., Ivezić, Ž., et al. 2012, AJ, 143, 105

Boubert, D., Belokurov, V., Erkal, D., & Iorio, G. 2017, arXiv:1711.07493

Boylan-Kolchin, M., Bullock, J. S., Sohn, S. T., Besla, G., & van der Marel, R. P. 2013, ApJ, 768, 140

Brown, W. R., Geller, M. J., Kenyon, S. J., & Kurtz, M. J. 2005, ApJ, 622, L33

Bullock, J. S., & Johnston, K. V. 2005, ApJ, 635, 931

Cacciari, C., & Clementini, G. 2003, in Stellar Candles for the Extragalactic Distance Scale, ed. D. Alloin & W. Gieren (Lecture Notes in Physics, Vol. 635; Berlin: Springer), 105

Cáceres, C., & Catelan, M. 2008, ApJS, 179, 242

Carlin, J. L., Yam, W., Casetti-Dinescu, D. I., et al. 2012, ApJ, 753, 145

Carollo, D., Beers, T. C., Lee, Y. S., et al. 2007, Nature, 450, 1020

Catelan, M., Pritzl, B. J., & Smith, H. A. 2004, ApJS, 154, 633

Catelan, M., & Cortés, C. 2008, ApJ, 676, L135

Catelan, M. 2009, Ap&SS, 320, 261

Catelan, M., & Smith, H. A. 2015, Pulsating Stars (New York: Wiley, VCH)

Chambers, K. C., Magnier, E. A., Metcalfe, N., et al. 2016, arXiv:1612.05560

Clementini, G. 2010, Variable Stars, the Galactic halo and Galaxy Formation, 107

Clementini, G. 2014, in Proc. IAU Symp. 301, Precision Asteroseismology,ed. J. A. Guzik et al. (Cambridge: Cambridge Univ. Press), 129

Cohen, J. G., Sesar, B., Banholzer, S., & PTF Consortium, t. 2015, arXiv:1509.05997

Collins, M. L. M., Tollerud, E. J., Sand, D. J., et al. 2016, arXiv:1608.05710

Cooper, A. P., Cole, S., Frenk, C. S., et al. 2010, MNRAS, 406, 744

Cooper, A. P., D'Souza, R., Kauffmann, G., et al. 2013, MNRAS, 434, 3348

Cortés, C., & Catelan, M. 2008, ApJS, 177, 362-372

de Jong, J. T. A., Martin, N. F., Rix, H.-W., et al. 2010, ApJ, 710, 1664

Das, P., Williams, A., & Binney, J. 2016, MNRAS, 463, 3169

De Propris, R., Harrison, C. D., & Mares, P. J. 2010, ApJ, 719, 1582

Deason, A. J., Belokurov, V., & Evans, N. W. 2011, MNRAS, 416, 2903

Deason, A. J., Belokurov, V., Evans, N. W., & Johnston, K. V. 2013, ApJ, 763, 113

Deason, A. J., Belokurov, V., Koposov, S. E., et al. 2014, ApJ, 787, 30

Demarque, P., Zinn, R., Lee, Y.-W., et al. 2000, AJ, 119, 1398

Diehl, H. T., Abbott, T. M. C., Annis, J., et al. 2014, Proc. SPIE, 9149, 0

Downes, R. A., Margon, B., Homer, L., & Anderson, S. F. 2004, AJ, 128, 2288

Drake, A. J., Catelan, M., Djorgovski, S. G., et al. 2013, ApJ, 763, 32

Drake, A. J., Catelan, M., Djorgovski, S. G., et al. 2013, ApJ, 765, 154

Drake, A. J., Graham, M. J., Djorgovski, S. G., et al. 2014, ApJS, 213, 9

Drake, A. J., Djorgovski, S. G., Catelan, M., et al. 2017, MNRAS, 469, 3688

Drlica-Wagner, A., Bechtol, K., Rykoff, E. S., et al. 2015, ApJ, 813, 109

Drlica-Wagner, A., Bechtol, K., Allam, S., et al. 2016, ApJ, 833, L5

Duffau, S., Zinn, R., Vivas, A. K., et al. 2006, ApJ, 636, L97

Duffau, S., Vivas, A. K., Zinn, R., Méndez, R. A., & Ruiz, M. T. 2014, A&A, 566, A118

Eadie, G. M., & Harris, W. E. 2016, ApJ, 829, 108

Eyer, L., & Mowlavi, N. 2008, Journal of Physics Conference Series, 118, 012010

De Lee, N. 2008, Ph.D. Thesis,

Fiorentino, G., Bono, G., Monelli, M., et al. 2015, ApJ, 798, L12

Flaugher, B., Diehl, H. T., Honscheid, K., et al. 2015, AJ, 150, 150

Foreman-Mackey, D., Hogg, D. W., Lang, D., & Goodman, J. 2013, PASP, 125, 306

Förster, F., Maureira, J. C., San Martín, J., et al. 2016, arXiv:1609.03567

Gawiser, E., van Dokkum, P. G., Herrera, D., et al. 2006, ApJS, 162, 1

Geha, M., Wechsler, R. H., Mao, Y.-Y., et al. 2017, ApJ, 847, 4

Girardi, L., Grebel, E. K., Odenkirchen, M., et al. 2004, A&A, 422, 205

Graham, M. J., Drake, A. J., Djorgovski, S. G., et al. 2013, MNRAS, 434, 3423

Grillmair, C. J. 2006, ApJ, 645, L37

Grillmair, C. J., & Carlin, J. L. 2016, Tidal Streams in the Local Group and Beyond, 420, 87

Grillmair, C. J., Hetherington, L., Carlberg, R. G., & Willman, B. 2015, ApJ, 812, L26

Hendel, D., Scowcroft, V., Johnston, K. V., et al. 2017, arXiv:1711.04663

Ibata, R., Irwin, M., Lewis, G. F., & Stolte, A. 2001, ApJ, 547, L133

Iorio, G., Belokurov, V., Erkal, D., et al. 2017, arXiv:1707.03833

Irwin, M. J., Bunclark, P. S., Bridgeland, M. T., & McMahon, R. G. 1990, MNRAS, 244, 16P

Irwin, M., & Hatzidimitriou, D. 1995, MNRAS, 277, 1354

Irwin, M. J., Belokurov, V., Evans, N. W., et al. 2007, ApJ, 656, L13

Ivezić, Ž., Vivas, A. K., Lupton, R. H., & Zinn, R. 2005, AJ, 129, 1096

Ivezić, Ž., Tyson, J. A., Abel, B., et al. 2008, arXiv:0805.2366

Jin, S., Martin, N., de Jong, J., et al. 2012, in ASP Conf. Ser. 458, Galactic Archaeology: Near-Field Cosmology and the Formation of the Milky Way, ed. W. Aoki, M. Ishigaki, T. Suda, T. Tsujimoto, & N. Arimoto (San Francisco, CA: ASP), 153

Johnston, K. V., Bullock, J. S., Sharma, S., et al. 2008, ApJ, 689, 936-957

Johnston, K. V., Sheffield, A. A., Majewski, S. R., Sharma, S., & Rocha-Pinto, H. J. 2012, ApJ, 760, 95

Jurić, M., Ivezić, Ž., Brooks, A., et al. 2008, ApJ, 673, 864-914

Jurcsik, J., Hurta, Z., Sódor, Á., et al. 2009, MNRAS, 397, 350

Kauffmann, G., White, S. D. M., & Guiderdoni, B. 1993, MNRAS, 264, 201

Keller, S. C., da Costa, G. S., & Prior, S. L. 2009, MNRAS, 394, 1045

Keller, S. C., Murphy, S., Prior, S., DaCosta, G., & Schmidt, B. 2008, ApJ, 678, 851-864

Kholopov, P. N., Samus, N. N., Frolov, M. S., et al. 1998, Combined General Catalogue of Variable Stars, 4.1 Ed (II/214A). (1998)

Kirby, E. N., Lanfranchi, G. A., Simon, J. D., Cohen, J. G., & Guhathakurta, P. 2011, ApJ, 727, 78

Klypin, A., Kravtsov, A. V., Valenzuela, O., et al. 1999, ApJ, 522, 82

Koposov, S.E., Belokurov, V., Torrealba, G., et al. 2015a, ApJ, 805, 130

Law, D. R., Johnston, K. V., & Majewski, S. R. 2005, ApJ, 619, 807

Law, D. R., & Majewski, S. R. 2010, ApJ, 718, 1128

Law, D. R., & Majewski, S. R. 2016, Tidal Streams in the Local Group and Beyond, 420, 31

Lee, M. G., Park, H. S., Park, J.-H., et al. 2003, AJ, 126, 2840

Lee, M. G., Yuk, I.-S., Park, H. S., et al. 2009, ApJ, 703, 692

Lomb, N. R. 1976, Ap&SS, 39, 447

Longmore, A. J., Fernley, J. A., & Jameson, R. F. 1986, MNRAS, 220, 279

LSST Science Collaboration, Abell, P. A., Allison, J., et al. 2009, arXiv:0912.0201

Majewski, S. R., Skrutskie, M. F., Weinberg, M. D., & Ostheimer, J. C. 2003, ApJ, 599, 1082

Marconi, M., Cignoni, M., Di Criscienzo, M., et al. 2006, MNRAS, 371, 1503

Marconi, M. 2009, American Institute of Physics Conference Series, 1170, 223

Martin, N. F., Nidever, D. L., Besla, G., et al. 2015, ApJ, 804, L5

Mateo, M., Nemec, J., Irwin, M., & McMahon, R. 1991, AJ, 101, 892

Mateo, M., Fischer, P., & Krzeminski, W. 1995, AJ, 110, 2166

Mateo, M. L. 1998, ARA&A, 36, 435

Martínez, J., Förster, F., Protopapas, P., et al. 2017, ApJ, submitted

McConnachie, A. W. 2012, AJ, 144, 4

Medina, G. E., Muñoz, R. R., Vivas, A. K., et al. 2017, ApJ, 845, L10

Medina, G. E., Muñoz, R. R., Vivas, A. K., et al. 2017, ApJ, submitted

Molnár, L., Pál, A., Plachy, E., et al. 2015, ApJ, 812, 2

Moore, B., Ghigna, S., Governato, F., et al. 1999, ApJ, 524, L19

Moretti, M. I., Dall'Ora, M., Ripepi, V., et al. 2009, ApJ, 699, L125

Newberg, H. J., Yanny, B., Rockosi, C., et al. 2002, ApJ, 569, 245

Newberg, H. J., Yanny, B., Cole, N., et al. 2007, ApJ, 668, 221

Newberg, H. J., Willett, B. A., Yanny, B., & Xu, Y. 2010, ApJ, 711, 32

Oluseyi, H. M., Becker, A. C., Culliton, C., et al. 2012, AJ, 144, 9

Oosterhoff, P. T. 1939, The Observatory, 62, 104

Palaversa, L., Ivezić, Ž., Eyer, L., et al. 2013, AJ, 146, 101

Pickering, E. C. 1901, Harvard College Observatory Circular, 54, 1

Pila-Díez, B., de Jong, J. T. A., Kuijken, K., et al. 2015, A&A, 579, A38

Pillepich, A., Vogelsberger, M., Deason, A., et al. 2014, MNRAS, 444, 237

Prior, S. L., Da Costa, G. S., & Keller, S. C. 2009, ApJ, 704, 1327

Roderick, T. A., Jerjen, H., Da Costa, G. S., & Mackey, A. D. 2016, MNRAS,

Rong, Y., Guo, Q., Gao, L., et al. 2017, MNRAS, 470, 4231

Saha, A. 1985, ApJ, 289, 310

Saha, A., Monet, D. G., & Seitzer, P. 1986, AJ, 92, 302

Sand, D. J., Strader, J., Willman, B., et al. 2012, ApJ, 756, 79

Sanderson, R. E. 2016, ApJ, 818, 41

Sanderson, R. E., Secunda, A., Johnston, K. V., et al. 2016, arXiv:1609.06406

Sanderson, R. E., Secunda, A., Johnston, K. V., & Bochanski, J. J. 2017, MNRAS, 470, 5014

Scargle, J. D. 1982, ApJ, 263, 835

Schlafly, E. F., & Finkbeiner, D. P. 2011, ApJ, 737, 103

Schlegel, D. J., Finkbeiner, D. P., & Davis, M. 1998, ApJ, 500, 525

Schwarzschild, M. 1940, Harvard College Observatory Circular, 437, 1

Sesar, B., Ivezić, Ž., Lupton, R. H., et al. 2007, AJ, 134, 2236

Sesar, B., Ivezić, Ž., Grammer, S. H., et al. 2010, ApJ, 708, 717

Sesar, B., Jurić, M., & Ivezić, Ž. 2011, ApJ, 731, 4

Sesar, B., Ivezić, Ž., Stuart, J. S., et al. 2013, AJ, 146, 21

Sesar, B., Grillmair, C. J., Cohen, J. G., et al. 2013, ApJ, 776, 26

Sesar, B., Banholzer, S. R., Cohen, J. G., et al. 2014, ApJ, 793, 135

Sesar, B., Hernitschek, N., Mitrović, S., et al. 2017a, AJ, 153, 204

Sesar, B., Hernitschek, N., Dierickx, M. I. P., et al. 2017b, ApJ, 844, L4

Siegel, M. H. 2006, ApJ, 648, L83

Simon, J. D., & Geha, M. 2007, ApJ, 670, 313

Simon, J. D., Geha, M., Minor, Q. E., et al. 2011, ApJ, 733, 46

Slater, C. T., Nidever, D. L., Munn, J. A., et al. 2016, ApJ, 832, 206

Stellingwerf, R. F. 1978, ApJ, 224, 953

Taylor, M. B. 2005, Astronomical Data Analysis Software and Systems XIV, 347, 29

Taylor, M. B. 2006, Astronomical Data Analysis Software and Systems XV, 351, 666

Torrealba, G., Catelan, M., Drake, A. J., et al. 2015, MNRAS, 446, 2251

Tsujimoto, T., Miyamoto, M., & Yoshii, Y. 1997, Hipparcos - Venice '97, 402, 639

Valdes, F., Gruendl, R., & DES Project. 2014, in ASP Conf. Ser. 485, Astronomical Data Analysis Software and Systems XXIII, ed. N. Manset, & P. Forshay (San Francisco, CA: ASP), 379

VanderPlas, J., Connolly, A. J., Ivezic, Z., et al. 2012, in Proc. Conf. Intelligent Data Understanding (CIDU), ed. K. Das, N. V. Chawla, & A. N. Srivastava (Boulder, CO: NCAR), 47

VanderPlas, J. T., & Ivezić, Ž. 2015, ApJ, 812, 18

Vivas, A. K., Zinn, R., Andrews, P., et al. 2001, ApJ, 554, L33

Vivas, A. K., Zinn, R., Abad, C., et al. 2004, AJ, 127, 1158

Vivas, A. K., & Zinn, R. 2006, AJ, 132, 714

Vivas, A. K., Olsen, K., Blum, R., et al. 2016, AJ, 151, 118

Walker, M. G., Mateo, M., & Olszewski, E. W. 2009, AJ, 137, 3100

Warnick, K., Knebe, A., & Power, C. 2008, MNRAS, 385, 1859

Watkins, L. L., Evans, N. W., Belokurov, V., et al. 2009, MNRAS, 398, 1757

Watkins, L. L., Evans, N. W., & An, J. H. 2010, MNRAS, 406, 264

Wetterer, C. J., & McGraw, J. T. 1996, AJ, 112, 1046

White, S. D. M., & Frenk, C. S. 1991, ApJ, 379, 52

Willman, B., Blanton, M. R., West, A. A., et al. 2005, AJ, 129, 2692

Xue, X.-X., Rix, H.-W., Ma, Z., et al. 2015, ApJ, 809, 144

York, D. G., Adelman, J., Anderson, J. E., Jr., et al. 2000, AJ, 120, 1579

Zechmeister, M., Kürster, M. 2009, A&A, 496, 577

Zinn, R. 1993, The Globular Cluster-Galaxy Connection, ASP Conference Series, Vol 48, 38

Zinn, R., Horowitz, B., Vivas, A. K., et al. 2014, ApJ, 781, 22

Zolotov, A., Willman, B., Brooks, A. M., et al. 2009, ApJ, 702, 1058

Zucker, D. B., Belokurov, V., Evans, N. W., et al. 2006, ApJ, 643, L103

Zucker, D. B., Belokurov, V., Evans, N. W., et al. 2006, ApJ, 650, L41